TUM School of Engineering and Design

Experimental Investigation of the Thermal Conductivity through the Layers of the Electrode-Separator Stack in Lithium-Ion Cells

Marco Steinhardt, M.Sc.

Vollständiger Abdruck der von der TUM School of Engineering and Design der Technischen Universität München zur Erlangung des akademischen Grades eines

Doktors der Ingenieurswissenschaften (Dr.-Ing.)

genehmigten Dissertation.

Vorsitz:		Prof. Dr.-Ing. Hartmut Spliethoff
Prüfer/in der Dissertation:	1.	Prof. Dr.-Ing. Andreas Jossen
	2.	Prof. Dr. rer. nat. Hans Jürgen Seifert

Die Dissertation wurde am 16.03.2022 bei der Technischen Universität München eingereicht und durch die TUM School of Engineering and Design am 27.07.2022 angenommen.

Abstract

In situations such as safety-critical thermal runaway or while charging or discharging at extremely high rates, significant temperature increases and gradients occur within lithium-ion cells. Strong temperature increase and gradients have a negative effect on both aging and power availability, making thermal cell models highly significant. High-fidelity simulations require precise thermal parameters such as thermal conductivity to properly model the temperature distributions used for cell design studies, aging predictions, safety assessments, or other simulation purposes. Precise parameterization takes into account the dependence of the thermal conductivity on battery states such as cell temperature, state of charge (SOC), external pressure, or state of health (SOH). The determination of thermal conductivity is usually time-consuming, costly, and subject to considerable measurement uncertainties. To support high-fidelity simulations, this thesis focuses on the development of low-effort and accurate thermal conductivity measurement methods for lithium-ion cells. In addition, a critical literature review summarizes the experimental results of other studies and suggests further research directions. The results of this thesis are limited to the through-plane direction of the electrode-separator stack, as this is the dominant heat flow direction for common battery thermal management systems (BTMSs).

Two measurement methods were developed in this thesis, one for prismatic cells and another used for the cylindrical cell format. For the first time, the well-known guarded hot plate (GHP) method was adapted for the prismatic format and validated with a stainless steel reference material. In order to evaluate the through-plane conductivity, the influence of the prismatic housing had to be compensated for, which was accomplished through measurements of the electrical resistivity and the use of theories such as the Wiedemann-Franz law. The method is demonstrated between -10 and +40 °C at external pressures of 37.1 and 74.2 kPa. For the cylindrical format, this thesis is one of the first demonstrations of the variant-convective cooling (VCC) method, which simultaneously measures the thermal conductivity and the heat capacity. This method is characterized by its low experimental effort and a complex evaluation process and was demonstrated between +10 and +40 °C at three different SOCs on an 18650 and a 21700 cell format. In addition to the experiments, the literature review in this thesis addresses all other cell formats, further length scales and findings on the SOH dependence of the through-plane conductivity.

According to the experimental results of this thesis, the through-plane conductivity of the electrode-separator stack decreases significantly by -1.5 to -0.5% K^{-1} with increasing temperature. Changes in the SOC can affect the thermal conductivity by 9%, which is above the 6% measurement uncertainty determined for the two methods in this thesis. Increasing the external pressure from 37.1 to 74.2 kPa for the prismatic cell increased the through-plane conductivity by 11.9%. The literature review showed a decrease in thermal conductivity as the age of the cell increased, but more research is needed to confirm the mechanisms and the origin of the SOH dependence. In addition, a better quantification of the thermal contact resistance would be helpful and thermal conductivity measurement data at elevated temperatures is required for safety simulations. This should be the focus of further research.

Kurzfassung

Während des thermischen Durchgehens oder schnellen Ladens/Entladens, ist in Lithium-Ionen-Zellen mit einem erheblichen Temperaturanstieg und -gradienten zu rechnen. Dieser Anstieg und die Gradienten haben eine negative Auswirkung auf Zellalterung und Leistungsverfügbarkeit. Daher sind in hochgenauen Batteriesimulationen präzise thermische Parameter wie die Wärmeleitfähigkeit notwendig, um beispielsweise in Zelldesignstudien, Alterungsvorhersagen und Sicherheitsbewertungen die Temperatur in der Zelle richtig vorherzusagen. Eine Parametrierung der Wärmeleitfähigkeit muss neben der Genauigkeit auch die Abhängigkeiten von der Zelltemperatur, Außendruck, SOC und SOH berücksichtigen. Die Bestimmung der Wärmeleitfähigkeit ist meist zeitaufwendig, kostenintensiv und mit erheblichen Messunsicherheiten behaftet. Zur Unterstützung von hochgenauen Batteriesimulationen konzentriert sich diese Arbeit deshalb auf die Entwicklung von aufwandsarmen und genauen Wärmeleitfähigkeitsmessungen für Lithium-Ionen-Zellen. Darüber hinaus fasst eine Übersichtsarbeit die experimentellen Ergebnisse anderer Studien zusammen und erarbeitet Empfehlungen für zukünftige Forschungsansätze. Diese Arbeit beschränkt sich auf die orthogonale Wärmeleitfähigkeit des Elektroden-Separator-Stapels, da dies die dominante Wärmeflussrichtung für übliche Wärmemanagementsysteme ist.

In dieser Arbeit wurden zwei Messmethoden für die Wärmeleitfähigkeit entwickelt, wobei erstere Methode an einer prismatischen Zelle und letztere an zylindrischen Zellen demonstriert wurde. Für das prismatische Format wurde das erprobte Guarded-Hot-Plate (GHP) Verfahren für Lithium-Ionen-Zellen adaptiert und mit einem Edelstahl-Referenzmaterial validiert. Um die Wärmeleitfähigkeit berechnen zu können, musste der Einfluss des prismatischen Gehäuses kompensiert werden, was durch elektrische Widerstandsmessungen und der Anwendung des Wiedemann-Franz-Gesetzes gelang. Das Verfahren für die prismatische Zelle wurde zwischen -10 und +40 °C bei Außendrücken von 37,1 und 74,2 kPa angewendet. Für das zylindrische Format ist diese Arbeit eine der ersten Weiterentwicklungen der Variant-Convective-Cooling (VCC) Methode, welche gleichzeitig die Wärmeleitfähigkeit und -kapazität bestimmen kann. Die VCC-Methode zeichnet sich durch einen geringen experimentellen Aufwand und einen komplexen Auswerteprozess aus. Eine Demonstration der VCC-Methode wurde zwischen +10 und +40 °C bei drei verschiedenen SOCs für eine 18650er und eine 21700er Zelle durchgeführt. Die Übersichtsarbeit befasst sich abschließend mit allen anderen Zellformaten, weiteren Längenskalen und Erkenntnissen zur SOH-Abhängigkeit der orthogonalen Wärmeleitfähigkeit.

Den Ergebnissen dieser Arbeit zufolge nimmt die Wärmeleitfähigkeit des Elektroden-Separator-Stapels mit steigender Temperatur deutlich um -1,5 bis -0,5% K^{-1} ab. Durch Änderungen im SOC konnte die Wärmeleitfähigkeit in dieser Arbeit um 9% beeinflussen werden, was über der ermittelten Messunsicherheit von 6% liegt. Eine Erhöhung des Außendrucks von 37,1 auf 74,2 kPa für die prismatische Zelle erhöhte die Wärmeleitfähigkeit um 11,9%. Die Übersichtsarbeit ergab eine Abnahme der Wärmeleitfähigkeit mit zunehmendem Alter der Zelle, jedoch benötigt es weitere Forschungsarbeiten, um den genauen Ursprung der SOH-Abhängigkeit zu erklären. Darüber hinaus wäre eine bessere Quantifizierung der thermischen Kontaktwiderstände im Stapel und Messdaten bei erhöhten Temperaturen für Sicherheitssimulationen wünschenswert. Dies sollte der Schwerpunkt weiterer Forschung sein.

Contents

Abbreviations

Please note that the list below is based on the main part of this thesis and does not fully cover the included papers. Each paper itself includes a complete individual definition.

ASTM	American Society for Testing and Materials
BEV	battery electric vehicle
BTMS	battery thermal management system
CC	constant current
CMIP6	Coupled Model Intercomparison Project Phase 6
CRM	component-resolved model
EV	electric vehicle
FEM	finite element method
G	graphite
GHP	guarded hot plate
HEV	hybrid electrical vehicle
LCM	lumped-circuit model
LCO	lithium cobalt oxide
LFP	lithium iron phosphate
LRM	layer-resolved model
NCA	lithium nickel cobalt aluminum oxide
NCM	lithium nickel cobalt manganese oxide
NMC	lithium nickel manganese cobalt oxide
OCV	open circuit voltage
ODE	ordinary differential equation
PDE	partial differential equation

SDM . . . . . single-domain model

SEI . . . . . solid electrolyte interphase

SOC . . . . . state of charge

SOH . . . . . state of health

TIS . . . . . thermal impedance spectroscopy

VCC . . . . . variant-convective cooling

Symbols

Please note that the list below is based on the main part of this thesis and does not fully cover the included papers. Each paper itself includes a complete individual definition.

$A_\perp$ . . . . . Cross-sectional area perpendicular to the heat flux in m^2

Bi . . . . . Biot number

C_{cell} . . . . . Lumped heat capacity of the cell in $\mathrm{J\,K^{-1}}$

c_{cell} . . . . . Specific heat capacity of the cell in $\mathrm{J\,kg^{-1}\,K^{-1}}$

c_p . . . . . Specific heat capacity at constant pressure in $\mathrm{J\,kg^{-1}\,K^{-1}}$

CCC . . . . . Cell cooling coefficient in $\mathrm{W\,K^{-1}}$

d_A . . . . . Thickness of anode coating in m

d_{aCC} . . . . . Thickness of anode current collector in m

d_C . . . . . Thickness of cathode coating in m

d_{cCC} . . . . . Thickness of cathode current collector in m

d_{cell} . . . . . Thickness of cell in thermal conductivity measurement in m

d_i . . . . . Layer thickness in the electrode-separator stack in m

d_L . . . . . Characteristic length in the Biot theory in m

d_r . . . . . Thickness of thermal reference material in m

d_S . . . . . Thickness of separator in m

d_x . . . . . Thickness of test sample in thermal conductivity measurement in m

E_a . . . . . Activation energy in $\mathrm{J\,mol^{-1}}$

ε . . . . . Porosity of stack layer

G_{Rk} . . . . . Geometric factor for evaluating thermal conductivity

h_{BTMS} . . . . . Heat transfer coefficient to the battery thermal management system in $\mathrm{W\,m^{-2}\,K^{-1}}$

I_{cell} . . . . . Electric cell current (positive for charge) in A

$k_\perp$ . . . . . Thermal through-plane conductivity of the electrode separator stack in $\mathrm{W\,m^{-1}\,K^{-1}}$

k_A . . . . . Thermal conductivity of anode coating in $\mathrm{W\,m^{-1}\,K^{-1}}$

k_{aCC} . . . . . Thermal conductivity of anode current collector in $\mathrm{W\,m^{-1}\,K^{-1}}$

k_C . . . . . Thermal conductivity of cathode coating in $\mathrm{W\,m^{-1}\,K^{-1}}$

k_{cCC} . . . . . Thermal conductivity of cathode current collector in $\mathrm{W\,m^{-1}\,K^{-1}}$

$k_{housing}$ . . . . . Thermal conductivity of the cell housing in $\mathrm{W\,m^{-1}\,K^{-1}}$

k_i . . . . . Thermal conductivity of the layer in the electrode-separator stack in $\mathrm{W\,m^{-1}\,K^{-1}}$

k_L . . . . . Thermal conductivity in the Biot theory in $\mathrm{W\,m^{-1}\,K^{-1}}$

k_m . . . . . Thermal conductivity obtained through measurements in $\mathrm{W\,m^{-1}\,K^{-1}}$

$k_{mandrel}$ . . . . . Thermal conductivity of the mandrel inside the jelly roll in $\mathrm{W\,m^{-1}\,K^{-1}}$

$k_{overhang}$ . . . . . Thermal conductivity of the anode overhang in $\mathrm{W\,m^{-1}\,K^{-1}}$

k_φ . . . . . Thermal conductivity in azimuth coordinate direction in $\mathrm{W\,m^{-1}\,K^{-1}}$

k_r . . . . . Thermal conductivity in the radial coordinate direction in $\mathrm{W\,m^{-1}\,K^{-1}}$

k_S . . . . . Thermal conductivity of separator in $\mathrm{W\,m^{-1}\,K^{-1}}$

k_z . . . . . Thermal conductivity in height coordinate direction in $\mathrm{W\,m^{-1}\,K^{-1}}$

$k_{||}$ . . . . . Thermal in-plane conductivity of the electrode-separator stack in $\mathrm{W\,m^{-1}\,K^{-1}}$

P_h . . . . . Heat rate of electrical heater in W

φ . . . . . Azimuth in cylindrical coordinate system in rad

ϕ_{ref} . . . . . Reference value in the Arrhenius law

Q_{cell} . . . . . Usable battery capacity in Ah

ΔQ . . . . . Change in the usable battery capacity in Ah

$\dot{q}$ . . . . . Volumetric heat rate in $\mathrm{W\,m^{-3}}$

$\dot{Q}_{BTMS}$ . . . . . Heat rate that is dissipated to the battery thermal management system in W

$\dot{Q}_x$ . . . . . Heat rate in the thermal conductivity measurement in W

$\dot{Q}_{cell}$ . . . . . Total heat rate within the cell in W

$\vec{q}_x$ . . . . . Heat flux in thermal conductivity measurements in $\mathrm{W\,m^{-2}}$

r . . . . . Radius in the cylindrical coordinate system in m

$R_{c,housing}$ . . . . . Thermal contact resistance between stack and cell housing in $\mathrm{cm^2\,K\,W^{-1}}$

$R_{c,n}$ . . . . . Thermal contact resistance of stack interface n in $\mathrm{cm^2\,K\,W^{-1}}$

R_{in} . . . . . Lumped internal thermal cell resistance in $\mathrm{K\,W^{-1}}$

R_{out} . . . . . Lumped external thermal cell resistance in $\mathrm{K\,W^{-1}}$

ρ . . . . . Volumetric mass density in $\mathrm{kg\,m^{-3}}$

ρ_{cell} . . . . . Average volumetric mass density of the cell in $\mathrm{kg\,m^{-3}}$

T . . . . . Temperature in K

t . . . . . Time in s

$t_{1/2}$ . . . . . Rise time of laser flash method in s

T_{amb} . . . . . Ambient temperature in K

T_{err} . . . . . Error in the simulated temperature in K

T_{ref} . . . . . Reference temperature in the Arrhenius law in K

ΔT_{cell} . . . . . Spatial temperature difference within the cell in K

$\Delta T_{max,ccc}$ . . . . Spatial temperature difference of the cell cooling coefficient in K

ΔT_r . . . . . Spatial temperature difference along the reference material in K

ΔT_{system} . . . . . Spatial temperature difference between cells in K

ΔT_t . . . . . Temporal temperature difference in K

$\Delta T_{t,s}$ . . . . . Temporal temperature difference on the cell surface in K

ΔT_x . . . . . Spatial temperature difference in thermal conductivity measurements in K

$\overline{T}_{cell}$ . . . . . Mean cell temperature in K

U_{cell} . . . . . Voltage at the terminals of the cell in V

U_{ocv} . . . . . Open circuit voltage in V

U_Ω . . . . . Ohmic overvoltage in V

$U_{p,n}$ . . . . . Polarization voltage in V

x . . . . . X coordinate in the Cartesian coordinate system in m

$\underline{Z}$ . . . . . Electrical cell impedance in Ω

z . . . . . Height in cylindrical coordinate system in m

$\Delta\underline{Z}$ . . . . . Change in electrical cell impedance in Ω

1 Introduction into heat transfer inside lithium-ion batteries

According to climate change simulations, human-induced global temperature rise will reach tipping points in the climate system in a few decades if countermeasures are not taken. Tipping points are events that cause an irreversible and self-sustaining acceleration of climate change, such as the melting of the ice sheets (1-3 °C) or the thawing of permafrost soils (>5 °C) [1]. For this reason, the 2015 Paris Climate Agreement obliges all parties to keep the temperature rise below 2 °C and continue efforts to limit the rise to 1.5 °C above which grave consequences for human and non-human life are predicted [2]. Both temperature limits and the observed global temperature increase are shown in Figure 1.1 a). In addition, simulations of the global temperature increase in the Coupled Model Intercomparison Project Phase 6 (CMIP6) [3] show that the increase in temperature is primarily caused by humans. Given the proximity of the global temperature increase to the 1.5 °C temperature limit and the slope of the increase, it seems obvious that human countermeasures are becoming increasingly necessary.

Road transport, including passenger and freight transport, was responsible for 11% of global greenhouse gas emissions in 2018 (58 Gt CO_2e) [4]. Greenhouse gas emissions are usually measured in CO_2 equivalents (CO_2e), taking into account various gases such as carbon dioxide CO_2, nitrous oxide N_2O and methane CH_4 based on their global warming potential shown in Figure 1.1 b) [5]. The global warming potentials are used to calculate the carbon dioxide equivalent, which compares the effects of each greenhouse gas with those of CO_2. Roelfsema et al. [6] forecast global greenhouse gas emissions in 2030 in various scenarios. According to their results, even the measures contained within the Paris Agreement are not enough to keep the temperature rise below 2 °C. This implies that current measures to reduce greenhouse gas emissions will have to be tightened in the future if significant harms are to be avoided. Given the need to drastically reduce emissions, the question arises as to which measures can have the greatest impact with the least effort. In the road transport sector for example, viable alternatives are already emerging to replace many fossil-fuel-powered vehicles. Figure 1.1 b) shows the sum of direct and indirect emissions from five sectors. It can be seen that using electric vehicles (EVs) can reduce emissions by a maximum of 11%, which corresponds to their entire share of the road transport sector.

In 2020, Knobloch et al. [7] examined the net emission reduction of EVs in 59 regions of the world compared to petrol cars for the index year 2015. They found that replacing petrol cars with EVs would have saved up to 64% of CO_2 emission, depending heavily on the country where the EV was used and manufactured (see Figure 1.2). In this study, petrol cars include non-plug-in hybrid electrical vehicles (HEVs) and cars that run on petrol or diesel. Their method of calculating emissions per driving distance is shown on the left-hand side of Figure 1.2. Knobloch et al. [7] considered the emissions from production and end-of-life as well as the emissions during the use of the car. They also divided the emissions into electrical and non-electrical emissions. Differences between regions are explained by the share of fossil fuels in the country's electricity mix. In addition, Knobloch et al. [7] took into account regional differences in tank-to-wheel emissions when using petrol cars, which reflects that cars in the

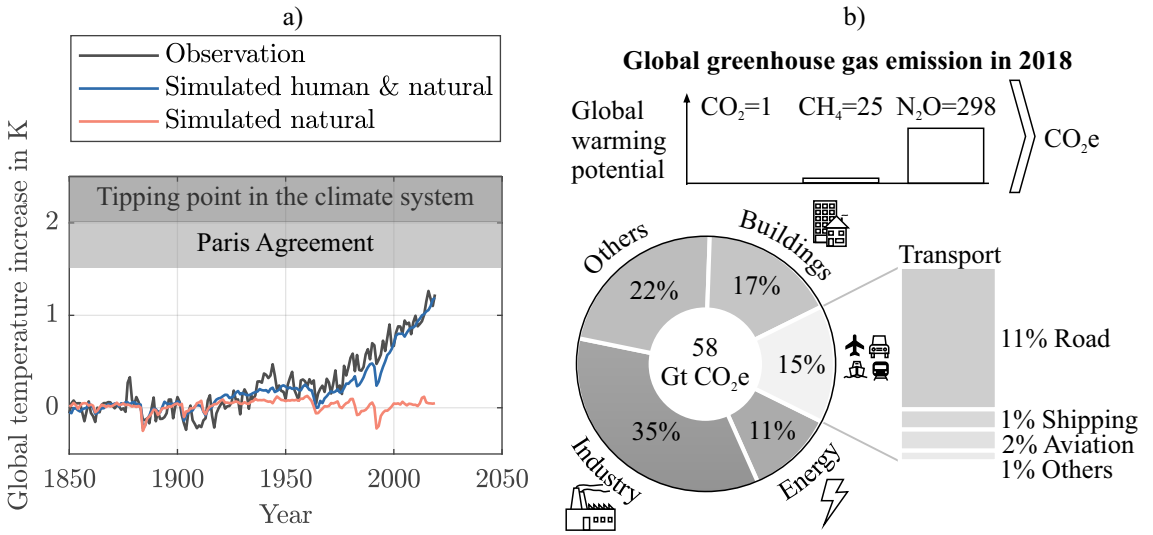

Figure 1.1: Climate change and the fraction of road transport on the global greenhouse gas emission. a) Global average temperature increase in accordance with the Paris Agreement with CMIP6 simulations [3] showing the human impact on climate change. b) Global greenhouse gas emission in 2018 with the fraction of each sector and transportation subsectors [4].

USA have higher energy consumption than in France. It should be noted that this study assumes a location-independent energy consumption of 190 $\mathrm{Wh\,km^{-1}}$ for the EV without regional differences. Knobloch et al. [7] therefore assumes that user behavior will change when switching from petrol cars to EVs.

The emission reduction calculated by Knobloch et al. [7] for five selected countries based on their respective energy mixes in 2015 is shown in the radar chart in Figure 1.2. In Germany, for example, a petrol car has a calculated median emission of 282 $\mathrm{gCO_2e\ km^{-1}}$, while an EV reduces this emission to 212 $\mathrm{gCO_2e\ km^{-1}}$, which means a 25% decrease in greenhouse gas emissions. In France, with a higher proportion of nuclear energy in the energy mix than in Germany, a reduction in emissions of 64% is assumed. In the USA, which accounts for the highest proportion of global transport emissions, the 46% reduction is between that of Germany and France. Due to the higher shares of coal in their respective energy mixes, EVs in China are predicted to lead to an emissions reduction of only 10% and in India, EVs would increase emissions by as much as 15%. This shows that the electrification of the road transport sector was already able to reduce greenhouse gas emissions in 2015 and, as shown by the example of France, a reduction of 64% was possible.

Recent studies on the potential for greenhouse gas emissions reduction by switching to EVs have suggested even greater differences. For example, the International Council on Clean Transportation [8] calculated an emissions change in 2021 of between -19% and -69% for the countries in Figure 1.2. Thus, they calculate that the replacement of petrol cars by EVs would also reduce greenhouse gases in India. For Germany, the International Council on Clean Transportation came to a stronger emission reduction of -58% in 2021 than Knobloch et al. [7] in 2015. This more optimistic reduction of -58% can be explained by assuming a longer EV life of 243 000 km, lower electricity emissions and lower emissions for battery production of 54 kg $\mathrm{CO_2e\ kWh^{-1}}$. In any case, both studies predict a significant reduction in greenhouse gas emissions from the switch to EVs in the transport sector.

Lithium-ion cells are a key component of a battery electric vehicle (BEV), responsible for around a third of total BEV costs [10] and 41% of non-electric greenhouse gas emissions (see Figure 1.2). Despite

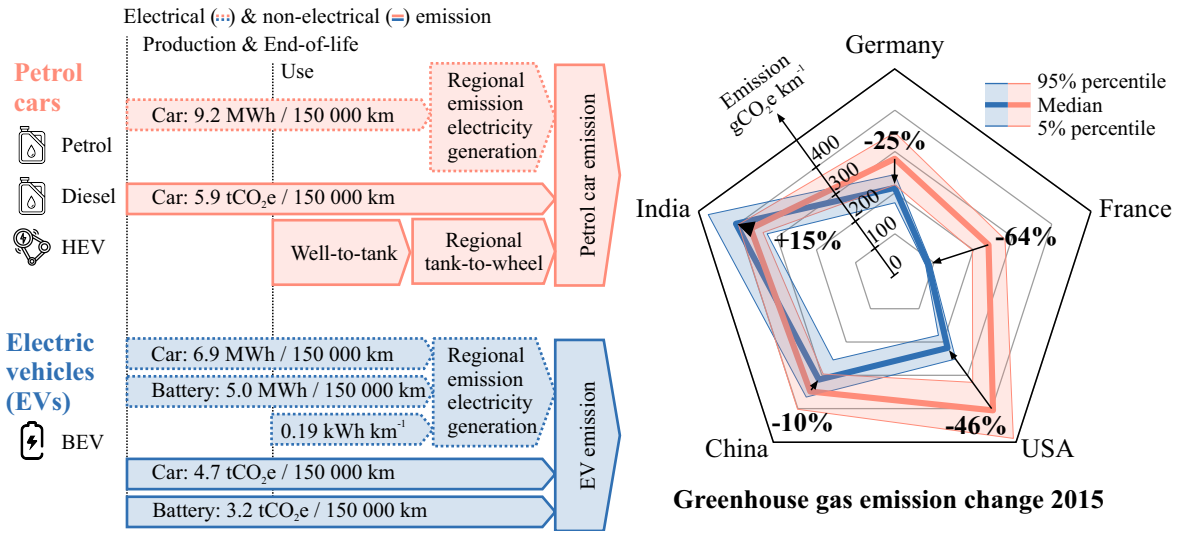

Figure 1.2: Greenhouse gas emission change due to electrification of passenger road transport considering the local emissions of electricity generation in 2015 [7]. EV calculations are based on a battery energy of 70 kWh, a battery mass of 350 kg, and a battery lifetime of 150 000 km [9].

the non-negligible environmental impact of the battery itself, the net beneficial effects on greenhouse gas emissions are leading governments to incentivize the transition to EVs. Measures include purchase subsidy, tax exemptions, emission standards, or investments in charging infrastructure to increase the market share of EVs [11]. In response to these pro-EV policy measures, many new production lines for battery cells with a volume over 300 GWh per year are planned in Europe and more production is needed worldwide to cope with the growing EV deployment [12]. In addition, an increasing number of car manufacturers such as Volkswagen AG, General Motors Company, or Mercedes-Benz Group are announcing an end to production of cars with internal combustion engines between 2030 and 2035 [13]. The current trend towards more EVs with increasing sales since 2015 [11] underscores the need for more research in the field of lithium-ion batteries in order to further improve their performance, costs, and sustainability.

Current development and production targets for lithium-ion batteries focus on improving performance and cost [14], which exacerbates thermal problems during the use-phase [15]. For example, increasing the specific energy often comes at the cost of inactive material such as the current collectors [16], leading to an increase in volumetric heat and causing a more inhomogeneous temperature distribution [15, 17]. In addition, new high-energy active materials such as lithium- and manganese-rich lithium nickel cobalt manganese oxide (NCM) can increase heat generation by four times compared to conventional materials (e.g. lithium nickel cobalt aluminum oxide (NCA)) [18]. Thermal issues can become a problem in situations such as fast charging if the temperature rise reaches certain temperature thresholds (e.g. 50 °C [19]) or temperature gradients arise inside the battery [20, 21]. Above 60 °C, battery aging accelerates [22] and between 80 and 120 °C safety-critical reactions are triggered [23–25] which can release between 5 and 21 times of the rated energy during thermal runaway [26]. This shows that energy density, safety and the charging performance of a battery all influence each other as they are coupled via temperature.

It is expected that battery development strategies for mobile high-energy applications will shift towards an ecologically optimized battery [14], which can be achieved at the production, use, and end-of-life

Table 1.1: Comparison of the volumetric heat rate of a high-energy and a high-power parallel circuit with similar maximum charging power. The considered high-energy (3.35 Ah, INR18650 MJ1) and high-power cell (2.5 Ah, US18650VTC5A) was manufactured by LG Chem Ltd and Sony, respectively.

	High energy: MJ1		High power: VTC5A		VTC5A (5p) / MJ1 (9p)
	(1p)	(9p)	(1p)	(5p)	
Number of parallel cells	1	9	1	5	56 %
Maximum charging current / A	3.35	30.15	6.00	30.00	100 %
Electrical pulse resistance (10 s) [a] / mΩ	43.2	4.8	25.4	5.1	106 %
Cell volume / cm^3	17.5	157.5	16.6	83.0	53 %
Volumetric heat rate [b] / $mW\,cm^{-3}$	27.7	27.7	55.2	55.2	199 %
Rated energy / Wh	12.2	109.6	9.0	45.0	41 %

a) Calculated from the voltage difference after a current pulse of 1 C at an state of charge (SOC) of 50%. **b)** The heating rate is calculated by multiplying the square of the maximum charging current by the electrical pulse resistance.

phase. For the production phase, using lithium iron phosphate (LFP) instead of ternary layer oxides as cathode material can be considered more sustainable due to the greater abundance of its constituents and its longer cycle life [14]. Although LFP cells have lower cell-level energy densities, using a cell-to-pack design can achieve pack-level energy densities that are comparable to current EV packs [27]. Due to the acceptable energy density with cell-to-pack design, higher safety and longer service life, LFP cells are promised a renaissance in EVs [28]. From a thermal point of view, LFP cells have lower thermal conductivity than lithium nickel manganese cobalt oxide (NMC) or NCA cells [29], which could increases temperature gradients with greener battery designs.

Downsizing the battery is another design measure to save CO_2. In Figure 1.2 the production emission of 3.2 tCO_2e correlates with the installed battery energy. Less installed energy means less EV range, but this metric could be replaced by metrics such as the P3-Charge-Index [30]. The P3-Charging-Index classifies an EV as suitable for long-distance journeys if 300 km can be charged within 20 min, which corresponds to the average break time at German motorway service stations. Favoring kilometers per minute, may lead to a shift from high-energy to high-power electrode designs, which can increases the heat generation per volume. In Table 1.1, for example, a parallel connection of five high-power cells and nine parallel high-energy cells can be charged with approximately the same current, which corresponds to the same P3-Charging-Index. In terms of emissions, the high-power solution would certainly be superior, since four cells can be saved in this parallel connection. However, the volumetric heat generation increases by 99% with the high-power solution, since the same ohmic losses are distributed over almost half the cell volume. Therefore, this more environmentally friendly, high-power solution would produce a faster temperature increase.

Batteries can also be ecologically optimized in the use and end-of-life phase, which also affects the thermal behavior of the cell. For the use phase, optimizing battery life is a key measure as it directly affects the total battery emissions over the total mileage of the EV (see Figure 1.2). The battery thermal management system (BTMS), which includes all components of a battery system to control cell temperature, can be used to extend battery life. For example, an ecologically optimized BTMS can reduce greenhouse gas emissions by 25% by extending the lifetime of the cell [31]. From a ecologically cell design perspective, a trend towards large-volume battery cells is likely, as this would facilitate cell dismantling and thus recycling [17]. However, large-volume lithium-ion cells often increase the

characteristic length between the cell core and the cell's surroundings, which increases the temperature gradients according to Biot theory.

Overall, a profound understanding of heat transfer to enable the prediction of temperature rise and spatial temperature gradients is becoming increasingly important in view of current efforts to improve safety, service life, fast charging and energy density. The importance of heat transfer in lithium-ion cells will not diminish when the focus of development and battery design shifts toward more sustainable battery production. Thermal models based on precise parameters such as thermal conductivity and heat capacity are essential for an optimized battery design. Therefore, this thesis focuses on the exact experimental determination of thermal conductivity in order to make it easier for thermal models to find the optimal design for lithium-ion batteries.

1.1 Fundamentals of lithium-ion batteries

There are different length scales at which research on lithium-ion cells is carried out [32] from the atomic scale [33–35] to battery systems scale [36, 37]. This work considers the stack, cell, and system scales shown in Figure 1.3 with a focus on the full-cell scale. In Figure 1.3 a), a double-coated electrode-separator stack is shown, which comprises two current collectors, two anode coatings, two cathode coatings, and two separator layers [38–40]. In the following, the electrode-separator stack is referred to simply as the stack. The porous active coatings store the chemical energy, the porous separators enables lithium-ion flux, and the current collectors comprise the pathway of the electrons to the outer cell terminals [41]. The electron flux in the solid phase and the lithium ion flux in the liquid electrolyte during charging are represented by the black arrows in Figure 1.3 a). The stack and the cell housing completes the full-cell shown in Figure 1.3 b). The stack is either wound or stacked during production to fit into a prismatic, cylindrical or pouch cell format. The electrical cell current (I_{cell}) generates heat that can increase the stack temperature. In most BTMS, the heat within the stack is dissipated perpendicular to the stack, which is shown by the red arrows in Figure 1.3 b). For this reason, this thesis focuses on through-plane conductivity ($k_{\perp}$). It is not just the stack that generates heat, the cell-internal connection from the stack to the terminals [42] and the cell interconnection of the battery system release thermal energy [16]. To limit temperature increase, BTMSs are utilized to transport the heat to the environment. An example BTMS for prismatic cells is shown in Figure 1.3 c).

An example of the heat equation for a 2D thermal model of a cylindrical cell is given in Equation 1.1. To the left of Equation 1.1 is the heat stored in the material, which is the product of the radius in the cylindrical coordinate system (r), the volumetric mass density (ρ) and the specific heat capacity (c_p) at constant pressure. Parameters such as density are location-dependent (r,z), since the cell housing has a different heat capacity than the stack. On the far right in Equation 1.1, the heat rate ($r\dot{q}(r,z,t)$) takes into account the reversible and irreversible heat generation. The term between heat capacity and the heat rate describes the heat flux balance, which depends on the thermal conductivity and the temperature gradient $\vec{\nabla}T(r,z,t)$. The layered structure of the stack in Figure 1.3 a) is often abstracted as a homogeneous material with an anisotropic conductivity in the in-plane ($k_{||}$) and through-plane direction ($k_{\perp}$). In the case of cylindrical cells (Equation 1.1), the through-plane direction is aligned with the radial coordinate ($k_r = k_{\perp}$) and the in-plane is aligned with the axial coordinate ($k_z = k_{||}$). Equation 1.2 and 1.3 define $k_{\perp}$ and $k_{||}$, respectively. Accordingly, $k_{\perp}$ and $k_{||}$ depend on the layer thicknesses (d_i) and conductivity (k_i) of the anode coating (d_A,k_A), the cathode coating (d_C,k_C), the separator layer (d_S,k_S), the anode current collector (d_{aCC},k_{aCC}) and the cathode current collector

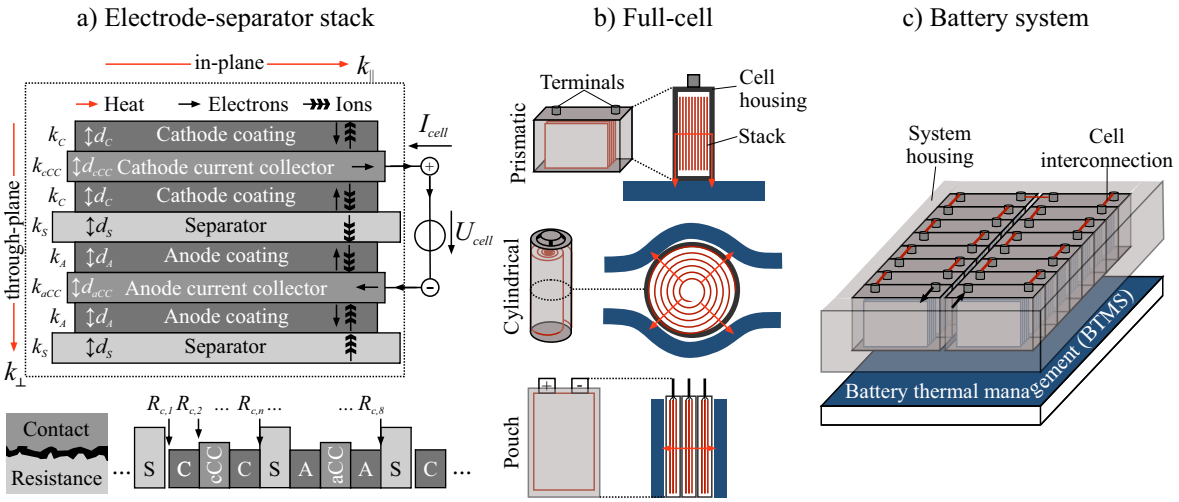

Figure 1.3: Definition of the length scales studied in this thesis with their heat generation, direction of heat flow and heat dissipation through the BTMS highlighted in blue. a) Stack scale with the definition of the through-plane ($k_\perp$) and in-plane ($k_{||}$) thermal conductivity, the layer thicknesses (d_i) and the layer conductivities (k_i). b) Full-cell scale with the main heat flow direction to the BTMS. c) Battery system scales with a BTMS cooling plate under a prismatic battery system.

(d_{cCC},k_{cCC}), which are shown in Figure 1.3. In addition, $k_\perp$ depends on the cumulative thermal resistances between the stack-layers $\sum_n(R_{c,n})$.

$$r\rho(r,z)c_p(r,z)\frac{\partial T(r,z,t)}{\partial t} = \vec{\nabla}\cdot\left(\begin{pmatrix} rk_r(r,z) & 0 \\ 0 & rk_z(r,z)\end{pmatrix}\vec{\nabla}T(r,z,t)\right) + r\dot{q}(r,z,t) \tag{1.1}$$

$$k_\perp = \frac{\sum_i d_i}{\sum_n(R_{c,n}) + \sum_i \frac{d_i}{k_i}} \tag{1.2}$$

$$k_{||} = \frac{\sum_i d_i k_i}{\sum_i d_i} \tag{1.3}$$

Heat, a form of dynamic energy defined as the disordered motion of microscopic particles [43], is generated in each layer of the stack in Figure 1.3 a). The total heat rate ($\dot{Q}_{cell}$) within the cell can be described by the energy-balance-method using thermodynamic phenomena or by the local-heat-generation-method using transport and kinetic phenomena [44]. A common exemplar of the energy-balance-method is Equation 1.4, introduced by Bernardi et al. [45] and simplified by Gu et al. [46]. Accordingly, $\dot{Q}_{cell}$ depends on the current (I_{cell}) and voltage (U_{cell}) at the cell terminals, the open circuit voltage (U_{ocv}) and the entropic heat coefficient ($\partial U_{ocv}/\partial T$). Equation 1.4 assumes no phase change or mixing effects, no concentration gradients in the cell, uniform reaction rates, and a single reaction contributing to $\dot{Q}_{cell}$ [46]. On the other hand, the local-heat-generation method from Rao

et al. [44] distinguishes between heat in electrochemical interfaces and bulk phases. While the heat derived from the energy-balance method has to be distributed evenly over the entire stack [47], the local-heat-generation method enables a layer-specific calculation. The local-heat-generation method therefore appears to be superior, but little experimental validation exist and certain processes such as the reversible Peltier effect are often neglected [48–50]. Heubner et al. [51] used a single-layer lithium cobalt oxide (LCO)-graphite (G) cell with a reference electrode and a temperature sensor for each layer and analyzed the individual heat contribution of the stacked layers by a galvanostatic intermittent titration technique. Their measurement results showed a clear difference in the local heat generation with the lowest heat fraction in the separator and the highest in the cathode. Zhu et al. [52] also measured dominant heat generation in the cathode for a single-layer NMC-G cell and a C-rate of 0.5. They expressed the difficulty of measuring the individual heat fraction in the stack, which they achieved using a Swagelok battery with local infrared temperature measurement. Due to the difficulties with the local-heat-generation method, the energy-balance-method as in Equation 1.4 is usually favored in thermal models.

$$\dot{Q}_{cell} = I_{cell}(U_{cell} - U_{ocv}) + I_{cell}T\frac{\partial U_{ocv}}{\partial T} \tag{1.4}$$

Electrical connections within the cell or between the cells can contribute significantly to the overall heat generation. For example, the electrical connections inside the commercial high-energy cell MJ1 from LG Chem Ltd. have an ohmic resistance of 2.7 mΩ [42], which is 6% of the cell's total pulse resistance (10 s) of 44.7 mΩ [53]. This releases about 6% of the cell's heat rate outside of the stack. Outside the cell, the connection to the external circuit creates additional electrical resistances, which are between 0.2 and 0.4 mΩ for spot-welded 18650 cells [54]. In addition to the resistance of the cell connection, system components such as cell connectors or safety contactors increase the overall heat rate of every battery system. According to Hosseinzadeh et al. [55], the interconnection resistance between the cells increases the pure cell resistance by 1% to 10%. Keyser et al. [16] compared the heat generation between a 10s1p module and a single cell and observed an increase in heat generation of up to 33% due to the connections between the cells in the module. This increase is in line with the measured resistance increase in the DriveBattery2015 research project, which was financially supported by the Federal Ministry for Economic Affairs and Energy (BMWi) under the grant number 03ET6060F [56]. Compared to the cell resistance of a high-power and high-energy cell investigated in DriveBattery2015, the system resistance for the high-energy (96s5p) and high-power system (96s10p) increased by 36% and 34%, respectively. This shows that cell external heat sources should not be neglected, especially with high power utilization.

The BTMS regulates the cell temperature by heating or cooling, preferably without causing temperature differences within (ΔT_{cell}) or between (ΔT_{system}) the cells [20, 37]. BTMS design goals often specify a maximum of 2 °C for ΔT_{cell} [57] and 3 to 5 °C for ΔT_{system} [57–59]. In addition to optimal temperature control and low temperature differences, energy consumption, effects on battery aging, costs, weight increase, safety, and reliability are further quality measures for BTMSs. [60]. BTMSs can be divided into cooling and heating systems [61, 62] or active and passive systems, with the passive type using the ambient temperature (T_{amb}) without auxiliary power consumption. Active cooling systems such as air, liquid, or refrigerant cooling are commonly used in EVs. While air cooling (e.g. Toyota Prius [63]) offers low system complexity and cost, it displays low cooling performance, high temperature gradients and requires the highest additional volume [62, 64]. On the other hand, refrig-

erant cooling (e.g. BMW i3 [63]) has a high degree of efficiency, the strongest cooling performance, small temperature gradients between cells, the lowest additional volume, but the highest costs and system complexity [64]. With battery heating, which can be further subdivided into internal and external heating [60], the heating speed is an additional quality measure. Optimized cooling and heating can be the key to faster charging of batteries in low or high ambient temperatures [15, 27]. Every interaction between the BTMS and the cell causes temperature differences, which in turn depend on the thermal conductivity within the cell. The thermal conductivity is therefore an important parameter for the optimization of cooling and heating of lithium-ion cells.

1.2 Multiphysical modeling of lithium-ion cells

Lithium-ion cell models are used to improve battery design [65–67], aging rates [68–70], state estimation [71–73], safety [74–76], cost and sustainability [31]. For instance, Sturm et al. [66] used an electrochemical and a thermal model to improve the inter-tab design of cylindrical lithium-ion cells for fast charging. For aging studies, Schimpe et al. [70] applied a thermal model for calendar and cyclic aging to determine a degradation-aware current derating framework, which can increase battery lifetime by 65%. Feng et al. [75] found implications for safer battery systems such as the application of thermal resistance layers between cells with a thermal model coupled with a chemical decomposition model. During operation, safety is increased by an accurate state estimation, which was improved by Feng et al. [73] with an electrochemical-thermal cell model. Lander et al. [31] used a life-cycle-cost model and a carbon footprint model to improve costs and sustainability through efficient BTMS. The construction of a comprehensive model for a lithium-ion cell usually requires the linking of state variables from various physical models, which are explained in the following (see Figure 1.4).

Electrical models of battery cells translate the electrical power demand of the respective application into quantities such as the current (I_{cell}) and the voltage (U_{cell}) at the cell terminals [77]. Battery modelers can choose between mechanistic models such as the electrochemical models [66, 78], or phenomenological models such as electrical equivalent circuits [79–81]. Equivalent circuits usually contain a SOC-dependent open circuit voltage (OCV) (U_{ocv}), an ohmic overvoltage U_Ω and n resistance-capacitance parallel connections that simulate the polarization voltages $U_{p,n}$ [79, 80] (see Equation 1.5). In the state-space representation, the state vector of the equivalent circuit contains the SOC and $U_{p,n}$, which is shown in Figure 1.4. The parameters of the electrical model such as the electrical cell impedance ($\underline{Z}$) depend strongly on the mean cell temperature ($\overline{T}_{cell}$), which is shown in Figure 1.4 at marker ①. For example, the electrical pulse resistance (100 ms) can decrease exponentially by 33% with a temperature increase from 10 to 40 °C [53]. Many electrical parameters are temperature-sensitive according to Arrhenius's law in Equation 1.6, which contains a reference value (ϕ_{ref}), the activation energy (E_a), the gas constant of 8.314 $\mathrm{J\,mol^{-1}\,K^{-1}}$ and a reference temperature (T_{ref}) [82]. In addition to the average temperature of the cell ($\overline{T}_{cell}$), internal temperature differences (ΔT_{cell}) can also influence cell performance. Troxler et al. [83], for example, measured a decrease in $\underline{Z}$ by 25% with a temperature difference of 40 °C.

$$U_{cell} = U_{ocv} + U_\Omega + \sum U_{p,n} \tag{1.5}$$

$$\phi = \phi_{ref} \cdot \exp\left[\frac{E_a}{8.314\,\mathrm{J\,mol^{-1}\,K^{-1}}}\left(\frac{1}{T_{ref}} - \frac{1}{T}\right)\right] \tag{1.6}$$

Aging models of lithium-ion cells are important when the timescale of the simulation exceeds many days or when many full cycles need to be simulated. In general, the aging of a lithium-ion cell causes a decrease in battery capacity (ΔQ) and an increase in electrical impedance ($\Delta \underline{Z}$), both of which are used as the state variables of aging models. $\overline{T}_{cell}$ during storage or cycling has a dominant influence on the loss of capacity and performance [84, 85], which is highlighted in Figure 1.4 (marker ②). As can be seen from the temperature color bar, there is an optimum temperature with a minimum aging rate that is approximately between 15 and 45 °C [62, 86, 87]. The optimal aging temperature results from the balance struck between lithium-plating and the growth of the solid electrolyte interphase (SEI), which accelerate at low or high temperatures, respectively [22, 88]. ΔT_{cell} can also influence the aging of the battery, but the influence has been less studied in the literature, probably because ΔT_{cell} cannot be effectively controlled. Fleckenstein et al. [89] simulated the effects of ΔT_{cell} on aging and found no significant effects on ΔQ or $\Delta \underline{Z}$. Hunt et al. [20] showed that cooling the tabs of a pouch cell instead of the surface reduced the capacity loss from 9.2% to 1.2% after 1000 cycles and explained this improvement with a lower ΔT_{cell} of the tab cooling configuration. Cavalheiro et al. [90] and Gonzalez et al. [91] showed that temperature gradients between cells connected in parallel reduce the capacity faster (49.3%) than in the reference cell without gradients (12.2%). Werner et al. [21] also concluded that ΔT_{cell} negatively affects ΔQ and the polarization resistance in $\Delta \underline{Z}$. They additionally observed a negative influence of the rate of temperature rise $\partial T/\partial t$ on ΔQ and $\Delta \underline{Z}$, which was attributed to mechanical stresses. These results are supported by Carter et al. [92], who found a significant increase in aging from lithium plating with increasing temperature gradients through the stack. This shows that thermal models are of great importance for aging simulations, as many mechanisms depend on temperature.

Mechanical models of lithium-ion cells can be used to determine mechanical aging processes [93]. A common input for mechanical models is $\overline{T}_{cell}$ to account for eigenstrain from thermal expansion [94–96]. As indicated by marker ③ in Figure 1.4, thermal expansion increases linearly with temperature, which can lead to a change in the mechanical stresses within the stack [95, 97]. In addition, mechanical parameters such as the elastic modulus of separators can decrease by a factor of two when the temperature is increased from 20 to 50 °C [98]. In general, strain and stress are the state variables in mechanical models. At the system boundary of the cell, the pack housing can interact with the mechanical model due to the cell tension [99].

Not only is temperature a strong input/output variable for mechanical, electrical and aging models, there is also a strong coupling between these models. Marker ④ in Figure 1.4 shows the key relationships. The electrical model must, for example, make the SOC and I_{cell} available to the aging model so that cyclical and calendar aging can be calculated [68, 100, 101]. On the other hand, the aging models return ΔQ and $\Delta \underline{Z}$ or state of health (SOH) to the electrical model to improve the accuracy in the simulated U_{cell} and I_{cell} [68, 101]. In addition, the SOC represents a dominant input/output between mechanical and electrical models in order to calculate the internal strain caused by the lithiation of active particles [93, 102]. Changes in mechanical states such as stress can cause a change in porosity ε, which has a strong influence on the electrical impedance of the electrical model [103, 104]. The consideration of mechanical aging can be influenced by the stress inside the active particle [105, 106],

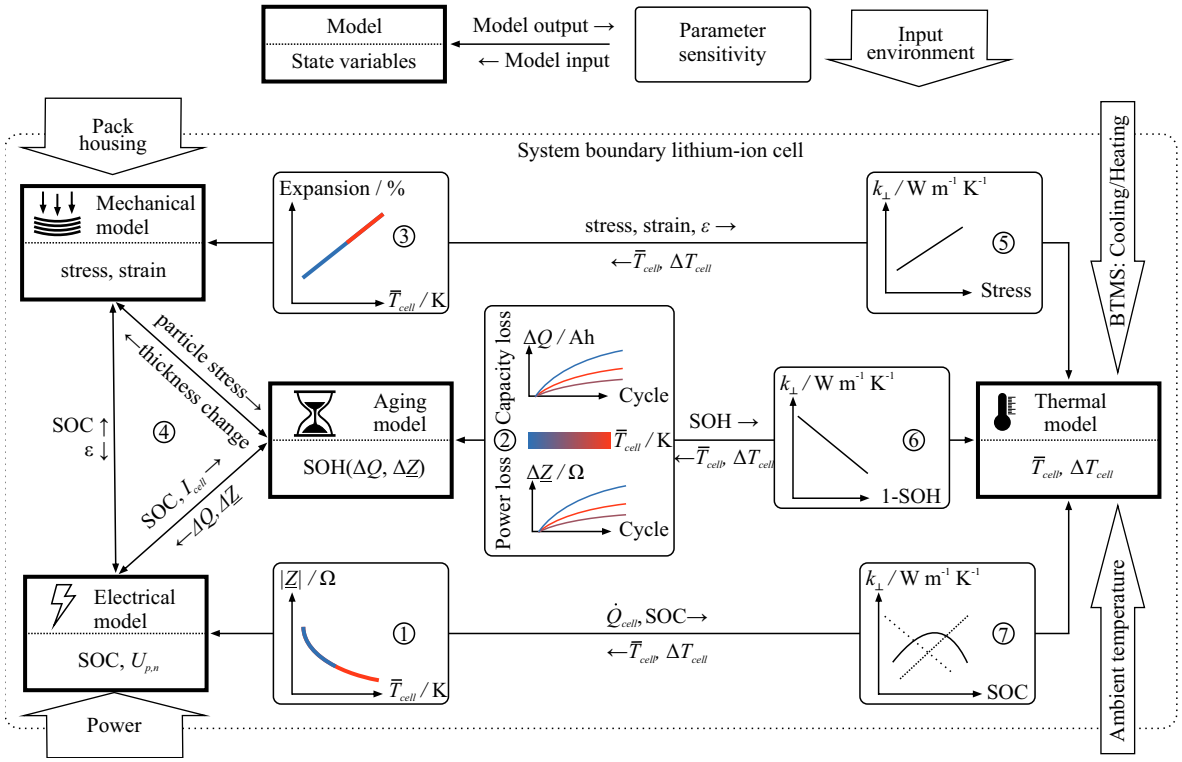

Figure 1.4: Influence of the cell temperature $\overline{T}_{cell}$ and gradients ΔT_{cell} on the multi-coupled physics in lithium-ion cells. An example of the influence of the thermal model on electrical models, aging models and mechanical models is given by marker ①, ② and ③ and the interaction between the three models is shown by marker ④. The feedback to the thermal model via $k_\perp$ is shown by markers ⑤, ⑥, and ⑦.

which represents a coupling between the mechanical and the aging model in order to take into account mechanisms such as particle cracking. On the other hand, an irreversible change in thickness of the stack [107], which is determined by the aging model, can change mechanical parameters such as the porosity [108]. This example gives an insight into the coupled interactions in lithium-ion batteries.

Thermal models are the link between ambient temperature and BTMS, and are important to improve the accuracy of all other cell models shown in Figure 1.4. In addition, mechanical aging models and electrical models are also coupled to the thermal model. SOC, SOH, porosity, and mechanical stress inside the cell can influence thermal parameters, especially $k_\perp$. The specific heat capacity (c_p) and in-plane conductivity ($k_{||}$) can be presumed to be unaffected, since the mass fractions of the cell components and the current collector parameters are less sensitive to mechanical, age-related, electrical, or thermal changes. Marker ⑤ in Figure 1.4 shows the correlation of $k_\perp$ to the mechanical stress inside the stack. For example, Richter et al. [109] observed a linear increase in anode thermal conductivity of about 54% when the compressive pressure was increased from 2.3 to 11.5 bar. This pressure dependence of $k_\perp$ is also reflected in our investigations at the cell level [40]. Furthermore, porosity [110] and changing layer thicknesses (strain) are possible influences from mechanical models on $k_\perp$. With respect to SOH, Kovachev et al. [111] showed that $k_\perp$ decreased by 23% for a cycle-aged pouch cell with an SOH of 80% (see marker ⑥, Figure 1.4). In addition, the SOC of the electrical model also has an influence on $k_\perp$, but there is no consensus on their functional relationship (see ⑦, Figure 1.4). For example, Bazinski et al. [112] measured a linearly decreasing relationship with SOC, Vertiz et al. [113] measured a parabolic relationship, and Murashko et al. [114] measured a linearly

increasing relationship. In summary, there are many interdependencies between the thermal and other models in Figure 1.4, which underscores the importance of temperature on thermal parameters.

1.3 Thermal models for lithium-ion cells

As explained in Section 1.1, thermal models are an integral part of investigating the aging, performance, safety, and sustainability of lithium-ion cells. This section gives an insight into various thermal models with different levels of complexity and discusses their advantages and disadvantages. In addition, deviations between simulated and measured temperature in the literature are analyzed. As a last step, uncertainties in $k_{\perp}$ and their influence on temporal ΔT_t and spatial ΔT_{cell} temperature difference are discussed.

Thermal models can be classified according to the number of dimensions used for the model geometry. Figure 1.3 b) shows an example of 2D and 3D geometries for the three cell formats. Depending on the thermal boundary conditions, 0D and 1D geometries are also suitable simplifications. For example, Fleckenstein et al. [115] used a 1D-heat-equation to evaluate the results of the thermal impedance spectroscopy (TIS), which was possible due to the establishment of adiabatic conditions at the positive and negative cell terminals. Lumped-capacitance models (0D), which neglect temperature gradients within the cell, offer sufficient accuracy under mild cooling conditions [116, 117]. Since thermal conductivity $k_{\perp}$ is neglected in 0D-models with lumped capacitance, these are not dealt with in the following.

In addition to the dimension of the geometry, thermal models can also be classified by spatial resolution. At the atomic level, molecular dynamics simulations are used to correlate crystal structures of active materials with their thermal conductivity [59, 118] or heat capacity [119]. Particle-resolved models on the micrometer scale can be used to investigate the effects of porosity and binder content on the effective thermal conductivity of the porous stack-layer [120–122]. One scale above the particle models are the thermal cell models shown in Figure 1.5, represented by the 2D geometry of a cylindrical cell.

The **layer-resolved model (LRM)** takes into account the spiral effect of the jelly roll and thermal contact resistance between the stack-layers. As shown in Figure 1.5, the LRM contains multiple domains such as the cell housing ($k_{housing}$) in blue, the anode overhang in light red, and the spiral jelly roll that contains one domain for each stack-layer. The anode overhang is an electrochemically inactive jelly roll with no cathode that reduces lithium plating, conducts heat but has no heat generation [123]. Due to the spiral winding of the stack, the heat flow drifts with the rotation of the Archimedean spiral [124]. Within the class of LRMs, there are different levels of homogenization of the stack-layers [125]. Some models resolve each layer of the stack [94, 126, 127] and some use one domain for the current collectors and one for the rest of the stack [124]. According to Queisser et al. [125], the level of homogenization has a strong influence on the temperature field in pouch cells. In the case of wound stacks as shown in Figure 1.5, the spiral geometry can play an essential role, which is the case with lead-acid batteries [124]. Lithium-ion cells are typically not significantly affected by the spiral geometry, but this can change with a low number of turns or a low $k_{\perp}/k_{||}$ ratio [124]. Nevertheless, thermal contact resistance between the stack-layers ($R_{c,n}$) can decrease the $k_{\perp}/k_{||}$ ratio to such an extent that the use of a LRM is necessary. In addition, if a local-heat-generation method is used to model the stack, a LRM is recommended.

The **component-resolved model (CRM)** in Figure 1.5 offers low simulation errors with less com-

putational effort compared to the LRM. In the study by Queisser et al. [125], for example, the CRM simulation time was reduced to 5% of the time required for the LRM. The CRM replaces the spiral jelly roll of the LRM with a homogeneous domain with anisotropic thermal conductivity ($k_{||}$, $k_{\perp}$). Neglecting the spiral geometry of CRMs can lead to significant temperature errors (>25%) [125, 128], but this is very often accepted in lithium-ion research because of the reduced simulation time. For cylindrical cells, the error of CRMs largely depends on the number of windings and the ratio between $k_{\perp}$ and $k_{||}$ [124]. Due to different thermal contact resistances and thicknesses of the stack layers, the ratio between $k_{\perp}$ and $k_{||}$ can differ greatly, which is why no general statement can be made about the extent of errors with CRMs. The domain for the anode overhang in CRMs can be expressed in terms of a single or isotropic thermal conductivity ($k_{overhang}$), but most studies neglect the difference between jelly roll and overhang [39, 67, 129]. Any influence of $R_{c,n}$ is taken into account by $k_{\perp}$ in CRMs (see Equation 1.2), but the contact resistance at the housing interface ($R_{c,housing}$) is still a separate parameter. In addition, further components such as the mandrel ($k_{mandrel}$) can be considered separately in this model class. CRMs are used, for example, to investigate the effects of different BTMS configurations [18, 67] or are part of thermal characterization methods [40, 42, 115].

The **single-domain model (SDM)** is the simplest version of the spatially resolved thermal models, but still offers a good method of analyzing temperature gradients within the cell. In SDMs, all components of the cell are represented by a single domain with anisotropic thermal conductivity (k_{φ}, k_r) in the direction of the coordinate axes (φ and r in Figure 1.5). In the case of cylindrical cells, a hollow cylinder that neglects any point of discontinuity due to thermal contact resistance represents the cell. For surface cooling of cylindrical cells, as shown in Figure 1.3 b), the SDM can provide sufficient modeling accuracy, but for top/bottom cooling, the uncertainty can increase to unacceptable levels [67]. Therefore, the boundary conditions must be carefully checked before using an SDM. The advantage of SDM stems from the reduced computational effort, which is why SDMs are often used when simulating several cells in a battery system [130, 131].

The **lumped-circuit model (LCM)** is the fastest solution for thermal models, but the interpretation of temperature gradients and the parameterization with literature values can be difficult [115]. The fast simulation time of LCMs is achieved through the use of ordinary differential equations (ODEs) instead of partial differential equations (PDEs). A prominent candidate for LCM use is the first-order equivalent circuit shown in Figure 1.5. In the case of cylindrical cells that are cooled on the shell, the internal thermal resistance R_{in} of the LCM corresponds to the k_r of the SDM. Further components of the first-order LCMs are the heat capacity (C_{cell}) and the outer thermal resistance (R_{out}) between the shell of the cell and the ambient temperature (T_{amb}). The functional relationship between R_{in} and the stack conductivities ($k_{||}$, $k_{\perp}$) is simple for pouch cells [132], but complex for prismatic and cylindrical cells due to the wound geometry of the stack [40, 42, 110]. In addition, LCMs often concentrate the spatially distributed heat rate ($\dot{Q}_{cell}$) in the core of the cell [130, 132], which is a great simplification. Because of this simplification, the temperature gradient for LCM can be overestimated, which can be countered by using higher-order equivalent circuit models [115].

Deviations between the simulated and measured temperature can arise due to geometry-related uncertainties as well as uncertainties in thermal model parameters. Thermal models are very often validated by comparing the measured and simulated increase in surface temperatures ($\Delta T_{t,s}$) during cell operation [39, 66, 133]. Table 1.2 lists the validation results for $\Delta T_{t,s}$ of different thermal models, for different materials and cell formats, with different types of temperature excitations, and Biot numbers (Bi). The error between simulation and experiment is usually less than 2.2 °C or less than 15% of the

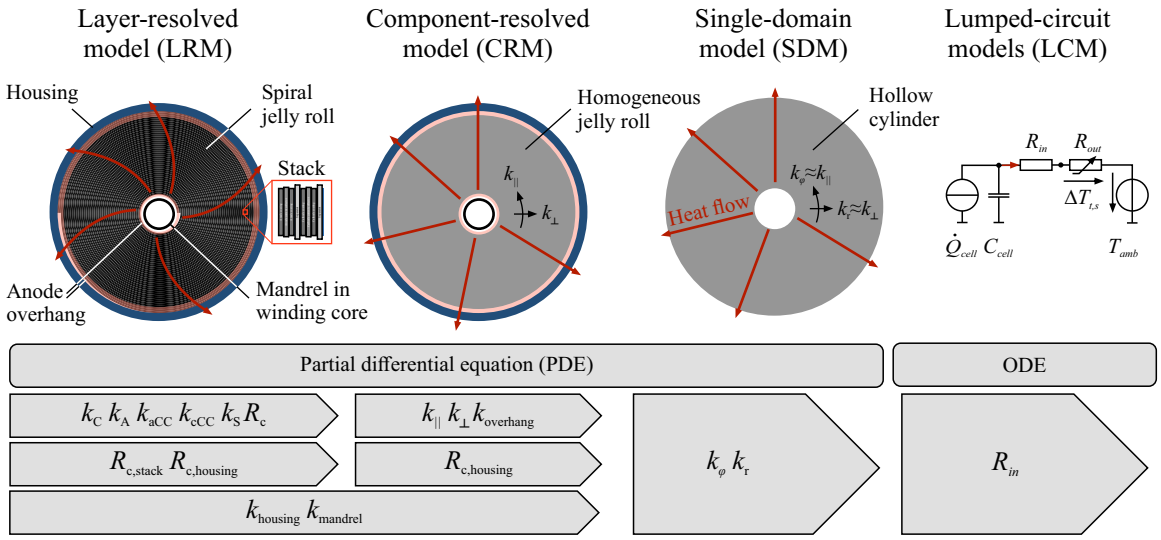

Figure 1.5: Thermal models for lithium-ion cells with different spatial resolutions, represented by a 2D geometry of a cylindrical cell. LRM: Multiple domains for components such as the housing and for each layer of the stack. CRM: Multiple domains for each component, but stack-layers are not resolved. SDM: Only one domain for the entire cell without components such as the mandrel. LCM: A lumped heat capacity and resistance network forms an ordinary differential equation (ODE).

maximum temperature increase. It should be noted that this error could have many causes, such as: uncertainty in the heat generation calculation, thermal parameters, thermal boundary conditions, or uncertainties in the temperature measurement. According to Table 1.2, an increased model complexity (e.g. LRM vs. LCM) does not necessarily improve the modeling errors (T_{err}) for $\Delta T_{t,s}$. In the work of Akbarzadeh et al. [130],for example, the LCM even outperformed the more complex SDM.

Spatial temperature differences (ΔT_{cell}) within the cell are rarely validated for thermal models, most likely due to the effort required to install temperature sensors inside the cell. Past experiments with internal temperature sensors [134–137] have examined temperature differences of up to 30 °C. However, very few studies use the internal temperature to validate thermal models. The validations with internal temperature sensors in Table 1.2 show a maximum error for ΔT_{cell} between surface and core of 1.2 °C or a relative error of 26% compared to the maximum difference. If one compares the errors in ΔT_{cell} of the different model classes, there seems to be a connection between model complexity and temperature error, since the errors with LRM are smaller than with LCM. It is important to note that a full summary of all thermal model validations is beyond the scope of this thesis, so the results in Table 1.2 may be subject to sample variance.

The importance of the accuracy in determining $k_\perp$ for the result of the thermal modeling can be estimated using dimensionless quantities such as the Biot number in Equation 1.7. A high Biot number (> 1) defines the temperature gradient within a cooled or heated body as high [142], ergo $k_\perp$ plays an important role in describing the temperature distribution. Looking at the LCM in Figure 1.5, the Biot number divides R_{in} by R_{out}, which gives the proportion of the internal temperature difference to the external temperature difference. Alternatively, the heat transfer coefficient h_{BTMS} to the BTMS multiplied by the characteristic length (d_L) divided by the thermal conductivity (k_L) in the direction of heat flux to the BTMS gives the Biot number. In the field of lithium-ion cells, a Biot number below 0.1 is often used to justify the use of lumped-capacitance models [69, 106, 116], which neglect internal temperature distribution ($R_{in} = 0,\ k \to \infty$). However, there is criticism of the use of the

Table 1.2: Error between simulated and measured temperature T_{err} during the validation of thermal models for lithium-ion cells. Model definition for LRM, CRM, SDM and LCM can be found in Figure 1.5.

Ref.	Model	$\frac{Q_{cell}}{\text{Ah}}$	Material, format	Excitation	Biot		
Error in simulated surface temperature $\Delta T_{t,s}$						$\frac{\max \lvert T_{err} \rvert}{\text{°C}}$	$\frac{\max \lvert T_{err} \rvert}{\max \Delta T_{t,s}}$
[27]	LRM-2D	-	-, Cylindr.	CC 1C	-	0.5 a)	6% a)
[133]	CRM-3D	40	LFP-G, Prismatic	CC 1C	0.40	0.5	8%
[39]	SDM-3D	38	NMC-G, Prismatic	CC 1C	0.16	0.8	3%
[138]	SDM-3D	3.57	NCA-G, Cylindr.	Pulse 1C	0.2	-	<1%
[130]	SDM-3D	43	NMC-/, Prismatic	CC 2C	0.5	2.2	14%
[130]	LCM	43	NMC-/, Prismatic	CC 2C	0.5	1.6	10%
[139]	LCM	20	LFP-G, Prismatic	Pulse	0.05	0.42	-
[140]	LCM	60	LFP-G, Prismatic	Pulse 1C	0.32	2.0 a)	15% a)
Error in spatial temperature difference ΔT_{cell}						$\frac{\max \lvert T_{err} \rvert}{\text{°C}}$	$\frac{\max \lvert T_{err} \rvert}{\max \Delta T_{cell}}$
[67]	LRM-3D	5.0	NMC-G, Cylindr.	T-Jump 20 °C	-	0.6 a)	5% a)
[67]	LRM-3D	5.0	NMC-G, Cylindr.	CC 0.3C	-	0.2 a)	10% a)
[89]	CRM-3D	60	NMC-G, Prismatic	Pulse 2-4C	-	0.9	8%
[141]	LCM	2.3	LFP-G, Cylindr.	CC 6C	0.37	1.2	26%

a) Values are extracted from figures.

Biot number, since several characteristic lengths can exist, for example in tab cooling, and the heat rate in lithium-ion cells is spatially distributed [143]. For this reason, Hales et al. [144] defined the cell cooling coefficient CCC in Equation 1.8 which divides the heat rate absorption from the BTMS ($\dot{Q}_{BTMS}$) by the temperature difference between the hottest point of the cell and the cooling medium ($\Delta T_{max,ccc}$). For example, the CCC is 0.24 $\mathrm{W\,K^{-1}}$ for tab cooling and 12.32 $\mathrm{W\,K^{-1}}$ for immersion cooling [31]. From the author's point of view, both Bi and CCC are valuable measures to evaluate the temperature gradients within a cell and thus the importance of $k_{\perp}$. The CCC, as not completely dimensionless, offers more information on the cooling and heating state but Bi is more frequently used in the field of lithium-ion cells and is more generic.

$$Bi = \frac{R_{in}}{R_{out}} = \frac{h_{BTMS} d_L}{k_L} \tag{1.7}$$

$$CCC = \frac{\dot{Q}_{BTMS}}{\Delta T_{max,ccc}} = (R_{in} + R_{out})^{-1} \tag{1.8}$$

Figure 1.6 a) and b) shows the influence of $k_{\perp}$ on the jelly roll temperature in a prismatic lithium-ion cell. To demonstrate the influence, we [145] simulated the maximum temperature increase (a)) and the maximum temperature difference (b)) within the jelly roll with two different heat transfer coefficients (h_{BTMS}) and two different values for $k_{\perp}$. A value of 10 and 376 $\mathrm{W\,m^{-2}\,K^{-1}}$ for h_{BTMS} was used for passive air surface cooling [146] and an active liquid surface cooling BTMS [147], respectively. The range of values for $k_{\perp}$ was taken from Chapter 2 [40], which takes into account uncertainties in the thermal conductivity of the stack-layers and layer thicknesses of an NMC-G stack. The constant heat

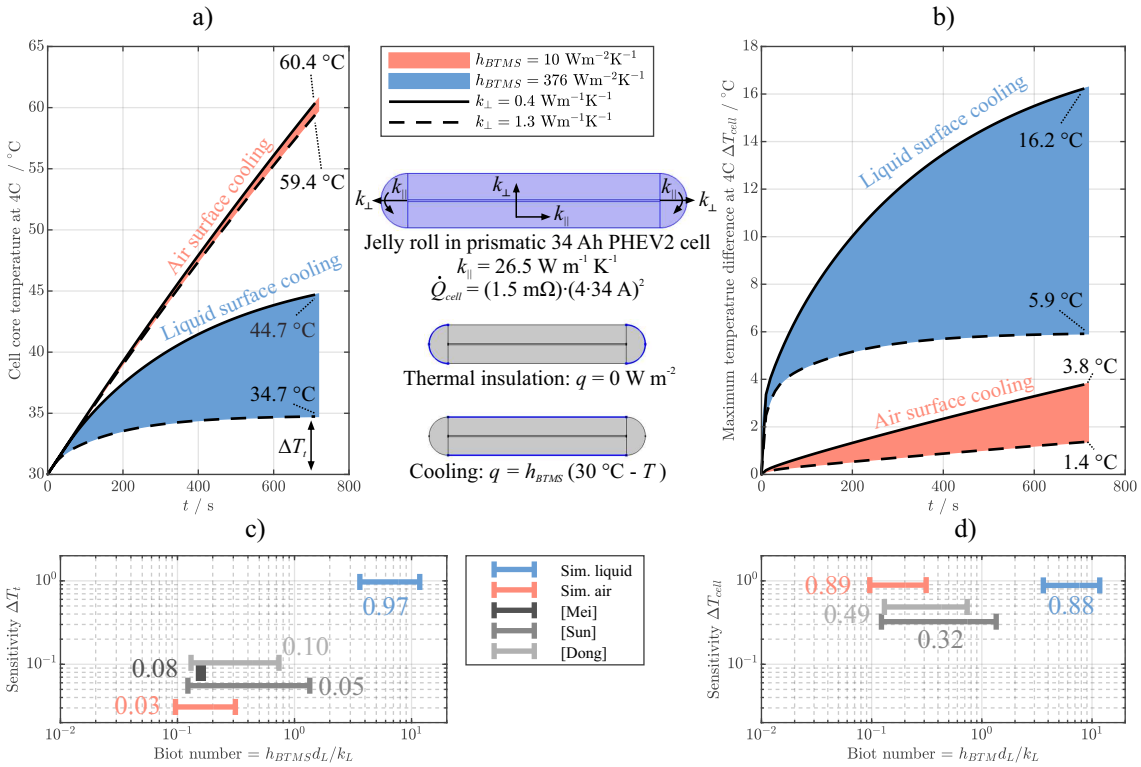

Figure 1.6: Influence of the through-plane conductivity $k_\perp$ on the temporal ΔT_t and spatial ΔT_{cell} temperature differences. a) Simulated temporal temperature difference in the core of a prismatic lithium-ion cell with air and liquid cooling heat transfer coefficients [145]. b) Simulated spatial temperature difference between the cell surface and the maximum temperature inside the cell [145]. c) Sensitivity of ΔT_t to different Biot numbers. d) Sensitivity of ΔT_{cell} to different Biot numbers. Sensitivities from a) and b) are compared to the sensitivity obtained by Mei et al. [39], Sun et al. [148], and Dong et al. [133].

.

rate $\dot{Q}_{cell}$ was determined from the ten-second resistance of 1.5 mΩ and a C-rate of 4. h_{BTMS} is used as a convective boundary condition on the straight lines of the 2D jelly roll that are normally in contact with the prismatic cell housing. An adiabatic boundary condition is defined for the windings, since a gas between the jelly roll and the housing normally isolates this part of the jelly roll. Figure 1.6 a) shows that with moderate air cooling, the core temperature of the cell reacts less sensitively to changes in $k_\perp$ with a variation in the end temperature of 59.4 and 60.4 °C. In contrast to this, the final temperature varies significantly between 34.7 and 44.7 °C with strong liquid cooling. Figure 1.6 a) confirms that uncertainties in $k_\perp$ become more serious for ΔT_t with increasing cooling intensity.

Figure 1.6 c) shows the sensitivity of the temperature rise (ΔT_t) as a function of the Biot number of the BTMS, which is calculated using Equation 1.9. For example, the variation in ΔT_t for the blue liquid cooling in Figure 1.6 a) is 51.4% (9.7±5.0 °C) and the variation in $k_\perp$ is 52.9% (0.85±0.45 W m^{-1} K^{-1}). The division of both variations according to Equation 1.9 results in a sensitivity for the temperature rise of 0.97 (Figure 1.6 c)). Figure 1.6 c) shows that most sensitivity studies were carried out at low Biot numbers around 0.3. In addition, the Biot-sensitivity plot shows that $k_\perp$ becomes important for thermal modeling with high Biot numbers. Many sensitivity studies [148, 149] rate the influence of $k_\perp$ on the increase in temperature as weak. The reason for this weak sensitivity rating is the low Biot number of these studies.

$$\text{Sensitivity} = \frac{\text{Variation temperature rise}}{\text{Variation thermal conductivity}} = \frac{\dfrac{0.5\,[\max(\Delta T_t) - \min(\Delta T_t)]}{0.5\,[\max(\Delta T_t) + \min(\Delta T_t)]}}{\dfrac{0.5\,[\max(k_\perp) - \min(k_\perp)]}{0.5\,[\max(k_\perp) + \min(k_\perp)]}} \tag{1.9}$$

$k_\perp$ influences the spatial temperature difference ΔT_{cell} significantly even at low Biot numbers. The sensitivity of ΔT_{cell} is calculated congruently to Equation 1.9 by replacing ΔT_t with ΔT_{cell}. For the air and liquid cooling scenarios in Figure 1.6 b), a sensitivity of 0.88 to 0.89 for ΔT_{cell} is determined (see Figure 1.6 d)). An uncertainty of $k_\perp$ of 10% accordingly causes an uncertainty of 8.9% in the maximum spatial temperature difference. Dong et al. [133] came to the same conclusion and rated the thermal conductivity as the most important thermal parameter for determining the temperature difference between the cell surface and the cell interior.

In summary, a multitude of thermal models exist in lithium-ion research, from the most complex 3D layer-resolved to the simplest 0D lumped circuit models (see Figure 1.5). Uncertainties in the thermal modeling can arise from simplifications of the geometry or from the thermal parameters used in the model. Accurate thermal models can simulate temperature with an error of less than 2.2 °C (see Table 1.2). $k_\perp$ is always an important parameter for the temperature differences within the cell and, in the case of strong cooling, also for the temperature increase (see Figure 1.6).

1.4 Characterization of the thermal conductivity in lithium-ion cells

After the introduction of various thermal models for lithium-ion cells and the assessment of the influence of the through-plane conductivity ($k_\perp$) on the thermal modeling, this section introduces some measurement methods for $k_\perp$. Equation 1.10 defines the measured thermal conductivity (k_m) for one-dimensional heat conduction in the steady state (see Figure 1.7). The measurands for the steady-state are accordingly the heat rate ($\dot{Q}_x$) of the heat flow flowing through the sample, the thickness (d_x) and the cross section ($A_\perp$) of the sample as well as the temperature difference (ΔT_x) between d_x. Depending on the test device, $\dot{Q}_x$ and $A_\perp$ can be replaced by the heat flux ($\vec{q}_x$) and ΔT_x and d_x by the temperature gradient ($\partial T / \partial x$).

$$k_m = \frac{\dot{Q}_x d_x}{A_\perp \Delta T_x} = \frac{\vec{q}_x}{\partial T / \partial x} \tag{1.10}$$

It is very important to analyze the measurement uncertainty for the thermal conductivity, since thermal parameters are more prone to errors than, for example, electrical quantities. This is a general statement that applies to batteries and all other materials. The reason for the increased uncertainty of thermal conductivity can be explained by the fact that electrical conductors and insulators differ by far more than those of thermal conductors and insulators. For example, dividing the thermal conductivity of copper and mineral wool gives $\approx 10^4$ [150] whilst the quotient of the electrical conductivity of copper and nickel oxide gives $\approx 10^{14}$ [151, 152]. Since conductors are less distinguishable from insulators, heat losses are likely to cause systematic errors in $\dot{Q}_x$ and thus in k_m. In addition, thermal variables such as temperature have a longer measurement chain than electrical variables such as voltage, which

is a disadvantage for measuring accuracy. Thermocouples, for example, convert the temperature into an electrical voltage according to the Seebeck effect, which has to be measured and then evaluated in the measurement software [153]. This chain therefore comprises two more steps than electrical voltage measurements.

In general, uncertainties in k_m result from uncertainties in $\vec{q}_x$ and the temperature gradient. The uncertainty in the context of this work includes random and systematic errors [154], while systematic errors can be further divided into static and dynamic errors. Common sensors for thermal conductivity measurements are resistance thermometers [42], thermocouples [155], radiation thermometers [156] and heat flow sensors [157]. In the area of lithium-ion cells, temperature sensors are usually not calibrated before thermal conductivity tests [155, 157, 158], which means that the error in the tolerance class must be used for uncertainty calculations. The applied thermocouples usually have a tolerance class between 0.20-1.00 °C. This means that with temperature differences (ΔT_x) of around 10 °C [157], the uncertainty in ΔT_x is between 2-10%. On the other hand, heat flux sensors have an uncertainty between 0.4-5.0% [111, 157]. Adding the uncertainty for ΔT_x and $\vec{q}_x$ gives an estimate of the uncertainty for k_m of 2.4-15% in the field of lithium-ion cells.

The lowest achievable uncertainty for thermal conductivity measurements is 1% [159]. Therefore, even standard reference materials that could be used for the calibration cannot guarantee a lower uncertainty. The lack of success in achieving smaller uncertainties can be explained by material variability caused by the production process [159]. Impurities, porosity, heat treatment and grain sizes, all of which are determined during production, can lead to significant fluctuations in thermal conductivity [159, 160]. This can be seen when comparing pure aluminum with the aluminum alloy 3003. Due to the manganese content of 1.1% in this alloy, the thermal conductivity drops by -35% from 237.5 to 155 $\mathrm{W\,m^{-1}\,K^{-1}}$ [161, 162]. It should be emphasized that 1% uncertainty can only be achieved with expert knowledge, homogeneous material with freely selectable dimensions and standardized test setups for thermal conductivity [159]. Therefore, a measurement uncertainty of less than 1% is very unlikely in the area of the lithium-ion cells, as this test item is very inhomogeneous with dimensions that cannot be selected.

Thermal conductivity measurements are often divided into transient and steady-state methods. Figure 1.7 shows the exponential temperature rise of a generic test sample heated on the left and cooled on the right. Any evaluation that uses the initial exponential increase can be classified as transient and the subsequent part as steady-state [163, 164]. As can be seen from Figure 1.7, transient methods are usually faster. In addition to the thermal conductivity, some transient methods can also evaluate the specific heat capacity, since $\partial T/\partial t$ is not equal to zero (see Table 1.3). Short measurement times and the possibility of evaluating several variables are at the expense of the higher complexity of the evaluation, which requires greater knowledge of the test sample. In addition, dynamic measurement errors weigh more heavily with transient methods, since temperature rise times of approximately 30 minutes [42] are closer to the time delays of conventional temperature sensors [153]. The advantages of the transient methods are the disadvantages of the stationary methods and vice versa. In addition, thermal contact resistance can be a challenge, but this is also the case with steady-state methods. Figure 1.7 shows, for example, that the use of the temperature difference between the heat source and the heat sink for ΔT_x is flawed, as this difference also includes thermal contact resistances.

Since lithium-ion cells are inhomogeneous test samples, an increased uncertainty in k_m is to be expected, which will further increase as a result of the transformation into $k_\perp$ (see Figure 1.7). For example, the inhomogeneity or anisotropy of the lithium-ion cell can violate the assumption of the

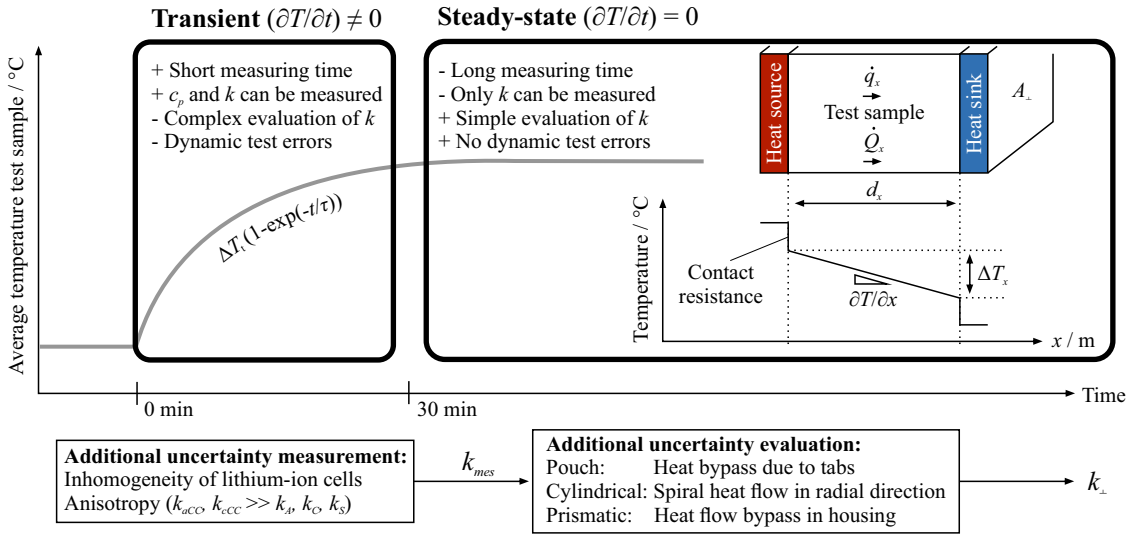

Figure 1.7: Definition of transient and steady-state measurements for the thermal conductivity by the deviation of the temperature $\partial T/\partial t$. For the steady-state, an exemplary course of temperature with thermal contact resistance in the measurement is shown. The block diagram highlights additional measurement uncertainties for $k_\perp$ compared to thermal conductivity measurements on homogeneous samples.

test method, which increases the uncertainty. In addition to the influence of lithium-ion cells on the accuracy of the test bench, transformations between k_m and $k_\perp$ can cause further uncertainties in the evaluation. For example, if a prismatic cell is clamped between the heat source and the heat sink (see Figure 1.7), the heat flow through the aluminum housing must be compensated for in order to evaluate $k_\perp$ [40]. The same applies to the spiral-shaped heat flows in cylindrical cells (see Figure 1.5) and the heat flow that bypasses the stack through the tabs in pouch cells. All of these effects can create additional uncertainties in the assessment of $k_\perp$ from measurements on full-cells.

The guarded hot plate (GHP) method in Figure 1.8 a) is one of the most common steady-state test methods for thermal conductivity [156]. In this test method, the test sample is clamped between a main heater and a cooling plate. Heat losses on the sides of the test sample are reduced with insulation materials and a guarded heater acts on the rear of the main heater to reduce heat losses. The guarded heater is controlled in such a way that the temperature difference between the two heaters disappears ($\Delta T = 0$ K), which is equivalent to an insulation with infinite thermal resistance. The measured conductivity (k_m) of the test cell is determined by the heat rate (P_h) in the main heater, the thickness of the cell (d_{cell}), the temperature difference along the cell (ΔT_{cell}) and the surface perpendicular to the heat flow ($A_\perp$). The advantage of the guarded hot plate lies in the low measurement uncertainty [163], which is 0.7% for the reference material Pyrex glass with a thermal conductivity of 1.14 $\mathrm{W\,m^{-1}\,K^{-1}}$ [165]. Depending on the material and temperature range, a general uncertainty of 1-6% is often given for this method [163, 164]. Disadvantages are long measurement times and the restriction to larger samples with low to medium conductivity (0.01-1.0 $\mathrm{W\,m^{-1}\,K^{-1}}$) [163, 166]. For lithium-ion cells, however, the measuring range is acceptable because $k_\perp$ is around 1.0 $\mathrm{W\,m^{-1}\,K^{-1}}$. The GHP method has been used twice in the area of the lithium-ion cells (see Table 1.3). Once for a pouch cell by Koch [167] and once for a prismatic cell, which is described in detail in Chapter 2 [40]. For the determination of $k_\perp$ of a prismatic cell, an uncertainty of 6% can be expected [40]. The GHP method cannot be used to determine for $k_\perp$ for cylindrical cells, since it requires test samples with flat surfaces.

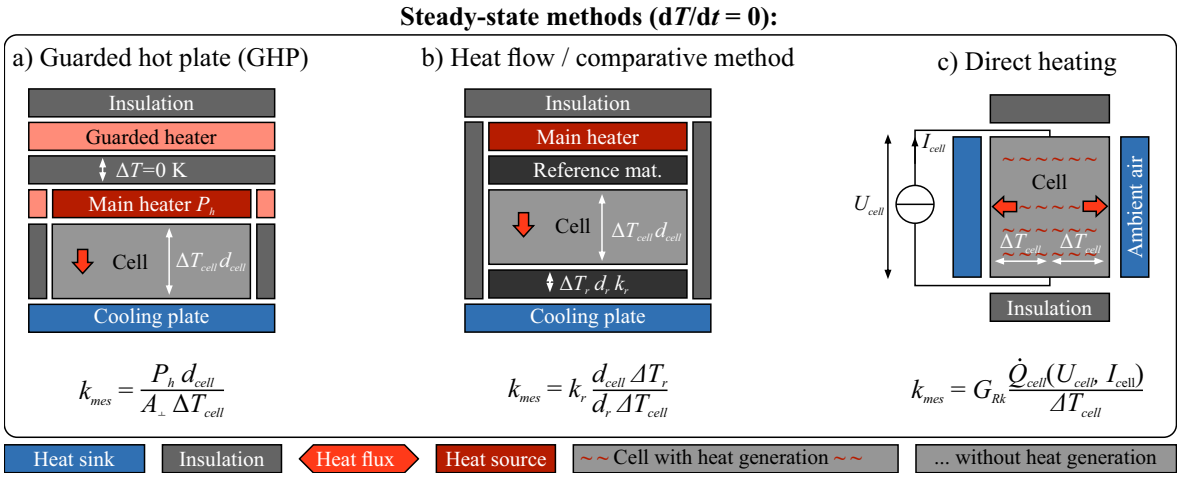

Figure 1.8: Test setups for steady-state thermal conductivity measurements with corresponding equations to evaluate k_m of the test sample.

The **heat flow or comparative method** in Figure 1.8 b) differs from the GHP method in the way in which the heat flow is determined. In this method, the heat flow is determined by a heat flux sensor or by a reference material with known thermal conductivity. With a heat flux sensor, the conductivity of the test sample is evaluated in the same way as with the guarded hotplate. In the comparative method, the temperature gradient along the test sample ($\Delta T_{cell}/d_{cell}$) is compared with the gradient along a standard reference material ($\Delta T_r/d_r$). Heat flow and comparative methods benefit from the ease of construction and operation, but have one of the largest uncertainties of between 3% and 20% [163]. At the material level, the comparative method is found more frequently in the area of lithium-ion cells [109, 168], while the heat flow method has been used twice for full-cells [112, 157]. For these full-cell demonstrations, an uncertainty of 2% [112, 157] was calculated, which is perhaps a little too optimistic as this uncertainty is below the general uncertainty range (3-10%) for the heat flow methods (see Table 1.3). As with the GHP method, $k_\perp$ for cylindrical cells cannot be measured using the heat flow or comparison method.

Direct heating, also known as the Kohlrausch method, is the only steady-state method in Figure 1.8 in which the heat is generated inside the test cell. The heating rate is calculated from the voltage (U_{cell}) and current (I_{cell}) of the test cell and the temperature difference (ΔT_{cell}) is often measured between the inner core and the outer surface. When internal temperature measurements are required, direct heating is a destructive method. Due to the spatial distribution of the heat rate, the evaluation is more complex than with the other steady-state methods. The conversion of the thermal resistance ($\Delta T_{cell}/\dot{Q}_{cell}$) into the measured thermal conductivity (k_m) requires a geometric factor (G_{Rk}), which must be determined for each sample geometry by means of complex finite element method (FEM) simulation. The uncertainty of direct heating is therefore difficult to assess, especially because of G_{Rk}. The Kohlrausch method, for example, has an uncertainty of between 2-10% [163]. Direct heating is the only steady-state method in Figure 1.8 that can be used for all three cell formats, but has thus far only been used for cylindrical and prismatic cells [110, 141]. Nevertheless, from the author's point of view, direct heating should also be possible for pouch cells. The uncertainty of direct heating in the area of lithium-ion cells remains unknown, as none of the authors [110, 141] carried out uncertainty calculations or validations with reference materials.

The **transient hot wire method** in Figure 1.9 a) uses a wire inserted in the test cell as a heat

source. This method determines k_m very quickly and accurately, but very often it is a destructive method [163, 164]. In addition, thermal contact resistance between the heating wire and the test cell can be a challenge [163]. The parallel version of the hot wire method is shown in Figure 1.9 a), which includes an additional thermocouple that measures the temperature field induced by a thin heating wire [169]. To evaluate k_m, analytical equations are defined in standards [169], but thermal FEM models can also be used if the sample shape deviates from simple geometries [170]. The parallel hot wire can be used up to 25 $\mathrm{W\,m^{-1}\,K^{-1}}$ [169], which is sufficient to determine $k_\perp$ of lithium-ion cells. If the heating wire and thermocouple are inserted into the cell's electrode-separator stack, the hot-wire method can be used for all cell formats. Cell instrumentation can be circumvented for pouch cells if two identical cells enclose the heating wire and the thermocouple, which was demonstrated by Zhang et al. [171].

The plane source method in Figure 1.9 b) has a similar principle of operation to the hot wire method, except that it is not a destructive method and has a larger measuring range between 0.005-500 $\mathrm{W\,m^{-1}\,K^{-1}}$ [164]. Instead of inserting the sensor into the sample, it is attached to the surface. The plane source sensor is very often used simultaneously as a heat source (P_h) and as a resistance temperature sensor (ΔT_{cell}). The evaluation of k_m is very complex, requires fitting procedures [172], great knowledge of the sample and considerable knowledge in handling this technique [164]. In addition, thermal contact resistances between the sensor and samples [164] as well as the heat capacity of the sensor [173] represent a challenge inherent in the plane source method. The uncertainties are generally between 2-5% according to the EN ISO 22007-2 standard. For lithium-ion cells, methods similar to the plane-source method have been used primarily for cylindrical cells [64, 158, 174], but this technique should be applicable to any cell format. The specified uncertainty for $k_\perp$ of cylindrical cells is between 5-7% [158, 174].

Laser flash is one of the most common transient methods for thermal conductivity, due to its wide temperature range from -100 to 3000 °C [163] and a wide measuring range between 0.1 and 1000 $\mathrm{W\,m^{-1}\,K^{-1}}$ [164]. A laser heats the front of the sample and an infrared camera measures the temperature response on the back. The evaluation of k_m is simplified to a single measured variable, namely the rise time ($t_{1/2}$), which is required to reach 50% of the total temperature rise. It should be noted that in most cases, laser flash does not measure k_m directly. Instead, density (ρ_{cell}) and specific heat capacity (c_{cell}) also have to be measured, which is a disadvantage of laser flash. The general uncertainty for laser flash is within 2-6% [164]. Although there is some doubt in the literature [175] that laser flash is appropriate for anisotropic lithium-ion cells, there are two demonstrations for pouch cells [132, 176]. Since laser flash requires flat surfaces, it cannot be used for cylindrical cells. In addition, the determination of $k_\perp$ in prismatic cells with laser flash is much more difficult because the housing conducts the heat of the flash around the inner cell volume.

TIS in Figure 1.9 d) is a common method of measuring the thermal conductivity and heat capacity of lithium-ion cells, as it only requires standard equipment in battery laboratories. The TIS was first introduced by Barsoukov et al. [177], who still used an external heat source, which was later replaced by an internal heat source by Schmidt et al. [178]. The setup in Figure 1.9 d) shows this advanced version of the TIS, in which the heat is generated inside the cell and the ambient air acts as the heat sink [115, 178]. In order to direct the heat flow, insulation is required and the surface temperature (ΔT_{cell}) is measured at the contact surface with the ambient air. To perform the TIS, a sinusoidal heat rate ($\dot{Q}_{cell} = f(U_{cell} I_{cell})$) in the frequency range between 0.1-100 Hz [179] excites the cell, which results in a complex thermal impedance ($\Delta T_{cell}/\dot{Q}_{cell}$). This thermal impedance is often

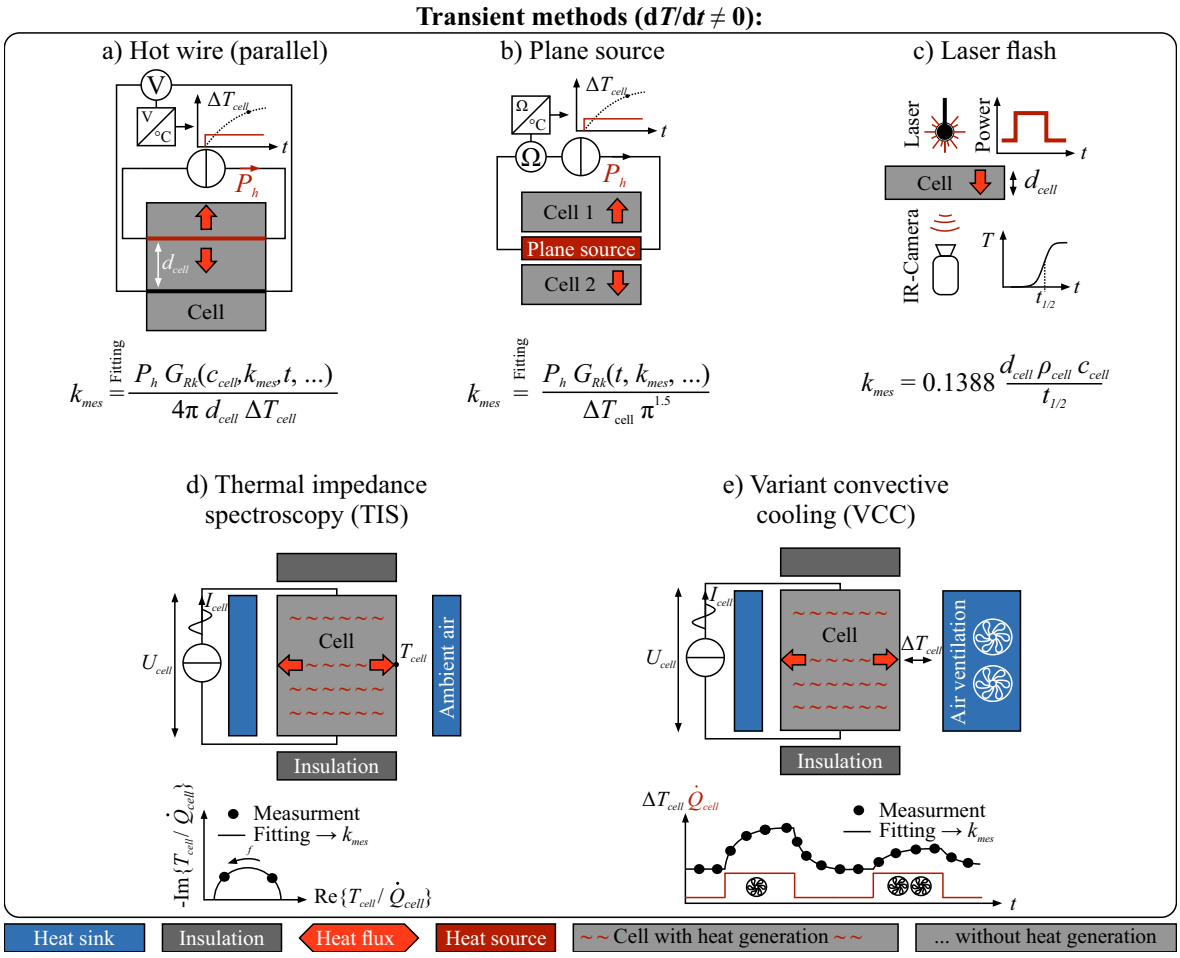

$$k_{mes} \overset{\text{Fitting}}{=} \frac{P_h\, G_{Rk}(c_{cell}, k_{mes}, t, \ldots)}{4\pi\, d_{cell}\, \Delta T_{cell}}$$

$$k_{mes} \overset{\text{Fitting}}{=} \frac{P_h\, G_{Rk}(t, k_{mes}, \ldots)}{\Delta T_{cell}\, \pi^{1.5}}$$

$$k_{mes} = 0.1388\, \frac{d_{cell}\, \rho_{cell}\, c_{cell}}{t_{1/2}}$$

Figure 1.9: Test setups for transient thermal conductivity measurements with corresponding equation to evaluate k_m of the test sample.

approximated by a semicircle in the Nyquist diagram, as shown in Figure 1.9 d). Therefore, at least two measurements at two different frequencies [179] are required in order to evaluate $k_\perp$ by fitting the model to the measurement data. The choice of temperature sensor [179] and the complexity of the fitting model [115] have a significant influence on the measurement uncertainty. For example, the use of only one capacitance-resistance network (see LCM Figure 1.5) for the fitting model can induce an uncertainty of more than 100% during the TIS evaluation [115]. In addition, dynamic errors in the temperature sensor may have to be compensated for, as they can change with the frequency of the heat rate [115]. Further disadvantages of the TIS result from the long measurement time, which can be in the order of days, and the unspecified measurement uncertainty for lithium-ion cells (see Table 1.3).

The **variant-convective cooling (VCC)** method measures thermal parameters by varying the convective boundary condition, which was first introduced by Bryden et al. [180]. Alternative names for VCC are: Bryden method [42] or 1D-steady-state approach [138]. VCC uses the same test equipment as the TIS with the exception of the heat sink, which must be able to change the thermal boundary condition on the surface of the sample. In reality, changing boundary conditions are often achieved by varying the ventilation speed within the climatic chamber. The heating rate is induced by an alternating square pulse [130, 138] or sinusoidal current [42] - similar to the TIS method. The heating rate is determined either by measuring I_{cell} and U_{cell} or by an electrochemical model [138, 181], which is particularly necessary for large cells. VCC method consists of two heating phases with different

Table 1.3: Summary of thermal conductivity test methods with information on the test efforts and applicability for measuring $k_\perp$ in lithium-ion cells. Methods developed in this work are shaded gray. ❑: The method cannot be applied for lithium-ion cells. ☆: The method could be applied but there is no demonstration. ✓: The method has been applied for lithium-ion cells. ●: The specific heat capacity of the lithium-ion cell can be evaluated simultaneously. ❍: The specific heat capacity has to be known to evaluate $k_\perp$.

Method (uncertainty)[c)]		Standard	Cell test duration	$\frac{I_{cell}}{\text{A}}$	Applicability for $k_\perp$ & (uncertainty) Cylindr.	Pouch	Prismatic
Steady-state							
GHP	(1-6%)	C177-13 [b)]	h	0	❑	✓ (-) [d)]	✓ (6%) [d)]
Heat flow	(3-10%)	C518-98 [b)]	h	0	❑	✓ (2%) [e)]	☆
Direct heating	(2-10%)	-	h	$\neq 0$	✓ (-) [a) f)]	☆	✓ (-) [f)]
Transient							
Hot wire	(1-10%)	D5930-17 [b)]	min ●	0	☆ [a)]	✓ (-) [g)]	☆ [a)]
Plane source	(1-7%)	D7984-21 [b)]	s, min ●	0	✓ (5-7%) [h)]	☆	☆
Laser flash	(2-6%)	E1461-13 [b)]	min ❍	0	❑	✓ (-) [i)]	❑
TIS	(-)	-	h, d ●	$0, \neq 0$	✓ (-) [k)]	✓ (-) [k)]	✓ (-) [k)]
VCC	(-)	-	h ●	$0, \neq 0$	✓ (6%) [l)]	✓ (-) [l)]	✓ (-) [l)]

a) Instrumented cell with internal sensors. **b)** American Society for Testing and Materials (ASTM). **c)** General uncertainties are taken from [163, 164, 183]. **d)** Pouch [167], prismatic [40]. **e)** [112, 157]. **f)** Cylindrical [141], prismatic [110]. **g)** [137]. **h)** [64, 158, 174]. **i)** [132, 176]. **j)** [168]. **k)** Cylindrical [115, 177, 179], pouch [178], prismatic [184]. **l)** Cylindrical [42, 181], pouch [138], prismatic [130].

convective boundary conditions. Alternatively, rapid reductions in the ambient temperature can replace the heating phases [182], which is technically more difficult but can eliminate the problem of inhomogeneous heating rates in large-size cells. $k_\perp$ is determined in the VCC by a thermal model that is fitted to the measurement data. The VCC is slightly faster than the TIS (see Table 1.3), less prone to dynamic temperature errors, but more affected by heat sink temperature variation. Another advantage of VCC is that there is a specification of the measurement uncertainty of 6% for cylindrical cells [42], which is described in Chapter 3.

Table 1.3 compares the described measurement methods for the thermal conductivity in general and in particular for lithium-ion cells. The general uncertainty and the ASTM standard are listed, which is useful for assessing the lowest achievable uncertainty, maturity, and instrument availability for the methods. In order to quantify the measurement effort for lithium-ion cells, the test duration is listed from demonstrations in the literature and the filled circle shows whether c_p is required or is being evaluated at the same time. Note that the laser flash method requires additional heat capacity measurements that increase the test duration. Before choosing a method in Table 1.3, it must be determined whether cell operation can be tolerated. If a cell current is required for the method ($I_{cell} \neq 0$ A), it can lead to battery degradation or mechanical or electrochemical disturbances that disrupt $k_\perp$ evaluation (see Figure 1.4). In addition, there is an additional uncertainty due to the heat rate in the inner tabs of the cell [42], since this heat is not generated in the electrode-separator stack. According to Table 1.3, it must be mentioned that only very few studies on lithium-ion cells indicate the uncertainty for $k_\perp$ of their measurement method. When the uncertainty in the study has been determined, it is indicated in the last three columns of Table 1.3 in parentheses.

According to Table 1.3, TIS and VCC are the best methods for measuring $k_\perp$ of lithium-ion cells. This is mainly due to their applicability (✓) without cell instrumentalization to all three cell formats

shown in the last columns in Table 1.3. The plane-source method offers the same adaptability, but there are no demonstrations for the pouch and prismatic formats. If measurement uncertainty is the main factor in the choice of method, the heat flow method for pouch and the GHP for the prismatic format can be recommended. For future TIS and VCC investigations, it is strongly recommended to carry out an uncertainty analysis of the test setup.

The contribution of this work to the field of $k_\perp$ measurements for lithium-ion cells is indicated by the gray shaded cells in Table 1.3. In this work, the GHP was used for the first time for the prismatic cell format, which is described in Chapter 2 [40]. This investigation showed that the extremely low measurement uncertainty of the GHP is worsened by the heat flux flowing through the prismatic aluminum housing. Another contribution to the $k_\perp$-field concerns advancement of the new VCC method introduced by Bryden et al. [180] in 2018. Together with Al-Zareer et al. [138, 181] and Akbarzadeh et al. [130], this thesis [42] extends the idea of Bryden et al. [180] to determine both c_{cell} and $k_\perp$ using the VCC test procedure. Demonstrations for the VCC on two cylindrical formats are discussed in Chapter 3 [42], which also contains the only uncertainty assessment for VCC so far. From the author's point of view, the combination of TIS and VCC could be another new method for measuring the thermal conductivity, as they are similar in terms of heat rate generation. In addition, the evaluation of measurement uncertainties, comparisons of test methods on the same test sample and the proof of applicability of the plane source method for the pouch and prismatic format are further potential research directions.

1.5 Thesis outline

The increasing awareness of climate change in recent decades has increased the importance of lithium-ion cells as an effective tool for reducing greenhouse gas emissions in the transport sector (see Figure 1.1). Switching from petrol cars to BEVs can save up to 64% of CO_2 emissions in the transport sector if the CO_2 footprint of electricity generation is similar to that of France in 2015 (see Figure 1.2). Today, most BEVs use lithium-ion cells with a liquid electrolyte, a graphite anode and a transition metal cathode. For such lithium-ion cells, the temperature is an important state, since the electrochemical, the mechanical and the aging properties are significantly influenced by the temperature (see Figure 1.4). Due to this temperature behavior, thermal models are very important improving the understanding of lithium-ion cells, which is particularly the case when discharging or charging with high power and during the safety-critical thermal runaway. The thermal conductivity ($k_\perp$) through the layers of the electrode-separator stack is an important parameter of any thermal model of lithium-ion cells (see Figure 1.5). Uncertainties in $k_\perp$ can influence the simulation of both the temperature rise over time and the spatial temperature difference within the cell (see Figure 1.6). Therefore, a precise determination of $k_\perp$ for different cell formats, battery states and boundary conditions is very important for research on lithium-ion cells.

As shown in Figure 1.10, Chapter 2 of this thesis deals with $k_\perp$ in prismatic cells and the influence of temperature and external compression pressure on $k_\perp$. When the first experiments in this thesis were planned, there was only one $k_\perp$ study [110] on prismatic lithium-ion cells and only two studies [110, 112] that varied the mean cell temperature during the determination of $k_\perp$. Werner et al. [110] observed a sharp decrease in $k_\perp$ with increasing temperature of -0.9% K^{-1} for a prismatic LCO-G cell, while Bazinski et al. [112] did not measure any temperature dependence for an LFP-G pouch cell. To address the question of whether the temperature dependence is determined by the cell format or the

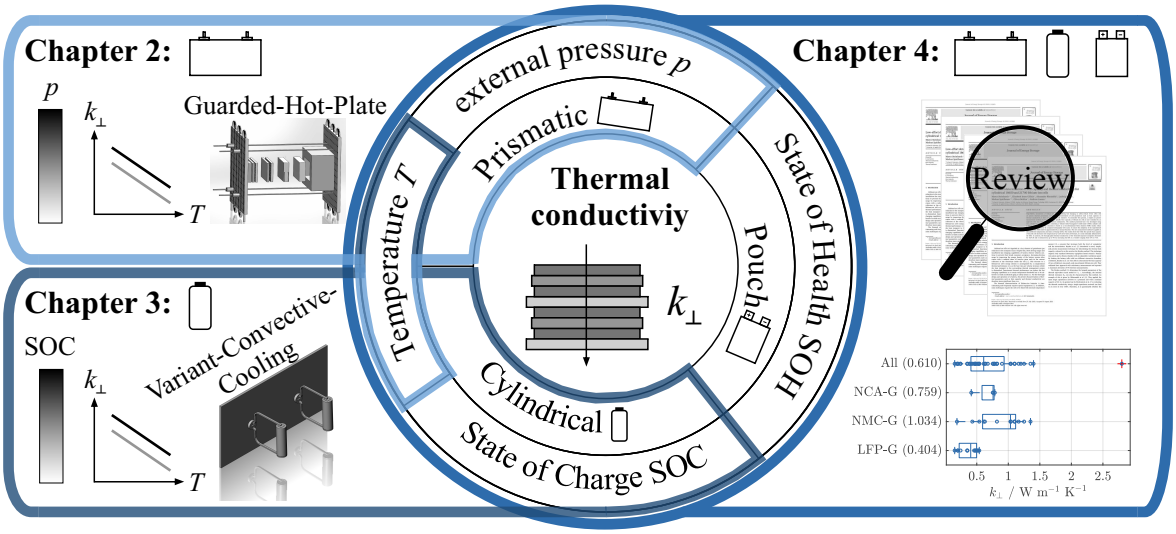

Figure 1.10: Structure and outline of this thesis.

active material, the study in Chapter 2 measures the $k_\perp$ of a prismatic NMC-G cell. In addition, the study in Chapter 2 is the first application of the guarded hot plate method for prismatic cells, with which the dependence of $k_\perp$ on external pressure was examined for the first time.

Chapter 3 deals with $k_\perp$ measurements for 18650 and 21700 cylindrical cells and the dependencies of $k_\perp$ on temperature and SOC. Before the introduction of the variant-convective cooling method for the specific heat capacity by Bryden et al. [180], only thermal impedance spectroscopy could measure $k_\perp$ for all three cell formats (see Table 1.3). The variant-convective cooling method was later extended by Akbarzadeh et al. [130], Al-Zareer et al. [138] and this thesis to measure the parameter $k_\perp$. The contribution of this thesis is described in Chapter 3. In addition to the introduction of a new $k_\perp$ measurement method for cylindrical cells, Chapter 3 offers the first uncertainty estimate for the variant-convective cooling method.

Chapter 4 concludes this thesis by giving an overview of measurement results for thermal parameters in the literature for all three cell formats and all dependencies on battery states. This literature review not only deals with $k_\perp$, but also the specific heat capacity. While Chapter 2 and 3 focus on the full-cell scale, the literature review also looks at cell components and stacks. The main objective is to recommend thermal conductivity and heat capacity values for thermal models obtained through statistical meta-analyses. In addition, this literature review reveals gaps in knowledge and further potential research directions for thermal parameters of lithium-ion cells.

2 Thermal conductivity in prismatic cell formats

The research article [40] in this chapter entitled *Thermal conductivity inside prismatic lithium-ion cells with dependencies on temperature and external compression pressure* deals with $k_\perp$ measurements on prismatic battery cells, as this cell format is the least studied in the literature. In this paper, the cell temperature was varied to determine the temperature dependence of $k_\perp$, a particularly important parameter for lithium-ion cell safety simulation. In addition, the external pressure was varied on the two largest surfaces of the cell in order to investigate the influence of the thermal contact resistances on $k_\perp$. As shown in Figure 2.1, the guarded hot plate method for prismatic cells is adapted to the prismatic format in this thesis, since this method promises one of the lowest uncertainties for thermal conductivity.

Experimental The guarded hot plate method is designed for a prismatic PHEV2 cell with NMC-G stack, manufactured by VARTA Microbattery GmbH. The test apparatus consists of a cooling plate, main- and guarded-heater, insulating materials and four springs with a defined spring constant. The test bench was validated with a stainless steel reference material at different pressures and temperatures, which resulted in a measurement uncertainty of 2.2%. To evaluate $k_\perp$ from the measurement data, the heat flow in the cell housing must be compensated for, which requires an exact determination of the thermal conductivity of the aluminum housing. This was accomplished by measuring the electrical resistivity and using a method proposed by Woodcraft [185] to determine the thermal conductivity of the aluminum through the electrical resistivity.

Theory and modeling In order to determine the $k_\perp$ of the stack from the measured thermal conductivity, three evaluation steps were developed and demonstrated in this study. First, the heat flow

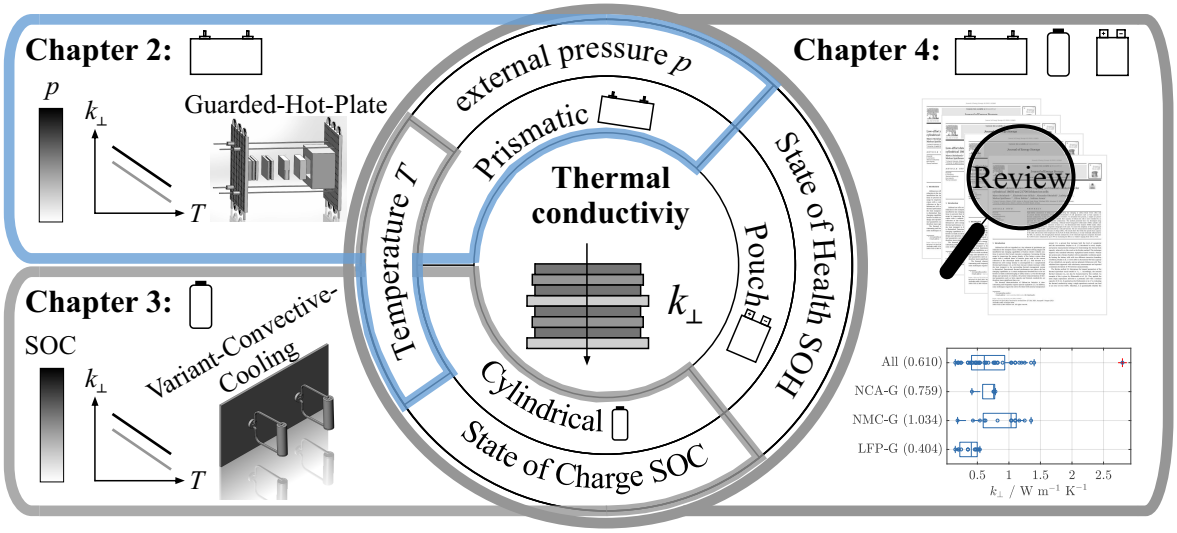

Figure 2.1: Scope of Chapter 2.

through the housing is compensated for by the previously determined thermal conductivity of the aluminum housing. The contact area between the jelly roll and the inner housing is then taken into account. Finally, the effects of the windings are accounted for through FEM simulations in order to arrive at $k_{\perp}$. Because of these evaluation steps, the uncertainty for $k_{\perp}$ increases from 2.2% to 6%, which negates the initial uncertainty advantage of the guarded hot plate method.

Results and discussion The developed experiment and the subsequent evaluation method were used between -10 and 50 °C at two different external pressures of 37.1 and 74.2 kPa. The increase in temperature showed a strong decrease in $k_{\perp}$ with increasing temperature of less than -1% K^{-1}. In addition, $k_{\perp}$ increased by 11.9% when the external pressure was increased. Pressure-dependent thermal contact resistances explained the pressure dependency. However, it cannot be completely ruled out that changes in the geometry of the jelly roll or changes in the layer thickness of the stack also contributed to the pressure dependency of $k_{\perp}$. The measured temperature dependence agrees with the work of Werner et al. [110], but does not agree with the work of Bazinski et al. [112] and Sheng et al. [155], which indicates the need for additional studies on the temperature dependence.

Author contribution The design and concept of the test bench was developed by Maximilian Stiegler and Marco Steinhardt. The measurements were planned, carried out and evaluated by Marco Steinhardt. Elisabeth Irene Gillich supported the development of the evaluation and validation. The manuscript was written by Marco Steinhardt and review and editing was done by all other authors.

Thermal conductivity inside prismatic lithium-ion cells with dependencies on temperature and external compression pressure

Marco Steinhardt, Elisabeth Irene Gillich, Maximilian Stiegler, Andreas Jossen

Journal of Energy Storage 32, p. 101680, 2020

Permanent weblink:
https://doi.org/10.1016/j.est.2020.101680

Journal of Energy Storage 32 (2020) 101680

Contents lists available at ScienceDirect

Journal of Energy Storage

journal homepage: www.elsevier.com/locate/est

Thermal conductivity inside prismatic lithium-ion cells with dependencies on temperature and external compression pressure

Marco Steinhardt*, Elisabeth Irene Gillich, Maximilian Stiegler, Andreas Jossen

Technical University of Munich (TUM), Institute for Electrical Energy Storage Technology (EES), Arcisstrasse 21, Munich, 80333, Germany

ARTICLE INFO

Keywords:
Li-ion battery
Thermal conductivity
Thermal contact resistance
Thermal resistance

ABSTRACT

Significant temperature increases and gradients inside lithium-ion battery cells are highly likely during extreme fast charging and discharging, with adverse effect on aging and safety. To assess the temperature inside the cell, the thermal conductivity of the electrode-separator composite must be determined precisely. Furthermore, the dependency of the thermal conductivity on battery states like the cell temperature or composite layer pressure has to be considered. In this work, these dependencies are investigated for a large-format lithium-ion cell with a flat-wound jelly roll and prismatic aluminum hardcase with a Nickel Manganese Cobalt (NMC) cathode and graphite anode. A precise thermal conductivity test bench with defined compression boundaries for the battery cell is constructed in compliance with the guarded heater principle. Validation tests with a stainless steel reference material prove a high accuracy and robustness against changes in compression pressure. In addition, a novel method to obtain the thermal conductivity of the aluminum cell-case is introduced. According to the measurement result, the thermal conductivity increases by 11.9% when the compression pressure rises by 37.1 kPa, which is explained by thermal contact resistances. Compared to the absolute value at 20 °C, the thermal conductivity decreases with increasing temperature by more than -1% per K.

1. Introduction

Several car manufacturers have started to mass-produce electric vehicles with lithium-ion batteries as a result of stricter political CO_2 emission targets. From the perspective of the consumer, shorter driving range and longer charging time still remain major disadvantages compared to cars with internal combustion engines [1]. Extreme fast charging with an 80% change in state of charge (*SoC*) within 10 min constitutes a major thermal challenge for lithium-ion cells and their thermal management systems [2]. Furthermore, cell design strategies aiming at higher energy densities are often accompanied by higher heat losses for equal charging power [1]. This represents a trade-off between fast charging and energy density due to thermal aspects.

Temperature rise and spatial temperature gradients inside the cell are among the main thermal challenges during fast charging. Most safety devices in lithium-ion cells are designed for an upper operational temperature of 60 °C [3] to reduce the risk of thermal runaway events with onset temperatures starting from 80 °C [4]. Waldmann et al. [5] examined the relationship between C-rate and temperature rise with values up to 15.7 °CC^{-1}. This emphasizes the need for active cooling if C-rates of 6 C are demanded. Thermal gradients inside the cell tend to rise with equal magnitude of 3.19 °CC^{-1}, which was measured by Waldmann et al. [6] for a 18650 cylindrical cell in radial direction. These gradients can reduce the lifetime of the cell [7], or can be a safety issue if the margin between 60 and 80 °C is exceeded. Temperature rise and gradients are both affected by the thermal conductivity inside the cell. Hence, thermal conductivity proves to be a decisive parameter in the area of fast charging.

The thermal conductivity inside lithium-ion cells is anisotropic due to the layered structure of the separator electrode composite. This composite is often reduced to a uniform medium with a through-plane $k_{\perp}$ and an in-plane $k_{||}$ thermal conductivity. The through-plane direction represents the major heat flux direction for most prismatic hardcase cells [8]. In contrast to $k_{||}$, $k_{\perp}$ includes thermal contact resistances between the layers [9], which are dependent on the mechanical boundary conditions. Vishwakarma et al. [10] claim that $k_{\perp}$ cannot be calculated by thermal conductivity values measured on material level if thermal contact resistances remain at a significantly high level. By implication, $k_{\perp}$ has to be measured for every cell type and boundary condition on stack or cell level if accurate modeling accuracy is important.

If high thermal modeling accuracy is important, dependencies on battery states like temperature or *SoC* have to be considered as well. For the temperature dependency of $k_{\perp}$, all available measurement data for

* Corresponding author.
E-mail address: marco.steinhardt@tum.de (M. Steinhardt).

https://doi.org/10.1016/j.est.2020.101680
Received 18 April 2020; Received in revised form 28 June 2020; Accepted 15 July 2020

Table 1
Reported temperature dependency $(dk/dT)/k_{20}$ of the thermal conductivity in through-plane direction of the electrode-separator-composite $k_{\perp}$. Additional information is given on the cell case, external compression pressure during measurement, electrode structure and material composition.

Authors	Case & pressure	Electrode geometry	Anode	Ψ_A	d_A/d_{Cu}	Cathode	Ψ_C	d_C/d_{Al}	k_{20}	$(dk/dT)/k_{20}$
Bazinski et al. [11]	Pouch foil; +0.5 bar	Stack	Graphite	n/a	n/a	LCO	n/a	n/a	0.35 W m^{-1} K^{-1}	0.0%K^{-1}
Werner et al. [8]	Prismatic Steel; 0 bar	Jelly Roll	Graphite	48%	8.5	LCO	29%	4.0	1.10 W m^{-1} K^{-1}	–0.9%K^{-1}
Sheng et al. [12]	Prismatic Al 3003; −0.9 bar	Stack	Graphite	n/a	0.3	LFP	n/a	0.8	0.54 W m^{-1} K^{-1}	+0.1%K^{-1}
Sheng et al. [12]	Al-plastic film; –0.9 bar	Stack	Graphite	n/a	n/a	LFP	n/a	n/a	0.52 W m^{-1} K^{-1}	+0.1%K^{-1}
Sheng et al. [12]	Al-plastic film; –0.9 bar	Stack	Graphite	n/a	n/a	NMC	n/a	n/a	0.66 W m^{-1} K^{-1}	+0.1%K^{-1}

double-coated unit cells is listed in Table 1. In this work, the relative temperature dependence $(dk/dT)/k_{20}$ is defined by the slope of the linear regression dk/dT divided by the absolute value k_{20} at 20 °C. Bazinski et al. [11] performed the first measurements on a 14 Ah pouch cell with LFP cathode showing no significant dependency on temperature. Two years later, Werner et al. [8] measured a significant decline with increasing temperature by -0.91%K^{-1} on a 6.8 Ah lithium cobalt oxide (LCO) prismatic hardcase cell. This finding was supported by measurements at layer level, showing that this bottom-up approach correlated closely with full cell measurements. In 2019, Sheng et al. [12] observed a marginal increase of +0.1%K^{-1} for three self-made battery cells composed of commercial NMC and LFP cell cores embedded in either a hardcase or an aluminum-plastic pouch foil.

Comparing $(dk/dT)/k_{20}$ in Table 1 reveals a strong disagreement between the result found by Werner et al. [8] those of Bazinski et al. [11] and Sheng et al. [12]. This discrepancy could be caused by different thermal contact resistances that result from the case material or external compression pressures. Measurements by Sheng et al. [12] on LFP cathodes discard any dominant effect of the cell case, while the external pressure may yield different findings on $(dk/dT)/k_{20}$. The electrode geometry serves as another explanation, while Werner et al. [8] remains the only investigation with a flat-wound jelly roll geometry.

According to Loges et al. [13], $(dk/dT)/k_{20}$ is influenced by the electrode structure, the active material composition and thickness ratio of anode d_A and cathode d_C coating to their copper d_{Cu} and aluminum d_{Al} current collectors. Comparing the cathode coatings in Table 1 draws the conclusion that LCO cathodes exhibit a completely different temperature dependency than NMC or LFP. Werner et al. [8] is the only investigation that states porosity values for anode Ψ_A and cathode Ψ_C, which discard this parameter for any explanations. Finally, the significant difference in thickness ratios between Werner et al. [8] and Sheng et al. [12] is probably another reason for different $(dk/dT)/k_{20}$ values.

This work aims to clarify some disagreements in literature on $(dk/dT)/k_{20}$ by repeating the work of Werner et al. [8] on cell level with an NMC cathode coating. Furthermore, the dependency on external compression pressure is part of the scope for evaluating the influence of thermal contact resistances, which did not form part of any investigation in Table 1.

The remainder of this paper is organized in three sections. In the experimental Section 2, the cell being tested and the measurement technique based on the guarded heater principle is described and validated with a standard reference material. Furthermore, thermal conductivity tests are shown at cell level with different temperatures and external pressure. All necessary information for transforming the thermal conductivity at cell level to the unit cell level is given in the theory and modeling Section 3. The unit cell in this paper is defined as a cube consisting of the smallest repetition of the cell layers keeping conform with the definition of Bandhauer et al. [14]. An overview of the entire transformation process is given in Fig. 7 a). The last Section 4 combines the experimental and theoretical results and discusses the temperature and pressure dependency with the findings in Table 1.

2. Experimental

2.1. Cell and reference material

The cell being tested is a prismatic hardcase PHEV-2 cell with a nominal capacity of 34 Ah, a graphite anode and NMC-111 ($Li(Ni_{1/3}Co_{1/3}Mn_{1/3})O_2$) cathode. The cell has been manufactured by VARTA Microbattery GmbH (Germany) for research purposes and is equipped with an internal Type K thermocouple inserted into the center of the jelly roll and one reference electrode. The maximum continuous C-rate for charge and discharge is specified by 2 C. An electrical resistance of 1.5 mΩ is rated for a 10 s current pulse response. The cell in question has never been operated before this investigation and has been stored at a *SoC* of 15%.

Fig. 1 a) and b) shows a computer-aided design (CAD) drawing and photograph of the cell that contains a single vertical flat wound jelly roll. Fig. 1 c) and d) indicate length specifications of the jelly roll and the cell case, which are important for the conductivity calculations in subsequent sections. The case, with thicknesses ($d_{c,t}$, $d_{c,b}$, $d_{c,s}$) ranging between 0.7 and 1.5 mm, has no physical contact with the jelly roll except for the two largest surfaces. This contact area is marked in Fig. 1 c) by the red rectangular at a height $d_{jr,h}$ of 82 mm and a length d_s of 117 mm. The case is made of AW-3003 aluminum alloy (AlMn1Cu) with a 1.1% manganese composition. This alloy is a common case material for prismatic battery cells [14] and its thermal conductivity ranges between 160 and 190 Wm^{-1}K^{-1} [15].

Table 2 lists geometrical parameters of the unit cell layers consisting of two double coated electrodes, two separator layers and one layer for each current collector (CC). Accordingly, the ratio of coating to current collector thickness for this cell is 4.3 for d_C/d_{Al} and 6.0 for d_A/d_{Cu}, which are both in the range reported by Loges et al. [13]. The heights and lengths listed in Table 2 can be used to calculate the ratio of anode overhang. Dividing their areas results in an anode overhang of 9.8%, which corresponds to the value published by Lewerenz et al. [16].

To evaluate the measurement error of the test bench introduced in the following subsection, a suitable reference material had to be selected. Details of this procedure following the criteria defined by Hust et al. [17] can be found in Appendix A. In result of this, a cuboid (150x25x91 mm) made of 1.4301 (X5CrNi18-10) stainless steel was purchased for quantifying the measurement error in this study. The reference material is shown in Fig. 1 a) (tag 6).

2.2. Test bench

The thermal conductivity test bench is based on the single-specimen guarded hot plate method, which is one of the most accurate steady-state measurement techniques [18]. Fig. 2 a) shows an overview of the whole test bench placed in a climate chamber that provides a stream of air with defined temperature T_{air}. The test object is stacked with other components between two aluminum plates, while the right plate (tag 2) serves as a heat sink containing a water-glycol (50:50) coolant with the temperature $T_{coolant}$. An equal temperature for T_{air} and $T_{coolant}$ is used at all times, to ensure that heat losses from the component stack to the environment remain equal. To keep radial heat losses to a minimum, a

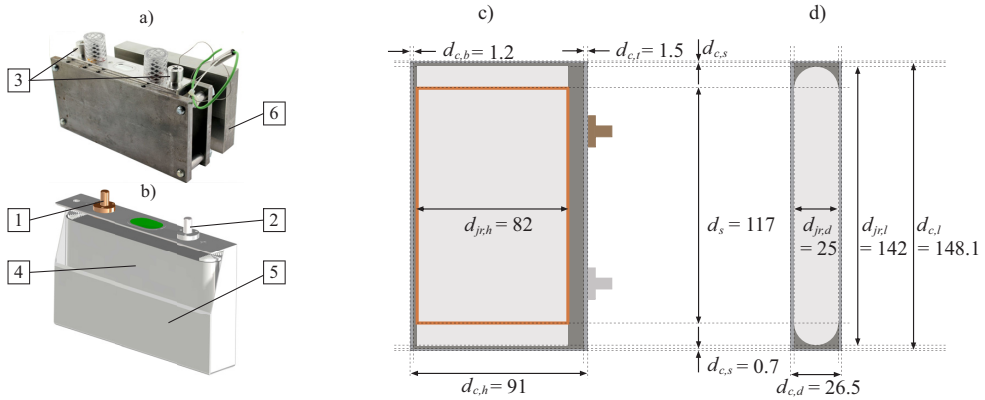

Fig. 1. Photograph a) and CAD drawing b) of reference material and cell being tested with corresponding vertical c) and horizontal d) section planes. Length specification are given in mm for the jelly roll and prismatic hardcase. 1: Negative terminal. 2: Positive terminal. 3: Feed-through for internal sensors. 4: Jelly roll. 5: Case. 6: Stainless steel reference material.

Table 2
Specification of the electrode-separator-composite given by the cell manufacturer. Length and height of the separator have not been specified.

Unit cell layer	Height / mm	Thickness / µm	Porosity / %	Length / m
2x NMC 111	74.0	64.0	27	10.9
1x Al CC	74.5	15.0	0	10.9
2x separator	n/a	21.6	42	n/a
2x graphite	77.0	59.5	30	11.5
1x Cu CC	77.5	10.0	0	11.5

4 cm thick isolation made of Styrodur® 3000 CS from BASF (tag 3) is wrapped around the stack with a thermal conductivity of 0.033 W m^{-1} K^{-1}. With a maximum temperature difference between the test object and T_{air} of 10.366 K during all measurements, lateral heat losses are smaller than 0.121 W.

A defined force F_{spring} can be applied to the stack by four springs (tag 1) with a spring constant of 47.734 N mm^{-1}. In the following experiments, the cumulative force of the springs ($4 \cdot F_{spring}$) was always set to 500 or 1000 N. This translates to a compression pressure of 36.6 and 73.3 kPa for the reference material and 37.1 and 74.2 kPa for the cell being tested. The difference in compression pressure between the reference material and the cell is caused by different cross section areas specified in subsection 2.1.

Fig. 2 b) shows details on the measurement stack consisting of a guarded heater (tag 4), the main heater (tag 5), the test object (tag 6) and a heat flow equalizer (tag 7) that provides a uniform heat flow for the test object. The main heater generates the heat flux $\dot{Q}$ for measuring thermal conductivity, which passes through the test object, the equalizer and finally sinks on the right aluminum plate. To assure equal and low contact resistances, Keratherm KP 92 thermal grease made by Kerafol with a thermal conductivity of 10 W m^{-1} K^{-1} is used between any contact surface passed by $\dot{Q}$.

A guarded heater (tag 4) is deployed to minimize heat losses on the left side of the main heater. Both heaters consists of a heating wire, which is paste between Styrodur® isolation and a copper plate with a thickness of 1 cm. The copper plates equalize the concentrated heat flux of the heating wires while the Styrodur® directs the heat flux towards the test object. Two Pt100 temperature sensors are installed to measure the temperature of the guarded heater copper plate T_{GH} and the main heating wire T_H.

The linear power supply GPD 3303D from GW-Instek supplies the electrical power for both heaters. The main heater operates in constant current mode I_H and the corresponding voltage drop U_H is measured with separated sense wires by the NI-9228 card made by National Instruments. The current of the guarded heater I_{GH} is automatically adjusted to reduce the difference between T_H and T_{GH}, which never exceeded ± 0.0467 K. Hence, heat losses at the backside of the heater

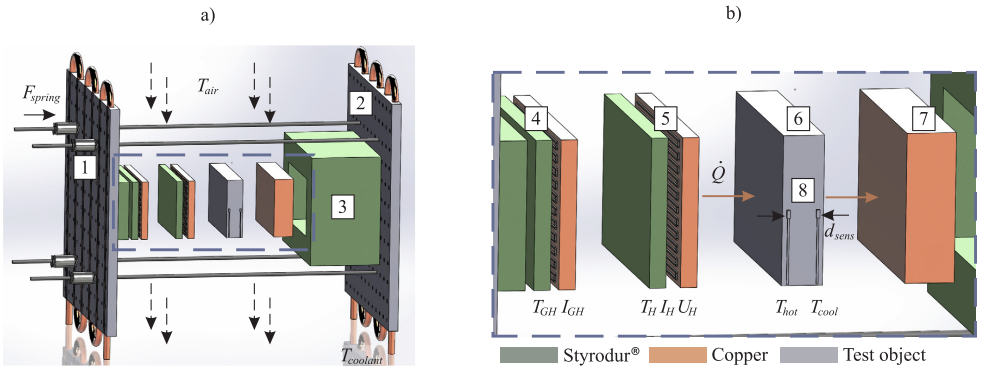

Fig. 2. Overview a) and details b) of the thermal conductivity test bench for prismatic battery cells used in this work. 1: Four springs for defined compression force F_{spring}. 2: Heat exchanger serving as heat sink. 3: Radial heat isolation. 4: Guarded heater. 5: Main heater generating heat flow $\dot{Q}$. 6: Test object (cell or reference material). 7: Heat flow equalizer. 8: Temperature sensors for test object.

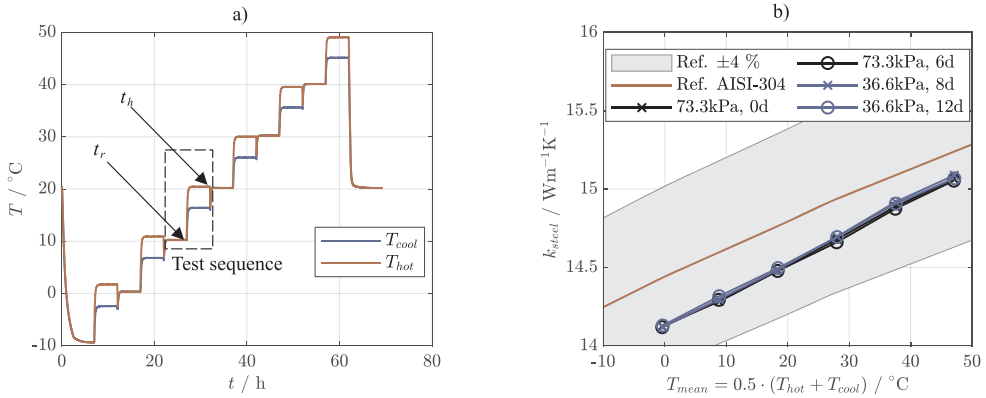

Fig. 3. a) Temperature readings during test bench validation with a stainless steel reference sample showing the evaluation point during the heating phase t_h and the rest phase t_r for one test sequence. b) Test bench validation with AISI-304 reference [19] at two compression pressures with four measurement taken between day 0 and 12.

are never greater than 2.1 mW.

The temperature gradient ($T_{hot} - T_{cool}$) in Fig. 2 is measured by two DIN EN 60751 conform 100 Ω platinum-chip temperature sensors (JUMO PCA 1.2005.1L F0,15). Both sensors are attached on the lateral surface of the test object at a distance of d_{sens}. Acquiring the temperature gradient at the lateral surface brings the advantage of not being influenced by thermal contact resistances compared to the acquisition at the two largest object surfaces. Before the sensors were attached, readings were calibrated between -10 and 40 °C with a Fluke Calibration 1524 Thermometer and a FLUKE-TEMP-5622-05-P temperature sensor with an accuracy of 0.04 °C. After the calibration, the deviation of T_{hot} and T_{cool} from the reference never exceeded 0.013 °C. In general, all temperature sensors are acquired by the National Instruments module NI-9261 in four-wire high-resolution mode, with a sample rate of 1 Hz.

2.3. Test validation

Fig. 3 a) shows the general test procedure used for any thermal conductivity measurement in this work by the temperature readings of T_{cool} and T_{hot}. The whole measurement is split into six test sequences for six different set temperatures between -10 and 40 °C. Every test sequence contains a rest and a heating phase. At the beginning of the rest phase, $T_{coolant}$ and T_{air} is set to the desired temperature. Effects arising from the temperature history are eliminated by this rest phase and measurement errors can be analyzed and calibrated at its end t_r. After the rest phase, the heating phase starts with equal duration. At the end of the heating phase t_h, the heating power is switched off automatically and $T_{coolant}$ and T_{air} are adjusted to a new set point.

Eq. 1 is always used for calculating the measured thermal conductivity k_{mes}. The constant electrical current of the main heater I_H and the measured heater voltage U_H are multiplied representing the heat flux of the main heater $\dot{Q}$. The parameter d_{sens} is the distance between two temperature sensors (see Fig. 2 b)) and A is the cross-section area of the test object orthogonal to the heat flow. The temperature difference ΔT_{h-c} between T_{hot} and T_{cool} is measured at the end of the rest t_r and heating phase t_h. The subtraction of $\Delta T_{h-c}(t_r)$ from $\Delta T_{h-c}(t_h)$ constitutes an online calibration with the assumption that any temperature difference at t_r is only caused by measurement errors. By this online calibration, long time drifts and nonlinear uncertainties can be reduced.

$$k_{mes} = \frac{I_H \cdot U_H \cdot d_{sens}}{A \cdot (\Delta T_{h-c}(t_h) - \Delta T_{h-c}(t_r))} \tag{1}$$

Fig. 3 a) shows the temperature readings for the reference material

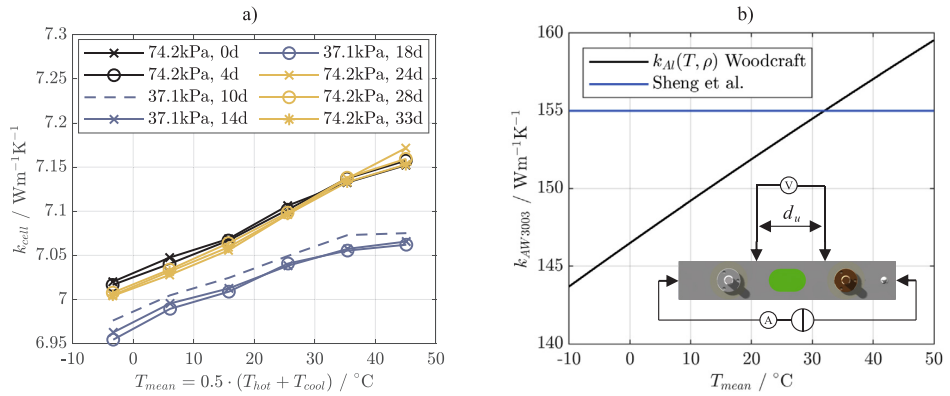

Fig. 4. a) Thermal conductivity of the cell k_{cell} at different pressures between 37.1 and 74.2 kPa with the first measurement started at day 0 and the last at day 33. b) Thermal conductivity of the aluminum alloy k_{AW3003}, which is used for the case conductivity k_{case} by Sheng et al. [12] (blue line) and in this work (black line). In this work, k_{AW3003} is calculated by electrical resistivity measurements ρ and the procedure developed by Woodcraft [22] $k_{Al}(T, \rho)$. The setup for the electrical resistivity measurements comprises one current source and one voltage sensing in the middle part of the cell. (For interpretation of the references to colour in this figure legend, the reader is referred to the web version of this article.)

Table 3
Chemical composition of stainless steel standards.

Component	1.4301 [20]	AISI-304 [19]
C / %	0.07	0.08
Mn / %	2.00	2.00
Si / %	1.00	1.00
Cr / %	17.5 - 19.5	18.0 - 20.0
Ni / %	8 - 10.5	8 - 12

introduced in Subsection 2.1, with I_H set to 2.11 A, a measured heater voltage U_H between 22.519 and 22.549 V at t_h and a temperature sensor distance d_{sens} of 17.04 mm. $T_{coolant}$ and T_{air} were varied between -10 and 40 °C in increments of 10 °C. The duration of the rest and heating period was set to 5 h, resulting in a total measuring time of 60 h. The black and blue line in Fig. 3 b) represents the evaluation of this measurement data by Eq. 1 at an external compression pressure of 36.6 and 73.3 kPa. In these four measurements k_{steel} of the reference material shows a monotonous linear increase with temperature.

For the measurement uncertainties of the test bench to be evaluated, a suitable and reliable reference curve for the thermal conductivity of 1.4301 stainless steel between –10 and 50 °C is necessary. In accordance with the DIN EN 10088-3 standard [20], Stainless steel 1.4301 has a composition listed in Table 3 that is close to the AISI 304 (American Iron and Steel Institute) standard [19]. Bogaard [19] collected thermal conductivity measurements on AISI-304 from 15 references on 20 different samples within a temperature range between 200 and 1600 K. From this data collection, Bogaard [19] created one recommended curve for AISI-304 steel with a maximum deviation of ± 4% from the measurement data. This reference curve is shown in Fig. 3 b) as a red line with the grey shaded uncertainty of ± 4%.

Comparing the red reference curve with the measurement data in black and blue in Fig. 3 reveals a maximum deviation of –2.2% which is contained within the common ± 4% uncertainty band. Furthermore, the measurement data shows equal temperature dependency to the reference curve, and indicates no influence on the applied pressure. One important aspect for detecting changes in thermal conductivity is the reproducibility and the absence of long-time drifts in the measurement data. Comparing all blue and black curves to the black measurement at day 0 results in a maximum deviation of 0.25% with no long-time drifts within a period of at least 12 days.

2.4. Cell thermal conductivity

Once the test bench had been validated, the reference object was replaced by the cell under test described in Subsection 2.1. The test plan was the same as the validation test in Subsection 2.3, apart from increasing the duration of the rest and heating period to 7 h and reducing the heater current I_H to 1.43 A with a decline in U_H to 15.284 to 15.304 V. These adjustments were made to guarantee equal temperature gradients to the validation test with a sufficient stationary time behavior. Temperature sensors for T_{cool} and T_{hot} of the same type with the same calibration procedure were attached to the cell surface with a distance d_{sens} of 18.01 mm. Furthermore, the internal cell temperature T_{int} was recorded during every conductivity test. In total, eight conductivity tests with different external pressures were conducted.

Fig. 4 a) shows the evaluation of the measurement data by Eq. 1. Equal line colors indicate the same compression pressure starting at day 0 with 74.2 kPa as a time reference point, followed by the blue lines with a reduced pressure of 37.1 kPa after 10 days and the yellow lines with a switch back to 74.2 kPa after 24 days. Dashed lines indicate measurements with insufficient waiting time between pressure adjustments, which might be necessary due to visco-elastic relaxation processes described by Oh et al. [21]. All measurements show a rise in thermal conductivity with increasing mean temperature. Analyzing the recorded data via linear regression reveals a higher slope of 3.2 mW m^{-1} K^{-2} at 74.2 kPa than for 37.1 kPa with a value of 2.2 mW m^{-1} K^{-2}. The precision measured by the individual value to the mean value of all measurements at equal preload and mean temperature shows a maximum deviation of ± 0.2% proving an excellent measurement quality. Comparing the black and yellow lines also shows a reversible change in thermal conductivity, leading to the assumption that no plastic deformation occurred when the compression pressure changed.

2.5. Case thermal conductivity

The thermal conductivity values presented in Fig. 4 a) arise from the parallel connection of the case conductivity k_{case} and the internal part k_{int} of the battery cell. The conductivity of the case k_{case} has to be known in order to separate k_{int} from the entire cell k_{cell}. However, no suitable thermal conductivity measurements are found in literature for the aluminum alloy AW 3003 in the temperature range between –10 and 50 °C. Woodcraft introduced a method for predicting the thermal conductivity of aluminum alloys by electrical resistivity measurements that is described in [22] and used for k_{case} in this work.

For this approach, the electrical resistivity at room temperature is measured in first place. A measurement setup for this is depicted in Fig. 4 b) which applies and measures an electrical current to the smallest case surfaces and measures the potential drop along the mid length of the case with a sense contacts distance d_u of 23.18 mm. The cross-section area of the case can be computed by subtracting the outer cell area ($d_{c,h} \cdot d_{c,d}$) from the internal cell area, which is the product of ($d_{c,h} - d_{c,b} - d_{c,t}$) and ($d_{c,d} - 2{\cdot}d_{c,s}$). With a cross section of the case of 196 mm^2 and an electrical resistance of 5.24 $\mu\Omega$ the case resistivity was computed to 44.19 nΩm, which closely correlates with the value listed in [23] of 43 nΩ m for 3003 alloy, with the temper H18 and corresponding thermal conductivity of 155 W m^{-1} K^{-1}.

Woodcraft's [22] approach prescribes that the electrical resistivity needs to be greater than 31 nΩm, which is fulfilled by the aluminum alloy in this work. Next, the residual resistivity due to electron-defect interactions is computed to 17.79 nΩm and a beta factor of 0.7261 is derived using Wiedemann-Franz's law, which varies with the purity of the alloy. Finally, the thermal conductivity is determined from Woodcraft's equation that is based on 29 measurements subjected to 15 different aluminum alloys. The associated results for the aluminum alloy in this work are plotted in Fig. 4 b) in addition to the constant value used by Sheng et al. [12]. To estimate the uncertainty of this method, the electrical resistance in [23] of 43 nΩm is applied in the same way with the method of Woodcraft yielding a thermal conductivity of 155.88 W m^{-1} K^{-1}. Comparing this result with 155 W m^{-1} K^{-1} quantifies the uncertainty as 0.6%.

3. Theory and modeling

3.1. Unit cell conductivity

Due to the layered structure, the unit cell exhibits two faces with a through-plane $k_\perp$ and four faces with an in-plane thermal conductivity $k_{||}$, which are defined by Eq. 2 and 3. Both parameters are affected by the layer thickness and thermal conductivity values of anode (d_A, k_A), cathode (d_C, k_C), separator (d_S, k_S), anode current collectors (d_{Cu}, k_{Cu}) and cathode current collector (d_{Al}, k_{Al}). For double-coated electrodes, all active materials and the separator have to be considered twice.

$$k_\perp = \frac{2{\cdot}(d_A + d_S + d_C) + d_{Cu} + d_{Al}}{2{\cdot}\left(\frac{d_A}{k_A} + \frac{d_S}{k_S} + \frac{d_C}{k_C}\right) + \frac{d_{Cu}}{k_{Cu}} + \frac{d_{Al}}{k_{Al}}} \tag{2}$$

$$k_\parallel = \frac{2{\cdot}(d_A{\cdot}k_A + d_S{\cdot}k_S + d_C{\cdot}k_C) + d_{Cu}{\cdot}k_{Cu} + d_{Al}{\cdot}k_{Al}}{2{\cdot}(d_A + d_S + d_C) + d_{Cu} + d_{Al}} \tag{3}$$

In three-dimensional thermal finite element method (FEM) models,

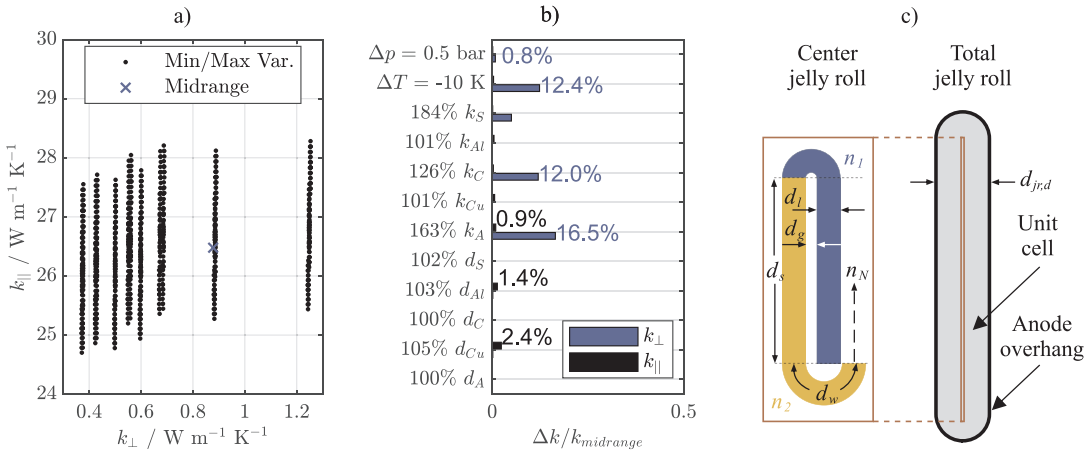

Fig. 5. a) Uncertainty range of $k_{||}$ and $k_\perp$ for the unit cell taking k_{Max} and k_{Min} from Table 4 and uncertainties in layer thicknesses. b) Sensitivity of $k_\perp$ and $k_{||}$ around mid-range values from a) with changes in pressure Δp, temperature ΔT, thermal conductivity values of unit cell layers (k_S, k_{Al}, k_C, k_{Cu}, k_A) and layer thicknesses (d_S, d_{Al}, d_C, d_{Cu}, d_A). c) Geometric definition for estimating the thickness of the jelly roll gap d_g.

$k_{||}$ and $k_\perp$ are often parameterized by measurements on unit cell layers [24] that have no dependency on pressure or temperature. To estimate the uncertainties of this method, Table 4 lists minimum k_{Min} and maximum k_{Max} values measured on layer level. Further uncertainties in Eq. 2 and 3 arise from measurement errors of the layer thicknesses that are quantified to ± 0.5 μm for common micrometers.

To illustrate the impact of these uncertainties, Eq. 2 and 3 are applied 2^{10} times using all possible combinations of minimum and maximum values for the thermal conductivity or layer thickness. Black dots in Fig. 5 a) show the results of this min/max variation with a range from 0.371 to 1.254 W m^{-1} K^{-1} for $k_\perp$ and 24.7 to 28.3 W m^{-1} K^{-1} for $k_{||}$. Considering the mid-range of k_{Min} and k_{Max} as the most likely scenario leads to values for $k_\perp$ and $k_{||}$ of 0.878 and 26.5 W m^{-1} K^{-1} highlighted by the blue cross in Fig. 5 a). Dividing the mid-range result by the largest deviation from the min/max variation computes to an uncertainty for $k_{||}$ of 6% and for $k_\perp$ of 58%.

Fig. 5 b) illustrates the sensitivity of $k_{||}$ and $k_\perp$ by varying only one parameter around the mid-range value. For example, the maximum value for k_C amounts to 126% of its mid-range of 0.725 W m^{-1} K^{-1} affecting $k_\perp$ by 12%. Uncertainties for the thicknesses ranging from 100 to 105% are calculated with a measurement uncertainty of 0.5 μm regarding the thickness values in Table 2. According to Fig. 5 b), $k_\perp$ is sensitive to the thermal conductivity values of the active materials (k_A, k_C) and the separator k_S, while $k_{||}$ is mostly affected by the thickness values of the current collectors (d_{Al}, d_{Cu}).

Table 4 lists the relative pressure dependency $(dk/dp)/k_{2bar}$ for changes in thermal conductivity and the Young's modulus E for changing layer thicknesses ε to estimate the pressure dependency of $k_{||}$ and $k_\perp$. When pressure is increased by 0.5 bar, the active materials (d_A, d_C) and the separator thicknesses d_S decline by -0.1 to –0.3%. Taking the changes in layer thickness in combination with $(dk/dp)/k_{2bar}$ for a pressure increase of 0.5 bar alters the mid-range value in Fig. 5 a) by 0.2% for $k_{||}$ and 0.8% for $k_\perp$.

The temperature dependency of the layer thermal conductivity $(dk/dT)/k_{20}$ and the linear thermal expansion coefficient α are listed in Table 4. For $(dk/dT)/k_{20}$ no measurement data on electrolyte soaked NMC, separator or graphite could be found in literature. Therefore, missing temperature dependencies are taken from Werner et al. [8],

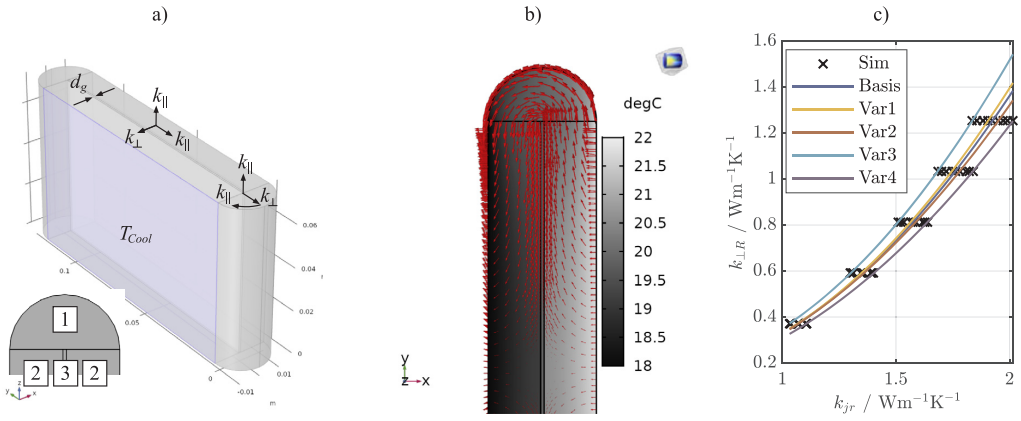

Fig. 6. a) Geometry of thermal FEM model consisting of the volumes windings (1), stack (2) and jelly roll gap (3) used for the functional relation between k_{jr} and $k_{\perp R}$. b) Heat flow (red arrows) and temperature field inside the jelly roll with d_g=0.8 mm and a temperature gradient of 4 °C between the jelly roll case contact areas. c) Functional relation between k_{jr} and $k_{\perp R}$ for the basis scenario and variation in d_g and $k_{||}$ specified in Table 5. (For interpretation of the references to colour in this figure legend, the reader is referred to the web version of this article.)

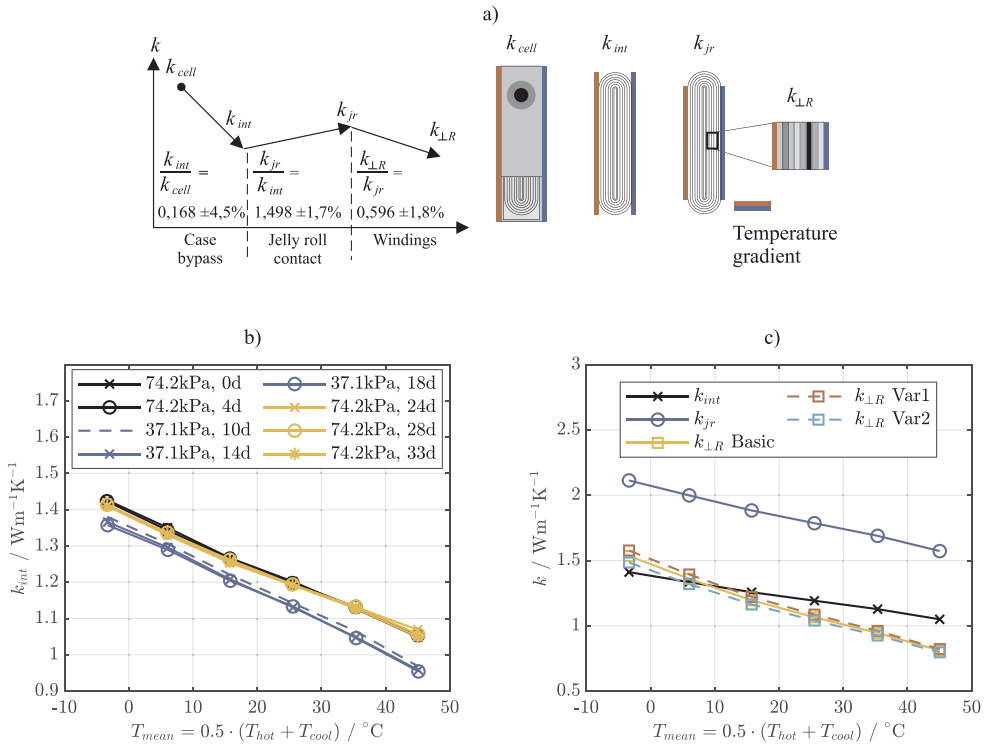

Fig. 7. a) Overview of transformation process from k_{cell} to $k_{\perp R}$ with transformation factors and their uncertainties for the data presented in c) at 25.5 ˚C. b) Internal cell conductivity k_{int} after the case bypass from Fig. 4 a) has been compensated for. c) Exemplary transformation from k_{int} to $k_{\perp R}$ for the measurement started at day 33.

which are measured on dry samples and calculated into electrolyte-soaked values. To estimate the influence of a -10 ˚C temperature drop on $k_{||}$ and $k_{\perp}$, the layer thicknesses are multiplied by $(1 + \alpha \cdot (-10\ ^{\circ}C))$ and the mid-range of k_{max} and k_{min} is multiplied by $(1 + (dk/dT)/k_{20} \cdot (-10\ ^{\circ}C))$. When these adjustments are combined with Eq. 2 and 3, this leads to a change in $k_{||}$ of 0.4% and $k_{\perp}$ by 12.4%. This postulates a strong temperature dependency for $k_{\perp}$ of -1.24%K^{-1}.

3.2. Jelly roll gap

During cell production, the electrode-separator composite is rolled around a winding core [35]. Due to this winding process, an argon-filled gap in the middle of the jelly roll may remain, which is illustrated in Fig. 5 c). Bandhauer et al. [14] assumed the thickness of this gap d_g to be 0.5 mm for a prismatic jelly roll with a unit cell thickness of approximately 0.28 mm. For external heat flows passing the jelly roll between its largest case contact faces, this jelly roll gap might constitute

Table 4
Parameters for calculating $k_{||}$ and $k_{\perp}$ according to Eq. 2 and 3 with measurements on unit cell layers. The minimum k_{Min} and maximum k_{Max} reported thermal layer conductivity in literature, the pressure dependency of the thermal conductivity $(dk/dp)/k_{2bar}$, the Young's modulus E and corresponding strain ε at 0.5 bar, the temperature dependency $(dk/dT)/k_{20}$ of the cell layers and the linear thermal expansion coefficient α are used to evaluate uncertainties and the temperature or pressure dependency of $k_{||}$ and $k_{\perp}$.

Unit cell layer	k_{Min}/ W m^{-1} K^{-1}	k_{Max} / W m^{-1} K^{-1}	$(dk/dp)/k_{2bar}$/ % bar^{-1}	E / MPa	ε(0.5 bar) / %	$(dk/dT)/k_{20}$ / % K^{-1}	α / 10^{-6} K^{-1}
NMC [a]	0.54 [25][b]	0.91 [28][b]	0.5 [28] [c]	40 [30][g]	–0.1	n/a[d]	12 - 13 [32]
Al (pure)	235 [26]	240 [26]	[c]	70 · 10^3 [31]	0.0	0.0 [26]	23.1 [31]
Separator [a]	0.10 [25][b]	1.13 [29]	-0.6 [h] [25]	20 [30][g]	-0.3	n/a[e]	44 [33]
Graphite [a]	0.36 [27][b]	1.58 [25][b]	3.95 [i] [25,28] [c]	33 [30][g]	-0.2	n/a[f]	55 [34]
Cu (pure)	394 [26]	404 [26]		120 · 10^3 [31]	0.0	0.0 [26]	16.5 [31]

[a] Soaked with electrolyte.
[b] Measured around room temperature.
[c] No dependency is assumed.
[d] For LCO cathode derived from dry measurements -1.7%K^{-1} [8].
[e] Derived from dry measurements -0.0%K^{-1} [8].
[f] Derived from dry measurements -1.0%K^{-1} [8].
[g] For 0.2 MPa.
[h] Mid-range of -3.4 - 2.2 % bar^{-1}.
[i] Mid-range of 0.9 - 7.0 % bar^{-1}.

Table 5
Fitting parameters for Eq. 8 shown in Fig. 6 c) for the functional relation between k_{jr} and $k_{\perp R}$.

	Basis	Var1	Var2	Var3	Var4
d_g/mm	0.8	1.0	0.6	1.0	0.6
$k_{\|\|}$/W m^{-1} K^{-1}	26.5	26.5	26.5	24.7	28.3
a/W^{-1} m K	0.4474	0.4818	0.4038	0.5294	0.3739
b	–0.3091	–0.3802	–0.2173	–0.4222	–0.1972
c/W m^{-1} K^{-1}	0.1903	0.2283	0.1406	0.2442	0.1319

a significant heat barrier, because argon exhibits a low thermal conductivity of 0.0179 W m^{-1} K^{-1} [31]. As external heat flows are applied for the test procedure in Section 2, the influence of the jelly roll gap requires further research. The most important parameter for this study is the thickness of the jelly roll gap d_g, which is estimated using the relationship between the total electrode length d_{el}, the thickness of the electrode separator composite d_l and the thickness of the flat-wound jelly roll $d_{jr,d}$.

To determine this relationship, the length of the straight jelly roll sections d_s and the half windings d_w is added N times until the value of d_{el} is reached. For simplicity, in Eq. 4 every winding process comprises a straight and a winding section. In contrast to d_s, the length of the half winding section depends on the winding number n and the gap thickness d_g as stated by Eq. 5. Inserting Eq. 5 into 4 and applying the Gaussian arithmetic series allows Eq. 6 to be derived. The total thickness of the wound electrode d_{et} can be calculated from Eq. 7 with the knowledge of N.

$$d_{el} = \sum_{n=1}^{N} (d_w(n) + d_s) \tag{4}$$

$$d_w(n) = 0.5 \cdot \pi \cdot (n \cdot d_l + d_g) \tag{5}$$

$$d_{el} = N \cdot (d_s + 0.5 \cdot \pi \cdot d_g) + 0.5 \cdot \pi \cdot d_l \cdot \frac{N \cdot (N+1)}{2} \tag{6}$$

$$d_{et} = N \cdot d_l + d_g \tag{7}$$

Due to the internal sensors, the capacity of the cell under test decreased by 7%, which is translated to a 7% shorter unit cell length $d_{el,uc}$ of 10.137 m compared to the cathode length in Table 2. Solving Eq. 6 with this value for $d_{el,uc}$, an assumed $d_{g,uc}$ of 1 mm for the internal sensors, d_s of 117 mm according to Fig. 1 and a value for $d_{l,uc}$ of 315.2 μm results in 74 unit cell layers N_{uc}. According to Eq. 7, the corresponding thickness $d_{et,uc}$ is equal to 24.32 mm.

Furthermore, the anode overhang discussed in Subsection 2.1 is considered in order to estimate the total thickness of the jelly roll. This overhang has a total length $d_{el,ao}$ of 600 mm and a thickness $d_{l,ao}$ of 112.7 μm, with a single layer for the current collector d_{Cu} and anode coating d_A and two separator layers d_S. Assuming the overhang appears only on the outer windings, $d_{g,ao}$ is equal to $d_{et,uc}$ of the unit cell winding. Solving Eq. 6 for the anode overhang with the same value for d_s as for the unit cell results in four anode overhang layers N_{ao}. The overall thickness of the jelly roll $d_{jr,d}$ is 24.8 mm, which is a plausible value, as in its dry state the jelly roll has to fit into the 25 mm of free space between the case walls.

Due to solid electrolyte interface formation and particle rearrangement, the thickness of the unit cell in its dry state increases during the formation process [36]. This irreversible and the total dilation is calculated by the work of Sauerteig et al. [37] with the knowledge of the cathode mass loading and the porosity of the anode. Applying these equations with a cathode mass loading of 21.1 mg cm^{-2} results in an irreversible dilation of 2.51 μm and a total dilation of 6.55 μm. Adding 2.51 μm to $d_{l,uc}$ in its dry state will increase $d_{jr,d}$ to 25.0 mm after the formation process at zero state of charge. The remaining dilation of 4.04 μm until total dilation is reached constitutes a 1.3% increase in $d_{l,uc}$ compared to the thickness after formation. This increase from zero to full state of charge matches the range of Bauer et al. [36] of 1–2% for a NMC graphite unit cell. Taking the 2% as an extreme scenario will rise $d_{jr,d}$ to 25.4 mm. Assuming the free space between the case walls stays constant, d_g changes between 0.6 and 1.0 mm.

3.3. From unit cell to jelly roll conductivity

As already discussed by Werner et al. [8], the main thermal contact between the electrodes inside a prismatic cell with their environment is at the two largest surfaces of the case. Considering a planar stack without windings and a temperature gradient between the largest cell faces, each heat flow is influenced only by $k_{\perp}$. In the case of a flat-wound electrode geometry, the overall jelly roll conductivity is also affected by $k_{||}$ due to heat flows through the windings.

In this study, the approach by Werner et al. [8] was used under the boundary condition of this work and the consideration of the jelly roll gap. Furthermore, instead of analytic calculation, a three-dimensional FEM model was created in COMSOL Multiphysics 5.4 to evaluate the correlation between $k_{\perp}$ and k_{jr}. The geometry of this model is depicted in Fig. 6 a) with a total height in the z-direction equal to the height of the cathode listed in Table 2. The length in the y-direction of the case contact area indicated in purple is set to d_s, while the overall thickness in the x-direction amounts to $d_{jr,d}$. The total jelly roll is subdivided into two winding volumes (tag 1), two electrode stack volumes (tag 2) and one volume for the jelly roll gap (tag 3) defined by d_g. The thermal conductivity of the winding and stack volumes are anisotropic with a cylindrical coordinate system for the winding section and a Cartesian for the stacked volumes. For any simulation, the thermal conductivity is assumed to be independent of temperature. All boundaries are thermally isolated except for the two case contact areas with an isothermal boundary of T_{cool} and T_{hot} of 18 °C and 22 °C.

Fig. 6 b) shows the simulation results for a jelly roll gap of 0.8 mm and a through-plan and in-plane conductivity of 0.8125 and 26.5 W m^{-1} K^{-1}. The surface integral over the case contact areas results in a total heat of 2.107 W, leading to an effective thermal conductivity between the largest stack surfaces of 1.575 W m^{-1} K^{-1}. The red vector field illustrates the direction of the heat flow with the arrow length on a logarithmic scale. According to this simulation, the major heat flow is conducted through the winding volumes. The surface integral of the heat flux entering the gap volume gives rise to a heat of 0.1975 W which accounts for 9.4% of the total heat flux. This fraction increases to 28.7% if no gap volume is present.

The primary aim of the simulation is to establish a correlation between the through-plane conductivity of the unit cell with contact resistances $k_{\perp R}$ and the jelly roll k_{jr} that is influenced by d_g and $k_{||}$. Both parameters can only be determined by their ranges of 0.6 to 1.0 mm and 24.7 to 28.3 W m^{-1} K^{-1}. Therefore, a parametric sweep was performed with the mentioned ranges and four equidistant values for $k_{\perp R}$ between 0.3710 and 1.2188 W m^{-1} K^{-1}. The simulation results are displayed in Fig. 6 c) as black crosses. For constant values for d_g and $k_{||}$ the correlation between $k_{\perp R}$ and k_{jr} reveals a quadratic relationship. Five quadratic least square fits are depicted in Fig. 6 c) with the blue line demonstrating the most likely basis scenario, with mid-range values for d_g of 0.8 mm and $k_{||}$ of 26.5 W m^{-1} K^{-1}. The yellow (Var1) and red (Var2) lines indicate only a variation in the parameter d_g marking the uncertainties in the jelly roll gap. The two remaining variations (Var3 and 4) in purple and cyan constitute the upper and lower bound by varying d_g and $k_{||}$. All parameters for Fig. 6 c) and Eq. 8 are listed in Table 5.

$$k_{\perp R} = a \cdot k_{jr}^2 + b \cdot k_{jr} + c \tag{8}$$

3.4. From cell to jelly roll conductivity

Fig. 7 illustrates the overall evaluation process, starting with the measured cell conductivity k_{cell} and ending at the quantity of interest $k_{\perp R}$. The case bypass has to be first compensated for leading to the internal conductivity k_{int}, which consists of the gas volume inside the cell and the jelly roll. The thermal conductivity k_{jr} of the jelly roll is derived from the knowledge of the contact area between the jelly roll and the cell case. Subsection 3.3 addressed the correlation between k_{jr} and $k_{\perp R}$. To complete the evaluation process from k_{cell} to $k_{\perp R}$, the relation between k_{cell} and k_{jr} is explained in this subsection.

To evaluate the internal cell conductivity k_{int}, Eq. A.3 has to be resolved to k_{int}, which is shown by Eq. 9. The conductivity value for the case k_{case} is extracted from Fig. 4 b) with the same mean temperature as the cell measurement.

$$k_{int} = \frac{A_{cell}}{A_{cell} - A_{case}} \cdot k_{cell} - \frac{A_{case}}{A_{cell} - A_{case}} \cdot k_{case} \tag{9}$$

Applying Eq. 9 to k_{cell} in Fig. 4 will result in the internal conductivity k_{int} in Fig. 7 b). Due to the high value of k_{case}, k_{int} is approximately six times smaller than k_{cell}. Furthermore, the dependency on the mean temperature T_{mean} alters its sign from a rising to a falling characteristic with increasing temperature.

The correlation between k_{int} and k_{jr} in Eq. 10 is defined by the ratio of the internal surface of the case A_{int} and the contact area between the case and the jelly roll A_{jr}. A_{int} is determined by Eq. A.2 and A_{jr} is the product of the cathode height in Table 2 and the jelly roll contact length d_s.

$$k_{jr} = \frac{A_{int}}{A_{jr}} \cdot k_{int} \tag{10}$$

An example of the overall chain of transformation from k_{int} to $k_{\perp R}$ is illustrated in Fig. 7 c) for the cell measurement that started at day 33, with a compression pressure of 74.2 kPa. At 25.5 °C, k_{int} amounts to 1.192 W m^{-1} K^{-1} after the case is compensated for. Moreover, k_{int} is converted to k_{jr} using Equation 10, calculating to a conductivity value of 1.786 W m^{-1} K^{-1}. By applying Eq. 8, $k_{\perp R}$ amounts to 1.065 W m^{-1} K^{-1} for the basis scenario with a range of 0.972 (Var2) and 1.178 W m^{-1} K^{-1} (Var1).

To analyze the uncertainty for $k_{\perp R}$, the root square sum of each uncertainty in the chain of transformation shown in Fig. 7 a) is calculated. This approach is in accordance with the uncertainty analysis of Sheng et al. [12]. The maximum uncertainty of 2.2% for k_{cell} was determined in Subsection 2.3. The case bypass introduces an uncertainty of 4.5% including errors in the approach by Woodcraft and the electrical resistivity measurement. Assuming an absolute error for d_s of 2 mm quantifies the uncertainty of the jelly roll contact to be 1.7%. Finally, 1.8% uncertainty exists, which arises from the jelly roll gap variation Var1 and Var2. Building the root square sum of all uncertainties results in a total value of 5.6% for $k_{\perp R}$.

4. Results and discussion

In Fig. 8, the conductivity $k_{\perp R}$ for external compression pressures of 37.1 a) and 74.2 kPa b) is analyzed according to the procedure presented in Section 3. Cross markers show the transformed measurement data from Fig. 4 a) and their best linear fits are highlighted in solid lines. These three lines represent the most likely scenario (Bias, black) and the lower (Var2) and upper (Var1) bound regarding the uncertainty for the jelly roll gap d_g. The gray-shaded area fills the span between Var3 and Var4 including uncertainties in d_g and $k_{||}$. No linear fit is drawn for Var3 and Var4 in Fig. 8, because $k_{||}$ is assumed to not change significantly with differences in temperature or pressure, which was discussed in Section 3.

Values for $k_{\perp R}$ taken at 20 °C for the basis scenario represented by the black lines ranging from 1.047 to 1.171 W m^{-1} K^{-1} correlate closely with the range of 0.371 and 1.254 W m^{-1} K^{-1} calculated from the unit cell layer measurements in Fig. 5. Higher values up to 1.6 W m^{-1} K^{-1} in Fig. 8 can be explained by the fact that most values in Table 4 are measured at around room temperature.

The following subsections discuss how $k_{\perp R}$ change with changes in external pressure and mean temperature of the cell. Treating $k_{\perp R}$ as constant, will cause errors in the determination of temperature gradients inside the cell. According to the analysis in Appendix B, an overestimation of $k_{\perp R}$ of +10% will translate to an error in temperature gradient of -9.1%.

4.1. Dependency on external pressure

An increase of about (11.9 ± 0.3)% at 20 °C is observed for $k_{\perp R}$ when the external compression pressure is changed from 37.1 to 74.2 kPa for the basic scenario and the variations Var1 and Var2. This enhancement can be the result of reduced thermal contact resistances R_{tc}, a smaller jelly roll gap d_g or an increased thermal conductivity of the material $k_{\perp}$ at 74.2 kPa. An increase of 37.1 kPa at the largest cell surfaces converts to a rise in pressure at the jelly roll to case contact of approximately 0.5 bar, if no significant interaction of the case is assumed. According to Fig. 5 b), this enlargement in through-plane pressure affects $k_{\perp}$ by an increase of only 0.8%. Referring to the strain values in Table 4, the cell thickness will change less than 0.3% at this pressure increase. This precludes any dominant effect arising from changes in d_g or d_{sens}. Therefore, only changing thermal contact resistances R_{tc} appears as the main cause for the observed changes in $k_{\perp R}$.

Eq. 11 [38] calculates the effect on the overall thermal conductivity $k_{\perp R}$ by the sum of thermal contact resistances R_{tc} between the layers and the case-separator interface. Hence, R_{tc} is determined by Eq. 12 with the knowledge of $k_{\perp R}$ and $k_{\perp}$. The maximum value for R_{tc} at 37.1 kPa can be estimated by the highest value of $k_{\perp}$ of 1.254 W m^{-1} K^{-1} in Fig. 5 and $k_{\perp R}$(20 °C, 37.1 kPa) in Fig. 8 of 1.047 W m^{-1} K^{-1}. According to this estimation, R_{tc} is lower than 553 μm^{2}KW^{-1}. This range correlates with the results found by Ponnappan et al. [9], who measured values between 300 and 400 μm^{2}KW^{-1} and the results of Ye et al. [38] of 150 μm^{2}KW^{-1}.

$$k_{\perp R}(T, p) = \frac{d_{l,uc}}{\frac{d_{l,uc}}{k_{\perp}(T)} + R_{tc}(p)} \tag{11}$$

$$R_{tc}(p) = \frac{d_{l,uc}}{k_{\perp R}(T, p)} - \frac{d_{l,uc}}{k_{\perp}(T)} \tag{12}$$

$$R_{tc}(37.1\text{ kPa}) - R_{tc}(74.2\text{ kPa}) = \frac{d_{l,uc}}{k_{\perp R}(T, 37.1\text{ kPa})} - \frac{d_{l,uc}}{k_{\perp R}(T, 74.2\text{ kPa})} \tag{13}$$

The absolute value for R_{tc} can not be determined with the measurement results in Fig. 8. Nevertheless, by the assumption of a pressure independent thermal conductivity $k_{\perp}(T)$ the difference between R_{tc} (37.1 kPa) and R_{tc}(74.2 kPa) can be derived from Eq. 13. For the Basic scenario at 20 °C this difference amounts to 32.2 μm^{2}KW^{-1}. In the results of Ponnappan et al. [9], R_{tc} reached saturation at 300 μm^{2}KW^{-1} for pressures higher than 50 psi (3.4 bar). This gives rise to the assumption of a further enhancement of $k_{\perp R}$ of the cell investigated here, if the external compression pressure is further increased.

4.2. Dependency on temperature

Dividing the slopes of the linear regression of the base cases in Fig. 8 by the thermal conductivity value at 20 °C results in a temperature dependence of -1.49%K^{-1} at 37.1 kPa and -1.27%K^{-1} at 74.2 kPa. These values correspond with the calculated values in Fig. 5 a) of –1.24%K^{-1} and correlate closely with the measurement results by Werner et al. [8] shown in Table 1. Nevertheless, these values disagree with the observations made by Bazinski et al. [11] and Sheng et al. [12].

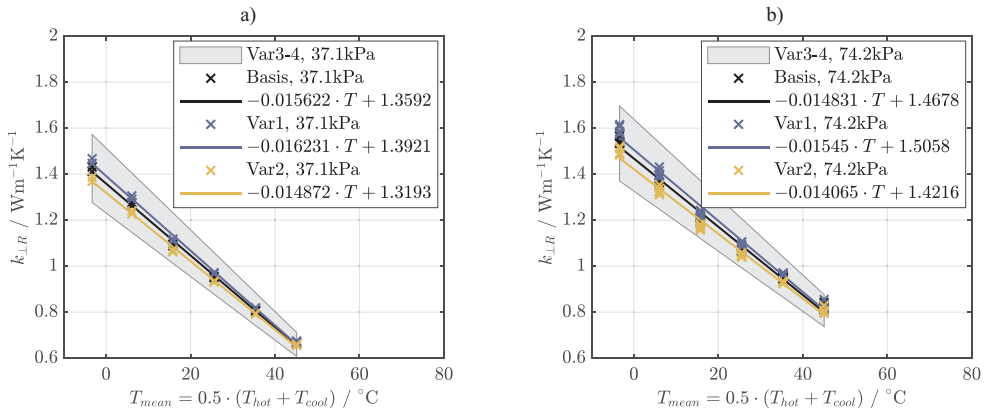

Fig. 8. Through-plane thermal conductivity of the unit cell $k_{\perp R}$ at an external compression pressure of 37.1 a) and 74.2 kPa b). For deriving the temperature dependency, linear regression parameters are given for the basis scenario and the parameter variation Var1 and Var2, which considers different jelly roll gap thicknesses d_g. Var3 and Var4 include uncertainties in $k_{||}$ and d_g marking the extreme upper and lower bound.

Several factors affect the temperature dependency of $k_{\perp R}$ [13] [3], which also explain the different findings in literature:

1. Material composition (e.g. binder, electrolyte, active materials, carbon black, separator coatings).
2. Electrode structure (e.g. porosity, particle size distribution and shape, particle-particle interface).
3. Thickness ratio of inactive to active material (d_A/d_{Cu}, d_C/d_{Al}).
4. Layer-to-layer contact resistance R_{ct}.

Most investigations listed in Table 1 reveal less detailed information on material composition or electrode structure. However, the LFP cathode system is characterized by a low temperature dependency resulting from lower particle sizes around 2 μm [39], compared to NMC with sizes around 10 μm [40]. Maleki et al. [3] measured the thermal conductivity of negative electrode material without electrolyte for particle sizes ranging from 6 to 75 μm. Compared to the base sample with a temperature dependency of -0.01%K^{-1} and a particle size of 6 μm, the temperature dependency for a sample with a particle size of 75 μm decreases to -0.38%K^{-1}.

PVDF binder, applied in most commercial active materials, might be one of the main causes for the negative temperature dependency. In the work of dos Santos et al. [41], the thermal conductivity of PVDF decreased from 0.26 to 0.18 W m^{-1} K^{-1} for a temperature increase from 20 to 100 °C. This corresponds to a temperature dependence of -0.56%K^{-1}. At temperatures higher than 100 °C, the thermal conductivity of PVDF starts rising rapidly. Based on $(dk/dT)/k_{20}$ of PVDF, it can be assumed, that $k_{\perp R}$ in Fig. 8 will keep decreasing until 100 °C. Furthermore, varying weight portion of PVDF could explain different findings in Table 1.

As discussed by Loges et al. [13], the thickness ratio of electrodes influences the overall thermal conductivity. This also applies for the temperature dependency, which gets closer to zero if the current collectors become more dominant. Therefore, the low values of d_A/d_{Cu} and d_C/d_{Al} given by Sheng [12] listed in Table 1 may be the reason for the positive temperature dependency observed in the measurements for the prismatic LFP hardcase cell.

Thermal contact resistance between the cell layers can change the temperature dependency of $k_{\perp R}$. Ponnappan et al. [9] and Gaitonde et al. [42] observed no significant change of R_{tc} over temperature. A dominant temperature independent R_{tc} would compensate any temperature dependence of $k_{\perp R}$ close to zero. Nevertheless, due to thermal swelling, thermal contact resistances may also influence the slope of the linear curve by changing the layer-to-layer pressure.

5. Conclusion

This work investigates the through-plane thermal conductivity inside a prismatic NMC lithium-ion cell at different temperatures and external pressures. For detecting changes in thermal conductivity, high precision and accuracy of the measurement procedure is inevitable. Therefore, a test bench is designed in compliance with the guarded heater principle and validated extensively with a standard reference material. The validation proves excellent measurement quality for the test bench, which is adaptable to different prismatic formats and pouch cells.

The hardcase of prismatic cells constitutes the major thermal interface between the inner jelly roll and the cell surrounding. The thermal conductivity of the case is thus an important quantity for this work. Therefore, a nondestructive measurement technique was introduced that determines the thermal conductivity of the cell case by means of electrical resistivity measurements. This method was first applied in the field of battery research and is useful for any thermal investigation with prismatic cells.

Most prismatic hardcase cells have to be installed with an external pressure to counter swelling of the jelly roll. The manufacturer of the PHEV2 cell in this work specified this pressure between 37.1 and 74.2 kPa. Increasing the pressure within this range rises the thermal through-plane conductivity by 11.9%. Thermal contact resistances between the cell layers of 32.2 μm^{2}KW^{-1} explained this thermo-mechanical interaction. Future work will look into measurements with more than two pressure values to gain more information on the course of thermal conductivity.

The thermal conductivity of the investigated cell decreases linearly with increasing temperature. Compared to the absolute value at 20 °C, this decrease amounts to more than 1% per K. Taking this temperature dependency into account may improve thermal modeling at extreme temperatures, which is especially the case in the area of abuse simulations. Therefore, future studies on the progression of the thermal conductivity above 40 °C are recommended.

CRediT authorship contribution statement

Marco Steinhardt: Conceptualization, Data curation, Formal analysis, Funding acquisition, Investigation, Methodology, Project administration, Resources, Software, Supervision, Validation, Visualization, Writing - original draft. **Elisabeth Irene Gillich:** Methodology, Validation, Writing - review & editing, Funding acquisition. **Maximilian Stiegler:** Validation, Software, Writing - review & editing.

Andreas Jossen: Writing - review & editing, Funding acquisition.

Declaration of Competing Interest

The authors declare that they have no known competing financial interests or personal relationships that could have appeared to influence the work reported in this paper.

Acknowledgements

This work was supported financially by the German Federal Ministry of Education and Research (BMBF) [03XP0027G MiBZ] and Federal Ministry for Economic Affairs and Energy (BMWi) [03ET6153C iMoBatt]. The authors thank Korbinian Schmidt from the Institute for Electrical Energy Storage Technology at the Technical University of Munich for his practical support.

Appendix A. Selection of reference material

The reference material in this study was selected in accordance with four selection criteria stated by Hust et al. [17]:

1. The material should be homogeneous and isotropic.
2. Thermal conductivity should not vary with time.
3. The material should be available, machinable and inexpensive.
4. The material should have similar thermal conductivity as the material to be measured.

According to Maglić et al. [43], possible candidates meeting the first three criteria are copper (400 $Wm^{-1}K^{-1}$), tungsten (173 $W\ m^{-1}\ K^{-1}$), austenitic stainless steel (15 $W\ m^{-1}\ K^{-1}$) and Pyrex glass (1 $W\ m^{-1}\ K^{-1}$). For the fourth criterion to be met, the thermal conductivity of the cell k_{cell} has to be estimated. In this investigation, the heat flow is applied between the largest cell surfaces passing through the case and the jelly roll. The thermal conductivity of this parallel connection k_{cell} can be calculated by Eq. A.1, which is a weighted average of k_{case} and the inner part of the cell k_{int} mainly influenced by the jelly roll. The weighting is defined by the cross-section areas for the outer dimension of the full cell A_{cell} and the internal area A_{int}, which are defined by Eq. A.2 and A.3.

$$k_{cell} = \frac{k_{int} \cdot A_{int} + k_{case} \cdot (A_{cell} - A_{int})}{A_{cell}} \tag{A.1}$$

$$A_{int} = (d_{c,h} - d_{c,t} - d_{c,b}) \cdot (d_{c,l} - 2 \cdot d_{c,s}) \tag{A.2}$$

$$A_{cell} = d_{c,h} \cdot d_{c,l} \tag{A.3}$$

Suitable values for k_{int} and k_{case} are necessary for estimating k_{cell}. Werner et al. [8] measured values between 1.0 and 1.5 $W\ m^{-1}\ K^{-1}$ for the whole jelly roll. Taking the mid-range of 1.25 $W\ m^{-1}\ K^{-1}$ for k_{int} and the mid-range of AW-3003 of 175 $W\ m^{-1}\ K^{-1}$ results in 7.99 $W\ m^{-1}\ K^{-1}$ for k_{cell}. This result narrows the choice of suitable reference material to either austenitic stainless steel or Pyrex glass. As stainless steel was already used by Bazinski [11] in the field of battery research, this material was applied for quantifying the measurement error in this study.

Appendix B. Effects on temperature gradient

Werner et al. [8] described the one-dimensional temperature distribution $T(x)$ from the cell core ($x = 0$) to the cell surface ($x = X$) by Eq. B.1 at stead-state condition ($dT(x)/dt = 0$). For this equation, the volumetric heat generation $\dot{q}$ is assumed constant over time and space and an adiabatic boundary condition is applied in the cell core. At the cell surface, a convective boundary with a heat transfer coefficient h and a cooling fluid temperature T_{fluid} is chosen. Eq. B.2 defines the incorrect temperature distribution $T_e(x)$ by multiplying $k_{\perp R}$ with an relative error in thermal conductivity e_k.

$$T(x) = T_{fluid} + \frac{\dot{q} \cdot X^2}{2 \cdot k_{\perp R}} \left(1 - \frac{x^2}{X^2} + \frac{2 \cdot k_{\perp R}}{h \cdot X}\right) \tag{B.1}$$

$$T_e(x) = T_{fluid} + \frac{\dot{q} \cdot X^2}{2 \cdot k_{\perp R} \cdot (1 + e_k)} \left(1 - \frac{x^2}{X^2} + \frac{2 \cdot k_{\perp R} \cdot (1 + e_k)}{h \cdot X}\right) \tag{B.2}$$

The quadratic Eq. B.1 has an absolute maximum at $x = 0$. Therefore, the maximum temperature gradient inside the cell exists between the cell core $T(x = 0)$ and the cell surface $T(x = X)$. Uncertainties in $k_{\perp R}$ have an impact on this temperature difference. Eq. B.3 defines this impact by the relative error in the maximum temperature gradient inside the cell $e_{\Delta T}$. Combining the Eqs. B.1 to B.3, will result in the relation between $e_{\Delta T}$ and e_k in Eq. B.4.

$$\frac{T_e(x = 0) - T_e(x = X)}{T(x = 0) - T(x = X)} = 1 + e_{\Delta T} \tag{B.3}$$

$$e_{\Delta T} = \frac{1}{1 + e_k} - 1 \tag{B.4}$$

According to Eq. B.4, $e_{\Delta T}$ is only affected by e_k at steady-state conditions. Overestimating $k_{\perp R}$ by $+10\%$ will therefore result in underestimating the temperature gradient by $e_{\Delta T} = -9.1\%$.

References

[1] Y. Liu, Y. Zhu, Y. Cui, Challenges and opportunities towards fast-charging battery materials, Nat. Energy 4 (7) (2019) 540–550, https://doi.org/10.1038/s41560-019-0405-3.

[2] S. Ahmed, I. Bloom, A.N. Jansen, T. Tanim, E.J. Dufek, A. Pesaran, A. Burnham, R.B. Carlson, F. Dias, K. Hardy, M. Keyser, C. Kreuzer, A. Markel, A. Meintz, C. Michelbacher, M. Mohanpurkar, P.A. Nelson, D.C. Robertson, D. Scoffield, M. Shirk, T. Stephens, R. Vijayagopal, J. Zhang, Enabling fast charging – a battery

technology gap assessment, J Power Sources 367 (2017) 250–262, https://doi.org/10.1016/j.jpowsour.2017.06.055.
[3] H. Maleki, J. Selman, R. Dinwiddie, H. Wang, High thermal conductivity negative electrode material for lithium-ion batteries, J Power Sources 94 (1) (2001) 26–35, https://doi.org/10.1016/S0378-7753(00)00661-3.
[4] R. Spotnitz, J. Franklin, Abuse behavior of high-power, lithium-ion cells, J Power Sources 113 (1) (2003) 81–100, https://doi.org/10.1016/S0378-7753(02)00488-3.
[5] T. Waldmann, G. Bisle, B.-I. Hogg, S. Stumpp, M.A. Danzer, M. Kasper, P. Axmann, M. Wohlfahrt-Mehrens, Influence of cell design on temperatures and temperature gradients in lithium-ion cells: an in operando study, J Electrochem Soc 162 (6) (2015) A921–A927, https://doi.org/10.1149/2.0561506jes.
[6] T. Waldmann, M. Wohlfahrt-Mehrens, In-operando measurement of temperature gradients in cylindrical lithium-ion cells during high-current discharge, ECS Electrochemistry Letters 4 (1) (2015) A1–A3, https://doi.org/10.1149/2.0031501eel.
[7] M. Klett, R. Eriksson, J. Groot, P. Svens, K. Ciosek Högström, R.W. Lindström, H. Berg, T. Gustafson, G. Lindbergh, K. Edström, Non-uniform aging of cycled commercial lifepo4//graphite cylindrical cells revealed by post-mortem analysis, J Power Sources 257 (2014) 126–137, https://doi.org/10.1016/j.jpowsour.2014.01.105.
[8] D. Werner, A. Loges, D.J. Becker, T. Wetzel, Thermal conductivity of li-ion batteries and their electrode configurations – a novel combination of modelling and experimental approach, J Power Sources 364 (2017) 72–83, https://doi.org/10.1016/j.jpowsour.2017.07.105.
[9] R. Ponnappan, T.S. Ravigururajan, Contact thermal resistance of li-ion cell electrode stack, J Power Sources 129 (1) (2004) 7–13, https://doi.org/10.1016/j.jpowsour.2003.11.006.
[10] V. Vishwakarma, C. Waghela, Z. Wei, R. Prasher, S.C. Nagpure, J. Li, F. Liu, C. Daniel, A. Jain, Heat transfer enhancement in a lithium-ion cell through improved material-level thermal transport, J Power Sources 300 (2015) 123–131, https://doi.org/10.1016/j.jpowsour.2015.09.028.
[11] S.J. Bazinski, X. Wang, Experimental study on the influence of temperature and state-of-charge on the thermophysical properties of an lfp pouch cell, J Power Sources 293 (2015) 283–291, https://doi.org/10.1016/j.jpowsour.2015.05.084.
[12] L. Sheng, L. Su, H. Zhang, Experimental determination on thermal parameters of prismatic lithium ion battery cells, Int J Heat Mass Transf 139 (2019) 231–239, https://doi.org/10.1016/j.ijheatmasstransfer.2019.04.143.
[13] A. Loges, S. Herberger, D. Werner, T. Wetzel, Thermal characterization of li-ion cell electrodes by photothermal deflection spectroscopy, J Power Sources 325 (2016) 104–115, https://doi.org/10.1016/j.jpowsour.2016.05.082.
[14] T. Bandhauer, S. Garimella, T.F. Fuller, Electrochemical-thermal modeling to evaluate battery thermal management strategies: i. side cooling, J Electrochem Soc 162 (1) (2014) A125–A136, https://doi.org/10.1149/2.0571501jes.
[15] W. Hesse, Aluminium-Werkstoff-Datenblätter: Deutsch, 7th ed., Beuth Wissen, Beuth Verlag GmbH, Berlin, 2016.
[16] M. Lewerenz, G. Fuchs, L. Becker, D.U. Sauer, Irreversible calendar aging and quantification of the reversible capacity loss caused by anode overhang, Journal of Energy Storage 18 (2018) 149–159, https://doi.org/10.1016/j.est.2018.04.029.
[17] J.G. Hust, P.J. Giarratano, Thermal Conductivity and Electrical Resistivity Standard reference materials: austenitic stainless steel, SRM's 735 and 798, from 4 to 1200 (march 1975). NBS Special Publication 260-46 (1975).
[18] Springer handbook of materials measurement methods, in: H. Czichos, T. Saito, L. Smith (Eds.), Springer handbooks, Springer, Berlin, 2006.
[19] R.H. Bogaard, Thermal Conductivity of Selected Stainless Steels, in: T. Ashworth, D.R. Smith (Eds.), Thermal Conductivity 18, Springer Verlag, Boston, MA, 2012, pp. 175–185, , https://doi.org/10.1007/978-1-4684-4916-7_20.
[20] DIN EN 10088-3, Stainless steels - part 3: Technical delivery conditions for semi-finished products, bars, rods, wire, sections and bright products of corrosion resisting steels for general purposes; german version en 10088-3:2014, 2014, 10.31030/2102108.
[21] K.-Y. Oh, B.I. Epureanu, J.B. Siegel, A.G. Stefanopoulou, Phenomenological force and swelling models for rechargeable lithium-ion battery cells, J Power Sources 310 (2016) 118–129, https://doi.org/10.1016/j.jpowsour.2016.01.103.
[22] A.L. Woodcraft, Predicting the thermal conductivity of aluminium alloys in the cryogenic to room temperature range, Cryogenics 45 (6) (2005) 421–431, https://doi.org/10.1016/j.cryogenics.2005.02.003.
[23] C. Vargel, Corrosion of Aluminium, 1. ed., Elsevier, Amsterdam, 2004.
[24] J. Sturm, A. Rheinfeld, I. Zilberman, F.B. Spingler, S. Kosch, F. Frie, A. Jossen, Modeling and simulation of inhomogeneities in a 18650 nickel-rich, silicon-graphite lithium-ion cell during fast charging, J Power Sources (412) (2019) 204–223.
[25] F. Richter, S. Kjelstrup, P.J. Vie, O.S. Burheim, Thermal conductivity and internal temperature profiles of li-ion secondary batteries, J Power Sources 359 (2017) 592–600, https://doi.org/10.1016/j.jpowsour.2017.05.045.
[26] R.W. Powell, C.Y. Ho, P.E. Liley, Thermal conductivity of selected materials, NSRDS-NBS 8 (1966).
[27] O.S. Burheim, M.A. Onsrud, J.G. Pharoah, F. Vullum-Bruer, P.J.S. Vie, Thermal conductivity, heat sources and temperature profiles of li-ion batteries, ECS Trans 58 (48) (2014) 145–171, https://doi.org/10.1149/05848.0145ecst.
[28] F. Richter, P.J. Vie, S. Kjelstrup, O.S. Burheim, Measurements of ageing and thermal conductivity in a secondary nmc-hard carbon li-ion battery and the impact on internal temperature profiles, Electrochim. Acta 250 (2017) 228–237, https://doi.org/10.1016/j.electacta.2017.07.173.
[29] Y. Yang, X. Huang, Z. Cao, G. Chen, Thermally conductive separator with hierarchical nano/microstructures for improving thermal management of batteries, Nano Energy 22 (2016) 301–309, https://doi.org/10.1016/j.nanoen.2016.01.026.
[30] D. Sauerteig, N. Hanselmann, A. Arzberger, H. Reinshagen, S. Ivanov, A. Bund, Electrochemical-mechanical coupled modeling and parameterization of swelling and ionic transport in lithium-ion batteries, J Power Sources 378 (2018) 235–247, https://doi.org/10.1016/j.jpowsour.2017.12.044.
[31] D.R. Lide, CRC Handbook of chemistry and physics, 2003–2004: A ready-reference book of chemical and physical data, 84th ed., CRC Press, Boca Raton, Fla., 2003.
[32] E.J. Cheng, K. Hong, N.J. Taylor, H. Choe, J. Wolfenstine, J. Sakamoto, Mechanical and physical properties of lini 0.33 mn 0.33 co 0.33 o 2 (nmc), J Eur Ceram Soc 37 (9) (2017) 3213–3217, https://doi.org/10.1016/j.jeurceramsoc.2017.03.048.
[33] S. Yan, J. Deng, C. Bae, X. Xiao, Thermal expansion/shrinkage measurement of battery separators using a dynamic mechanical analyzer, Polym Test 71 (2018) 65–71, https://doi.org/10.1016/j.polymertesting.2018.08.028.
[34] C. Bindra, V.A. Nalimova, D.E. Sklovsky, W.A. Kamitakahara, J.E. Fischer, Statics and dynamics of interlayer interactions in the dense high-pressure graphite compound lic2, Physical Review B 57 (9) (1998) 5182–5190, https://doi.org/10.1103/PhysRevB.57.5182.
[35] A. Schilling, J. Schmitt, F. Dietrich, K. Dröder, Analyzing bending stresses on lithium-ion battery cathodes induced by the assembly process, Energy Technology 4 (12) (2016) 1502–1508, https://doi.org/10.1002/ente.201600131.
[36] M. Bauer, M. Wachtler, H. Stöwe, J.V. Persson, M.A. Danzer, Understanding the dilation and dilation relaxation behavior of graphite-based lithium-ion cells, J Power Sources 317 (2016) 93–102, https://doi.org/10.1016/j.jpowsour.2016.03.078.
[37] D. Sauerteig, S. Ivanov, H. Reinshagen, A. Bund, Reversible and irreversible dilation of lithium-ion battery electrodes investigated by in-situ dilatometry, J Power Sources 342 (2017) 939–946, https://doi.org/10.1016/j.jpowsour.2016.12.121.
[38] Y. Ye, L.H. Saw, Y. Shi, K. Somasundaram, A.A. Tay, Effect of thermal contact resistances on fast charging of large format lithium ion batteries, Electrochim. Acta 134 (2014) 327–337, https://doi.org/10.1016/j.electacta.2014.04.134.
[39] L. Chen, Z. Chen, S. Liu, B. Gao, J. Wang, Effects of particle size distribution on compacted density of lithium iron phosphate 18650 battery, J. Electrochem. Energy Convers. Storage 15 (4) (2018) 2277, https://doi.org/10.1115/1.4040825.
[40] P.-C. Tsai, B. Wen, M. Wolfman, M.-J. Choe, M.S. Pan, L. Su, K. Thornton, J. Cabana, Y.-M. Chiang, Single-particle measurements of electrochemical kinetics in NMC and NCA cathodes for li-ion batteries, Energy Environ. Sci. 11 (4) (2018) 860–871, https://doi.org/10.1039/c8ee00001h.
[41] W.N. dos Santos, C.Y. Iguchi, R. Gregorio, Thermal properties of poly(vinilidene fluoride) in the temperature range from 25 to 210 °C, Polym Test 27 (2) (2008) 204–208, https://doi.org/10.1016/j.polymertesting.2007.10.005.
[42] A. Gaitonde, A. Nimmagadda, A. Marconnet, Measurement of interfacial thermal conductance in lithium ion batteries, J Power Sources 343 (2017) 431–436, https://doi.org/10.1016/j.jpowsour.2017.01.019.
[43] Compendium of Thermophysical Property Measurement Methods: vol. 2 Recommended Measurement Techniques and Practices, in: K.D. Maglić, A. Cezairliyan, V.E. Peletsky (Eds.), Springer US, Boston, MA and s.l., 1992, , https://doi.org/10.1007/978-1-4615-3286-6.

3 Thermal conductivity in cylindrical cell formats

The research article [42] in this chapter entitled *Low-Effort Determination of Heat Capacity and Thermal Conductivity for Cylindrical 18650 and 21700 Lithium-Ion Cells* deals with $k_\perp$ measurements on a 18650 and 21700 cylindrical cell. Since there are contradictory results for the temperature dependence of $k_\perp$ in the literature, this article also considers the influence of temperature. In addition, the SOC of the cells is changed in order to observe the SOC dependency. In contrast to Chapter 2, theoretical calculations are used to determine $k_\perp$ from literature data. With the theoretically calculated $k_\perp$, statements about the physical origin of temperature and SOC dependency are provided. In addition, the variant-convective cooling method was further developed in this thesis, which determines $k_\perp$ of cylindrical cells with low experimental effort.

Experimental In this study, a wind tunnel for battery cells was used to cool the cylindrical cells at different air velocities, which is a more developed variant of the experimental set-up presented by Rheinfeld et al. [116]. For each measurement, the cell was self-heated ($I_{cell} \neq 0$) twice at two different convective cooling conditions established by different air velocities. $k_\perp$ tests were performed at three different SOCs and at three different starting temperatures between 10 and 40 °C with four to ten repetitions. For the variant-convective cooling method, a precise analysis of the measurement errors and the optimal setting of the operating point is very important, which is demonstrated in this study.

Theory and modeling The evaluation of the variant-convective cooling method results in a concentrated thermal resistance R_{in} (see Figure 1.5) with an unknown correlation to the desired $k_\perp$. With a 2D FEM model of the cell, created using computed tomography scans, the relationship between R_{in} from the measurement evaluation and $k_\perp$ was developed in this article. In addition, heat loss and

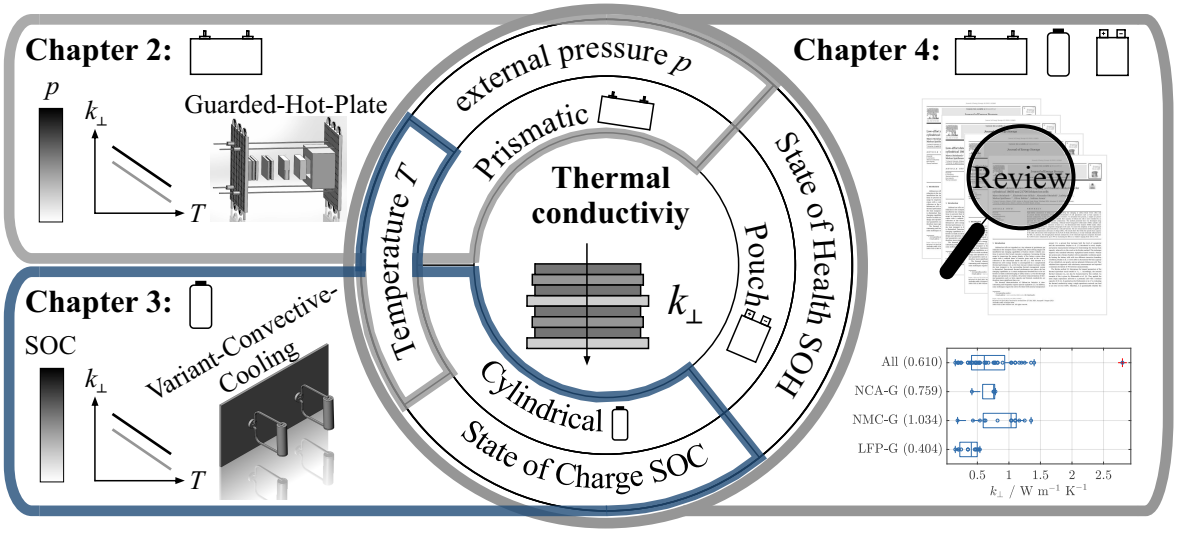

Figure 3.1: Scope of Chapter 3.

generation at the cell terminals were taken into account by the FEM model and the significance of the spiral effect of the jelly roll was discussed (see Figure 1.5). Bruggeman's theory was used to determine the thermal conductivity of the stack-layers from the literature. This theoretically calculated thermal conductivity of the stack-layers is then used to formulate a prediction of the magnitude, temperature and SOC dependence of $k_{\perp}$.

Results and discussion For both cylindrical cells, a negative temperature dependence of -0.5% K^{-1} was observed for $k_{\perp}$, which is lower than for the prismatic cell in Chapter 2. With an increasing SOC from 10% to 71%, the thermal conductivity increased by 7%, which agreed very well with the theoretical calculations in this article. Accordingly, the SOC dependency probably arises due to changes in the active particles in the anode and cathode, but the influence of SOC-dependent thermal contact resistances between the layers cannot be completely ruled out. In addition, the 21700 format showed a 4% higher $k_{\perp}$ than the 18650 format, which could be caused by thermal contact resistance between the jelly roll and the cell housing.

Author contribution The wind tunnel used in this study was planned, developed and built in collaboration between Alexander Rheinfeld, Ludwig Kraft and Marco Steinhardt. The experiment was planned, carried out and analyzed by Elisabeth Irene Gillich and Marco Steinhardt. The computed tomography scans were carried out by Elisabeth Irene Gillich and Markus Spielbauer at the Hochschule München. Oliver Bohlen supported every uncertainty analysis in this study. The manuscript was written by Marco Steinhardt and review and editing was carried out by all other authors.

Low-effort determination of heat capacity and thermal conductivity for cylindrical 18650 and 21700 lithium-ion cells

Marco Steinhardt, Elisabeth Irene Gillich, Alexander Rheinfeld, Ludwig Kraft, Markus Spielbauer, Oliver Bohlen, Andreas Jossen

Journal of Energy Storage 42, p. 103065, 2021

Permanent weblink:
https://doi.org/10.1016/j.est.2021.103065

Journal of Energy Storage 42 (2021) 103065

Contents lists available at ScienceDirect

Journal of Energy Storage

journal homepage: www.elsevier.com/locate/est

Low-effort determination of heat capacity and thermal conductivity for cylindrical 18650 and 21700 lithium-ion cells

Marco Steinhardt [a,*], Elisabeth Irene Gillich [a], Alexander Rheinfeld [a], Ludwig Kraft [a], Markus Spielbauer [a,b], Oliver Bohlen [b], Andreas Jossen [a]

[a] Technical University of Munich (TUM), Institute for Electrical Energy Storage Technology (EES), Arcisstrasse 21, 80333 Munich, Germany
[b] University of Applied Sciences Munich, Lothstrasse 64, 80335 Munich, Germany

ARTICLE INFO

Keywords:
Li-ion battery
Thermal conductivity
Heat capacity
Thermal resistance

ABSTRACT

High-fidelity simulations of lithium-ion cells describing fast charging or safety-critical events often rely on precise thermal parameters. Usually, the determination of cell parameters such as heat capacity or thermal conductivity is time consuming and cost intensive. To streamline this process, a simple yet precise measurement method for determining the specific heat capacity of lithium-ion cells is now extended by an approach that also captures their thermal conductivity. The method presented here was developed using two cylindrical cell formats, each containing a lithium–nickel–manganese–cobalt-oxide (NMC) cathode and a silicon-graphite anode. The extension is based on a two-dimensional finite element (FEM) model, whose geometry is parameterized by computed tomography (CT) scans. To ensure the simplicity of the experimental evaluation, the FEM model is approximated by a rational function. The new measurement method is applied at three different temperatures and states of charge (SOC). The results show that while the specific heat capacity of the jelly roll increases with temperature by 0.2%/K for both cell formats, it is only minimally influenced by the SOC. In contrast, the through-plane thermal conductivity of the electrode-separator-composite decreases by -0.5%/K and is enhanced by up to 9% by increasing the SOC in a window ranging from 10% to 71%.

1. Introduction

Lithium-ion cells are regarded as a key element of greenhouse gas reduction in the transport sector. Despite this, short driving ranges and insufficient fast charging capabilities of battery electric vehicles continue to prevent their broad consumer acceptance. Increasing driving range by improving the energy density of the battery system often comes with a reduced share of inactive parts such as the current collectors or the electrolyte inside the cell [1]. This increase in a lithium-ion cell's energy density is accompanied by a compromised thermal performance [2], as the heat rate per volume increases whilst the heat transport to the surrounding thermal management system is diminished. Deteriorated thermal performance can reduce the fast charging capabilities as a certain temperature-threshold has to be adhered to avoids accelerated aging or safety issues [1]. For the thorough design and operation of a battery, the precise characterization of thermal parameters such as heat capacity and thermal conductivity are therefore more significant than ever.

The thermal characterization of lithium-ion batteries is time-consuming and frequently requires special equipment [3]. In addition, some techniques require the cell to be fitted with internal temperature sensors [4], a process that increases both the level of complexity and the uncertainties. Bryden et al. [5] introduced a novel, simple, and precise measurement technique for determining the thermal heat capacity, referred to in this work as the Bryden method. This technique requires only standard laboratory equipment based around a battery test system and a climate chamber with an adjustable ventilation speed. By heating the battery cells with two different convective boundary conditions, Bryden et al. [5] were able to characterize the heat capacity of two cylindrical, one pouch, and one prismatic lithium-ion cell. They validated their approach with calorimetry measurements and reported a maximum deviation of 4% between measurements.

The Bryden method [5] determines the lumped parameters of the thermal equivalent circuit model in Fig. 1. Accordingly, the internal thermal resistance R_{in} can also be characterized by this method. An example of this is given by Akbarzadeh et al. [6]. They applied the same single capacitance network to a prismatic cell with a nominal capacity of 43 Ah. As pointed out by Fleckenstein et al. [7], evaluating the thermal conductivity using a single-capacitance network can lead to an error of over 100%. Therefore, it is questionable whether the

* Corresponding author.
E-mail address: marco.steinhardt@tum.de (M. Steinhardt).

https://doi.org/10.1016/j.est.2021.103065
Received 19 April 2021; Received in revised form 27 July 2021; Accepted 5 August 2021
Available online 19 August 2021

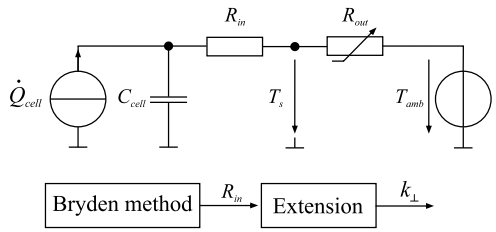

Fig. 1. Thermal equivalent circuit model applied by the Bryden method [5], which includes the heat rate inside the cell $\dot{Q}_{cell}$, the lumped heat capacity C_{cell}, the internal R_{in} and external R_{out} thermal resistance, and the ambient temperature T_{amb} of the cell. The magnitude of R_{out} can be controlled by the surrounding air velocity, which affects the temperature at the shell of the cell T_s. The extension of the Bryden method [5] is visualized by the block diagram below the circuit model.

approach of Akbarzadeh et al. [6] provides sufficient accuracy under different test conditions.

Al-Zareer et al. [8] extended the Bryden method [5] to three cylindrical 18650 cells. In contrast to Akbarzadeh et al. [6], they used a three-dimensional FEM model to evaluate the heat capacity and anisotropic thermal conductivity, thus avoiding the errors inherent in the single-capacitance network. In addition, a single-particle electrochemical model was employed to determine the heat generation inside the cell. Despite the accuracy of these methods, the FEM model introduces additional complexity that may prevent their wide application by experimental researchers.

The main objective of this study is to provide an easy yet precise extension of the Bryden method [5] that overcomes the aforementioned issues of validity and complexity. Specifically, the extension comprises a transformation of the internal resistance R_{in} into the effective thermal conductivity $k_\perp$, as highlighted in the block diagram in Fig. 1. Special attention is paid to a simple evaluation of the measurement data that will be demonstrated for a 18650 and a 21700 cell at different SOCs and temperatures. The aim of this investigation is to supply further insights into the dependencies of thermal conductivity on temperature and SOC, as there is still no coherent agreement in the literature [3].

This paper consists of three sections. Section 2, Experimental, introduces the test setup and the cells under investigation. It also discusses the test protocol and calculates the measurement uncertainties. The evaluation of the thermal conductivity is described in Section 3. This section also contains the estimates of thermal conductivity and heat capacity; both of these thermal properties are estimated on the basis of material measurements found in the literature. Finally, Section 4 presents the results regarding the thermal conductivities and heat capacities of the 18650 and 21700 cells at different temperatures and SOCs.

2. Experimental

2.1. Test setup and cells

Two cylindrical high-energy lithium-ion cells are investigated in this paper. Both cells are manufactured by LG Chem Ltd. and differ in their dimensions. According to Sturm et al. [9], a silicon-graphite anode and an NMC-811 cathode are used in both cells. The cell specifications by LG Chem Ltd. are listed in Table 1.

To apply the Bryden method [5], the battery cell has to be heated using an alternating current profile. At least two heating phases are required in the presence of different convective boundary conditions. In this study, a wind tunnel for battery cells, which is a more evolved variant of the test setup introduced by Rheinfeld et al. [10], was deployed to maintain the required boundary conditions. A schematic representation of the entire test setup is given in Fig. 2(a) and a photograph is shown in Fig. 2(c). The inner air within the test setup is accelerated by two axial fans inside the left and right wing of the wind tunnel. Two heat exchangers are connected to a refrigerated bath circulator (Huber, CC-508) that controls the air temperature. The two turbulent air streams are converted to a laminar stream by an air rectifier (Wacosystems, WaveCore PET150) inside the middle tunnel. The air velocity v after the rectifier is measured by an anemometer (Höntzsch GmbH, ZS25) before it passes by the cell holder.

Table 1
Specifications of investigated cell formats according to the product specifications.

	18650	21700
Identification	INR18650 MJ1	INR21700 M50T
Manufacturer	LG Chem Ltd.	LG Chem Ltd.
Dimensions in mm	⌀18.5; 65.1	⌀21.1; 70.2
Nominal voltage	3.64 V	3.63 V
Capacity	3.35 Ah	4.85 Ah
Mass	49 g	69 g
Voltage range	[2.5; 4.2] V	[2.5; 4.2] V
Current range (continuous)	[−10; 3.35] A	[−7.28; 3.40] A

Fig. 2(b) shows a computer-aided design (CAD) drawing of the cell holder, to which two cells can be connected. This fixes the position of the cell inside the air stream and provides an electrical connection to the battery test system (BaSyTec, CTS). The test system controls the cell current I_{cell} and measures the cell voltage U_{cell} with four-terminal sensing. The electrical cell connection can be seen in Fig. 2(d). At Tag 2 (indicated), the sense and load connectors of the cell are soldered to a HILUMIN® steel strip that is spot welded to the cell terminal. U_{cell} therefore includes the voltage drop due to the electrical resistance between Tag 1 and 2. The magnitude of this external resistance Z_e was measured with a resistance meter (HIOKI, BT3562) and the results are listed in Table 3 with an uncertainty of 0.5%. The internal resistance Z_i of the negative and positive cell terminals were determined in the same manner after opening the cells and removing the jelly roll from the inner tab. A photograph of the test setup for the positive cell terminal with the soldered measuring wires can be seen in Fig. 2(f).

All temperatures are measured by 100 Ω platinum-chip sensors (JUMO PCA 1.2005.1L F0,15) connected to the National Instruments NI-9216 module in four-wire high-resolution mode, with a sample rate of 2 Hz. Before the sensors were attached, the Callendar–Van-Dusen coefficients were calibrated between −10 and 40 °C using a Fluke Calibration 1524 Thermometer and a FLUKE-TEMP-5615-6-P temperature sensor with an accuracy of 0.012 °C. As can be seen in Fig. 2(b), three temperature sensors were attached to each cell, one to the shell of the cell T_s and one each to the positive T_{tp} and negative T_{tn} terminal. Each sensor was glued to the metal surface and insulated from the ambient air temperature T_{amb} by a 1-cm-thick piece of insulation material (ArmaFlex®). A fully connected cell is shown in Fig. 2(e).

2.2. Test protocol and evaluation

Fig. 3 shows the overall test protocol represented by the cell voltage of the 18650 cell. The total test time of 60 days comprised three cycle tests, which were used to determine the state of health. Between the cycles, the cells were charged or discharged to a defined open circuit voltage (OCV) U_{ocv} prior to the thermal characterization. All cycle tests and SOC adjustments were conducted at an ambient temperature of 298 K. For the thermal characterization, T_{amb} was varied between 283 and 313 K.

During the cycle tests, the battery tester charged both cells at a constant current (CC) of 1 C, followed by a constant voltage (CV) step at 4.2 V. Once the cut-off current of 0.1 C was reached, the cell was left to rest for 0.75 h. Subsequently, a CC–CV discharge of 1 C to 2.5 V was conducted to determine the capacity of the cell. Both steps were repeated ten times for each cycle test. Dividing the discharged capacity during the cycle tests by the nominal capacity of the cell

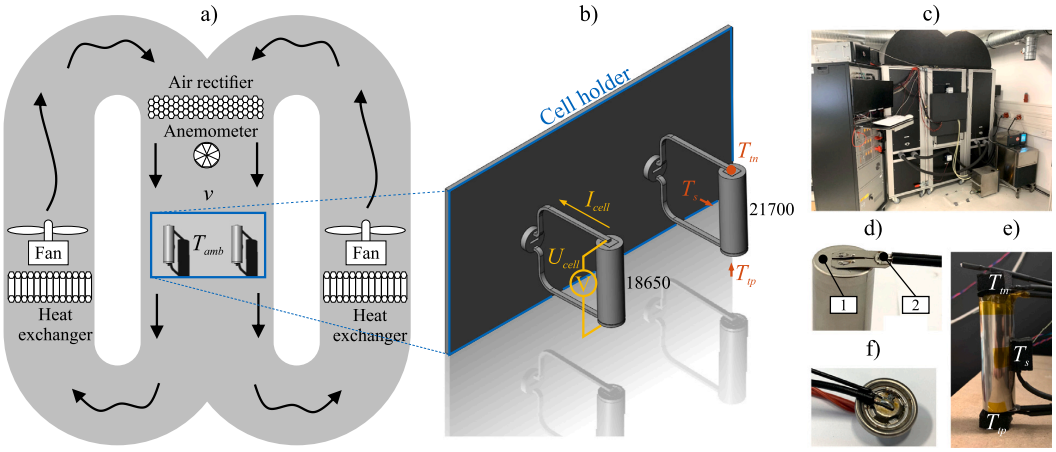

Fig. 2. Test setup for the heat capacity and thermal conductivity experiments. (a) Schematic illustration of the wind tunnel for battery cells with controllable air velocity v and ambient temperature T_{amb}. (b) Cell holder for two cylindrical cells inside the wind tunnel. (c) Photograph of the wind tunnel. (d) Electrical cell connection with measurement points for the electrical resistance Z_e at Tags 1 and 2. (e) Photograph of the attached temperature sensors, which are insulated from the ambient air. (f) Positive terminal of the 18650 cell with soldered sense and load wires for determining the internal electrical resistance Z_e.

Table 2
Relation between U_{ocv} and the resulting SOC at the end of the SOC adjustment shown in Fig. 3.

$\frac{U_{ocv}}{\mathrm{V}}$	SOC 18650	SOC 21700
3.42	10%	15%
3.63	33%	34%
3.93	70%	71%

Table 3
Electrical line resistances inside and outside the cell excluding the jelly roll. Z_e is the ohmic resistance between the measurement points in Fig. 2(d) for the negative and positive terminal. Z_i represents the ohmic resistance between the outer terminal and the internal connection point of the jelly roll in Fig. 2(f).

	18650	21700
External Z_e	1.03 mΩ	0.85 mΩ
Internal Z_i	2.71 mΩ	2.42 mΩ

computes to an average state of health of 92% and 96% for the 18650 and 21700 cells, respectively . The SOC adjustments in Fig. 3 were performed by conducting CC steps of 0.05 C until a defined U_{ocv} was reached, followed by a rest period of 24 h. As can be seen in Fig. 3, an open-circuit voltage U_{ocv} of 3.42, 3.64 and 3.93 V were used to terminate the CC phase of the SOC adjustments. Using the capacity from the cycle tests and integrating the cell current I_{cell} during the SOC adjustments, a specific SOC can be assigned to each U_{ocv}. Table 2 shows the assignments between U_{ocv} and SOC for both cell formats.

For each thermal characterization step, the cell has to be heated at least twice using an alternating current profile. Fig. 4(a) shows the heating process, which is subdivided into a rest, a heating, and a cooling phase at two different air velocities v. Additionally, the temperatures at the cell terminals (T_{nt}, T_{pt}) are shown for the lower air velocity of 0.6 $\mathrm{m\,s^{-1}}$. In Section 3.4, the increase in T_{nt} and T_{pt} is used to quantify the heat losses through the electrical connection. A sinusoidal current with a frequency of 0.05 Hz was chosen for the heating phase, as can be seen in Fig. 4(b). The amplitudes $\hat{I}_{cell}$ were set to 3.35 A and 3.5 A for the 18650 and 21700 cell, respectively. Fig. 4(b) also shows the total heat rate inside the cell $\dot{Q}_{cell}$. This is calculated using Eq. (1) by subtracting the heat loss inside the external impedance of the positive and negative cell connection Z_e from the total active power. The active power is the product of $\hat{I}_{cell}$, the amplitude of the cell voltage $\hat{U}_{cell}$ and the phase angle φ of the U_{cell} with respect to I_{cell}.

$$\dot{Q}_{cell} = 0.5\hat{U}_{cell}\hat{I}_{cell}\cos(\varphi) - 0.5\hat{I}_{cell}^2\,\mathrm{Re}\{Z_e\} \tag{1}$$

Conveniently, the heat rate inside the cell $\dot{Q}_{cell}$ depends only on electrical measurement quantities, which favors a small measurement uncertainty of $\dot{Q}_{cell}$. Reversible heat fractions even out along one cycle duration of the sinusoidal current [11]. Therefore, only irreversible heat contributes to the exponential temperature increase applied in the Bryden method [5]. Eq. (1) determines the resistive heat, which is considered the only significant heat phenomenon, if the cell is operated with a sinusoidal current [12]. Nevertheless, the uncertainty in $\dot{Q}_{cell}$ increases if the heat produced from mixing, heat produced from phase-changes or parasitic reactions occur inside the cell.

The Bryden method [5] uses Eqs. (2) and (3) to calculate the internal thermal resistance R_{in} and heat capacity C_{cell} of the cell. The external thermal resistance R_{out} and the temperature–time constant τ can be determined for every heating procedure. For a single heating procedure, Eq. (3) contains two unknown variables R_{in} and C_{cell}. For two heating procedures with differing convective boundary conditions (τ_1, τ_2, R_{out1}, R_{out2}), there is a system of equations with a single solution for R_{in} and C_{cell}. The solution is given by Eqs. (4) and (5).

$$R_{out} = \Delta T_s/\dot{Q}_{cell} \tag{2}$$

$$\tau = C_{cell}(R_{in} + R_{out}) \tag{3}$$

$$R_{in} = \frac{R_{out1} - (\tau_1/\tau_2)R_{out2}}{(\tau_1/\tau_2) - 1} \tag{4}$$

$$C_{cell} = \frac{\tau_1 - \tau_2}{R_{out1} - R_{out2}} \tag{5}$$

In contrast to the work of Bryden et al. [5], the temperature–time constant τ in Fig. 4(a) was obtained during the cooling phase rather than the heating phase. As can be seen in Fig. 4(b), $\dot{Q}_{cell}$ is not an idealized step function. Rather, the heat rate at the beginning of the heating phase is slightly higher than at the end, causing a faster increase in T_s. This effect is very likely caused by a decrease in the electrical impedance of the cell resulting from the increasing temperature. As a result, fitting τ at the beginning of the heating phase yields approximately 25% greater values. As the cooling phase is closer to an idealized step function, τ is fitted here using the objective function $p_1 \exp(-t/\tau) + p_3$. The temperature increase (ΔT_{s1}, ΔT_{s2}) and

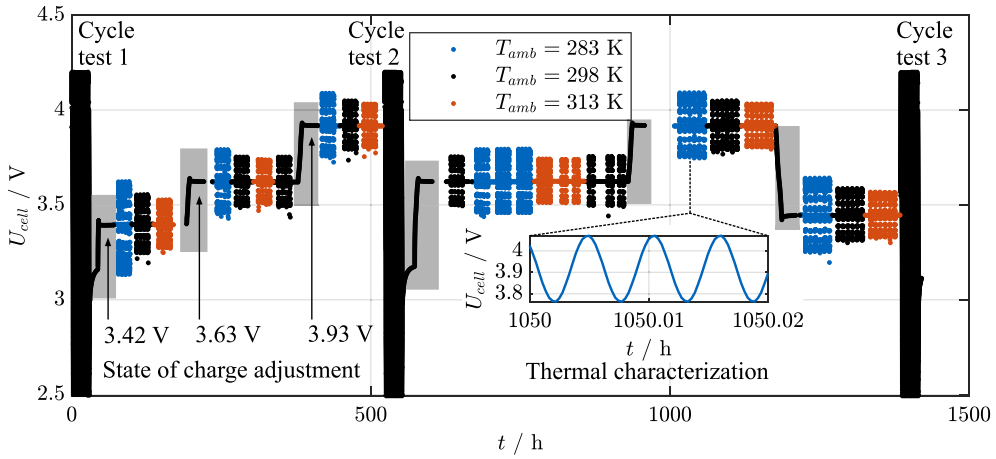

Fig. 3. Test protocol for the thermal characterization illustrated by the cell voltage of the 18650 cell. Three cycle tests determine the state of health of the cell. The thermal characterization was conducted at three different ambient temperatures and open circuit voltages of 3.42, 3.63 and 3.93 V.

Table 4
Measurement results for the lumped parameters heat capacity C_{cell} and internal resistance R_{in} for the 18650 cell at three different ambient temperatures and SOCs. For each result, the arithmetic mean and the 95% interval are given.

U_{ocv} V	T_{amb} K	R_{in} K W^{-1}	C_{cell} J K^{-1}	R_{out1} K W^{-1}	R_{out2} K W^{-1}	τ_1 s	τ_2 s
3.42	283	0.373 ± 0.03	42.4 ± 0.12	13.3 ± 0.03	4.2 ± 0.00	579.6 ± 1.07	193.2 ± 0.57
	298	0.407 ± 0.02	43.5 ± 0.09	14.0 ± 0.04	4.2 ± 0.01	625.6 ± 1.53	201.8 ± 0.66
	313	0.467 ± 0.02	44.7 ± 0.09	14.3 ± 0.03	4.2 ± 0.01	661.9 ± 1.14	210.8 ± 0.47
3.63	283	0.363 ± 0.03	42.2 ± 0.16	13.3 ± 0.25	4.2 ± 0.04	577.3 ± 9.99	190.9 ± 1.74
	298	0.391 ± 0.03	43.5 ± 0.09	13.9 ± 0.11	4.2 ± 0.02	621.4 ± 3.95	199.0 ± 0.92
	313	0.424 ± 0.05	44.9 ± 0.49	14.3 ± 0.14	4.2 ± 0.03	661.0 ± 7.13	209.2 ± 2.17
3.93	283	0.347 ± 0.02	42.2 ± 0.09	13.2 ± 0.03	4.1 ± 0.00	570.0 ± 0.81	189.3 ± 0.65
	298	0.407 ± 0.02	43.4 ± 0.08	14.1 ± 0.06	4.3 ± 0.03	629.4 ± 2.43	203.0 ± 1.10
	313	0.415 ± 0.02	44.8 ± 0.06	14.4 ± 0.03	4.3 ± 0.01	664.3 ± 1.49	209.7 ± 1.06

heat generation ($\dot{Q}_{cell1}$, $\dot{Q}_{cell2}$) are taken from the measurement data at the end of the heating phase.

The experimental data in Fig. 3 were evaluated using the aforementioned procedure. The results of this evaluation are listed in Tables 4 and A.14 for the 18650 and 21700 cell. Each of the nine battery states defined by T_{amb} and U_{ocv} was repeated four to ten times. Table 4 lists the arithmetic mean and the 95% confidence interval of these repetitions. The internal resistance R_{in} derived with this method ranges between 0.347 and 0.467 K W^{-1} for the 18650 cell. For the 21700 cell, lower values of between 0.302 and 0.437 K W^{-1} result. Dividing the heat capacity of the cell C_{cell} by the respective cell mass m_{cell} results in a specific heat capacity c_{cell} of between 909 and 968 J kg^{-1} K^{-1}. This range aligns with the results of 981 J kg^{-1} K^{-1} for the 26 650 NMC cell measured by Bryden et al. [5].

2.3. Measurement uncertainty

Measurement uncertainties can be quantified either by comparing the measurand with a reference material [3,4] or by analyzing the functional relation between the measurand and its underlying quantities [13]. For the first approach, it is important to select a reference material with similar characteristics, such as the test object [14]. For the thermal characterization of lithium-ion cells, quartz glass [4] can be used as an appropriate reference with a heat capacity of 745 J kg^{-1} K^{-1} and a thermal conductivity of 1.38 W m^{-1} K^{-1}. Thermal characterization techniques which generate the heat inside the cell also need equal electrical parameters. To the best knowledge of the author no reference exists with similar thermal and electrical properties to those of cylindrical lithium-ion cells. This also includes the anisotropic nature of the thermal conductivity of lithium-ion cells, which is not covered by any suitable reference material. Therefore, the uncertainties of the indirect measurands R_{in} and C_{cell} are computed with the uncertainties of underlying quantities such as $\hat{U}_{cell}$ or ΔT. For ease of use, the indirect quantities τ_1/τ_2 and $\Delta\tau = \tau_1 - \tau_2$ are introduced for subsequent calculations.

First the uncertainty in $\dot{Q}_{cell}$ from Eq. (1) is analyzed. The battery test system specifies a full-scale precision of 1 mV and 1 mA. Considering a cell current amplitude of 3.35 A, the uncertainty arising from the current measurement e_I calculates to 0.03%. For the 18650 cell, the smallest voltage amplitude $\hat{U}_{cell}$ is 109 mV, which results in an uncertainty of 0.91% for a precision of 1 mV. At the smallest voltage amplitude, an active power of 186 mW was measured, and the heat loss in Z_e of 6 mW can be computed at this operating point. Thus, $\dot{Q}_{cell}$ calculates to 180 mW with an absolute uncertainty for the active power of 1.748 mW ($e_U + e_I$) and an uncertainty for the heat loss in Z_e of 0.034 mW ($2e_I$ + 0.5%). Finally, the maximum uncertainty of $\dot{Q}_{cell}$ computes to 0.99%, which is the ratio of the total uncertainty of 1.782 mW and 180 mW.

The temperature increase ΔT in Fig. 4(a) was measured by the same temperature sensor, meaning that only gain and non-linearity errors contribute to the uncertainty in ΔT. Following the calibration process, the gain errors of the temperature sensor were below 0.02%. Changes in the laboratory temperature have a greater impact on the uncertainty of ΔT, which was analyzed for T_s over 24 h for both air velocities used in this study. Due to changes in the temperature of the laboratory, T_s can drift by 16 mK at 0.6 m s^{-1} and 6 mK at 3.1 m s^{-1}. Dividing this drift by the smallest temperature increase of 2.578 and 0.689 K results in a velocity-dependent uncertainty for ΔT of 0.62% and 0.87%, respectively. As R_{out} arises from the quotient of ΔT and $\dot{Q}_{cell}$, the two errors accumulate to form e_{Rout}. Therefore, the overall error for e_{Rout1} and e_{Rout2} amounts to 1.61% and 1.86%.

The uncertainty of the temperature–time constant τ in Eq. (3) is affected by dynamic errors in T_s. This error appears directly after the heating stops at t = 4 h in Fig. 4(a). This error can be neglected by starting the exponential curve fitting 20 s after the end of heating. Furthermore, measurement noise and control errors in T_{amb} can affect τ. This fitting error is identified by the 95% confidence interval. Accordingly, τ_1 exhibits an uncertainty of 0.02% and τ_2 an uncertainty of 0.1%. This translates into an uncertainty of 0.08% for the difference $e_{\Delta\tau}$ and 0.12% for the quotient e_{τ_1/τ_2}.

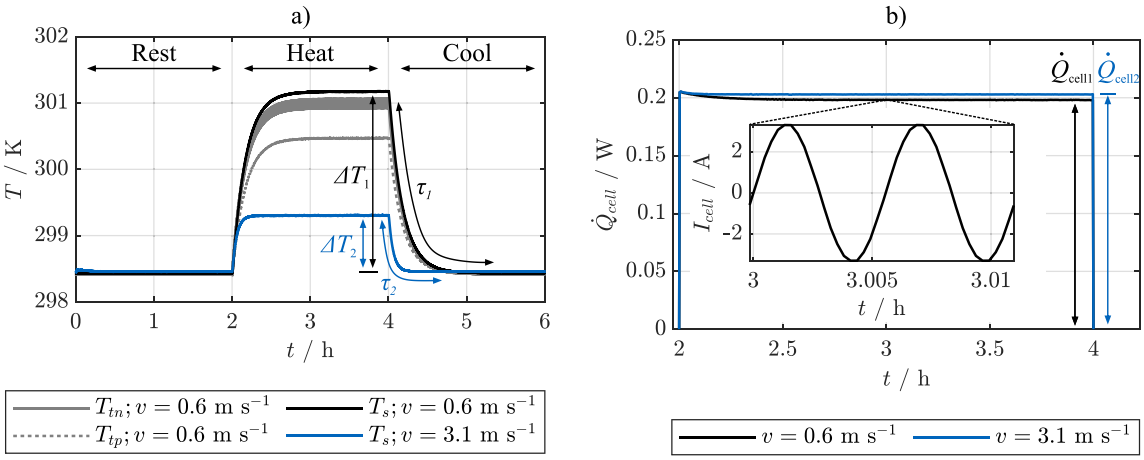

Fig. 4. Measurement readings during thermal characterization of the 18650 cell at U_{ocv} = 3.63 V with parameters for evaluating the heat capacity and thermal conductivity. (a) Cell temperature at the shell T_s during the rest, heating, and cooling phases at two different air velocities v of 0.6 and 3.1 m s^{-1}. For 0.6 m s^{-1}, the temperatures at the negative T_{tn} and positive terminal T_{tp} are displayed. Thicker lines indicate a higher alternating component arising from the sinusoidal cell current. (b) Heat rate inside the cell $\dot{Q}_{cell}$ during the heat phase caused by a sinusoidal cell current I_{cell} with an amplitude of 3.35 A and a cycle duration of 20 s.

Once the uncertainties of the measurement quantities have been analyzed, their propagation in Eqs. (4) and (5) can be computed. The relative uncertainty e_C of C_{cell} is defined by Eq. (6). Applying the linear term of the Taylor series for C_{cell} leads to Eq. (7). Eq. (8) formulates the relation between the uncertainty e_C and the measurement uncertainties e_i with their gain factors f_i. The gain factors prior to the difference of e_{Rout1} and e_{Rout2} is 0.230 for R_{out1} = 14.4 and R_{out2} = 4.3 (values are taken from Table 4). To determine the overall uncertainty for C_{cell}, the root sum square $\sqrt{\sum(f_i e_i)^2}$ of the measurement uncertainties e_i and their gain factors f_i is computed, which aligns with the procedure used by Sheng et al. [13]. Accordingly, the uncertainty e_C amounts to ±1.62%, which is the same order of magnitude as the deviation from calorimetry measurements of up to ±3.9% measured by Bryden et al. [5].

$$e_C = \frac{C_{cell} - \mathrm{Taylor}(C_{cell}; \Delta\tau, R_{out1}, R_{out2})}{C_{cell}} \tag{6}$$

$$e_C = \frac{\frac{\partial C_{Cell}}{\partial \Delta\tau}\Delta\tau e_{\Delta\tau} + \frac{\partial C_{Cell}}{\partial R_{out1}} R_{out1} e_{R_{out1}} + \frac{\partial C_{Cell}}{\partial R_{out2}} R_{out2} e_{R_{out2}}}{-C_{cell}} \tag{7}$$

$$e_C = \sum(f_i e_i) = -e_{\Delta\tau} + e_{R_{out1}} + \frac{-R_{out2}}{R_{out1} - R_{out2}}(e_{R_{out2}} - e_{R_{out1}}) \tag{8}$$

The uncertainty e_R for R_{in} is defined analogously to e_C using Eq. (9). Like Eqs. (7), (10) uses the Taylor series to separate different uncertainties. In the case of R_{in}, the quotient of τ_1 and τ_2 is used instead of $e_{\Delta\tau}$. Eq. (11) shows how e_R is affected by uncertainties in e_{τ_1/τ_2} and R_{out}. According to the three gain factors f_i, the uncertainty is minimized if the difference between R_{out1} and R_{out2} is maximized and the average of both thermal resistances is as low as possible. Using the values for R_{out} and τ in Table 4 at U_{ocv} = 3.93 V and T_{amb} = 313 K the gain factors f_i in Eq. (11) are 19.0 for e_{τ_1/τ_2}, 1.0 for $e_{R_{out1}}$, and 17.5 for the difference in $e_{R_{out}}$. This highlights the importance of low uncertainties for e_{τ_1/τ_2} and $(e_{R_{out2}} - e_{R_{out1}})$. Finally, e_R can be determined by the root sum square, which amounts to an uncertainty of ±5.19%.

$$e_R = \frac{R_{in} - \mathrm{Taylor}(R_{in}; \tau_1/\tau_2, R_{out1}, R_{out2})}{R_{in}} \tag{9}$$

$$e_R = \frac{\frac{\partial R_{in}}{\partial \frac{\tau_1}{\tau_2}}\frac{\tau_1}{\tau_2} e_{\tau_1/\tau_2} + \frac{\partial R_{in}}{\partial R_{out1}} R_{out1} e_{R_{out1}} + \frac{\partial R_{in}}{\partial R_{out2}} R_{out2} e_{R_{out2}}}{-R_{in}} \tag{10}$$

$$e_R = \sum(f_i e_i) = \frac{R_{out2} - R_{out1}}{\frac{\tau_1}{\tau_2} R_{out2} - R_{out1}} \frac{\frac{\tau_1}{\tau_2}}{\frac{\tau_1}{\tau_2} - 1} e_{\tau_1/\tau_2} - e_{R_{out1}} + \frac{-\frac{\tau_1}{\tau_2} R_{out2}}{\frac{\tau_1}{\tau_2} R_{out2} - R_{out1}}(e_{R_{out2}} - e_{R_{out1}}) \tag{11}$$

In conclusion, the maximum uncertainty e_C for determining C_{cell} using the Bryden method [5] amounts to ±1.62% in this paper. For R_{in}, the uncertainty is ±5.19%, which is three times the value of e_C. This illustrates the necessity of precise measurement equipment for determining R_{in}. Furthermore, the thermal through-plane conductivity $k_\perp$ is the final quantity of interest, not R_{in}. Therefore, further evaluation steps with additional uncertainties are necessary, which will be discussed in Section 3.4.

3. Theory

3.1. Thermal cell model

Eqs. (4) and (5) of the Bryden method [5] are based on the lumped capacitance model in Fig. 1. The model assumption constitutes a simplification of the energy conservation equation, which is considered valid for Biot numbers smaller than 0.1 [15]. For cylindrical cells, the Bi can be computed by the ratio of the heat transfer coefficient h_s and the thermal conductivity $k_\perp$ multiplied by the cell radius [16]. As discussed in Section 2.3, a high heat transfer coefficient at the cell surface h_s has to be used for at least one measurement to ensure an acceptably low measurement uncertainty for R_{in}. This suggests the existence of a conflict between reducing measurement uncertainty and maintaining the validity of the model assumption. Dividing the inverse of the external resistance R_{out1} of 14 K W^{-1} in Table 4 by the shell area of the 18650 cell results in a value for h_s of 19.4 W m^{-2} K^{-1}. This computes to a Biot number of 0.17, assuming a through-plane thermal conductivity $k_\perp$ of 1 W m^{-1} K^{-1} and a cell radius of 9 mm. As the Biot number exceeds 0.1 for both air velocities, a spatially resolved thermal model is used to extend the Bryden method [5].

The thermal model is created using COMSOL Multiphysics 5.4. The two-dimensional (2D) axisymmetric geometry of the 18650 cell

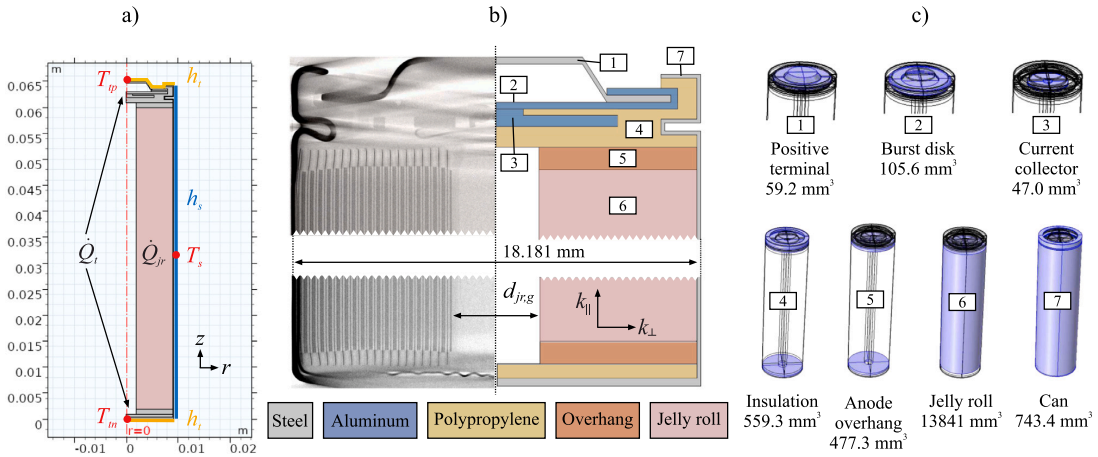

Fig. 5. Geometry and boundary conditions for the two-dimensional thermal model of the 18650 cell. (a) Thermal boundary conditions at the cell terminals h_t and the shell h_s, heat rates inside the terminals $\dot{Q}_t$, and the jelly roll $\dot{Q}_{jr}$, and positioning of the temperature sensor T_s, T_{tn}, and T_{tp}. (b) Detailed representation of the positive and negative terminal with dimensions taken from the illustrated CT images, and the definitions of seven cell domains. (c) Three-dimensional solids of revolution of the specific cell domains including their respective volume fractions.

is depicted in Fig. 5(a). A detailed description of the model equations and parameters can be found in Tables A.18 and A.20 respectively. All dimensions were either measured with a micrometer screw or taken from CT scans, as can be seen in Fig. 5(b). Beside the CT scan, seven different domains are illustrated for the cell model. The jelly roll gap with a diameter $d_{jr,g}$ of 3.82 mm for the 18650 cell is treated as a void volume. According to Li et al. [17], the top cap of the 18650 cell contains a positive terminal (Tag 1), a burst disk (Tag 2), and a current collector (Tag 3), all of which are insulated against the steel can by a sealing ring (Tag 4). The electrode-separator composite below the top cap is divided into an active jelly roll domain (Tag 6) and an inactive anode overhang (Tag 5). Solids of revolution of each two-dimensional domain are given in Fig. 5(c) along with their volume fractions.

Inside the cell, the total heat rate $\dot{Q}_{cell}$ is subdivided into the heat rate inside the active jelly roll $\dot{Q}_{jr}$ (Fig. 5, Tag 6) and inside the cell terminals $\dot{Q}_t$. As illustrated in Fig. 5(a), different convective boundary conditions are used for the terminals h_t and the shell h_s. The terminals are insulated by ArmaFlex® material with a thickness of 10 mm and a thermal conductivity of 0.035 $\mathrm{W\,m^{-1}\,K^{-1}}$. Neglecting the heat capacity of this volume, h_t can be determined by dividing the thermal conductivity by the thickness ($h_t = 3.5\ \mathrm{W\,m^{-2}\,K^{-1}}$). However, heat conduction can also occur through the electrical connection illustrated in Fig. 2(d). Therefore, the value of 3.5 $\mathrm{W\,m^{-2}\,K^{-1}}$ can only be treated as a lower bound for h_t. For this reason, the coefficients h_t and h_s are determined in Section 3.4 by fitting T_s, T_{tp}, and T_{tn} of the thermal model to the measurement data. Each material parameter in the model is considered isotropic, except for the thermal conductivity, which is defined for the in-plane $k_{\parallel}$ and through-plane directions $k_{\perp}$ of the cell's jelly roll. Due to the homogenization of the jelly roll, $k_{\perp}$ describes the thermal conductivity of each cell layer, thermal contact resistances between the layers [18] and the jelly-roll/case interface [19], and any effect arising from the homogenization of the spiral geometry [20].

3.2. Heat capacity estimation

For the 2D thermal model of the cell, the specific heat capacity c_{jr} and the volume density ρ_{jr} of the jelly roll must be specified. Both parameters are estimated from material properties given in the literature and will be compared with experimental results. As with the anode and cathode coatings, the separator is composed of porous layers consisting of a solid and a fluid phase. If the fluid phase contains electrolyte, it is henceforth referred to as a wet layer. If gases such as argon fill the voids, the layer is labeled dry. The volume fraction of the solid phase ε_S can be divided into an active material fraction ε_{AM} and a fraction containing the binder and carbon black (BCB) ε_{BCB}.

Loges et al. [21] defined the bulk density $\bar{\rho}$ and specific heat capacity $\bar{c}$ of the porous layers by way of Eqs. (12) and (13). The parameters used in both equations for each unit cell layer are listed in Table A.15. The results for $\bar{\rho}$ and $\bar{c}$ for each wet layer are shown in Table 5 for the 18650 cell and in Table A.17 for the 21700 cell. The mass of each layer m_i can be derived from $\bar{\rho}$, the thickness $d_{lt,i}$ and length $d_{ll,i}$ of the unit cell layers, and the height of the active jelly roll. The active jelly roll height is equal to the height of the Al collector for this calculation, which amounts to 58 and 63.5 mm [22] [9] for the 18650 and 21700 cell respectively. The sum of m_i in Table 5 (18650 cell) results in a total mass of the active jelly roll of 38.6 g, which is dominated by the anode and cathode coating. For the overhang mass, the overhanging height of the anode electrode and the separator of 2 mm (18650 cell) and 1.5 mm (21700 cell) are used in Table 6.

In addition to the mass of the jelly roll, the total masses of the non-jelly-roll domains m_{na} from Fig. 5(c) are listed in Table 6 computed by volumetric integration of the material densities. The total mass of the cell m_{cell} can be derived from the sum of the calculated jelly roll mass, the mass of the overhang, and the non jelly roll domains. To validate m_{cell}, the cell mass of each format was determined (Sartorius Talent TE313S, ±1 mg) without the insulation tube, with a deviation from the calculated mass of 0.2% and 0.4% for the 18650 and the 21700 cell respectively. Furthermore, both cell formats were opened inside a glove box to extract and weigh the non-jelly-roll mass m_{na}. For m_{na}, the maximum deviation of the measured values from the calculated is 2.8%. Due to the small deviation of m_{cell} and m_{na}, the jelly roll mass and the overhang mass can also be treated as validated.

$$\bar{\rho} = \rho_F \varepsilon_F + \rho_{AM} \varepsilon_{AM} + \rho_{BCB} \varepsilon_{BCB} \tag{12}$$

$$\bar{c} = \frac{c_F \rho_F \varepsilon_F + c_S \rho_S \varepsilon_S}{\bar{\rho}} \tag{13}$$

$$c_{jr} = \frac{\sum_{i=1}^{n} \bar{\rho}_i d_{lt,i} d_{ll,i} \bar{c}_i}{\sum_{i=1}^{n} \bar{\rho}_i d_{lt,i} d_{ll,i}} \tag{14}$$

The heat capacity of the jelly roll can be derived using the weighted average in Eq. (14). The layer thicknesses $d_{lt,i}$ and lengths $d_{ll,i}$ are listed in Tables 5 and A.17. As the electrodes are coated onto both sides of the current collectors, the accumulated coating length is approximately

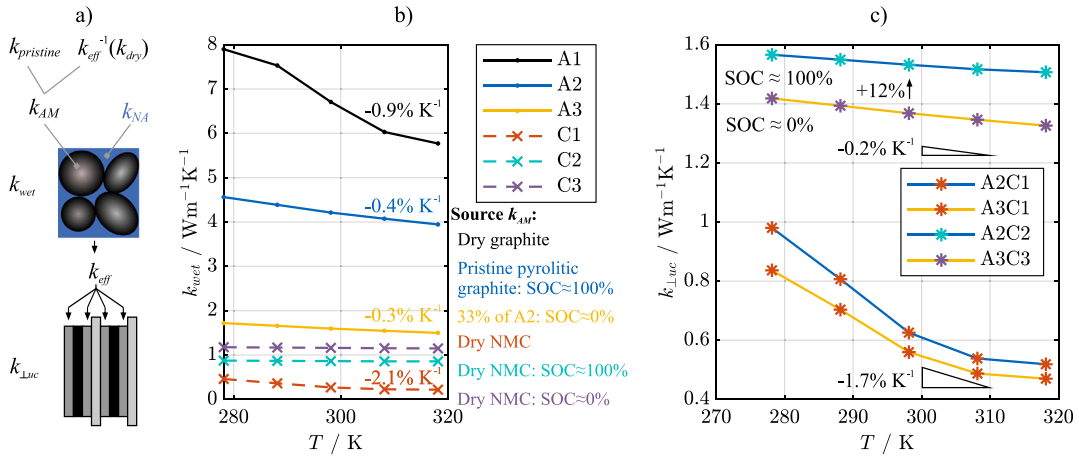

Fig. 6. Calculated thermal conductivity of the unit cell $k_{\perp uc}$ based on material properties taken from the literature, which are listed in Table A.16. (a) Process of gaining the wet conductivity k_{wet} either by pristine $k_{pristine}$ or dry material k_{dry} measurements and the Bruggeman theory in Eq. (18). (b) Result for k_{wet} for different graphites (A1, A2, A3) and NMC coatings (C1, C2, C2). (c) Through-plane conductivity $k_{\perp uc}$ for the 18650 cell with predicted dependencies on temperature and SOC.

Table 5
Structural parameters of wet 18650 unit cell layers and their temperature-dependent heat capacity $\bar{c}/(\mathrm{J\,kg^{-1}\,K^{-1}}) = c_0 + c_1(T/\ \mathrm{K} - 300)$.

	ϵ_F [22]	ϵ_{BCB} [22]	$d_{lt,i}$ / µm [22]	$d_{ll,i}$ / m [22][a]	$\bar{\rho}_i$ / g cm^{-3} [b]	m_i / g [c]	c_0 [d]	c_1 [d]
Anode	0.216	0.090	86.7	1.315	2.03	13.5	881.9	2.815
Cathode	0.171	0.084	66.2	1.230	3.87	18.3	852.5	1.733
Separator	0.450	0.000	12.0	1.400	1.06	1.0	1515.5	4.573
Cu-collector	0.000	0.000	11.0	0.700	8.96	4.0	385.6	0.099
Al-collector	0.000	0.000	17.3	0.670	2.70	1.8	892.4	0.635

[a]For double-coated electrodes, the length is accumulated.
[b]Bulk densities of porous layer $\bar{\rho}_i$ are calculated using Eq. (12) and the material densities in Table A.15.
[c]The total layer mass m_i is derived from the product of the layer thickness $d_{lt,i}$, and length $d_{ll,i}$, bulk density $\bar{\rho}_i$ and active jelly roll height of 58 mm [22].
[d]Calculated with Eq. (14).

Table 6
Weight of cell components with calculated temperature dependent heat capacities of non-active cell parts c_{na}, anode overhang c_{ao} and the jelly roll c_{jr}: $c/(\mathrm{J\,kg^{-1}\,K^{-1}}) = c_0 + c_1(T/\ \mathrm{K} - 300)$.

	18650	21700
Jelly roll mass $m_{jr} = \sum m_i$	38.6 g[c]	56.7 g[c]
Overhang mass m_{ao}	0.6 g[c]	0.7 g[c]
Non jelly roll mass m_{na}	(7.3[c]; 7.1[m]) g	(11.4[c]; 11.5[m]) g
Total cell mass m_{cell}	(46.5[c]; 46.4[m]) g	(68.8[c]; 68.5[m]) g
Jelly roll c_{jr}: c_0	834	878.8
Jelly roll c_{jr}: c_1	1.965 K^{-1}	1.975 K^{-1}
Overhang c_{ao}: c_0	809.9	859.7
Overhang c_{ao}: c_1	2.325 K^{-1}	2.299 K^{-1}
Non jelly roll c_{na}: c_0	570.1	565.4
Non jelly roll c_{na}: c_1	0.949 K^{-1}	0.9356 K^{-1}

m: measured. c: calculated by volume integration with the 2D thermal model.

twice the collector length. Applying Eq. (14) with the layer parameters in Table 5 results in a temperature-dependent heat capacity of the jelly roll c_{jr}. The absolute values c_0 and temperature slope c_1 of c_{jr} are listed in Table 6 for both cells. Dividing the temperature slope of 1.965 $\mathrm{J\,kg^{-1}\,K^{-2}}$ by c_{jr} at 300 K results in a temperature dependency of 0.2 $\%\,\mathrm{K^{-1}}$ for the heat capacity of the 18650 cell. Finally, we point out that an uncertainty of ±8.2% for c_{jr} is calculated in Table A.19.

3.3. Thermal conductivity estimation

In this section, the through-plane and in-plane thermal conductivity are calculated based on material measurements taken from the literature. This investigation allows the parametrization of various domains in the thermal model along with a more sophisticated analysis of the measurement results, which is presented in Section 4. It should be noted that this section concentrates on the thermal conductivity of the unit cell volume, which comprises two anode and cathode coatings, two separator sheets and two current collectors made of Al and Cu. Thermal contact resistances are not considered in the theoretical calculation, which is a common assumption in the literature [11]. Due to this assumption, the measured through-plane conductivity $k_\perp$ (Fig. 5) can differ from the calculated conductivity $k_{\perp uc}$ if thermal contact resistances are significant large [15]. The discussion of $k_\perp$ in Section 4 will return to the neglection of thermal contact resistances if a deviation between $k_\perp$ and $k_{\perp uc}$ is observed.

The thermal conductivity of the unit cell is defined by Eqs. (15) and (16). The thicknesses of the porous layers have to be considered twice for the unit cell. The layer thicknesses $d_{lt,i}$ are taken from Tables 5 and A.17. For an absolute estimation of $k_{\perp uc}$ and $k_\parallel$, an isotropic thermal conductivity of 0.83 and 1.44 $\mathrm{W\,m^{-1}\,K^{-1}}$ [18] is used for the wet NMC and graphite coatings. Thermal conductivity values for the current collectors are listed in Table A.15 and a value of 0.615 $\mathrm{W\,m^{-1}\,K^{-1}}$ [3] for the separator is assumed. For the 18650 cell, these parameters result in through-plane $k_{\perp uc}$ and in-plane $k_\parallel$ conductivities of 1.122 and 24.72 $\mathrm{W\,m^{-1}\,K^{-1}}$ at room temperature, respectively. For the 21700 format, $k_{\perp uc}$ and $k_\parallel$ calculate to 1.08 and 20.71 $\mathrm{W\,m^{-1}\,K^{-1}}$, respectively.

$$k_{\perp uc} = \frac{\sum_{i=1}^{n} d_{lt,i}}{\sum_{i=1}^{n} (d_{lt,i}/k_i)} \tag{15}$$

$$k_\parallel = \frac{\sum_{i=1}^{n} (d_{lt,i} \cdot k_i)}{\sum_{i=1}^{n} d_{lt,i}} \tag{16}$$

Table A.19 determines an uncertainty of ±21.4% for $k_{\perp uc}$, which is mostly affected by the porous layers k_i in Eq. (15). On the other hand, $k_\parallel$ is mainly influenced by the current collectors [3], for which accurate material values for k_i are available in the literature [23] and the dependency on SOC or temperature can be neglected. $k_\parallel$ is therefore considered to be constant throughout this paper. In contrast, Loges et al. [24] measured a negative dependency for NMC and graphite

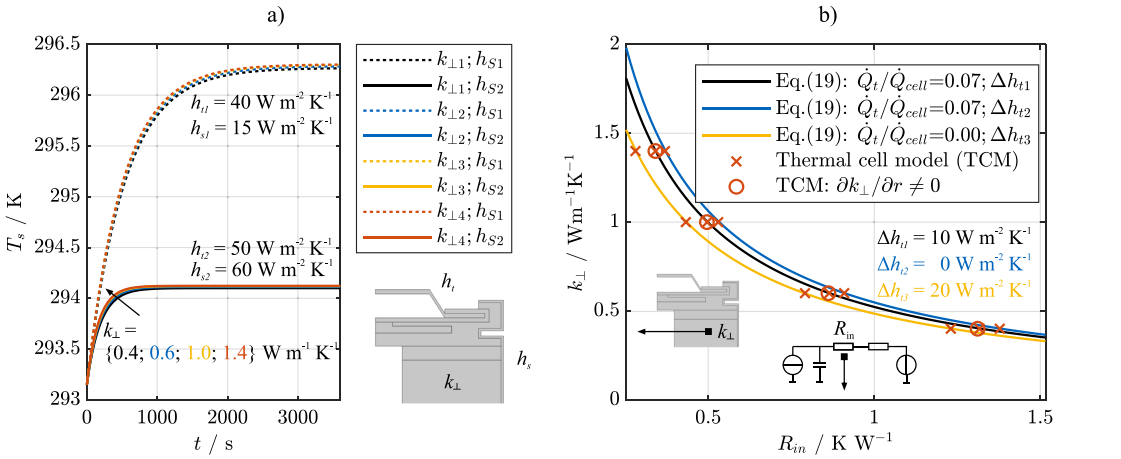

Fig. 7. Relation between lumped thermal resistance R_{in} in Eq. (4) and the through-plane thermal conductivity $k_\perp$ of the thermal model from Fig. 5. (a) Simulated heating phase of the thermal model for the 18650 format with varying through-plane conductivities ($k_{\perp1}$ - $k_{\perp4}$). (b) Relation between $k_\perp$ and R_{in} with corresponding Eq. (19) for different heat fractions $\dot{Q}_t/\dot{Q}_{cell}$ inside the cell terminals and varying heat transfer coefficient between the heating phases Δh_t. (For interpretation of the references to color in this figure legend, the reader is referred to the web version of this article.)

coatings. The effects of temperature on $k_{\perp uc}$ therefore need to be considered. Hardly any temperature-dependent measurement data for wet coatings is available in the literature. To overcome this, a method based on the work of Vadakkepatt et al. [25] for computing wet coatings from pristine materials or dry coatings is presented in the following paragraph.

The procedure for calculating the thermal conductivity of wet porous media k_{wet} is illustrated in Fig. 6(a). k_{wet} is derived with the aid of a model theory, based on the pristine thermal conductivity of non-active components k_{NA} and the active material k_{AM}. The Bruggeman model with varying exponent β developed by Vadakkepatt et al. [25] is utilized for subsequent calculations of the effective conductivity k_{eff}, which is widely applied in the lithium-ion battery community. This theory states that the thermal conductivity of the non-active material k_{NA} is calculated according to Eq. (17) [25]. The thermal conductivity of the mixture of binder and carbon black k_{BCB} is assumed to be equal to the conductivity of polyvinylidene fluoride (PVDF), listed for reference in Table A.16. For the fluid phase k_F, the thermal conductivity of LP50 electrolyte from BASF is used throughout this paper. The temperature-dependent conductivity of the electrolyte mixture LP50 is also listed in Table A.16. Please note, that the Bruggeman model only admits spherical particles, which are sufficiently far apart that their temperature field do not interact [25]. Therefore, these model assumptions are a possible source of uncertainty for the following calculations.

$$k_{NA} = \frac{\varepsilon_{BCB} k_{BCB} + \varepsilon_F k_F}{\varepsilon_{BCB} + \varepsilon_F} \tag{17}$$

$$k_{eff} = k_{AM} \varepsilon_{AM}^{\beta} + k_{NA}(1 - \varepsilon_{AM})^{1.5} \tag{18}$$

If the thermal conductivity k_{AM} and the volume fraction ε_{AM} of the active material is known, the effective thermal conductivity of the porous material k_{eff} can be estimated using Eq. (18) [25]. The Bruggeman exponent β is dependent on the ratio of k_{NA}/k_{AM}, which is linearly interpolated in this paper according to Table 7. If the k_{AM} for a certain active material is not available in the literature, it can be derived by dry measurement. In this case, the thermal conductivity of gases like argon or CO_2 has to be used for k_F and the dry measurement is considered to be k_{eff}. The thermal conductivity k_{AM} can then be calculated using the inverse function of the Bruggeman model k_{eff}^{-1}.

The results obtained by Eq. (18) for three wet anode (A1, A2, A3) and cathode (C1, C2, C3) coatings of the 18650 cell are shown in Fig. 6(b). The results for A1 and all cathode coatings are based on dry measurements, while those for the A2 and A3 coatings are taken from pristine data sources given in Table A.16. According to these calculations, the anode coatings range between 1 and 8 W m^{-1} K^{-1}. This represents an overestimation in comparison with the wet measurements of graphite given in the literature, which range between 0.36 and 1.58 W m^{-1} K^{-1} [3]. This overestimation of k_{wet} is due to model uncertainties of the applied Bruggeman model or the low anode porosity of the 18650 cell. For example, the average porosity ε_F of the six anode coatings measured by Loges et al. [24] amounts to 50.6%. A1 is discarded from further investigation due to the implausibly high values. In contrast, the estimations for the NMC cathode coatings of 0.218 to 1.176 W m^{-1} K^{-1} are closer to the measured range of 0.54 to 0.91 W m^{-1} K^{-1} reported in the literature [3]. Finally, it should be noted that all six estimations in Fig. 6(b) exhibit decreasing thermal conductivity with increasing temperature.

Table 7
Relation between Bruggeman's exponent β and the thermal conductivity ratio k_{NA}/k_{AM} of non-active to active material used in Eq. (18) [25].

k_{NA}/k_{AM}	β
0.0000	2.8000
0.0027	2.5206
0.0138	2.3274
0.1025	1.6137
0.2119	1.2528
0.3169	1.0473
0.4244	0.9144
0.9982	0.9071

Fig. 6(b) shows plots of A2 and A3 to estimate the impact of the full-cell SOC on k_{wet}. Both lines are based on pristine pyrolytic graphite [26], but A3 is reduced to 33% of A2, since, as Ju et al. [27] pointed out, that LiC_{12} can cause such a decrease. For LiC_6, the thermal conductivity reached approximately the same value as pristine graphite. The delithiated and lithiated NMC coatings C2 and C3 measured by Gotcu et al. [28] show decreasing k_{wet} with increasing SOC. According to this analysis, graphite and NMC exhibit an opposing dependency on SOC.

Fig. 6(c) shows the through-plane conductivity $k_{\perp uc}$ for the 18650 unit cell specified in Table 5, based on the four combinations of wet coatings shown in Fig. 6(b). A constant value of 0.615 W m^{-1} K^{-1} [3]

for the separator layer was used in all combinations. The temperature dependency lies within −0.2 and −1.7% K^{-1} depending on the cathode k_{wet}. As A3 and C3 can be considered as fully lithiated NMC and delithiated graphite, the SOC of 0% is assigned to the combination A3C3. The inverse situation applies for the combination A2C2, which is therefore considered the through-plane conductivity at 100% SOC. Both SOC assignments are approximations, as the degree of lithiation does not operate completely between 0.0 and 1.0 for both active materials. For example, if the SOC of the 18650 cell increases from 0% to 100%, the degree of lithiation of the anode increases from 0 to 0.85, while the degree of lithiation of the cathode decreases from 0.94 to 0.22 [22]. Based on these assumptions, the through-plane conductivity increases by 12% if the SOC increases from 0% to 100%, as highlighted in Fig. 6(c).

3.4. Thermal property evaluation

In this subsection, a functional relation is developed between the internal thermal resistance R_{in} and the through-plane conductivity $k_\perp$. For this relation, the simulation results of the thermal cell model in Section 3.1 are used instead of experimental data. With this technique, $k_\perp$ is a known quantity. For each simulation of the 18650 cell, the heat rate $\dot{Q}_{cell}$ was set to 232 mW, while a heat rate of 165 mW was chosen for the 21700 cell. Finally, realistic values for the convective boundaries h_t and h_s were determined.

To determine h_t and h_s, a steady-state optimization study with the thermal model from Section 3.1 was conducted for both cell formats. The objective of this optimization was a congruent temperature increase of T_s, T_{tn}, T_{tp} between the model and the experiments displayed in Fig. 4(a). The two air velocities v result in two coefficients at the shell (h_{s1}, h_{s2}) and two at the terminals (h_{t1}, h_{t2}). The arithmetic mean of all the experiments are listed in Table 8 together with their 95% confidence intervals. The results show that higher coefficients for the 18650 cell must be chosen and a positive correlation with the air velocity is observed.

Fig. 7(a) shows the surface temperature T_s of the 18650 cell model at four different through-plane conductivities between 0.4 and 1.4 $W\,m^{-1}\,K^{-1}$. For each thermal conductivity value, two simulations were conducted with a heat transfer coefficient at the shell of 15 and 60 $W\,m^{-2}\,K^{-1}$. At the terminals, h_{t1} and h_{t2} was set to 40 and 50 $W\,m^{-2}\,K^{-1}$, and the heat rate inside the terminals was adjusted to 7% of the total cell heat rate $\dot{Q}_{cell}$. Furthermore, the specific heat capacity of each domain was taken from Table 6 at 300 K. Applying the Bryden method [5] presented in Section 2.2 results in a heat capacity C_{cell} of (36.0 ± 1.0) $J\,K^{-1}$. This value is in agreement with the volume integral of the specific heat capacity, which is 37.2 $J\,K^{-1}$. Therefore, an uncertainty e_{mc} of 5.9% can be specified that arises from the model assumptions of the Bryden method [5], an unknown heat generation $\dot{Q}_t$, and heat convection at the terminal h_t.

Analyzing the simulation data in Fig. 7(a) with Eq. (4) results in four R_{in} values with corresponding $k_\perp$. These four value pairs are represented by four red crosses, which are shown in Fig. 7(b) interconnected by a black line. The black line follows a rational function $k_\perp = (P_1)/(R_{in}+P_2)$, which contains one asymptote P_2 with a maximum deviation from the red crosses of 0.003 $W\,m^{-1}\,K^{-1}$. Therefore, the rational function describes the relation between the lumped thermal resistance R_{in} and the through-plane thermal conductivity $k_\perp$ very precisely.

A sensitivity analysis showed a strong linear correlation between P_1 and P_2 with the heat rate ratio $\dot{Q}_t/\dot{Q}_{cell}$ as well as with the difference in heat transfer coefficient at the cell terminals $\Delta h = h_{t2} - h_{t1}$. Eq. (19) is formulated with due regard for this observation, with the five unknown constants p_1 to p_5. These five constants are determined by fitting Eq. (19) to the results of nine sensitivity simulations with varying Δh of 0, 10, 20 $W\,m^{-1}\,K^{-2}$ and $\dot{Q}_t/\dot{Q}_{cell}$ values of 0, 3.5, and 7%. Two of these additional simulations are illustrated in Fig. 7(b) by the red crosses, with the corresponding rational functions in blue and yellow, which display deviations of less than 0.7% between the crosses and the solid lines. Using Eq. (19) and the fitted constants in Table 8, a relation between R_{in} and $k_\perp$ can be established without the need for a complex thermal model.

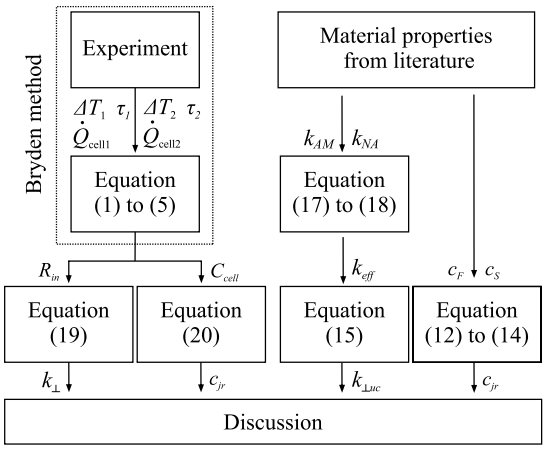

Fig. 8. Block diagram showing the experimental and theoretical approaches for deriving the thermal conductivity and specific heat capacity of cylindrical lithium-ion cells. The left-hand side illustrates the evaluation of the experimental data in Fig. 4. The right-hand side gives an overview of the theoretical determination of $k_{\perp uc}$ and c_{jr}.

The red crosses in Fig. 7 represent the simulation results of the thermal cell model with a constant thermal conductivity in radial direction $k_\perp$, which neglects the spiral geometry. This raises the question of whether the rational Eq. (19) is still valid if the radial conductivity $k_\perp$ depends on the radius ($\partial k_\perp/\partial r \neq 0$). Gomadam et al. [29] considered the effect of the spiral geometry by increasing $k_\perp$ by the quotient $(k_\parallel d_{uc}^2)/(4\pi^2 r^2)$. Accordingly, the impact of the spiral depends on the $k_\parallel$, the thickness of the unit cell d_{uc}, and the radius r. The increase in $k_\perp$ was simulated as an example for the parameter set of the 18650 cell in Fig. 7(a). The result of this simulation is represented by the red circles in Fig. 7(b). By comparing the red circles with the red crosses along the black line, it can be seen that the spiral geometry has a minor influence on the validity of Eq. (19). This agrees with the observation of Gomadam et al. [29] that thermal effects arising from the spiral geometry can be neglected for lithium-ion cells.

In conclusion, the through-plane conductivity $k_\perp$ can be evaluated with Eq. (19). The function parameters p_1 to p_5 for both cell formats and Δh_t are listed in Table 8. The heat rate ratio $\dot{Q}_t/\dot{Q}_{cell}$ is calculated with Eq. (1) using the ohmic resistances Z_i in Table 3. The values for R_{in} and C_{cell} are listed in Tables 4 and A.14. Most experimental studies in the field of lithium-ion cells do not evaluate the specific heat of the electrode stack or jelly roll, which renders comparisons with material measurements difficult. Instead, the specific heat capacity of the total cell $c_{cell} = C_{cell}/m_{cell}$ is evaluated [13] [4]. To enable comparison with the heat capacity estimations in Section 3.2, the heat capacity of the jelly roll c_{jr} is defined by Eq. (14), which compensates for the non-active cell components (m_{na}, c_{na}) listed in Table 6.

$$k_\perp = \frac{p_1 + p_2 \Delta h_t}{R_{in} + p_3 + p_4 \dfrac{\dot{Q}_t}{\dot{Q}_{cell}} + p_5 \Delta h_t} \tag{19}$$

$$c_{jr} = \frac{\dfrac{C_{cell}}{m_{cell}} - \dfrac{m_{na}}{m_{cell}} c_{na}}{1 - \dfrac{m_{na}}{m_{cell}}} \tag{20}$$

Table 8
Parameters in Eq. (19) for calculating $k_\perp$ based on the lumped thermal resistance R_{in}.

	18650	21700
p_1 / $\mathrm{m^{-1}}$	0.5660	0.5120
p_2 / $\mathrm{K\,m\,W^{-1}}$	−0.0017	−0.0022
p_3 / $\mathrm{K\,W^{-1}}$	0.0616	0.0552
p_4 / $\mathrm{K\,W^{-1}}$	−0.4408	−0.4448
p_5 / $\mathrm{K^2\,m^2\,W^{-2}}$	0.0018	0.0024
h_{t1} / $\mathrm{W\,m^{-2}\,K^{-1}}$	42.0 ± 1.4	34.7 ± 1.1
h_{t2} / $\mathrm{W\,m^{-2}\,K^{-1}}$	48.5 ± 2.2	35.4 ± 1.7
h_{s1} / $\mathrm{W\,m^{-2}\,K^{-1}}$	14.3 ± 0.4	11.3 ± 0.3
h_{s2} / $\mathrm{W\,m^{-2}\,K^{-1}}$	61.4 ± 0.3	43.8 ± 0.8

Table 9
Systematic measurement and model uncertainties of the Bryden method [5] and model simplifications from Eqs. (19) and (20).

Parameter	Uncertainty
R_{in}	$e_R = \pm 5.19\%$
$k_\perp$	$e_k = \pm 6.16\%$
C_{cell}	$e_C = \pm 1.62\%$
$c_{cell} = C_{cell}/m_{cell}$	$e_c = \pm 4.59\%$
c_{jr}	$e_{cjr} = \pm 4.71\%$

Eq. (19) introduces additional uncertainties for $k_\perp$, which have to be added to the measurement uncertainty detailed in Section 2.3. The largest uncertainty in Eq. (19) originates from the parameter Δh. For example, an uncertainty in Δh of 3.6 $\mathrm{W\,m^{-1}\,K^{-2}}$ can translate to an uncertainty in $k_\perp$ of 3.31%. This uncertainty and the measurement uncertainty e_R of 5.19% by the root sum square result in a total uncertainty for $k_\perp$ of 6.16%. Both uncertainties for R_{in} and $k_\perp$ are presented in Table 9.

To estimate the uncertainty e_c of c_{cell}, the root sum square of e_{mc} and e_C are used, resulting in $e_c = \pm 4.59\%$. This uncertainty can be compared with differential scanning calorimeters, which offer an uncertainty between 1.5 and 10% [30]. With lithium-ion cells, the derived value for e_c is close to the uncertainty of 3.82% of the technique developed by Sheng et al. [13], but worse than the uncertainty of 0.42% of the calorimeter used by Bazinski et al. [31].

For c_{jr}, an uncertainty for c_{na} of 10% is assumed, which is the upper bound of the uncertainty range of the differential scanning calorimetry [30]. Taking the smallest value for C_{cell} in Table 4 of 42.2 $\mathrm{J\,K^{-1}}$ and a value of 570.1 $\mathrm{J\,kg^{-1}\,K^{-1}}$ from Table 6 for c_{na}, the specific heat capacity of the jelly roll c_{jr} calculates to 971 $\mathrm{J\,kg^{-1}\,K^{-1}}$. Reducing c_{na} by 10% in this calculation increases c_{jr} (981 $\mathrm{J\,kg^{-1}\,K^{-1}}$), which constitutes an additional uncertainty of 1.06% for c_{jr}. Finally, the root sum square of e_c and 1.06% computes to $e_{cjr} = 4.71\%$ for the specific heat capacity of the jelly roll. It should be noted that a full validation of the uncertainties in Table 9 is beyond the scope of this paper. While the authors have a high level of confidence in the calculated uncertainties, the proposed measurement methods are so far conceptual and require further research in order to validate their robustness.

4. Results and discussion

This section discusses the heat capacity and thermal conductivity of a 18650 and a 21700 lithium-ion cell. An experimental and a theoretical approach were chosen to determine both thermal properties. The experimental approach is based on the measurements in Section 2, which are evaluated using the theory presented in Section 3.4. The process is illustrated on the left-hand side of Fig. 8. The experiments are conducted and evaluated according to the Bryden method [5]. Afterwards, R_{in} is transformed to $k_\perp$, which represents the extension of this work. Furthermore, the heat capacity of the cell C_{cell} is converted to the specific heat capacity of the jelly roll c_{jr} using Eq. (20).

Table 10
Linear regression parameters for the measured specific heat capacity of the jelly roll $c_{jr} = c_0 + c_1(T - 300\ \mathrm{K})$ in Fig. 9 with the respective temperature dependencies c_1/c_0. The given confidence intervals describe the uncertainty of the regression parameters. Systematic uncertainties of c_{jr} can be found in Table 9.

U_{ocv} / V	c_0 / $\mathrm{J\,kg^{-1}\,K^{-1}}$	c_1 / $\mathrm{J\,kg^{-1}\,K^{-2}}$	c_1/c_0 / $\mathrm{\%\,K^{-1}}$
18650 cell format			
3.42	1003.4 ± 1.2	1.9 ± 0.1	0.2 ± 0.01
3.64	1003.6 ± 2.6	2.2 ± 0.2	0.2 ± 0.06
3.93	1002.5 ± 1.2	2.1 ± 0.1	0.2 ± 0.03
21700 cell format			
3.42	908.0 ± 2.1	1.6 ± 0.2	0.2 ± 0.02
3.64	912.0 ± 2.7	1.6 ± 0.2	0.2 ± 0.04
3.93	910.5 ± 1.3	1.9 ± 0.1	0.2 ± 0.05

Table 11
Linear regression parameters for the measured through-plane thermal conductivity $k_\perp = k_0 + k_1(T - 300\ \mathrm{K})$ in Fig. 10 with the respective temperature dependencies k_1/k_0. The given confidence intervals describe the uncertainty of the regression parameters. Systematic uncertainties of $k_\perp$ can be found in Table 9.

U_{ocv} / V	k_0 / $\mathrm{W\,m^{-1}\,K^{-1}}$	k_1 / $\mathrm{mW\,m^{-1}\,K^{-2}}$	k_1/k_0 / $\mathrm{\%\,K^{-1}}$
18650 cell format			
3.42	1.225 ± 0.033	−7.4 ± 2.8	−0.6 ± 0.25
3.64	1.288 ± 0.041	−5.1 ± 3.7	−0.4 ± 0.30
3.93	1.298 ± 0.032	−6.1 ± 2.7	−0.5 ± 0.22
21700 cell format			
3.42	1.245 ± 0.049	−6.5 ± 4.1	−0.5 ± 0.35
3.64	1.357 ± 0.072	−13.4 ± 6.5	−1.0 ± 0.53
3.93	1.348 ± 0.047	−5.9 ± 3.9	−0.4 ± 0.30

Thereafter, the experimental values for $k_\perp$ and c_{jr} can be compared with the theoretical approach, which is shown on the right-hand side of Fig. 8. For the thermal conductivity $k_{\perp uc}$, the effective conductivity k_{eff} of each porous cell layer is calculated based on the theory of Bruggeman given in Section 3.3. For the specific heat capacity of the jelly roll c_{jr}, the heat capacities of the fluid c_F and solid c_S phase are considered in Section 3.2. The thermal conductivities $k_\perp$ and $k_{\perp uc}$ are treated differently in this study, as $k_\perp$ can contain thermal contact resistances as well as effects of the spiral geometry of the jelly roll.

4.1. Specific heat capacity

Fig. 9 shows the specific heat capacity of the jelly roll c_{jr} for three different temperatures and open circuit voltages U_{ocv}. Each measurement is represented by a dot and the solid lines display the linear regressions for each open circuit voltage. The constant c_0 and the slope c_1 of the linear regression together with the 95% confidence interval are listed in Table 10. Dividing the slope of the regression c_1 by the absolute value at 300 K c_0 gives the temperature dependency of the specific heat capacity.

The range of c_{jr} lies within 850 and 1050 $\mathrm{J\,kg^{-1}\,K^{-1}}$ for both cell formats. This agrees well with the range reported by Loges et al. [24] for wet NMC unit cells of 900 to 1100 $\mathrm{J\,kg^{-1}\,K^{-1}}$. In comparison with the theoretical estimations for c_0 given in Table 6, the measurement results at 300 K are 20% higher for the 18650 cell and 4% higher for the 21700 cell. The divergence between the measurement and the calculation could result from uncertainties in both techniques. According to Tables 9 and A.19, uncertainties justify a deviation of 12.91%, which explains the deviation of 4% for the 21700 cell but not the 20% of the 18650 cell. Further uncertainties for the theoretical c_{jr} can arise from the assumption that the pore and electrolyte volumes are equal. In reality, the volume of the electrolyte can exceed the volume of the pores [32]. For the 18650 cell, an additional electrolyte could explain the deviation of 20%, although this would worsen the match between the measured and calculated cell weights in Table 6.

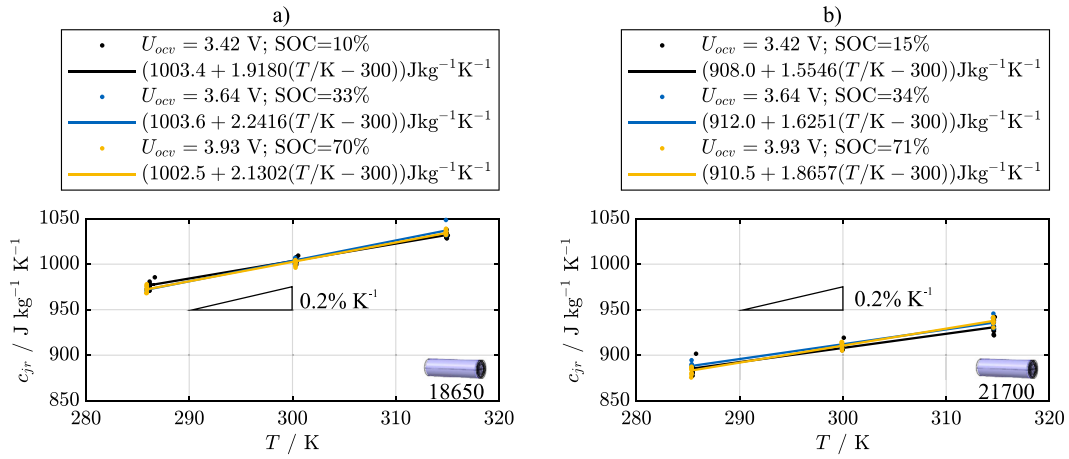

Fig. 9. Measured specific heat capacity of the jelly roll according to Eq. (20) with linear regressions at different open circuit voltages U_{ocv}. (a) 18650 cell. (b) 21700 cell.

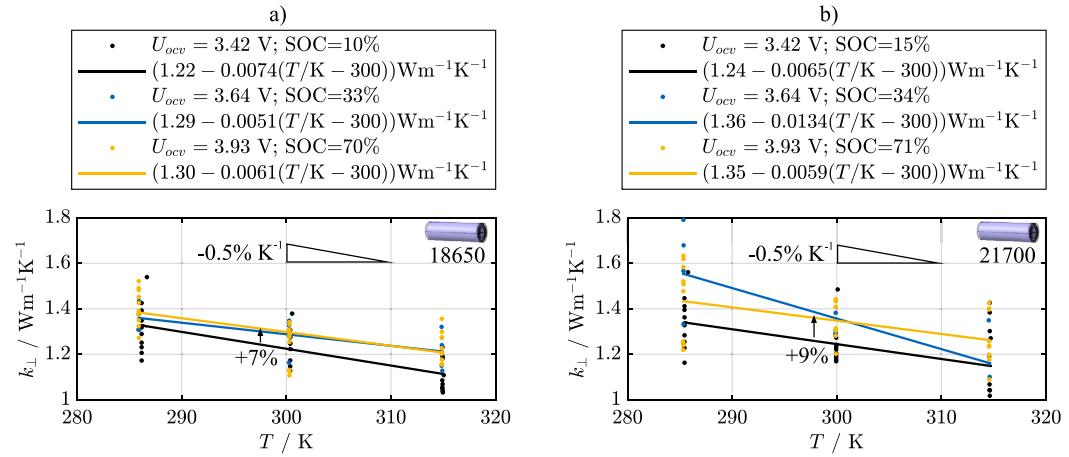

Fig. 10. Measured thermal conductivity of the jelly roll in through-plane direction according to Eq. (19) with linear regressions at different open circuit voltages U_{ocv}. (a) 18650 cell. (b) 21700 cell.

The heat capacities of both cell formats increase equally by 0.2 % K^{-1} with increasing temperature. This increase is independent from the SOC and agrees with the theoretical estimation in Table 6. No significant dependency on the SOC is observed either for the 18650 or for the 21700 format. Small changes in c_0 in Table 10 are within the given confidence interval of the linear regressions. The independence of c_{jr} from the SOC agrees with the observations of Bazinski et al. [31].

4.2. Through-plane conductivity

Fig. 10 shows the results for $k_\perp$ at varying SOC and temperatures. The quotient $\dot{Q}_t/\dot{Q}_{cell}$ in Eq. (19) lies within 4% to 9% for the 18650 cell. This change is mainly caused by changing heat losses inside the jelly roll at different ambient temperatures T_{amb}, while the heat losses inside the terminals remain constant. For the 21700 cell, $\dot{Q}_t/\dot{Q}_{cell}$ varies between 6% and 10%. The results for $k_\perp$ in Fig. 10 are presented in the same manner as for c_{jr}. This also applies to Table 11, which lists the constant k_0 and the slope k_1 of the linear regressions in Fig. 10, together with the 95% confidence interval and the temperature dependency k_1/k_0.

The thermal conductivity at 300 K and U_{ocv} = 3.64 V amounts to 1.29 and 1.36 W m^{-1} K^{-1} for the 18650 and 21700 cell, respectively. This constitutes a deviation of 15% and 26% compared to the theoretical values for $k_{\perp uc}$ derived with Eq. (15). Deviations of this magnitude are common in the literature. For example, Sheng et al. [13] observed a deviation between the measured and calculated through-plane conductivity of 56%. According to Tables 9 and A.19, the deviation between $k_\perp$ and $k_{\perp uc}$ of 15% (18650) and 26% (21700) in this paper can be explained by the calculated uncertainty of ±27.56% (±(6.16 + 21.4)%). One explanation for the observed deviation could be that the coating porosities of the 18650 cell are below 20%. According to Eq. (18), a low porosity shifts the effective conductivity towards the conductivity of the coating composite, which is usually higher than the conductivity of the electrolyte. The exact porosity of the 18650 cell is considered in the calculations illustrated in Fig. 6(c). By comparing k_0 in Table 11 at U_{ocv} = 3.42 V with $k_{\perp uc}$ from A3C3 at 300 K, it can be seen that there is a deviation of 11% from the measurement. This overestimation of A3C3

might be explained by the thermal contact resistances between the cell layers. It should also be mentioned that the measurement results $k_{\perp}$ can be higher than the calculated $k_{\perp uc}$ if the spiral geometry of the jelly roll causes a significant in-plane heat flow inside the current collectors [20].

A lower thermal conductivity $k_{\perp uc}$ was computed in Section 3.2 for the 21700 format, which is contradicted by the measurement results in Fig. 10. For example, $k_{\perp}$ is 4% higher for the 21700 format at an open circuit voltage of 3.93 V. This can be explained by thermal contact resistances between the jelly roll and the can. For example, Gaitonde et al. [19] measured a thermal conductance of 650 $\mathrm{W\,m^{-2}\,K^{-1}}$ for this interface. Due to the higher radius of the 21700 cell, the impact of this heat barrier is smaller than for the 18650 format.

The comparison of k_0 in Table 11 shows increasing $k_{\perp}$ with an increasing open circuit voltage of 7% and 9% for the 18650 and 21700 cell, respectively. This observation is in good accordance with the estimated 12% increase in $k_{\perp uc}$ found in Fig. 6(c). Consequently, it is reasonable to conclude that the changing thermal conductivity of the pristine graphite particle is responsible for this increase. Moreover, a thickness change in the electrode coatings induced by changes in SOC can cause an increase in the $k_{\perp}$. With increasing SOC, the graphite coating thickness increases more strongly than the NMC coating thickness decreases [33], which enhances the weight of the k_{anode} in Eq. (15). As the thermal conductivity of the anode is greater than the conductivity of the cathode, the $k_{\perp uc}$ will increase with SOC. Furthermore, the thickness change of the whole unit cell increases the mechanical stress inside the jelly roll [34], which might reduce the thermal contact resistance between the cell layers.

The temperature dependency k_1/k_0 in Fig. 10 lies within −0.4 and −0.6 $\%\,\mathrm{K^{-1}}$ for both cell formats. The high value of −1.0 $\%\,\mathrm{K^{-1}}$ for the 21700 format in Table 11 can be treated as an outlier. The derived values for k_1/k_0 are in accordance with the theoretical range in Fig. 6(c), which is between −1.7 and −0.2 $\%\,\mathrm{K^{-1}}$. In the literature, there is no agreement in regard to the temperature dependency of the through-plane conductivity $k_{\perp}$. For example, Sheng et al. [13] [4] and Liebig et al. [35] observed an increase in $k_{\perp}$ with increasing temperature. On the other hand, a decrease in conductivity with increasing temperature was measured by Werner et al. [11], Steinhardt et al. [3] and Murashko et al. [36].

5. Conclusion

This paper introduces a simple and precise method for measuring thermal conductivity, which also characterizes thermal heat capacity. The evaluation of both thermophysical properties requires only standard laboratory equipment, needs no special cell preparation, and saves a complex evaluation of the measurement data. To achieve a state-of-the-art level of uncertainty of 6.16% for thermal conductivity, the measurement settings have to be chosen carefully, which is described in this paper. Despite the confidence in the calculated uncertainty of 6.16%, further experiments are necessary to fully validate the robustness of the conceptual measurement method for the thermal conductivity. The method is demonstrated for one cylindrical 18650 and one 21700 cell at three different ambient temperatures and states of charge. For both cell formats, the state of charge has no dominant effect on the heat capacity. Only the cell temperature was found to affect the specific heat capacity of the jelly roll by 0.2 $\%\,\mathrm{K^{-1}}$. A rational function was used to remove the need for a complex finite element model to evaluate the measurement data. The through-plane conductivity of the electrode stack was evaluated and was found to decrease with increasing temperature by −0.5 $\%\,\mathrm{K^{-1}}$. Furthermore, an increasing thermal conductivity of 7% to 9% was observed with an increasing state of charge of between 10% and 71%. This increase could be due to the changing conductivity of the active materials or changing thermal contact resistances. Future work will concentrate on adapting the presented method for pouch and prismatic cell formats as well as on the effects of state of health on thermal conductivity. In addition, more research on the effects of thermal contact resistance and the spiral geometry of the jelly roll will be necessary to quantify their impact on thermal conductivity in through-plane direction. Finally, more repeated tests on different cells of the same type are planned to further increase the degree of trust in the precision of the proposed thermal characterization methods.

CRediT authorship contribution statement

Marco Steinhardt: Conceptualization, Data curation, Formal analysis, Funding acquisition, Investigation, Methodology, Project administration, Resources, Software, Supervision, Validation, Visualization, Writing – original draft. **Elisabeth Irene Gillich:** Conceptualization, Methodology, Writing – review & editing, Funding acquisition. **Alexander Rheinfeld:** Methodology, Writing – review & editing, Funding acquisition. **Ludwig Kraft:** Methodology, Writing – review & editing. **Markus Spielbauer:** Resources, Writing – review & editing. **Oliver Bohlen:** Resources, Writing – review & editing. **Andreas Jossen:** Conceptualization, Supervision, Writing – review & editing, Funding acquisition.

Declaration of competing interest

The authors declare that they have no known competing financial interests or personal relationships that could have appeared to influence the work reported in this paper.

Acknowledgments

This work was supported financially by the German Federal Ministry of Education and Research (BMBF) [03XP0027G MiBZ] and the Federal Ministry for Economic Affairs and Energy (BMWi) [03ET6153C iMoBatt]. The authors thank Korbinian Schmidt from the Institute for Electrical Energy Storage Technology at the Technical University of Munich for his practical support.

Appendix

Nomenclature can be found in Table A.12, Table A.13

Table A.12
Nomenclature: Greek symbols.

Symbols	
β	Bruggemann coefficient
$\overline{\rho}$	Bulk density of porous cell layer in $\mathrm{kg\,m^{-3}}$
ρ_{AM}	Density of active material in $\mathrm{kg\,m^{-3}}$
ρ_{BCB}	Density of binder and carbon black in $\mathrm{kg\,m^{-3}}$
ρ_F	Density of fluid phase in $\mathrm{kg\,m^{-3}}$
ρ_S	Density of solid phase in $\mathrm{kg\,m^{-3}}$
$\overline{\rho}_l$	Bulk density of cell layer in $\mathrm{kg\,m^{-3}}$
ρ_{jr}	Density of jelly roll in $\mathrm{kg\,m^{-3}}$
ϵ_{AM}	Volume fraction of active material
ϵ_{BCB}	Volume fraction of binder and carbon black
ϵ_S	Volume fraction of solid phase
ϵ_F	Volume fraction of fluid phase or porosity
φ	Phase angle of voltage with respect to current in rad
τ_1	Time constant at v_1 in s
τ_2	Time constant at v_2 in s
$\Delta\tau$	Difference between τ_1 and τ_2 in s

Table A.13
Nomenclature.

Symbols	
C_{cell}	Lumped heat capacity of the cell in $J\,K^{-1}$
$\bar{c}$	Bulk specific heat capacity of porous layer in $J\,kg^{-1}\,K^{-1}$
c_{jr}	Specific heat capacity of the jelly roll in $J\,kg^{-1}\,K^{-1}$
c_{na}	Specific heat capacity of non-active cell parts in $J\,kg^{-1}\,K^{-1}$
c_{ao}	Specific heat capacity of anode overhang in $J\,kg^{-1}\,K^{-1}$
$d_{jr,g}$	Diameter of the jelly roll gap in m
$d_{ll,i}$	Total length unit cell layer in m
$d_{lt,i}$	Thickness unit cell layer in m
d_{uc}	Total thickness of the unit cell in m
$e_{\Delta\tau}$	Measurement uncertainty in $\Delta\tau$
e_{τ_1/τ_2}	Measurement uncertainty in the ratio of τ_1 and τ_1
e_{mc}	Modeling uncertainty in C_{cell}
e_C	Measurement uncertainty in C_{cell}
e_R	Measurement uncertainty in R_{in}
e_{Rout1}	Measurement uncertainty in R_{out1}
e_{Rout2}	Measurement uncertainty in R_{out2}
e_I	Measurement uncertainty in $\hat{I}_{cell}$
e_U	Measurement uncertainty in $\hat{U}_{cell}$
e_k	Uncertainty in $k_\perp$
e_c	Uncertainty in c_{cell}
e_{jr}	Uncertainty in c_{jr}
f	Uncertainty gain factor
h_{s1}	Heat transfer coefficient at the shell of the cell at v_1 in $W\,m^{-2}\,K^{-1}$
h_{s2}	Heat transfer coefficient at the shell of the cell at v_2 in $W\,m^{-2}\,K^{-1}$
h_{t1}	Heat transfer coefficient at the terminal of the cell at v_1 in $W\,m^{-2}\,K^{-1}$
h_{t2}	Heat transfer coefficient at the terminal of the cell at v_2 in $W\,m^{-2}\,K^{-1}$
Δh	Difference between h_{t2} and h_{t1} in $W\,m^{-2}\,K^{-1}$
$\hat{I}_{cell}$	Amplitude of sinusoidal cell current in A
I_{cell}	Electrical cell current A
$k_{\perp uc}$	Thermal conductivity (through-plane) of the unit cell in $W\,m^{-1}\,K^{-1}$
$k_\perp$	Thermal conductivity (through-plane) of the jelly roll in $W\,m^{-1}\,K^{-1}$
$k_{\|\|}$	Thermal conductivity (in-plane) of the jelly roll and unit cell in $W\,m^{-1}\,K^{-1}$
k_{AM}	Thermal conductivity of the active material in $W\,m^{-1}\,K^{-1}$
k_{NA}	Thermal conductivity of the non-active material in $W\,m^{-1}\,K^{-1}$
$k_{pristine}$	Thermal conductivity of pristine material in $W\,m^{-1}\,K^{-1}$
k_{BCB}	Thermal conductivity of the binder and carbon black in $W\,m^{-1}\,K^{-1}$
k_{dry}	Thermal conductivity of porous material without electrolyte in $W\,m^{-1}\,K^{-1}$
k_{wet}	Thermal conductivity of porous material with electrolyte in $W\,m^{-1}\,K^{-1}$
k_{eff}	Thermal conductivity derived by the Brugemann model in $W\,m^{-1}\,K^{-1}$
k_F	Thermal conductivity of fluid phase in $W\,m^{-1}\,K^{-1}$
k_i	Thermal conductivity of cell layers in $W\,m^{-1}\,K^{-1}$
k_r	Thermal conductivity in radial direction in $W\,m^{-1}\,K^{-1}$
k_z	Thermal conductivity in axial direction in $W\,m^{-1}\,K^{-1}$
m_{cell}	Mass of the cell in kg
m_i	Mass of the cell layers in kg
m_{jr}	Mass of jelly roll in kg
m_{ao}	Mass of anode overhang in kg
m_{na}	Mass of the non jelly roll domains in kg
$\dot{Q}_{cell1}$, $\dot{Q}_{cell2}$	Heat rate inside the cell at v_1 and v_2 in W
$\dot{Q}_{jr}$	Heat rate inside the jelly roll in W
$\dot{Q}_t$	Heat rate inside the terminals in W
$\dot{q}$	Volume specific heat source in $W\,m^{-3}$
R_{in}	Thermal resistance inside the cell in $K\,W^{-1}$
R_{out1}, R_{out2}	Thermal resistance outside the cell at v_1 and v_2 in $K\,W^{-1}$
t	Time in s
T_{amb}	Ambient temperature of the cell in K
T_{tn}	Temperature at negative terminal of the cell in K
T_{tp}	Temperature at positive terminal of the cell in K
T_s	Temperature at the shell of the cell in K
ΔT_{s1}, ΔT_{s2}	Temperature increase at the shell of the cell at v_1 and v_2 in K
U_{cell}	Cell voltage in V
U_{ocv}	Open circuit voltage in V
$\hat{U}_{cell}$	Amplitude of sinusoidal cell voltage in V
v_1, v_2	Lower and upper air velocity in $m\,s^{-1}$
V_{jr}	Volume of jelly roll in m^3
V_{ao}	Volume of anode overhang in m^3
Z_i	Internal electrical impedance in Ω
Z_e	External electrical impedance in Ω

Table A.14
Measurement results for the lumped parameters heat capacity C_{cell} and internal resistance R_{in} for the 21700 cell at three different ambient temperatures and SOCs. For each result, the arithmetic mean and the 95% interval is given.

U_{ocv} / V	T_{amb} / K	R_{in} / $K\,W^{-1}$	C_{cell} / $J\,K^{-1}$	R_{out1} / $K\,W^{-1}$	R_{out2} / $K\,W^{-1}$	τ_1 / s	τ_2 / s
3.42	283	0.358 ± 0.02	56.8 ± 0.27	13.5 ± 0.05	4.7 ± 0.00	784.8 ± 0.84	286.4 ± 0.70
	298	0.396 ± 0.02	58.3 ± 0.16	14.0 ± 0.04	4.7 ± 0.01	839.6 ± 1.05	299.7 ± 0.53
	313	0.437 ± 0.05	59.7 ± 0.27	14.0 ± 0.03	4.8 ± 0.01	864.8 ± 1.60	312.5 ± 0.95
3.63	283	0.302 ± 0.07	57.1 ± 0.31	13.4 ± 0.12	4.7 ± 0.04	782.6 ± 6.26	283.8 ± 1.19
	298	0.375 ± 0.01	58.4 ± 0.05	14.0 ± 0.07	4.7 ± 0.02	836.9 ± 3.57	296.8 ± 1.21
	313	0.415 ± 0.06	60.1 ± 0.66	14.0 ± 0.04	4.7 ± 0.05	866.2 ± 8.22	310.4 ± 1.86
3.93	283	0.339 ± 0.03	56.7 ± 0.16	13.3 ± 0.03	4.6 ± 0.00	775.7 ± 0.89	281.2 ± 1.28
	298	0.363 ± 0.02	58.5 ± 0.13	14.1 ± 0.05	4.8 ± 0.02	844.0 ± 2.22	300.9 ± 1.41
	313	0.395 ± 0.03	60.1 ± 0.13	14.0 ± 0.03	4.8 ± 0.01	868.1 ± 2.03	312.4 ± 1.15

Table A.15
Material densities and temperature-dependent heat capacities $c/(\,J\,kg^{-1}\,K^{-1}) = c_{m3}T^{-3} + c_{m2}T^{-2} + c_0 + c_1T + c_2T^2 + c_3T^3$.

	ρ / $g\,cm^{-3}$	c_{m3} / 10^{-8}	c_{m2} / 10^{-6}	c_0 / 1	c_1 / 1	c_2 / 10^{-3}	c_3 / 10^{-4}
Graphite [21,37]	2.30	0	0	684.1	2.996 °C^{-1}	0	0
NMC [21,37]	4.70	0	0	757.1	1.978 °C^{-1}	0	0
PP Separator [21,38]	0.91	0	0	1148	7.938 °C^{-1}	15.24 °C^{-2}	3.737 °C^{-3}
Cu [38,39]	8.96	0	0	356	0.0988 K^{-1}	0	0
Al [38,40]	2.70	2.84 K^3	−6.64 K^2	785	0.906 K^{-1}	−1.12 K^{-2}	0
Steel 304 [41,42][a]	7.90	0	0	182.1	1.6185 K^{-1}	−2.02 K^{-2}	0
Electrolyte [21]	1.24	0	0	1610	1.398 °C^{-1}	4.457 °C^{-2}	0

[a]Recommended curve between 200 and 300 K.

Table A.16
Temperature-dependent thermal conductivity of dry and pristine materials used in lithium-ion cells.

Material	278 K	288 K	298 K	308 K	318 K
	k/ $W\,m^{-1}\,K^{-1}$				
Dry and porous:					
A1: Graphite in CO_2 [21]	2.46	2.34	2.08	1.87	1.79
C1: NMC in CO_2 [21]	0.24	0.20	0.17	0.15	0.14
C2: NMC delithiated in argon [28]	0.344	0.341	0.338	0.335	0.333
C3: NMC lithiated in argon [28]	0.441	0.437	0.433	0.429	0.426
Pristine and non-porous:					
A2: Pyrolitic graphite ⊥ [26]	10.4	9.99	9.58	9.26	8.96
A3: 33% of A2 [26,27]	3.42	3.30	3.16	3.06	2.96
PVDF [43]	0.282	0.273	0.263	0.253	0.244
LP50 [11]	0.180	0.177	0.175	0.172	0.170
CO_2 [44]	0.0151	0.0158	0.0166	0.0175	0.0183
Argon [44]	0.0166	0.0171	0.0176	0.0181	0.0186
Cu [23]	400.4	399.3	398.2	397.3	396.5
Al [23]	236.2	236.6	236.9	237.5	238.1

Table A.17
Structural parameters of wet 21700 unit cell layers and their temperature-dependent heat capacity $\bar{c}/(J\,kg^{-1}\,K^{-1}) = c_0 + c_1(T/\,K - 300)$.

	ε_F[a]	ε_{BCB}[a]	$d_{lt,i}$ / µm [9]	$d_{ll,i}$ / m [9][b]	$\bar{\rho}_i$ / $g\,cm^{-3}$[c]	m_i / g[d]	c_0[e]	c_1[e]
Anode	0.300	0.090	96.5	1.666	1.95	19.9	934.8	2.733
Cathode	0.300	0.084	76.2	1.604	3.43	26.6	898.1	1.727
Separator	0.450	0.000	18.0	1.810	1.06	2.2	1515.5	4.573
Cu-collector	0.000	0.000	12.0	0.905	8.96	6.2	385.6	0.099
Al-collector	0.000	0.000	13.6	0.811	2.70	1.9	892.4	0.635

[a]Values originate from the 18650 cell except for ε_F of the anode and cathode, which are adjusted to match the measured and calculated cell weights in Table 6.
[b]For double-coated electrodes, the length is accumulated.
[c]Bulk densities of porous layer $\bar{\rho}_i$ are calculated with Eq. (12) and the material densities in Table A.15.
[d]The total layer mass m_i is derived from the product of the layer thickness $d_{lt,i}$ and length $d_{ll,i}$, the bulk density $\bar{\rho}_i$ and the active jelly roll height of 63.5 mm [9].
[e]Calculated with Eq. (14).

Table A.18
Equations and boundary condition of the thermal model in Section 3.1 and Fig. 5.

Heat equation	
$r\rho(r,z)c(r,z)\frac{\partial T(r,z,t)}{\partial t} = \vec{\nabla}\cdot\left(\begin{pmatrix} rk_r(r,z) & 0 \\ 0 & rk_z(r,z)\end{pmatrix}\vec{\nabla}T(r,z,t)\right) + r\dot{q}(r,z,t)$	
Initial temperature	
$T(r,z,t=0\ \mathrm{s}) = T_{amb}$	
Heat source	
Domain 1–5	$\dot{q}(r,z,t) = \dot{Q}_t/(\sum_{n=1}^{5} V_n)$
Domain 6	$\dot{q}(r,z,t) = \dot{Q}_{jr}/(V_6)$
Boundary conditions	
Terminals	$\vec{n}\cdot\begin{pmatrix} rk_r(r,z) & 0 \\ 0 & rk_z(r,z)\end{pmatrix}\vec{\nabla}T(r,z,t) = rh_t(T_{amb}-T(r,z,t))$
Shell	$\vec{n}\cdot\begin{pmatrix} rk_r(r,z) & 0 \\ 0 & rk_z(r,z)\end{pmatrix}\vec{\nabla}T(r,z,t) = rh_s(T_{amb}-T(r,z,t))$

Table A.19
Uncertainty analysis for the specific heat capacity of the jelly roll c_{jr} in Eq. (14) and for the through-plane conductivity of the unit cell $k_{\perp uc}$ defined by Eq. (15). Every estimation e_i is based on the 18650 cell with $k_\perp = 1.122\ \mathrm{W\,m^{-1}\,K^{-1}}$ and $c_{jr} = 834\ \mathrm{J\,kg^{-1}\,K^{-1}}$.

Argument uncertainty	$e_i = \frac{\Delta k_{\perp uc}}{k_{\perp uc}}$	$e_i = \frac{\Delta c_{jr}}{c_{jr}}$
$163\% \cdot k_{anode}$ [a]	17.1%	–
$126\% \cdot k_{cathode}$ [a]	11.5%	–
$184\% \cdot k_{separator}$ [a]	5.9%	–
$101\% \cdot k_{Cu}$ [a]	0.0%	–
$101\% \cdot k_{Al}$ [a]	0.0%	–
$101\% \cdot d_{lt,anode}$ [b]	0.1%	0.0%
$102\% \cdot d_{lt,cathode}$ [b]	0.2%	0.0%
$108\% \cdot d_{lt,separator}$ [b]	0.5%	0.2%
$109\% \cdot d_{lt,Cu}$ [b]	0.3%	0.5%
$106\% \cdot d_{lt,Al}$ [b]	0.3%	0.0%
$115\% \cdot \bar{c}_{anode}$ [c,d,e]	–	5.5%
$112\% \cdot \bar{c}_{cathode}$ [c,d,f]	–	6.0%
$112\% \cdot \bar{c}_{separator}$ [c,d,g]	–	0.6%
$101\% \cdot \bar{c}_{Cu}$ [h]	–	0.1%
$101\% \cdot \bar{c}_{Al}$ [h]	–	0.1%
$\sqrt{\sum e_i^2}$	21.4%	8.2%

[a]Uncertainties are taken from [3].
[b]Uncertainties are based on a precision of 1 µm for common micrometer screws.
[c]Considers an uncertainty of 2% [28] for ε_F.
[d]Considers an uncertainty of 10.7% for c_F, which is determined by the deviation between [24] and [45].
[e]Considers an uncertainty of 19.5% for c_S [24,46].
[f]Considers an uncertainty of 13.7% for c_S [24,46].
[g]Considers an uncertainty of 25.3% for c_S [24,47].
[h]Considers an uncertainty of 1.5% for c_S, which is the lower uncertainty bound for differential scanning calorimeters [30].

Table A.20
Parameters of the thermal model in Section 3.1 and Fig. 5.

Domain	$\frac{\rho}{\mathrm{g\,cm^{-3}}}$	$\frac{c}{\mathrm{J\,kg^{-1}\,K^{-1}}}$	$\frac{k_r}{\mathrm{W\,m^{-1}\,K^{-1}}}$	$\frac{k_z}{\mathrm{W\,m^{-1}\,K^{-1}}}$
1, 7	Table A.15	Table A.15	Table A.16	$k_r = k_z$
2, 3	Table A.15	Table A.15	Table A.16	$k_r = k_z$
4	Table A.15	Table A.15	Table A.16	$k_r = k_z$
5	m_{ao}/V_{ao} [a,b]	c_{ao} [a]	0.041[c,e]; 0.042[d,e]	12.978[c,e]; 12.485[d,e]
6	m_{jr}/V_{jr} [a,b]	c_{jr} [a]	$k_\perp$	$k_{\|\|}$

[a]Taken from Table 6.
[b]Taken from Fig. 5.
[c]Applied for the 18650 cell.
[d]Applied for the 21700 cell.
[e]Analogous calculation as for $k_\perp$ and $k_{\|\|}$ with Eqs. (15) and (16) but with the Al collector and cathode layer replaced by the thermal conductivity of argon in Table A.16.

References

[1] Y. Liu, Y. Zhu, Y. Cui, Challenges and opportunities towards fast-charging battery materials, Nat. Energy 4 (7) (2019) 540–550, http://dx.doi.org/10.1038/s41560-019-0405-3.

[2] C.-F. Chen, A. Verma, P.P. Mukherjee, Probing the role of electrode microstructure in the lithium-ion battery thermal behavior, J. Electrochem. Soc. 164 (11) (2017) E3146–E3158, http://dx.doi.org/10.1149/2.0161711jes.

[3] M. Steinhardt, E.I. Gillich, M. Stiegler, A. Jossen, Thermal conductivity inside prismatic lithium-ion cells with dependencies on temperature and external compression pressure, J. Energy Storage 32 (2020) 101680, http://dx.doi.org/10.1016/j.est.2020.101680.

[4] L. Sheng, Z. Zhang, L. Su, H. Zhang, H. Zhang, Y. Fang, K. Li, W. Ye, Quasi steady state method to measure thermophysical parameters of cylindrical lithium ion batteries, J. Power Sources 485 (2021) 229342, http://dx.doi.org/10.1016/j.jpowsour.2020.229342.

[5] T.S. Bryden, B. Dimitrov, G. Hilton, C. Ponce de León, P. Bugryniec, S. Brown, D. Cumming, A. Cruden, Methodology to determine the heat capacity of lithium-ion cells, J. Power Sources 395 (2018) 369–378, http://dx.doi.org/10.1016/j.jpowsour.2018.05.084.

[6] M. Akbarzadeh, T. Kalogiannis, J. Jaguemont, J. He, L. Jin, M. Berecibar, J. van Mierlo, Thermal modeling of a high-energy prismatic lithium-ion battery cell and module based on a new thermal characterization methodology, J. Energy Storage 32 (2020) 101707, http://dx.doi.org/10.1016/j.est.2020.101707.

[7] M. Fleckenstein, S. Fischer, O. Bohlen, B. Bäker, Thermal Impedance Spectroscopy - A method for the thermal characterization of high power battery cells, J. Power Sources 223 (2013) 259–267, http://dx.doi.org/10.1016/j.jpowsour.2012.07.144.

[8] M. Al-Zareer, A. Michalak, C. Da Silva, C.H. Amon, Predicting specific heat capacity and directional thermal conductivities of cylindrical lithium-ion batteries: A combined experimental and simulation framework, Appl. Therm. Eng. 182 (2021) 116075, http://dx.doi.org/10.1016/j.applthermaleng.2020.116075.

[9] J. Sturm, A. Frank, A. Rheinfeld, S.V. Erhard, A. Jossen, Impact of electrode and cell design on fast charging capabilities of cylindrical lithium-ion batteries, J. Electrochem. Soc. 167 (13) (2020) 130505, http://dx.doi.org/10.1149/1945-7111/abb40c.

[10] A. Rheinfeld, S. Kosch, S.V. Erhard, P.J. Osswald, B. Rieger, A. Jossen, Electro-thermal modeling of large format lithium-ion pouch cells: A cell temperature dependent linear polarization expression, J. Electrochem. Soc. 163 (14) (2016) A3046–A3062, http://dx.doi.org/10.1149/2.0701614jes.

[11] D. Werner, A. Loges, D.J. Becker, T. Wetzel, Thermal conductivity of Li-ion batteries and their electrode configurations – A novel combination of modelling and experimental approach, J. Power Sources 364 (2017) 72–83, http://dx.doi.org/10.1016/j.jpowsour.2017.07.105.

[12] J.P. Schmidt, A. Weber, E. Ivers-Tiffée, A novel and precise measuring method for the entropy of lithium-ion cells: dS via electrothermal impedance spectroscopy, Electrochim. Acta 137 (2014) 311–319, http://dx.doi.org/10.1016/j.electacta.2014.05.153.

[13] L. Sheng, L. Su, H. Zhang, Experimental determination on thermal parameters of prismatic lithium ion battery cells, Int. J. Heat Mass Transfer 139 (2019) 231–239, http://dx.doi.org/10.1016/j.ijheatmasstransfer.2019.04.143.

[14] J.G. Hust, P.J. Giarratano, Thermal Conductivity and Electrical Resistivity Standard Reference Materials: Austenitic Stainless Steel, SRM's 735 and 798, from 4 to 1200 (March 1975), in: NBS Special Publication, vol. 260–46, U.S. Department of Commerce, 1975.

[15] Y. Ye, L.H. Saw, Y. Shi, K. Somasundaram, A.A. Tay, Effect of thermal contact resistances on fast charging of large format lithium ion batteries, Electrochim. Acta 134 (2014) 327–337, http://dx.doi.org/10.1016/j.electacta.2014.04.134.

[16] R. Mahamud, C. Park, Spatial-resolution, lumped-capacitance thermal model for cylindrical Li-ion batteries under high Biot number conditions, Appl. Math. Model. 37 (5) (2013) 2787–2801, http://dx.doi.org/10.1016/j.apm.2012.06.023.

[17] W. Li, K.R. Crompton, C. Hacker, J.K. Ostanek, Comparison of current interrupt device and vent design for 18650 format lithium-ion battery caps, J. Energy Storage 32 (2020) 101890, http://dx.doi.org/10.1016/j.est.2020.101890.

[18] S.D. Lubner, S. Kaur, Y. Fu, V. Battaglia, R.S. Prasher, Identification and characterization of the dominant thermal resistance in lithium-ion batteries using operando 3-omega sensors, J. Appl. Phys. 127 (10) (2020) 105104, http://dx.doi.org/10.1063/1.5134459.

[19] A. Gaitonde, A. Nimmagadda, A. Marconnet, Measurement of interfacial thermal conductance in Lithium ion batteries, J. Power Sources 343 (2017) 431–436, http://dx.doi.org/10.1016/j.jpowsour.2017.01.019.

[20] B. Shi, H. Zhang, Y. Qi, L. Yang, Calculation model of effective thermal conductivity of a spiral-wound lithium ion battery, J. Therm. Stresses 27 (6) (2018) 572–579, http://dx.doi.org/10.1007/s11630-018-1060-x.

[21] A. Loges, S. Herberger, D. Werner, T. Wetzel, Thermal characterization of Li-ion cell electrodes by photothermal deflection spectroscopy, J. Power Sources 325 (2016) 104–115, http://dx.doi.org/10.1016/j.jpowsour.2016.05.082.

[22] J. Sturm, A. Rheinfeld, I. Zilberman, F.B. Spingler, S. Kosch, F. Frie, A. Jossen, Modeling and simulation of inhomogeneities in a 18650 nickel-rich, silicon-graphite lithium-ion cell during fast charging, J. Power Sources 412 (412) (2019) 204–223, http://dx.doi.org/10.1016/j.jpowsour.2018.11.043.

[23] R.W. Powell, C.Y. Ho, P.E. Liley, Thermal Conductivity of Selected Materials, in: NSRDS-NBS, vol. 8, U.S. Department of Commerce, 1966.

[24] A. Loges, S. Herberger, P. Seegert, T. Wetzel, A study on specific heat capacities of Li-ion cell components and their influence on thermal management, J. Power Sources 336 (2016) 341–350, http://dx.doi.org/10.1016/j.jpowsour.2016.10.049.
[25] A. Vadakkepatt, B. Trembacki, S.R. Mathur, J.Y. Murthy, Bruggeman's exponents for effective thermal conductivity of lithium-ion battery electrodes, J. Electrochem. Soc. 163 (2) (2015) A119–A130, http://dx.doi.org/10.1149/2.0151602jes.
[26] Y.S. Touloukian, C.Y. Ho, R.W. Powell, P.G. Klemens, Thermal conductivity nonmetallic solids, in: Thermophysical Properties of Matter, Vol. 2, Defense Technical Information Center (Ed.), 1970.
[27] W. Ju, C. Zhu, Z. Wei, Intercalated ion tuning of the cross-plane thermal transport properties of graphite, AIP Adv. 10 (9) (2020) 095225, http://dx.doi.org/10.1063/5.0023229.
[28] P. Gotcu, W. Pfleging, P. Smyrek, H.J. Seifert, Thermal behaviour of LixMeO2 (Me = Co or Ni + Mn + Co) cathode materials, Phys. Chem. Chem. Phys. : PCCP 19 (19) (2017) 11920–11930, http://dx.doi.org/10.1039/C7CP00513J.
[29] P.M. Gomadam, R.E. White, J.W. Weidner, Modeling heat conduction in spiral geometries, J. Electrochem. Soc. 150 (10) (2003) A1339, http://dx.doi.org/10.1149/1.1605743.
[30] H. Czichos, T. Saito, L. Smith (Eds.), Springer Handbook of Materials Measurement Methods, in: Springer Handbooks, Springer, Berlin, 2006, URL http://dx.doi.org/10.1007/978-3-540-30300-8.
[31] S.J. Bazinski, X. Wang, Experimental study on the influence of temperature and state-of-charge on the thermophysical properties of an LFP pouch cell, J. Power Sources 293 (2015) 283–291, http://dx.doi.org/10.1016/j.jpowsour.2015.05.084.
[32] F.J. Günter, C. Burgstaller, F. Konwitschny, G. Reinhart, Influence of the electrolyte quantity on lithium-ion cells, J. Electrochem. Soc. 166 (10) (2019) A1709–A1714, http://dx.doi.org/10.1149/2.0121910jes.
[33] F.B. Spingler, S. Kücher, R. Phillips, E. Moyassari, A. Jossen, Electrochemically stable in situ dilatometry of NMC, NCA and graphite electrodes for lithium-ion cells compared to XRD measurements, J. Electrochem. Soc. 168 (4) (2021) 040515, http://dx.doi.org/10.1149/1945-7111/abf262, URL https://iopscience.iop.org/article/10.1149/1945-7111/abf262/pdf.
[34] S.P. Nadimpalli, V.A. Sethuraman, D.P. Abraham, A.F. Bower, P.R. Guduru, Stress evolution in lithium-ion composite electrodes during electrochemical cycling and resulting internal pressures on the cell casing, J. Electrochem. Soc. 162 (14) (2015) A2656–A2663, http://dx.doi.org/10.1149/2.0341514jes.
[35] G. Liebig, U. Kirstein, S. Geißendörfer, F. Schuldt, C. Agert, The impact of environmental factors on the thermal characteristic of a lithium–ion battery, Batteries 6 (1) (2020) 3, http://dx.doi.org/10.3390/batteries6010003.
[36] K.A. Murashko, J. Pyrhönen, J. Jokiniemi, Determination of the through-plane thermal conductivity and specific heat capacity of a Li-ion cylindrical cell, Int. J. Heat Mass Transfer 162 (2020) 120330, http://dx.doi.org/10.1016/j.ijheatmasstransfer.2020.120330.
[37] J. Landesfeind, J. Hattendorff, A. Ehrl, W.A. Wall, H.A. Gasteiger, Tortuosity determination of battery electrodes and separators by impedance spectroscopy, J. Electrochem. Soc. 163 (7) (2016) A1373–A1387, http://dx.doi.org/10.1149/2.1141607jes.
[38] VDI-Wärmeatlas: Mit 320 Tabellen, eleventh ed., in: VDI-Buch, Springer Vieweg, Berlin, 2013, http://dx.doi.org/10.1007/978-3-642-19981-3.
[39] U. Grigull, W. Blanke, Thermophysikalische Stoffgrößen, in: Wärme- und Stoffübertragung, Springer Berlin Heidelberg, Berlin, Heidelberg, 1989, http://dx.doi.org/10.1007/978-3-662-10545-0.
[40] Y. Takahashi, T. Azumi, Y. Sekine, Heat capacity of aluminum from 80 to 880 K, Thermochim. Acta 139 (1989) 133–137, http://dx.doi.org/10.1016/0040-6031(89)87016-9.
[41] Y.S. Touloukian, C.Y. Ho, Part II: Thermophyslcal properties of seven materials, in: Thermophysical Properties of Selected Aerospace Materials, Vol. 2, Defense Technical Information Center (Ed.), 1977.
[42] R.H. Bogaard, P.D. Desai, H.H. Li, C.Y. Ho, Thermophysical properties of stainless steels, Thermochim. Acta 218 (1993) 373–393, http://dx.doi.org/10.1016/0040-6031(93)80437-F.
[43] W.N. dos Santos, C.Y. Iguchi, R. Gregorio, Thermal properties of poly(vinilidene fluoride) in the temperature range from 25 to 210degC, Polym. Test. 27 (2) (2008) 204–208, http://dx.doi.org/10.1016/j.polymertesting.2007.10.005.
[44] P. Linstrom, NIST chemistry WebBook, NIST standard reference database 69. http://dx.doi.org/10.18434/T4D303.
[45] S.C. Chen, C.C. Wan, Y.Y. Wang, Thermal analysis of lithium-ion batteries, J. Power Sources 140 (1) (2005) 111–124, http://dx.doi.org/10.1016/j.jpowsour.2004.05.064.
[46] P. Bohn, G. Liebig, L. Komsiyska, G. Wittstock, Temperature propagation in prismatic lithium-ion-cells after short term thermal stress, J. Power Sources 313 (2016) 30–36, http://dx.doi.org/10.1016/j.jpowsour.2016.02.055.
[47] V. Vishwakarma, A. Jain, Measurement of in-plane thermal conductivity and heat capacity of separator in Li-ion cells using a transient DC heating method, J. Power Sources 272 (2014) 378–385, http://dx.doi.org/10.1016/j.jpowsour.2014.08.066.

4 Meta-analysis on thermal conductivity in lithium-ion cells

The review article [29] in this chapter entitled *Meta-Analysis of Experimental Results for Thermal Capacity and Thermal Conductivity in Lithium-Ion Batteries: A Critical Review* deals with $k_\perp$ measurements on all cell formats through a critical literature review. In addition, the influence of all battery states mentioned in Figure 4.1, including the state of health, is analyzed. The review is labeled as a meta-analysis because of the approach of recommending values for $k_\perp$ using statistical methods, which allows a more objective appraisal to the field [186]. In addition to $k_\perp$, the review article deals with the in-plane conductivity and the specific heat capacity of all components that are necessary to determine the parameters of the thermal models shown in Figure 1.5.

Data collection Work on this review began with the definition of the scope with regard to length scales and sources of information. It was decided to use a length scale ranging from cell components such as current collectors to full cells, which excludes, for example, thermal parameters of battery systems. In addition, only peer-reviewed journal articles were considered, which excluded dissertations and bachelor or master theses from the analysis. The key words were then identified and used for the literature research in online databases. This literature search found every article that mentioned thermal conductivity or heat capacity measurements in the title, in key words or in the abstract. In addition, the authors' reference management systems were screened for suitable data.

Data analysis After the data was collected, the measurement results from the literature were labeled and exported to a database. The temperature and SOC dependencies were then calculated using linear

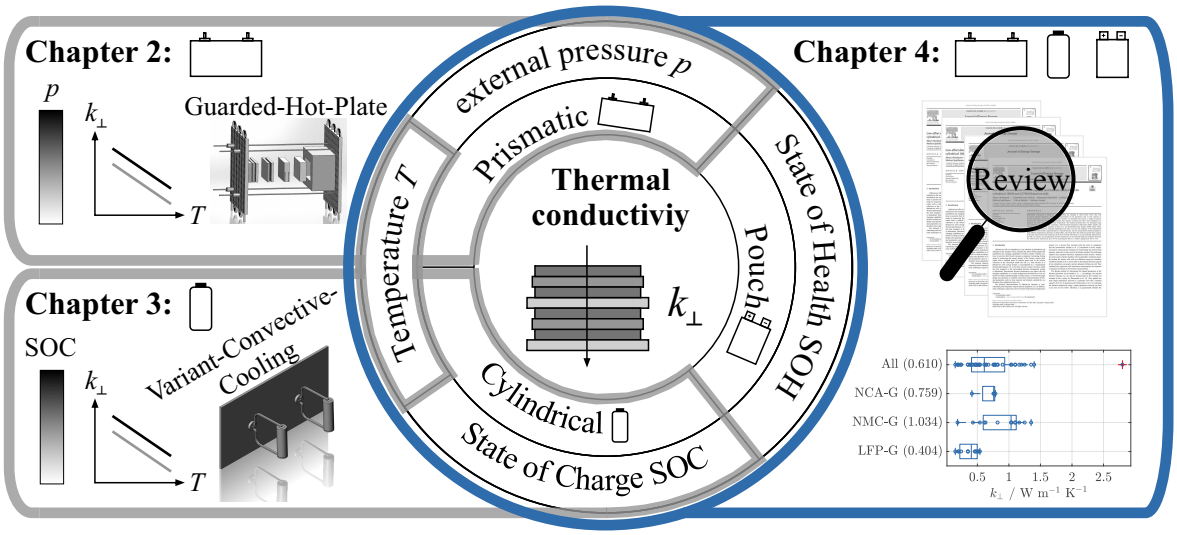

Figure 4.1: Scope of Chapter 4.

regressions. The data quantity for each test object is visualized in bar charts to reveal knowledge gaps for experimental researchers. Boxplot calculations are used to recommend values for thermal conductivity and heat capacity for thermal modeling of lithium-ion cells. In addition, the boxplot calculations identified outlying measurements that exceeded the quartile by 1.5 times the interquartile range.

Results and discussion According to this meta-analysis, the $k_{\perp}$ of lithium-ion cells is between 0.15 and 1.4 $\mathrm{W\,m^{-1}\,K^{-1}}$. The active material has a pronounced influence on $k_{\perp}$. For example, NMC-G stacks exceed the $k_{\perp}$-median of LFP-G by almost three times. With increasing SOC, a variation in the $k_{\perp}$ of -7% to 33% has been observed in the literature. In addition, $k_{\perp}$ decreases with age by up to 23%, but the number of studies on SOH dependence is very small. There are contradictory results for the temperature dependence, observing either a negative or a positive correlation. Thermal contact resistances between the stack-layers can influence $k_{\perp}$, which could explain deviations between measured and calculated $k_{\perp}$ in the literature. Despite the importance of thermal contact resistance, its exact magnitude in commercial lithium-ion cells is unknown and further research is needed.

Author contribution The scope and keywords of this review were defined by Jorge V. Barreras, Haijun Ruan and Marco Steinhardt. The literature research and data analysis was carried out by Marco Steinhardt and supported by Jorge V. Barreras and Haijun Ruan. The results were discussed by Jorge V. Barreras, Haijun Ruan and Marco Steinhardt. The manuscript was written by Marco Steinhardt and review and edited was done by all other authors.

Meta-analysis of experimental results for heat capacity and thermal conductivity in lithium-ion batteries: A critical review

Marco Steinhardt, Jorge V. Barreras, Haijun Ruan, Billy Wu, Gregory J. Offer, Andreas Jossen

Journal of Power Sources 552, p. 230829, 2022

Permanent weblink:
https://doi.org/10.1016/j.jpowsour.2021.230829

Journal of Power Sources 522 (2022) 230829

Contents lists available at ScienceDirect

Journal of Power Sources

journal homepage: www.elsevier.com/locate/jpowsour

Review article

Meta-analysis of experimental results for heat capacity and thermal conductivity in lithium-ion batteries: A critical review

Marco Steinhardt [a,*,1], Jorge V. Barreras [b,c,1], Haijun Ruan [c,d,1], Billy Wu [c,d], Gregory J. Offer [b,c], Andreas Jossen [a]

[a] Technical University of Munich (TUM), Institute for Electrical Energy Storage Technology (EES), Arcisstrasse 21, 80333, Munich, Germany
[b] Department of Mechanical Engineering, Imperial College London, London, UK
[c] The Faraday Institution, Didcot, UK
[d] Dyson School of Design Engineering, Imperial College London, London, UK

HIGHLIGHTS

- Statistical recommended medians and uncertainties taken from thermal experiments.
- Heat capacity and thermal conductivity analyzed from component to cell level.
- Limited data available on thermal contact resistances between stack layers.
- Temperature, state of charge and state of health dependencies discussed.
- Identification of knowledge gaps and research directions for thermal parameters.

GRAPHICAL ABSTRACT

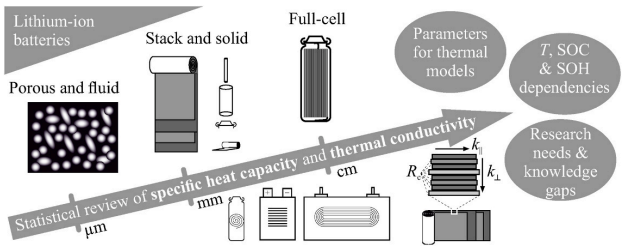

ARTICLE INFO

Keywords:
Li-ion battery
Heat capacity
Thermal conductivity
Thermal contact resistance

ABSTRACT

Scenarios with rapid energy conversion for lithium-ion batteries are increasingly relevant, due to the desire for more powerful electric tools or faster charging electric vehicles. However, higher power means higher cooling requirements, affecting the battery temperature and its thermal gradients. In turn, temperature is a key quantity influencing battery performance, safety and lifetime. Therefore, thermal models are increasingly important for the design and operation of battery systems. Key parameters are specific heat capacity and thermal conductivity. For these parameters, this paper presents a comprehensive review of the experimental results in the literature, where the median values and corresponding uncertainties are summarized. Whenever available, data is analyzed from component to cell level with the discussion of dependencies on temperature, state of charge (SOC) and state of health (SOH). This meta-analysis reveals gaps in knowledge and research needs. For instance, we uncover inconsistencies between the specific heat capacity of electrode-separator stacks and full-cells. For the thermal conductivity, we found that thermal contact resistance and dependencies on battery states have been poorly studied. There is also a lack of measurements at high temperatures, which are required for safety studies. Overall, this study serves as a valuable reference material for both modellers and experimenters.

* Corresponding author.
E-mail address: marco.steinhardt@tum.de (M. Steinhardt).
[1] These authors contributed equally to this work.

https://doi.org/10.1016/j.jpowsour.2021.230829
Received 21 September 2021; Received in revised form 8 November 2021; Accepted 23 November 2021
Available online 17 January 2022

1. Introduction

In 1991, Sony released the first video camera powered by lithium-ion cells [1] - an energy storage technology that nearly delivers twice the energy density than nickel–metal hydride batteries (NiMH) [2]. Today, lithium-ion cells are still applied in consumer electronics, but their market share is increasingly shifting towards electric vehicles (EV) [3] and energy storage systems. This general trend is expected to continue, supported by policies, regulations and technological advances [4].

One of the remaining technical challenges for lithium-ion batteries is the need to enhance their energy density and shorten charging time. However, as pointed out by Liu et al. [5], solving these challenges often results in thermal issues, i.e. a faster and non-uniform temperature increase. For example, Kraft et al. [6] observed that cells with a high-capacity cathode active material (lithium and manganese-rich) released up to four times as much heat during discharges compared to cells with a commonly used cathode active material (nickel-rich). On the other hand, Barreras et al. [7] showed that the problem of non-uniform temperatures during EV fast charging can be solved with innovative balancing concepts, but at the expense of additional cost and complexity, and the cooling needs are still significant.

Indeed, temperature is an important battery state that affects energy efficiency [8], ageing rates [9,10], electrical power capability [10] and the state of safety [11]. For instance, cell temperatures below −20 °C should be avoided for storage and operation as the electrolyte may begin to freeze [12,13]. Most lithium-ion cells can operate above −20 °C, but energy efficiency and the power capability are compromised. Especially high charging power induces accelerated aging due to lithium plating at low temperatures [9], which may even result in the formation and growth of lithium dendrites, leading to safety hazard, such as thermal runaway. It is widely accepted that the desired working temperature for lithium-ion cells starts between 10 and 20 °C and ends between 30 and 40 °C [12, 14]. However, as demonstrated by Schimpe et al. [10], the optimal temperature range is not constant, but depends on the SOC, the C-rates, and the targeted aging rates. In addition, it was shown by Yang et al. [15] and Rodrigues et al. [16] that the cell design has also a strong influence on the optimal temperature range. In general, temperatures above the desired range and up to 60 °C should be avoided, because of their impairing effect on aging, such as the rapid growth of the solid-electrolyte interface (SEI) [9] and electrolyte depletion [17]. 60 °C constitutes a safety margin of 20 °C for the first exothermic reaction of the SEI, which starts between 80 and 120 °C [18–20]. This exothermic reaction can lead to the self-sustaining and safety-critical thermal runaway event.

Due to the significance of the cell temperature T_{cell} for safety, lifetime and performance, battery developers use thermal cell models. For these models, the specific heat capacity c_p at constant pressure constitutes an essential parameter. If thermal gradients inside the cell can be neglected (low Biot number), the lumped capacitance model in Equation (1) is a reasonable modeling approach for T_{cell} [21,22]. Accordingly, the increase in T_{cell} depends strongly on the specific heat capacity c_p, which is reviewed in this paper. Further influences on T_{cell} accrue from the density ρ, volume V_{cell}, and surface A_{surf} of the cell. On the operational side, the heat generation rate inside the cell $\dot{q}V_{cell}$, the heat transfer coefficient h_{surf}, and the ambient temperature T_{amb} act on T_{cell}. For adiabatic boundary conditions ($h_{surf} = 0\ \mathrm{W\ m^{-2}\ K^{-1}}$), uncertainties in c_p would translate directly into uncertainties in $\partial T_{cell}/\partial t$. For example, an uncertainty of 10% in c_p would cause an uncertainty in $\partial T_{cell}/\partial t$ of 10%, which can drop to an uncertainty of 6% at lower heat transfer coefficients ($7\ \mathrm{W\ m^{-2}\ K^{-1}}$) [23].

$$c_p \rho V_{cell} \frac{\partial T_{cell}}{\partial t} = \dot{q} V_{cell} - h_{surf} A_{surf} (T_{cell} - T_{amb}) \tag{1}$$

$$c_p \rho \frac{\partial T_{cell}}{\partial t} = k_x \frac{\partial^2 T_{cell}}{\partial x^2} + k_y \frac{\partial^2 T_{cell}}{\partial y^2} + k_z \frac{\partial^2 T_{cell}}{\partial z^2} + \dot{q} \tag{2}$$

If significant temperature gradients inside the lithium-ion cell are expected, thermal cell models usually apply a version of the heat Equation (2). For example, this can be the case for safety simulations [24], pre-heating studies [25], or fast charging investigation [26]. The thermal conductivity influences the temperature field T_{cell} in Equation (2), which depends on the location (x,y,z) and the time t. Due to the layered structure of the electrode-separator stack, the thermal conductivity is anisotropic and described by a value in each Cartesian direction (k_x,k_y,k_z). It should be noted that Equation (2) is expressed in Cartesian coordinates (x,y,z) but can readily be expressed in cylindrical coordinates (r, z, φ).

Equations (1) and (2) emphasize the dependency of T_{cell} on intrinsic material parameters of the cell (c_p, k_x, k_y, k_z) and the operational conditions $(\dot{q}, h_{surf}, T_{amb})$. Despite the importance of material parameters for T_{cell}, review papers [2,27] summarizing their values are out of date. In 2011, Bandhauer et al. [2] analyzed the results of two thermal conductivity studies [28,29] and expressed the need for a better understanding of thermal contact resistances within full-cells and the lack for measurement data for cells with lithium-iron-phosphate (LFP) cathodes. Madani et al. [30] and Tang et al. [31] concentrated their reviews on the experimental methods rather than on the results. Shah et al. [27] published one of the most comprehensive reviews on thermal parameters in 2016. They summarized eleven experiments on material and six on full-cell level. Despite this increase in experiments since 2011, Shah et al. [27] considers the available data for thermal transport properties to be insufficient, so that further experiments are necessary to resolve the spread of the reported results and to identify rate-limiting thermal transport processes. Kantharaj et al. [32] published the latest review paper on thermal parameters in 2019. Based on ten thermal studies at the material level and nine at the full-cell level, they expressed the need to understand the relationship between thermal conductivity and particle size, shape and distribution. In addition, the thermal contact resistance within full-cells has to be further characterized according to Kantharaj et al. [32].

This paper extends the literature review by Shah et al. [27] and Kantharaj et al. [32] by a statistical summary of the measurement results for the specific heat capacity c_p and thermal conductivity k of lithium-ion cells and their components. The review is called meta-analysis because of the statistical procedures, which allows a more objective appraisal to the field [33]. The meta-analysis is limited to present-day lithium-ion cells with a liquid or gel electrolyte. Therefore, all-solid state cells are not considered. Furthermore, the experimental characterization methods are not described in detail, but will be examined in a future publication. This review paper aims to facilitate the parameterization of thermal cell models and to reveal missing measurements for experimental researchers. Accordingly, this review aims to:

- Summarize values for specific heat capacity and thermal conductivity and calculate corresponding uncertainty ranges and medians for thermal models.
- Discuss the dependencies of the thermal parameters on temperature, SOC and SOH.
- Identify knowledge gaps and research needs in the field of thermal parameters.

This review paper deals with the specific heat capacity in Section 2 and the thermal conductivity and thermal contact resistances in Section 3. Corresponding subsections are listed in Table 1. For the specific heat capacity, components inside lithium-ion cells are first analyzed. For this meta-analysis, we differentiate between porous (e.g. coatings), solid non-porous (e.g. current collectors), and fluid (e.g. electrolyte) components. The specific heat capacity of these components is then compared with the results of electrode-separator stacks and full-cells. Section 3 commences with the thermal conductivity of the electrode-separator stack and full-cells, which is described by a value in through-plane and in-plane direction. While the in-plane conductivity is predominately determined by the layer thicknesses of the current collectors [34],

Table 1
Subsections in this review paper with the measurement and evaluation levels of the thermal parameters and the applicability for models with different levels of homogenization. Applicability is assessed for layer-resolved models (LRM [28,35,36]), component-resolved models (CRM [6,37]) with multiple domains for components such as the cell housing or stack, and single-domain models (SDM [38]) with a single volume for the entire cell. For more information on the three thermal models and parameters selection guidelines, see the supplementary material. Note that "conductivity" refers to "thermal conductivity" in this work.

Subsection	Measurement level	Evaluation level	Applicability to models		
			LRM	CRM	SDM
2.1 Heat capacity of porous components and electrolytes	Cell component	Cell component	Y_d	Y_{AC}	Y_{AC}
2.2 Heat capacity of solid non-porous components	Cell component	Cell component	Y_d	Y_{AC}	Y_{AC}
2.3 Heat capacity of electrode-separator stacks	Full-cell, stack	Stack	N	Y_d	Y_{AC}
2.4 Heat capacity of full-cells	Full-cell	Full-cell	N	N	Y_d
3.1 Conductivity of electrode-separator stacks and full-cells	Full-cell, stack	Full-cell, stack	N	Y_d	Y_{AC}
3.2 Conductivity of solid non-porous components	Cell component	Cell component	Y_d	Y_{AC}	Y_{AC}
3.3 Conductivity of porous components	Cell component	Cell component	Y_d	Y_{AC}	Y_{AC}
3.4 Contact resistances	Full-cell, stack	Cell component	Y_d	Y_{AC}	Y_{AC}

Y_d: Can be used directly in the thermal model. Y_{AC}: Additional calculations are required for use in the thermal model. N: Cannot be used in the thermal model.

the through-plane conductivity is influenced by the thermal conductivity of the stack layers and thermal contact resistances between them. Both influencing quantities for the through-plane conductivity are reviewed in the last two subsections.

Table 1 provides further information about the measurement and evaluation level for the thermal experiments and names the thermal model, where parameterization benefits from the respective subsection either through direct (Y_d) application of the parameter or indirectly through a calculation (Y_{ac}). For model definitions and instructions on how to select the thermal parameters for each thermal model, see the supplementary material (https://doi.org/10.1016/j.jpowsour.2021.230829). Each thermal experiment can be divided into a measurement phase and an evaluation phase, with the latter using the measurement results to calculate the desired parameters such as the thermal conductivity. In some subsections, the measurement and evaluation level can be different. Subsection 2.3 can contain, for example, the specific heat capacity of a full-cell measurement, but the evaluation phase of which compensates for components other than the stack. In this case, the result is considered to be the specific heat capacity of the stack and not the full-cell.

2. Specific heat capacity

This section addresses various heat capacity experiments from component to full-cell level, which is illustrated in Fig. 1. Full-cell measurement are needed if the internal cell construction is unknown whereas heat capacities of cell components are a must for thermal cell design studies [39]. In addition, layer-resolved thermal models [36,40,41] require the specific heat capacity at the component level, while lumped-capacitance or single-domain models are more conveniently parameterized with averaged capacities from full-cell measurements [42]. Therefore, heat capacity measurements at both full-cell and component level are useful in battery research.

Calorimetric methods are mostly used to measure the specific heat capacity, which in principle measure the heat flow to the test object and the subsequent temperature increase. The most frequently used type of calorimeter is the differential scanning calorimeter with a measurement uncertainty between 1.5% and 10% [43]. Measurements that are more precise can be achieved with adiabatic calorimeters, which offer an uncertainty of 0.05%–2% [43]. Besides the calorimetric equilibrium methods, transient measuring regimes such as the hot disc method can be used to measure the specific heat capacity [44]. The advantage of transient methods is that more than one thermal parameter can be measured [44]. In the field of lithium-ion cells, thermal impedance spectroscopy is a prominent transient method for measuring the specific heat capacity [45–48].

Lithium-ion cells contain porous components with a porosity ε. These include the cathode and anode coatings and the separator, as shown on the left-hand side of Fig. 1. The specific heat capacity of such porous materials c_{por} can be calculated with Equation (3) [13]. c_{por} depends on the specific heat capacity of the fluid c_{fluid} and solid phase c_{solid}, which are weighted by their mass fraction. Therefore, the volume fraction ε has to be multiplied with the density of the fluid ρ_{fluid} and solid phase ρ_{solid}. The bulk density ρ_{bulk} of the porous material is calculated with Equation (4).

$$c_{por} = \frac{c_{fluid}\rho_{fluid}\varepsilon + c_{solid}\rho_{solid}(1-\varepsilon)}{\rho_{bulk}} \tag{3}$$

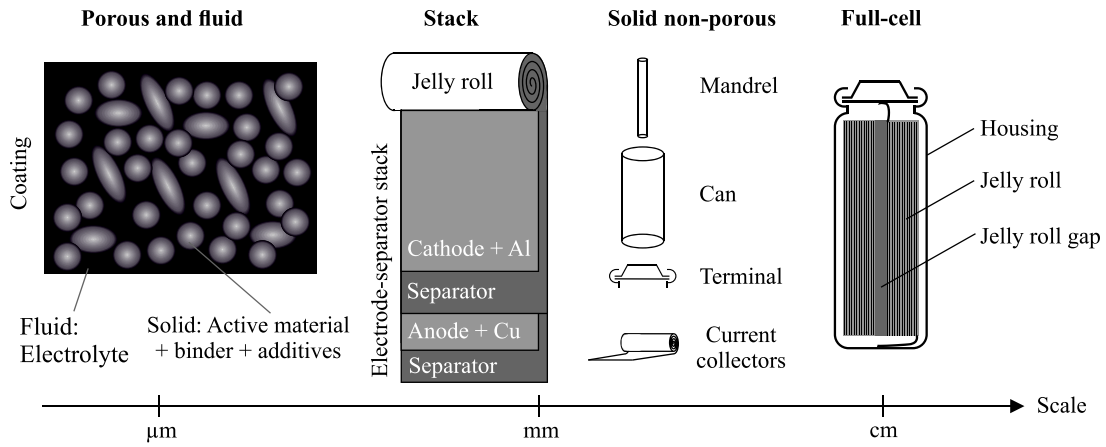

Fig. 1. Schematic of different scales for the specific heat capacity demonstrated for the cylindrical cell format.

$$\rho_{bulk} = \rho_{fluid}\varepsilon + \rho_{solid}(1-\varepsilon) \tag{4}$$

It should be emphasized that the solid phase of the anode, the cathode, and the separator is also a composite. According to Equations (5) and (6), the weight fractions $m_{scm,i}/\sum_i m_{scm,i}$, densities $\rho_{scm,i}$, and specific heat capacities $c_{scm,i}$ of solid composite materials can influence c_{solid} and ρ_{solid}. Anode and cathode coatings in lithium-ion cells typically consist of solid active particles, polymer binders and additives [49,50]. The solid phase of separators usually consists of microporous polymer membranes, non-woven fabric mats or inorganic composites [51]. These three separator categories can contain solid materials such as polyethylene terephthalate (PET), polypropylene (PP), polyethylene (PE), polyamide (PA), polyvinylchloride (PVC), polyester (PU), Al_2O_3, and SiO_2 [51–53].

$$c_{solid} = \sum_i \left(\frac{m_{scm,i}}{\sum_i m_{scm,i}} c_{scm,i} \right) \tag{5}$$

$$\rho_{solid} = \frac{\sum_i m_{scm,i}}{\sum_i \left(m_{scm,i}/\rho_{scm,i} \right)} \tag{6}$$

The stack level in Fig. 1 encompasses porous coatings, porous separator sheets, and non-porous current collector foils. These stack layers build the electrode-separator stack, which is wound to form the so-called jelly roll in case of cylindrical cell formats. The effective heat capacity of the electrode-separator stack c_{stack} is defined by Equation (7) [54], which is independent of the geometry. Instead, the mass of the dry anode and cathode coatings (m_{ano}, m_{cat}), the mass of the anode and cathode current collectors (m_{anoCC}, m_{catCC}), and the mass of the dry separator m_{sep} compared to the total mass of the stack m_{stack} determines the weighting of the heat capacities. The specific heat capacity of the separator c_{sep}, anode coating c_{ano} and cathode coating c_{cat} are dry porous heat capacities c_{por} in the sense of Equation (3). Whereas the heat capacity of the anode c_{anoCC} and cathode c_{catCC} current collector in Equation (7) are solid non-porous heat capacities. It should be noted that all of the masses in Equation (7) must include passive components such as the excess of the separator or the overhang of the anode electrode. For example, the area of the anode can exceed the area of the cathode by 9%, which reduces the risk of lithium plating on the edges of the electrode [55].

Besides the current collectors, full-cells contain further solid non-porous components in the cell housing such as the can and the terminal. Especially for cylindrical cells, the positive terminal can contain

Table 2
Measured specific heat capacity of porous electrode coatings and separators c_{por}, and electrolytes c_{fluid} applied in electrode-separator stacks of lithium-ion cells. All electrode coatings contain active material, binder and conductive additives. If there is electrolyte in the pore, the measurement is declared wet. Dry measurements contain inert gas inside the pores, which equates c_{por} with c_{solid}. No information provided is marked with (–).

No.	Ref.	Stack layer	Dry/wet	ρ_{solid} / g cm^{-3}	ρ_{bulk} / g cm^{-3}	ε / %	T / K	c_p / J kg^{-1}K^{-1}	$\alpha_{c_p,T}$[a] / K^{-1}
1	[13]	Graphite[b]	Dry	2.31	–	46	283 ± 50	710 ± 151	+0.4
2	[13]	Graphite[b]	Dry	2.31	–	47	283 ± 50	715 ± 149	+0.4
3	[13]	Graphite[b]	Dry	2.44	–	53	283 ± 50	696 ± 154	+0.4
4	[13]	Graphite[b]	Dry	2.15	–	51	283 ± 50	718 ± 139	+0.4
5	[13]	Graphite[b]	Dry	2.01	–	66	283 ± 50	720 ± 147	+0.4
6	[13]	Graphite[b]	Dry	2.46	–	43	283 ± 50	729 ± 149	+0.4
7	[59]	Graphite	Dry	–	1.621	–	323 ± 30	1134	0.0
8	[54]	Graphite	Wet	–	1.35	–	–	1437	–
9	[58]	Graphite[b]	Wet	–	–	31	326 ± 28	1097 ± 178	+0.8
10	[60]	Graphite[b]	Wet	–	2.5	–	–	700	–
11	[13]	Separator[b,d]	Dry	–	–	–	283 ± 50	1786 ± 436	+0.5
12	[13]	Separator[b,d]	Dry	–	–	–	283 ± 50	1614 ± 345	+0.4
13	[13]	Separator[b,d]	Dry	–	–	–	283 ± 50	1581 ± 337	+0.4
14	[13]	Separator[b,d]	Dry	–	–	–	283 ± 50	1234 ± 239	+0.4
15	[13]	Separator[b,d]	Dry	–	–	–	283 ± 50	1583 ± 367	+0.4
16	[13]	Separator[b,d]	Dry	–	–	–	283 ± 50	1600 ± 381	+0.5
17	[13]	Separator[e]	Dry	–	–	–	283 ± 50	1583 ± 340	+0.4
18	[13]	Separator[e]	Dry	–	–	–	283 ± 50	1683 ± 340	+0.4
19	[13]	Separator[f]	Dry	–	–	–	283 ± 50	1556 ± 354	+0.5
20	[59]	Separator	Dry	–	0.586	–	323 ± 30	3250	0.0
21	[61]	Separator[b]	Dry	–	0.91	–	311 ± 13	2475 ± 5	0.0
22	[54]	Separator	Wet	–	1.01	–	–	1978	–
23	[58]	Separator[b]	Wet	–	–	40	326 ± 28	1689 ± 141	+0.3
24	[60]	Separator[b]	Wet	–	1.2	–	–	700	–
25	[13]	LCO[b]	Dry	4.81	–	31	283 ± 50	697 ± 98	+0.3
26	[13]	LCO[b]	Dry	4.48	–	29	283 ± 50	707 ± 98	+0.3
27	[57]	LCO[c]	Dry	4.54	2.35	46 ± 3	423 ± 150	830 ± 156	+0.1
28	[62]	LCO/LMO	Dry	4.72	2.34	48	436 ± 138	862 ± 119	+0.1
29	[54]	LCO	Wet	–	2.33	–	–	1269	–
30	[13]	NMC[b]	Dry	3.88	–	37	283 ± 50	767 ± 95	+0.2
31	[13]	NMC[b]	Dry	3.93	–	22	283 ± 50	761 ± 89	+0.2
32	[13]	NMC[b]	Dry	4.24	–	36	283 ± 50	764 ± 94	+0.2
33	[57]	NMC[c]	Dry	4.32	2.45	42 ± 4	423 ± 150	898 ± 144	+0.1
34	[59]	NMC	Dry	–	2.580	–	323 ± 30	1068	0.0
35	[58]	NMC[b]	Wet	–	–	29	326 ± 28	952 ± 39	+0.2
36	[13]	LCO/NCA[b]	Dry	3.93	–	23	283 ± 50	737 ± 99	+0.3
37	[63]	LFP[c]	Dry	1.65	–	–	290 ± 100	735 ± 181	+0.2
38	[62]	LCO/LMO[c]	Dry	3.96	1.73	58	436 ± 138	904 ± 92	+0.1
39	[60]	LMO[b]	Wet	–	1.5	–	–	700	–
40	[13]	Electrolyte[g]	–	–	1.28	–	293 ± 40	1639 ± 58	+0.1
41	[13]	Electrolyte[h]	–	–	1.24	–	283 ± 50	1630 ± 74	+0.1
42	[54]	Electrolyte	–	–	1.130	–	–	2055	–
43	[59]	Electrolyte[g]	–	–	1.280	–	323 ± 30	229	0.0

a) The temperature dependency $\alpha_{c_p,T}$ is determined by dividing the slope of the linear regression $\partial c_p/\partial T$ by the heat capacity at 300 K. b) Extracted from a commercially available lithium-ion cell. c) Weight fraction of the active material greater than or equal to 90%. d) Contains PP. e) Manufactured by Celgard. f) Manufactured by Toray. g) LP30 from BASF. h) LP50 from BASF.

various subcomponents such as the current interrupt device (CID) [56]. Furthermore, some cylindrical cells contain a mandrel inside the jelly roll gap, which is used during the winding process. The specific heat capacity of the solid components outside the electrode stack c_n and their mass m_n introduce a difference between the heat capacity of the full-cell c_{cell} (Equation (8)) and c_{stack}.

$$c_{stack} = \frac{m_{ano}c_{ano} + m_{cat}c_{cat} + m_{sep}c_{sep} + m_{aCC}c_{aCC} + m_{cCC}c_{cCC} + m_{ele}c_{ele}}{m_{ano} + m_{cat} + m_{sep} + m_{aCC} + m_{cCC} + m_{ele}} \quad (7)$$

$$c_{cell} = \frac{m_{stack}c_{stack} + \sum_n (c_n m_n)}{m_{stack} + \sum_n (m_n)} \quad (8)$$

The specific heat capacities covered by Equations (3)–(8) are reviewed in the following subsections. Values for c_{solid} and c_{fluid} from Equation (3) are analyzed in subsection 2.1, which determines c_{ano}, c_{cat} and c_{sep}. Heat capacities for the current collectors (c_{aCC}, c_{cCC}) can be found in subsection 2.2. Subsections 2.3 and 2.4 cover direct measurements of c_{stack} and c_{cell}, respectively.

2.1. Heat capacity of porous components and electrolytes

Table 2 lists experimental results for porous c_{por} and fluid c_{fluid} materials used in lithium-ion cells and differentiates between whether the pores contain electrolyte (wet) or inert gas (dry). The mass fraction of the fluid phase $\rho_{fluid}\varepsilon/\rho_{bulk}$ becomes negligible compared to the solid phase if inert gas such as argon fills the pores. Therefore, dry c_{por} can be equated with c_{solid} in Equation (3). Most dry test samples in Table 2 were extracted from commercial electrodes and washed and dried afterwards to remove any remainders of the electrolyte [13]. If the test sample was measured right after the dissection or additional electrolyte was added before the measurement, the experiment is labeled wet. Table 2 further contains information on ρ_{solid}, ρ_{bulk}, and ε, which characterizes the composition and morphology.

If a reference contains more than one measurement point for c_p, Table 2 lists the mid-range, which is the arithmetic mean of minimum and maximum. Changes in c_p can arise from many sources such as measurement uncertainty or variations in battery states such as SOC, SOH or temperature T. If the reference varies the temperature, this variation is

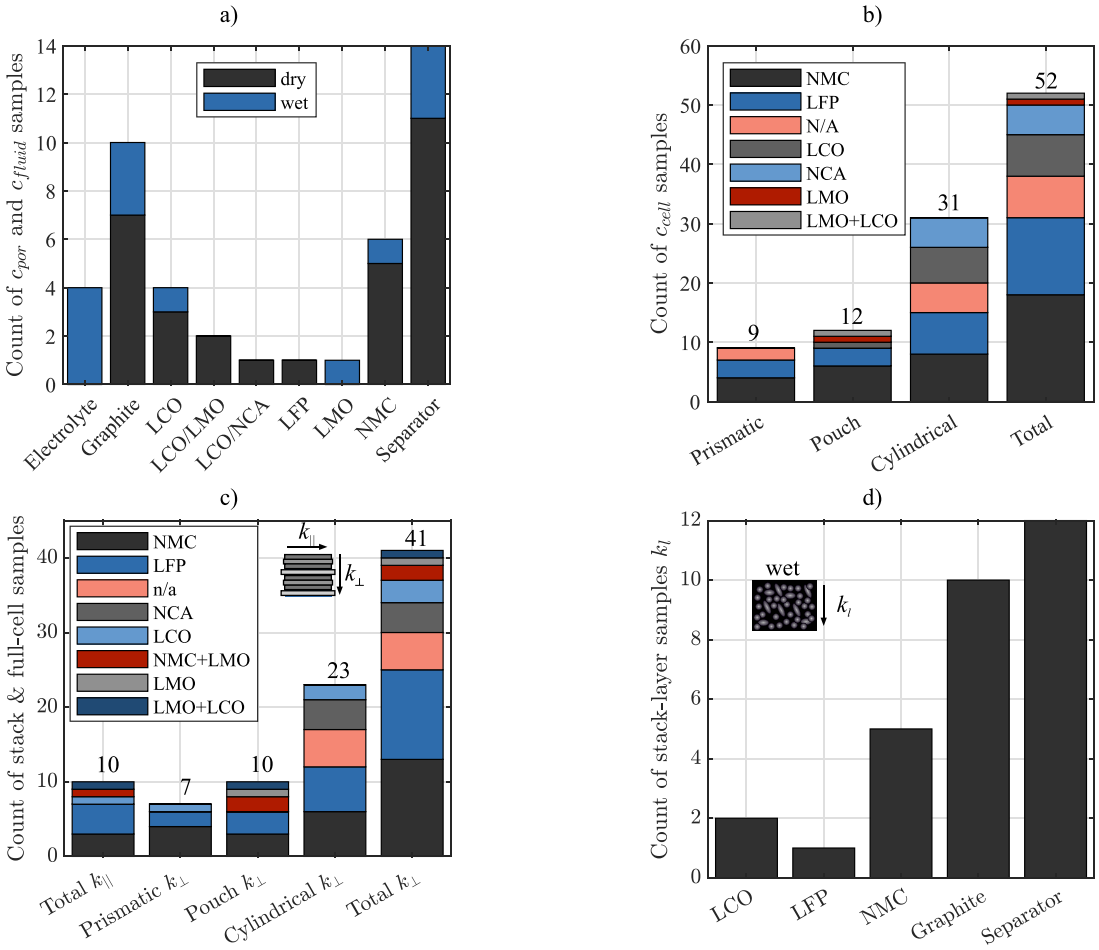

Fig. 2. Number of test samples that were subjected to specific heat capacity and thermal conductivity experiments in the field of lithium-ion cells. a) Porous components c_{por} and the electrolyte c_{fluid} used for the electrode-separator stack, which are listed in Table 2. The legend differentiates between test samples with an electrolyte inside the pores (wet) and dry test samples. b) Full-cell test samples c_{cell} filtered by the cell format and cathode chemistry from Table 6. c) Number for full-cell or stack samples in the in-plane $k_\parallel$ (Table 8) or through-plane $k_\perp$ (Table 9) directions of the electrode-separator stack. Each bar shows the count of the cathode chemistry used for the test sample. d) Number of wet stack layer samples k_l, which are listed in Table 11.

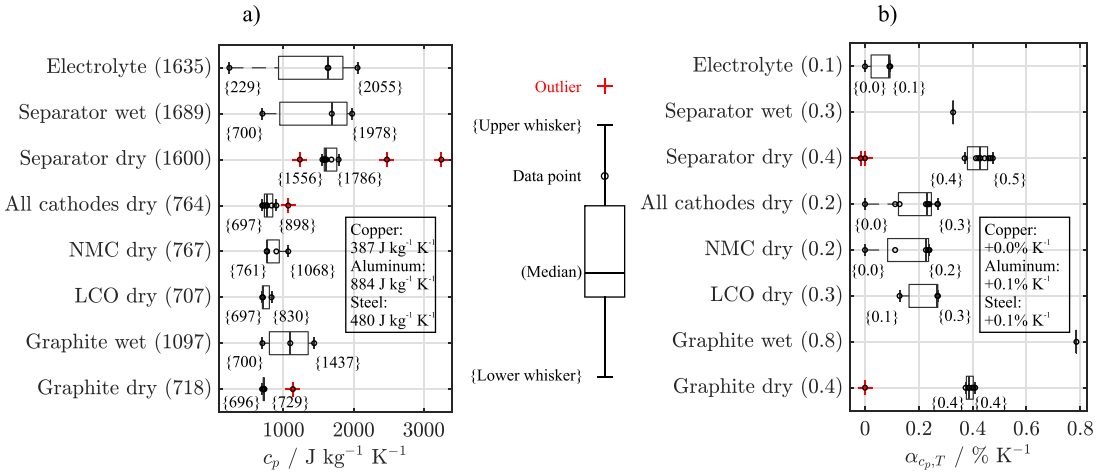

Fig. 3. Specific heat capacity of components used in lithium-ion cells, with recommended values for thermal modeling in round brackets (median). a) Boxplot for c_{por} (wet), c_{solid} (dry) and c_{fluid} (electrolyte), which are listed in Table 2. Specific heat capacities of selected non-porous components from Table 3 are given in the square box. b) Boxplot of the linear temperature dependence of the specific heat capacity $\alpha_{c_p,T}$ from Table 2. SOC and SOH dependency is not include due to the small data quantity.

also stated in Table 2 [54] by the mid-range and the deviation to the extrema. Furthermore, in case of varying temperature the temperature dependency $\alpha_{c_p,T}$ is fitted with a linear function: $p_1(T - 300\ \mathrm{K}) + p_2$. The temperature dependency is then defined by dividing the slope $p_1 = dc_p/dT$ with the heat capacity at 300 K ($p_2 = c_p(300\mathrm{K})$). As the SOH has not been mentioned by any reference and the SOC is only mentioned by Gotcu et al. [57], Loges et al. [13], and Liebig et al. [58], both states are not included in the header of Table 2.

The bar chart in Fig. 2 a) gives an overview of the 43 test samples in Table 2. Furthermore, the chart differentiates between wet and dry measurements. According to Fig. 2 a), every common cathode chemistry of lithium-ion cells is contained in Table 2 except for lithium-nickel-cobalt-aluminum-oxide (NCA). Note that LCO/NCA is a blended cathode. Uncertainties in the heat capacity can be estimated for electrolyte, graphite (G), lithium-cobalt-oxide (LCO), lithium-nickel-manganese-cobalt-oxide (NMC) and separators because more than one test sample was measured. However, this uncertainty estimate is not possible for the frequently used cathode material LFP or LMO because only one test sample was measured. On the anode side, no experiments have been conducted for lithium-titanate-oxide (LTO) and silicon-graphite coatings [13]. Note that the coating includes the active material, binder and additives and not the current collector. The amount of data for graphite, LCO, NMC and the separator material allows comparisons between dry and wet measurements, with which the validity of Equation (3) can be checked. For this reason, the porosity ε of the material is listed in Table 2.

Fig. 3 a) shows the boxplot of selected specific heat capacities with more than one entry in Table 2. In this review paper, the median is considered the recommended value for the thermal parameters, as it is the better choice in the case of skewed data or data with outliers [64]. First, the electrolyte is analyzed as the only non-porous material in Fig. 3 a) with a median heat capacity of 1635 J kg^{-1} K^{-1}. This median heat capacity can be explained by common electrolyte constitutes such as ethylene carbonate (EC, 1521 J kg^{-1} K^{-1} [65]) or dimethyl carbonate (DMC, 1855 J kg^{-1} K^{-1} [66]). As with solid composite materials, the specific heat capacity of liquid mixtures can be calculated using the weighted average in Equation (3) [67]. For example, the electrolyte LP30 (Table 2, No. 40) contains the carbonates EC and DMC [13] in equal weight fractions, which results in an average heat capacity of 1688 J kg^{-1} K^{-1} using Equation (3). This represents a slight deviation from the measured median of 3%.

The boxplot in Fig. 3 a) shows a lower and upper whisker of 229 and 2055 J kg^{-1} K^{-1} for the electrolyte, which constitute a deviation of ±80% from the mid-range. Especially the lower whisker (LP30, Table 2, No. 43) has to be treated with caution, due to its low capacity compared to the electrolyte constitutes. Therefore, more electrolyte experiments are required to identify outliers and narrow the range for the heat capacity. In addition, the influence of the $LiPF_6$ salt on the heat capacity of the electrolyte c_{fluid} has not yet been investigated. As the mass fraction of $LiPF_6$ in common electrolytes lies around 10% (LP30 11.5 wt% [68]), a significant impact on c_{fluid} cannot be neglected.

The boxplot in Fig. 3 a) shows a median heat capacity of 1600 J kg^{-1} K^{-1} for dry separator sheets. This median agrees well with common raw materials of separators [52] such as PET (1172 J kg^{-1} K^{-1} [69]), PE (1549 J kg^{-1} K^{-1} [70]), and PP (1634 J kg^{-1} K^{-1} [70]). According to the boxplot, No. 14 in Table 2 can be treated as an outlier, since the value of 1234 J kg^{-1} K^{-1} is below the lower whisker but a high weight fraction of PET could explain this result. On the upper side, No. 20 and 21 exceeds the upper whisker. In particular, the maximum of 3250 J kg^{-1} K^{-1} measured for a polyolefin separator does not correspond to the specific heat capacity of conventional polymers at 300 K [71]. In addition, inorganic separator materials such as Al_2O_3 or SiO_2 with a specific heat capacity of 866 and 746 J kg^{-1} K^{-1} [67] cannot serve as an explanation for the upper outlier. After the outliers have been identified, a value range for dry separators between 1556 and 1786 J kg^{-1} K^{-1} can be derived from the lower and upper whiskers of the boxplot. The corresponding mid-range of 1671 J kg^{-1}K^{-1} describes the specific heat capacity of dry separators with an uncertainty of ±7%.

The cathode coatings NMC and LCO show similar heat capacities with a median of 767 and 707 J kg^{-1} K^{-1}, respectively. Because of this slight deviation, there is no need to differentiate between the two cathode coatings according to Loges et al. [13]. This statement also seems to apply to LFP coatings with a specific heat capacity of 735 J kg^{-1} K^{-1} (Table 2, No. 37). For LFP and LMO, however, further measurements are required to clarify the question of whether differences in the heat capacity of lithium-ion cells can be explained by the cathode material. All of the dry cathode coatings in Table 2 have a median heat capacity near NMC of 764 J kg^{-1}K^{-1}. Taking into account the lower and upper whiskers, the mid-range heat capacity for all cathodes contains an uncertainty of ±13%.

The median for dry graphite coatings is 718 J kg^{-1} K^{-1} in Fig. 3 a), which contains the measurement results of seven test samples. Although these coatings contain polyvinylidene fluoride (PVDF) binder (1114 J kg^{-1} K^{-1} [72]) and carbon black (650 J kg^{-1} K^{-1} [72]), the median of 718 J kg^{-1} K^{-1} is close to pure graphite with a specific heat capacity of 706.9 J kg^{-1} K^{-1} [73]. The increase compared to pure graphite depends on the weight fraction of the binder. For example, a weight fraction of the PVDF binder of 5% [6] would increase the heat capacity of the graphite coating to 727 J kg^{-1} K^{-1}. Given the composition of graphite coatings in lithium-ion cells, the heat capacity of 1134 J kg^{-1} K^{-1} (Table 2, No. 7) is most likely an outlier, which is supported by the boxplot calculations. The mid-range capacity of dry graphite exhibits a minor uncertainty of ±2% compared to other materials in Fig. 3 a). The comparable lower uncertainty can be explained by the instance that all measurements contained in the median of 718 J kg^{-1} K^{-1} are conducted by Loges et al. [13]. Therefore, the ±2% range does not cover any other sources of uncertainty (e.g. measurement technique), which requires additional measurements in this field.

Using Equations (3) and (4) and the parameters in Table 2 to calculate c_{por} of wet coatings or separators can cause an uncertainty of up to 4%. This can be demonstrated by the experiments of Liebig et al. [58], because they indicated the porosity of the wet separator and the graphite coating (Table 2, No. 9, 23). For the demonstration, the median in Fig. 3 a) of dry graphite (c_{solid}) and the median of the electrolyte (c_{fluid}), a solid and fluid density of 2.31 and 1.28 g cm^{-3} (Table 2, No. 1, 40), and a porosity of 31% are used. These values result in a heat capacity of the wet graphite coating of 901 J kg^{-1} K^{-1}, which deviates by 2% from the measured capacity at 300 K (Table 2, No. 9). For the separator, a solid density of PP (0.89 g cm^{-3} [71]) is assumed, since the heat capacity of PP comes closest to the median of the separators in Fig. 3 a). With a porosity of 40%, the heat capacity of the wet separator is calculated according to Equation (3) as 1617 J kg^{-1} K^{-1}. This result for c_{por} corresponds to the measurement at 300 K with an uncertainty of 4% (Table 2, No. 23). Therefore, Equations (3) and (4) and Table 2 can be used as a powerful tool for determining the heat capacity of porous components of lithium-ion cells, if the researcher knows the porosity.

In general, the specific heat capacity at constant pressure c_p depends on the specific heat capacity at constant volume, the thermal expansion, the molar volume and the compressibility of the material - all variables with a temperature dependence [74]. The heat capacity at constant volume can be determined with quantum-mechanical calculations. For example, taking into account the vibrations of atoms, Einstein formulated an equation for the capacity at constant volume, which depends on the temperature [75]. Often no measurement data for the entire temperature range are given for compressibility [74], which makes solid-state physical calculations of the temperature dependency of c_p more difficult. Therefore, measured temperature dependencies for c_p are discussed without physical calculations in this review paper.

Fig. 3 b) shows the boxplot for the temperature dependency $\alpha_{c_p,T}$ listed in Table 2. As in Fig. 3 a), the ordinate of the box plot in Fig. 3 b) indicates the median of the temperature dependence in round brackets. According to the boxplot, the temperature dependency is positive for each material, with the lowest median being determined for the electrolyte (0.1% K^{-1}) and the highest for the wet graphite coating (0.8% K^{-1}). The boxplot in Fig. 3 b) contains only a single wet test sample for the separator and graphite, since Liebig et al. [58] is the only study that measured wet heat capacities at different temperatures. Therefore, the identification of outliers and the assessment of uncertainties for both materials is not possible. Nevertheless, the plausibility can be verified by comparing wet and dry temperature dependencies. According to Equation (3) and assuming a linear dependency, $\alpha_{c_p,T}$ for wet materials has to lie between the electrolyte and the corresponding dry material. This is the case for the wet separator in Fig. 3 b) but not for the wet graphite (Table 2, No. 9), which exceeds the temperature dependency of the dry coating by 0.4% K^{-1}. Therefore, further measurements are needed to clarify this discrepancy.

According to Fig. 3 b), dry separator material has a temperature dependency of 0.4 K^{-1}, which corresponds well to PP material. The heat capacity of PP increases from 1570 to 1920 J kg^{-1} K^{-1} for a temperature increase from 273 to 323 K [67]. This change in heat capacity divided by the heat capacity at 300 K of 1622 J kg^{-1} K^{-1} [71] gives a consistent temperature dependence of 0.4 K^{-1}. The consistency supports the suggestion of outliers in Fig. 3 b) for temperature dependencies around 0.0% K^{-1}. On the cathode side, LCO and NMC coatings show similar temperature dependencies of 0.2% K^{-1}, which also correspond to LFP and LMO (Table 2 No. 37, 38). In contrast, graphite coatings show a higher temperature dependency of 0.4 K^{-1} with one outlier that found no dependence (Table 2, No. 7). As with separators, the temperature dependence of dry graphite coatings corresponds very well to that of pure graphite of 0.4% K^{-1} [73].

Most of the investigations in Table 2 neither mention the SOC after the electrodes have been extracted from a full-cell nor the electrode lithiation degree in the case of in-house electrode manufacture. Exceptions are the test series of Loges et al. [13], Liebig et al. [58], and Gotcu et al. [57]. Most of the results of Loges et al. [13] and Liebig et al. [58] were conducted at a full-cell SOC of 0%, while Gotcu et al. [57] used an electrode lithiation degree of 100%. In addition, Loges et al. [13] varied the full-cell SOC between 0% and 100% of a commercial graphite and LCO/NCA coating. According to their results, the specific heat capacity of the dry graphite coating increases with increasing full-cell SOC by 19%. In contrast, the LCO/NCA cathode coating decreased by 7% when the full-cell SOC was changed from 0% to 100%. As a result, the specific heat capacity of the electrode-separator stack can rise or fall, which is discussed in Subsection 2.3. Loges et al. [13] did not provide any physical explanations for the SOC dependence, but the Kopp-Neumann law [75] could explain their observation. This law says that the effective heat capacity of a compound depends on its atomic mass fraction and the heat capacity of the components. Since lithium (3582 J kg^{-1} K^{-1} [76]) has a higher specific heat capacity than all intercalation hosts used in lithium-ion cells, the heat capacity of the active material must increase with the degree of lithiation. Nevertheless, there should be no connection between the heat

Table 3
Measured specific heat capacity of solid components outside the electrode-separators stack c_n and the current collectors (c_{aCC}, c_{cCC}). No information provided is marked with (–).

Material	$\frac{\rho}{\text{g cm}^{-3}}$	$\frac{T}{\text{K}}$	$\frac{c_p}{\text{J kg}^{-1}\text{ K}^{-1}}$	$\frac{\alpha_{c_p,T}{}^{g)}}{\text{K}^{-1}}$
Copper[a)]	8.96 [76]	316 ± 18 [82]	387 ± 2 [82]	+0.0
Aluminum[b)]	2.70 [76]	293 ± 40 [83]	884 ± 27 [83]	+0.1
Aluminum alloy 3003[c)]	2.73 [84]	–	893 [84]	–
Pouch foil[d)]	–	283 ± 50 [13]	1191 ± 208 [13]	+0.3
PP[e)]	0.95 [70]	300 ± 30 [70]	1634 ± 188 [70]	+0.4
PET[e)]	1.35 ± 0.05 [71]	300 ± 30 [69]	1172 ± 112 [69]	+0.3
PE[e)]	1.00 [70]	300 ± 30 [70]	1549 ± 130 [70]	+0.3
Stainless steel AISI 304[f)]	7.90 [85]	300 ± 30 [86]	480 ± 12 [86]	+0.1

a) Anode current collector, Negative cell terminal. b) Cathode current collector, Anode current collector (LTO) [87], Positive cell terminal. c) Prismatic cell housing [34,77,78], Cylindrical housing [45]. d) Aluminum polymer composite [13]. e) Pouch foil layer. f) Cylindrical housing [79,88], Prismatic cell housing [50], Cylindrical mandrel/center pin [80]. g) The temperature dependency $\alpha_{c_p,T}$ is determined by dividing the slope of the linear regression $\partial c_p/\partial T$ by the heat capacity at 300 K.

capacity and the SOC in full-cells, since the lithium content is retained for this control volume. Finally, it should be mentioned that the investigations in Table 2 do not reveal any details or variations in the SOH.

2.2. Heat capacity of solid non-porous components

A working lithium-ion cell not only contains porous and fluid components introduced in the previous subsection, but also solid non-porous components. To complete the electrode-separator stack in Fig. 1, for example, the non-porous current collectors for the anode and cathode are necessary, which are usually made of copper and aluminum [13,77]. Furthermore, in order to determine the heat capacity of a complete lithium-ion cell, other non-porous components such as the cell housing must be taken into account. In the case of pouch cells, the cell housing consists of the pouch foil, a composite of aluminum, polyamide and polyethylene (PE) [13]. Prismatic cell housings are usually made of aluminum alloys [77,78] or stainless steel [50]. Pouch and prismatic cell formats also have external current collectors made of copper and aluminum [36,38]. This is not the case for cylindrical cells where the housing acts as the negative or positive current collector. Usually stainless steel is applied for the housing of cylindrical cells [79] and the terminal of the top cap. Besides the housing and the external terminals, lithium-ion cells can contain other components such as the CID [56], electrical insulation layers [78] or mandrels inside the jelly roll [80]. All consist of the materials listed in Table 3 with their specific heat capacity, which are important parameters in order to determine the total specific heat capacity of a lithium-ion cell.

Pure copper has the lowest specific heat capacity in Table 3 of 387 J kg^{-1} K^{-1}. Furthermore, the temperature dependency $\alpha_{c_p,T}$ is negligible. In contrast, pure aluminum exhibits a small positive temperature dependency. Furthermore, the specific heat capacity of 884J kg^{-1} K^{-1} is approximately twice the magnitude of copper. Both heat capacities are well predictable by the Dulong–Petit law [81], which states that the molar heat capacity of solid elements c_m is equal to three times the universal gas constant ($c_m = 3{\cdot}8.314$ J mol^{-1} K^{-1}). Three times the gas constant divided by the molar masses of copper (63.5 g mol^{-1} [76]) and aluminum (27.0 g mol^{-1} [76]) gives a specific heat capacity of 393 and 923 J kg^{-1} K^{-1}, respectively. Both predictions of the Dulong–Petit law show a deviation of 2% and 4% from the mid-range heat capacity in Table 3.

According to Table 3, pure aluminum and aluminum alloys have a similar heat capacity. For example, a frequently used aluminum alloy for prismatic housings is EN AW-3003 [34,78] that contains 1.5% Mn, 0.6% Si, and 0.7% Fe [89]. The heat capacity of pure aluminum and the alloy 3003 differs in Table 3 by only 1%. Because of this small difference, the established assumption [40] of pure aluminum for prismatic cell housings appears appropriate for thermal cell models. For pure aluminum, $\alpha_{c_p,T}$ shows a positive correlation between the temperature and c_p. No experiments that vary the temperature were found for the alloy 3003.

With regard to the heat capacity, polymers and aluminum equally influence pouch foils of lithium-ion cells. The pouch foil exhibits a specific heat capacity of 1191 J kg^{-1} K^{-1}. This corresponds to a deviation of 35% compared to pure aluminum and 27% compared to the polymer PP in Table 3. However, pouch foils can also contain polymers other than PP. For example, the pouch foil AvALL158 (Avocet Steel Strip Ltd) suitable for electric vehicles with a total thickness of 158 µm contains PET (12 µm), adhesive (9 µm), polyamide PA (25 µm), aluminum (40 µm), and PP (70 µm). Similar ratios between the thickness of the polymer layer and the total thickness for the pouch foil were stated by Rheinfeld et al. [21] (72%) and Zhang et al. [90] (62%). Consequently, depending on the layer thickness and the polymers used in Table 3, the heat capacity of pouch foils can be between 884 and 1643 J kg^{-1} K^{-1}. Because of this large range of 759 J kg^{-1} K^{-1}, thermal models must take into account the exact construction of the pouch foil.

2.3. Heat capacity of electrode-separator stacks

Subsection 2.1 and 2.2 covered porous coatings, separator sheets and current collectors used in lithium-ion cells. These components form the electrode-separator stack, as shown in Fig. 1. This subsection gives an overview of experiments measuring the specific heat capacity of the entire stack c_{stack} and compares the results with the two previous subsections. According to Equation (7), c_{stack} depends heavily on the mass fractions of the stack components, which are listed in Table 4 for some lithium-ion cells based on the total cell mass m_{cell}.

Regardless of the cell format in Table 4, the cathode coating has the largest mass fraction of the electrode-separator stack and therefore the greatest influence on c_{stack}. This is due to the high density of the cathode coatings, which is about twice that of graphite (see Table 2). The separator has the smallest mass fraction and therefore less influence on c_{stack}. Table 4 also contains the mass fraction of cell components outside the electrode-separator stack $(\sum m_n)/m_{cell}$, whose impact on c_{cell} will be discussed in the next subsection.

Due to the high mass fraction of the stack m_{stack}/m_{cell}, the heat capacity of the stack c_{stack} has a significant influence on the heat capacity of the full-cell c_{cell}. In the case of pouch cells, for example, the mass fraction is between 94% and 96% in Table 4, while cylindrical cells have a fraction between 73% and 86%. Despite the importance of c_{stack}, less measurement data is available in the literature. c_{stack} can be measured either at the stack level [13] or at the full-cell level, while the full-cell level requires compensation for the non-stack components [45,47]. Table 5 lists the results of both approaches with the nominal capacity of the full-cell Q_{cell}, the active materials of the stack, the SOC and the temperature T during the experiment, the specific heat capacity c_{stack} and the temperature dependency $\alpha_{c_p,T}$.

With the exception of NCA, all common cathode materials are represented in Table 5. Most references state the SOC, but only Cheng et al. [96] performed heat capacity measurements at different SOCs. In contrast to the temperature T, with a median of the mid-ranges of 303 K, no reference states the SOH. The results of Barsoukov et al. [47] in Table 5 seem to overestimate c_{stack} as all other investigations measure significant lower heat capacities. In addition, some results (Table 5, No. 2, 3, 5) even exceed the heat capacity of common electrolytes c_{ele}, which

Table 4
Mass fractions of components within the electrode-separator stack and cell components outside the stack used in Equations (3) and (4) to calculate c_{stack} and c_{cell}. No information provided is marked with (–).

Ref.	$\frac{Q_{cell}}{Ah}$	$\frac{m_{cell}}{g}$	Format	Active material	$\frac{m_{cat}}{m_{cell}}$	$\frac{m_{ano}}{m_{cell}}$	$\frac{m_{ele}}{m_{cell}}$	$\frac{m_{aCC}}{m_{cell}}$	$\frac{m_{cCC}}{m_{cell}}$	$\frac{m_{sep}}{m_{cell}}$	$\frac{\sum m_n}{m_{cell}}$
[91]	2.6	44.3	Cylindr.	LCO/NMC-G	41%	18%	10%	7%	4%	3%	17%
[91]	1.5	43.1	Cylindr.	NMC-G	26%	15%	10%	17%	7%	3%	22%
[91]	1.1	39.0	Cylindr.	LFP-G	25%	13%	16%	10%	6%	3%	27%
[92]	3.35	45.4	Cylindr.	NCA-G	39%	26%	10%	6%	3%	2%	13%
[88]	7.5	320.0	Cylindr.[a)]	NCA-G	–	–	15%	–	–	5%	48%
[93]	41	865.0	Pouch[b)]	NMC/LMO-G	38%	25%	14%	10%	6%	4%	4%
[94]	–	791.0	Pouch	LCO/NCA-G	43%	21%	14%	9%	7%	2%	3%
[95]	3.8	88.2	Pouch	NMC-G	31%	17%	7%	24%	10%	7%	4%
[78]	8	328	Prismatic	LFP-G	–	–	15%	–	–	11%	16%

a) High-power type. b) High-energy type.

Table 5
Measured specific heat capacity of electrode-separators stacks c_{stack} in lithium-ion cells. Every stack consists of two anode coatings, two cathode coatings, two separator sheets and one current collector for each electrode. Each porous layer of the stack is soaked (wet) with electrolyte. No information provided is marked with (−).

No.	Ref.	$\frac{Q_{cell}}{\text{Ah}}$	$\frac{m_{cell}}{\text{g}}$	Active material	$\frac{\varepsilon_{ano}}{\%}$	$\frac{d_{ano}}{d_{aCC}}$	$\frac{\text{SOC}}{\%}$	$\frac{T}{\text{K}}$	$\frac{c_{stack}}{\text{J kg}^{-1}\text{K}^{-1}}$	$\frac{\alpha_{c_p,T}{}^{a)}}{\text{K}^{-1}}$
1	[45]	4.4	194	LFP-G[c)]	–	–	50	303	958	–
2	[47]	1.8	42.7	–	–	–	100	296	1800	–
3	[47]	1.5	39.5	–	–	–	100	296	1900	–
4	[47]	1.3	41.6	–	–	–	100	296	1200	–
5	[47]	1.4	40.9	–	–	–	100	296	2400	–
6	[13]	6.8	–	LCO-G[d)]	46	17	0	303 ± 30	882 ± 65	+0.2
7	[13]	28	–	NMC-G[c)]	51	7	0	303 ± 30	977 ± 63	+0.2
8	[13]	50	–	NMC-G[d)]	43	10	0	303 ± 30	985 ± 68	+0.2
9	[13]	60	–	NMC-G[d)]	53	12	0	297 ± 36	1036 ± 74	+0.2
10	[96]	37	805	NMC-G	–	–	55 ± 45[b)]	308 ± 20	953 ± 42	+0.2
11	[98]	3.4	49.0	NMC-SiG[d)]	21	16	40 ± 30[c)]	300 ± 15	1004 ± 34	+0.2
12	[98]	4.8	69.0	NMC-SiG[d)]	30	16	43 ± 28[c)]	300 ± 15	911 ± 28	+0.2
13	[13]	3.2	–	LCO/NCA-G[c)]	66	4	0	303 ± 30	976 ± 52	+0.2

a) The temperature dependency $\alpha_{c_p,T}$ is determined by dividing the slope of the linear regression $\partial c_{stack}/\partial T$ by the heat capacity at 300 K. b) The SOC dependency $\alpha_{c_p,SOC}$ is determined by dividing the slope of the linear regression $\partial c_{stack}/\partial$SOC by the heat capacity at a SOC of 50% amounts to −1%. c) High-power type. d) High-energy type. c) $\alpha_{c_p,SOC} = 0\%$.

is not possible according to the weighted average in Equation (7) and heat capacity of the electrolyte c_{ele} in Fig. 3.

Without the investigations of Barsoukov et al. [47], the median of all mid-ranges of c_{stack} in Table 5 amounts to 959 J kg^{-1} K^{-1}. This median lies within the heat capacity of the stack components from Fig. 3 a). The comparison of No. 6 with 7–10 in Table 5 confirms that LCO coatings have a lower heat capacity than NMC, which was shown in Fig. 3 a). In addition, c_{stack} only varies by ±77 J kg^{-1} K^{-1} (±8%), which could be caused by different stack designs (e.g. high energy or high power) or different battery states such as temperature.

According to Loges et al. [13], the porosity ε in general and the thickness ratio of the coating to the current collector of the anode $d_{ano}/\ d_{aCC}$ have a dominant influence on c_{stack}. Due to its low mass fraction of 3% (median Table 4), the separator usually has a minor influence. In addition, dry cathode coatings and aluminum collectors have a similar heat capacity of 798 ± 101 J kg^{-1} K^{-1}, which reduces the influence of variation in the cathode mass fractions on c_{stack}. On the other hand, No. 7 to 9 in Table 5 show that c_{stack} increases significantly with d_{ano}/d_{aCC}, which can be quantified by a linear correlation coefficient of +0.87. In contrast, the correlation with ε_{ano} is weaker with a linear correlation coefficient of +0.56. Because of the good correlation between d_{ano}/d_{aCC} and energy density [97], it is also expected that c_{stack} will correlate with energy density of the cell.

In addition to cell design parameters such as d_{ano}/d_{aCC}, battery states such as temperature can also cause differences in c_{stack}. The temperature dependency $\alpha_{c_p,T}$ of 0.2% K^{-1} of the stack corresponds with that of dry cathode materials in Fig. 3 b), which can be explained by the high mass fraction of cathode coatings in Table 4. The SOC dependency $\alpha_{c_p,SOC}$ shows a declining heat capacity of −1% when the SOC is increased from 0% to 100%, which constitutes a weak correlation (Table 5, No. 10). Due to the lack of measurement data with varying SOH, the dependency of this battery state for c_{stack} is unknown.

2.4. Heat capacity of full-cells

This subsection deals with the specific heat capacity of lithium-ion full-cells c_{cell} defined in Equation (8). As shown in Fig. 1, c_{cell} is determined by the heat capacity of solid components outside the electrode-separator stack and c_{stack}, which were discussed in Subsection 2.2 and 2.3, respectively. According to the mass fractions $(\sum m_c)/\ m_{cell}$ in Table 4, components outside the stack can influence c_{cell} by up to 48%. Therefore, a strong impact on c_{cell} is very likely especially in the case of housings made of steel with a lower heat capacity of 480 J kg^{-1} K^{-1} (Table 3) compared to the stack c_{stack}. Pouch cells, on the other hand, have a mass fraction of approximately 4%, which indicates a smaller deviation between c_{stack} and c_{cell}.

Fig. 2 b) shows the amount of heat capacity measurements that were carried out on full-cells. There are 52 experiments for c_{cell} in the literature, which are listed in Table 6. The cylindrical cell format is the most-studied format with 31 experiments followed by the pouch (12) and prismatic (9) format. In addition, Fig. 2 b) differentiates the cathode chemistry of the full-cells. Accordingly, the cathodes NMC, LFP, NCA and LCO have been well researched, while only one experiment exists for LMO (Table 6, No. 42). A graphite coating was used on the anode side in most of the studies, but some used LTO (Table 6, No.42, 52).

The temperature T in Table 6 indicates the temperature during the measurement of c_{cell}. Using the median of all mid-ranges in Table 6 results in a temperature of 299 K and a SOC of 50%. In contrast to T and SOC, the SOH is rarely given in the references. Only Geder et al. [99] (No. 8), Bazinski et al. [100] (No. 38), and Vertiz et al. [101] (No. 40) provide information on the SOH during the measurement. Furthermore, the investigation of Geder et al. [99] is the only experiment with varying SOH. They did not observe any significant influence of SOH on c_{cell}.

It is important to examine the uncertainty of c_{cell} when calculating this parameter from the heat capacity of the cell components in Tables 2 and 3. If a sufficiently low uncertainty can be achieved for the calculated c_{cell}, measurements on full-cells could be omitted if the researcher has sufficient information about the composition of the full-cell. One way to determine the uncertainty is to compare the measured and calculated value for c_{cell}. In Table 6, two references made this comparison. Sheng et al. [78] calculated a maximum deviation of 5% at 300 K from the measured c_{cell} (Table 6, No. 49), which is half the deviation of 9% observed by Vertiz et al. [101] (Table 6, No. 40). Hence, it seems possible to calculate c_{cell} with an uncertainty of 9%, but more research is needed to verify this uncertainty. Compared to the uncertainties of differential scanning calorimeters, which is between 1.5% and 5% depending on the calibration [43], there is no clear answer as to whether the calculation or the measurement is more accurate.

Fig. 4 a) shows a scatter plot of all data points listed in Table 6 if the temperature T is stated by the reference. Furthermore, the marker shape and color distinguish the cell format. If the SOC is stated by the reference, the marker face color is changed according to the gray-scale color bar. It can be seen that c_{cell} was measured between 250 K and 340 K, which can be viewed as the operating window for lithium-ion cells. No experiments for c_{cell} are available for safety simulations with temperatures above 340 K. In addition, there are no experiments below 250 K, which is still an operating temperature for military or aerospace applications [16].

The three horizontal lines in Fig. 4 a) indicate a format dependency of c_{cell}. Comparing the medians of the mid-ranges shows a lower c_{cell} for cylindrical cells (912 J kg^{-1} K^{-1}) than for prismatic (1041 J kg^{-1} K^{-1}) and pouch cells (1168 J kg^{-1} K^{-1}). The housing can explain the difference between the formats assuming the same values for c_{stack}. For example,

Table 6
Measured specific heat capacity of full lithium-ion cells c_{cell} according to Equation (8). No information provided is marked with (–).

No.	Ref.	$\frac{Q_{cell}}{Ah}$	$\frac{m_{cell}}{g}$	Format	Active material	$\frac{SOC}{\%}$	$\frac{T}{K}$	$\frac{c_{cell}}{J\ kg^{-1}K^{-1}}$	$\frac{\alpha_{c_p,T}{}^{a)}}{K^{-1}}$	$\frac{\alpha_{c_p,SOC}{}^{b)}}{\%}$
1	[48]	2	42.9	Cylindr.	–	–	293	1013	–	–
2	[48]	2.7	45	Cylindr.[d)]	–	–	293	907	–	–
3	[48]	1.1	39.4	Cylindr.[c)]	–	–	293	1011	–	–
4	[102]	–	–	Cylindr.	–	–	–	800	–	–
5	[103]	6	375	Cylindr.[c)]	–	–	–	795	–	–
6	[104]	5	96	Cylindr.	NMC	50	303	980 ± 2	–	–
7	[105]	3.49	49	Cylindr.	NMC-G	–	298	1046	–	–
8	[99]	2.15	44	Cylindr.[c)]	NMC-G	50	316	851 ± 9	–	–
9	[79]	2.4	44.7	Cylindr.	NMC	–	293 ± 40	1047 ± 115	+0.3	–
10	[79]	4.6	65.9	Cylindr.	NMC	–	293 ± 40	1013 ± 92	+0.2	–
11	[106]	2.25	42.3	Cylindr.	NMC-G	–	–	1100	–	–
12	[107]	4.15	67	Cylindr.[d)]	NMC-G	50	318 ± 20	874 ± 65	+0.4	–
13	[108]	4.4	82	Cylindr.[d)]	NMC-G	50 ± 50	–	1314 ± 31	–	5
14	[104]	2.5	76	Cylindr.	LFP	50	303	1148 ± 21	–	–
15	[109]	–	–	Cylindr.	LFP	100	–	1720	–	–
16	[109]	–	–	Cylindr.	LFP	100	–	1605	–	–
17	[110]	2.5	70	Cylindr.	LFP-G	50 ± 50	314 ± 19	1117 ± 36	+0.1	3
18	[106]	1.5	38.6	Cylindr.	LFP-G	–	–	1100	–	–
19	[111]	8	335	Cylindr.	LFP-G	–	–	998	–	–
20	[108]	2.5	70	Cylindr.[c)]	LFP-G	50 ± 50	–	1139 ± 14	–	2
21	[105]	3.57	48	Cylindr.	NCA-G	–	298	959	–	–
22	[105]	2.14	45	Cylindr.	LCO-G	–	298	1002	–	–
23	[29]	1.35	–	Cylindr.	LCO-G	–	315	1000 ± 40	–	–
24	[112]	2.6	–	Cylindr.	LCO	–	288 ± 10	893 ± 79	–	–
25	[113]	1.35	40	Cylindr.	LCO-G	–	318 ± 10	945 ± 125	−0.7	–
26	[106]	2.6	44	Cylindr.	LCO-G	–	–	1100	–	–
27	[83]	0.5	19	Cylindr.	LCO-G	48 ± 48	325 ± 15	820 ± 32	+0.1	−4
28	[110]	2.7	48	Cylindr.	NCA-G	50 ± 50	313 ± 18	830 ± 19	+0.1	2
29	[114]	2.75	45	Cylindr.	NCA-G	–	283 ± 30	1133 ± 24	−0.0	–
30	[108]	2.7	48	Cylindr.[d)]	NCA-G	50 ± 50	–	837 ± 11	–	3
31	[108]	3.1	48.5	Cylindr.[d)]	NCA-SiG	50 ± 50	–	1058 ± 31	–	6
32	[104]	10	198	Pouch	NMC	50	303	1160 ± 22	–	–
33	[115]	40	–	Pouch[d)]	NMC	–	298	860	–	–
34	[78]	9	222	Pouch	NMC	50	293 ± 40	1093 ± 113	+0.3	–
35	[116]	12	326.6	Pouch[c)]	NMC-G	–	–	1070	–	–
36	[117]	40	910	Pouch	NMC-G	–	315 ± 17	1138 ± 69	+0.3	–
37	[118]	37	560	Pouch	NMC-G	–	299	948	–	–
38	[100]	14	385	Pouch	LFP-G	50 ± 50	298 ± 30	1380 ± 251	+0.5	4
39	[78]	9	235	Pouch	LFP	50	293 ± 40	1085 ± 105	+0.3	–
40	[101]	14	–	Pouch	LFP-G	50 ± 50	–	1119 ± 5	–	−1
41	[119]	2.28	–	Pouch	LCO-G	50 ± 50	304	1091 ± 45	–	7
42	[87]	–	–	Pouch[c)]	LMO-LTO	50 ± 40	298	1056 ± 12	–	0
43	[90]	25	1154	Pouch	LMO/LCO-G	–	300	1243	–	–
44	[104]	5	276	Prismatic	NMC	50	303	1025 ± 13	–	–
45	[38]	43	840	Prismatic	NMC[d)]	50	298 ± 15	933 ± 39	+0.2	–
46	[120]	104	2032	Prismatic	NMC-G	50 ± 50	333 ± 8	1033 ± 73	+0.3	7
47	[121]	43	840	Prismatic	NMC[d)]	50	296 ± 23	978 ± 3	+0.0	–
48	[46]	42	–	Prismatic	LFP-G	50	295	1142	–	–
49	[78]	8	328	Prismatic	LFP-G	50 ± 50	293 ± 40	1174 ± 137	+0.2	4
50	[118]	20	610	Prismatic	LFP-G	–	299	1048	–	–
51	[22]	2.8	45	Prismatic	–	–	300	907 ± 13	–	–
52	[121]	23	550	Prismatic	LTO[c)]	50	296 ± 22	1146 ± 11	+0.0	–

a) The temperature dependency $\alpha_{c_p,T}$ is determined by dividing the slope of the linear regression $\partial c_{cell}/\partial T$ by the heat capacity at 300 K. b) The SOC dependency $\alpha_{c_p,SOC}$ is determined by dividing the slope of the linear regression $\partial c_{cell}/\partial$SOC by the heat capacity at 50% SOC. c) High-power type. d) High-energy type.

cylindrical steel-housings have a lower heat capacity than prismatic aluminum-housings and aluminum has a lower heat capacity than pouch foils (see Table 3). The median value for c_{stack} of 959 J kg^{-1} K^{-1} in Table 5 is exceeded by the prismatic and the pouch format. This is a contradiction because the pouch foil does not have much influence and the heat capacity of prismatic housings is below 976 J kg^{-1} K^{-1}.

There are several reasons that could explain a higher value in c_{cell} than c_{stack}. First, the stack design of the cells listed in Table 6 could be systematically different from the stacks listed in Table 5. For example, this would be the case if Table 5 only contains stacks of high-power cells and Table 6 contains only cells with a high-energy design. However, this is unlikely because Tables 5 and 6 contain high-energy and high-power stacks and cells with a variety of cathode chemistries. Second, a higher electrolyte volume than the pore volume [122,123] could increase c_{cell} compared to c_{stack} due to the high heat capacity of the electrolyte. For example, An et al. [123] recommended an electrolyte volume of 190% of the pore volume to enable long-term cycling capability and low impedance. Third, measurement errors can be used as an explanation. Nevertheless, the median of the pouch format deviates by 20% from 976 J kg^{-1} K^{-1}, which exceeds the measurement uncertainty of common measurement methods [43]. In conclusion, more research is needed to clarify the discrepancy between c_{stack} and c_{cell} for pouch and prismatic cells.

The median of all temperature dependencies $\alpha_{c_p,T}$ of c_{cell} in Table 6 amounts to +0.2 K^{-1}. This value matches the temperature dependency of wet electrode-separator stacks in Table 5. The negative dependency of −0.7 K^{-1} (Table 6, No. 25) can be treated as an outlier, since $\alpha_{c_p,T}$ of cell components lie within 0.0 and 0.4 K^{-1} according to Fig. 3 b) and Table 3. For the SOC dependency $\alpha_{c_p,SOC}$, Table 6 lists values between −4% and 7% for c_{cell}, which is in the same order of magnitude as the 2% that Loges et al. [13] measured for c_{stack}.

Temperature and SOC can influence c_{cell}, but also design parameters

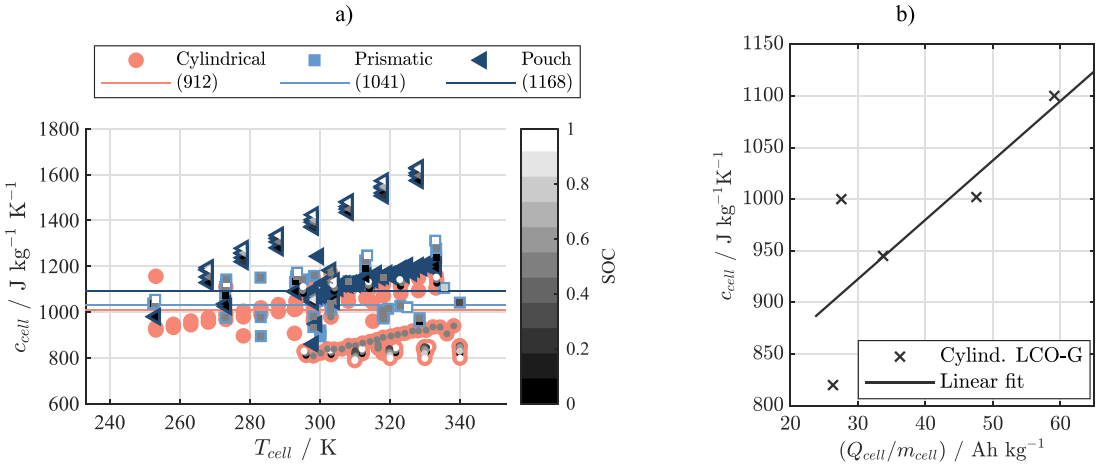

Fig. 4. Dependencies of the full-cell heat capacity c_{cell} on operational and design parameters of lithium-ion cells. a) Format, temperature, and SOC dependency with the format medians in round brackets. Each marker represents one measurement result from the references in Table 6. The marker face color is chosen according to the grayscale color bar, if the reference states the SOC. b) Correlation between c_{cell} of cylindrical lithium-ion LCO-G cells with their specific electrochemical capacity Q_{cell}/m_{cell}. (For interpretation of the references to color in this figure legend, the reader is referred to the Web version of this article.)

such as the layer thicknesses have an influence. High-energy cells usually have a higher ratio between the thickness of the active material and the current collectors (d_{ano}/d_{aCC}, d_{cat}/d_{cCC}). Loges et al. [13] pointed out that a thicker anode coating d_{ano} increases the specific heat capacity of the entire electrode because the low heat capacity of copper has less of an impact. Thus, an increase in d_{ano}/d_{aCC}, increases the specific heat capacity of the anode electrode. On the other hand, increasing d_{cat}/d_{cCC} has less of an impact on the cathode electrode, since most wet cathode coatings have a similar specific heat capacity as the aluminum current collector. This postulates a positive correlation between d_{ano}/d_{aCC} and c_{cell}, which implies a correlation between the energy density of the cell and c_{cell}.

With increasing coating thicknesses, the specific energy e_{cell} of the lithium-ion cell also increases. e_{cell} is often defined as the product of nominal voltage and electrical capacity divided by the cell mass $U_{cell}Q_{cell}/m_{cell}$. To examine the correlation between e_{cell} and c_{cell}, Fig. 4 b) shows c_{cell} as a function of the specific capacity Q_{cell}/m_{cell} listed in Table 6. Since only the heat capacities of cells with an LCO cathode and a graphite anode are used, the x-axis of Fig. 4 b) can be converted to e_{cell} by multiplying it with the nominal voltage of LCO-G (3.7 V [106]). In addition, only cylindrical cells are considered in order to reduce the influence of the cell housing on the correlation between e_{cell} and c_{cell}. The remaining data points are approximated in Fig. 4 b) using a linear regression. As postulated, the slope of the linear regression has a positive value of 5.8 J K^{-1} Ah^{-1} with a 95% confidence interval of ±8.1 J K^{-1} Ah^{-1}. The Pearson's linear correlation coefficient between Q_{cell}/m_{cell} and c_{cell} is 0.72. Therefore, as the specific energy of lithium-ion cells increases, the specific heat capacity of the cell is likely to increase as well.

3. Thermal conductivity and resistance

This section reviews thermal conductivity measurements on full-cells, electrode-separator stacks, single stack layers k_l, and thermal contact resistances R_c between theses layers. In comparison to the specific heat capacity, it is not straightforward to formulate an effective

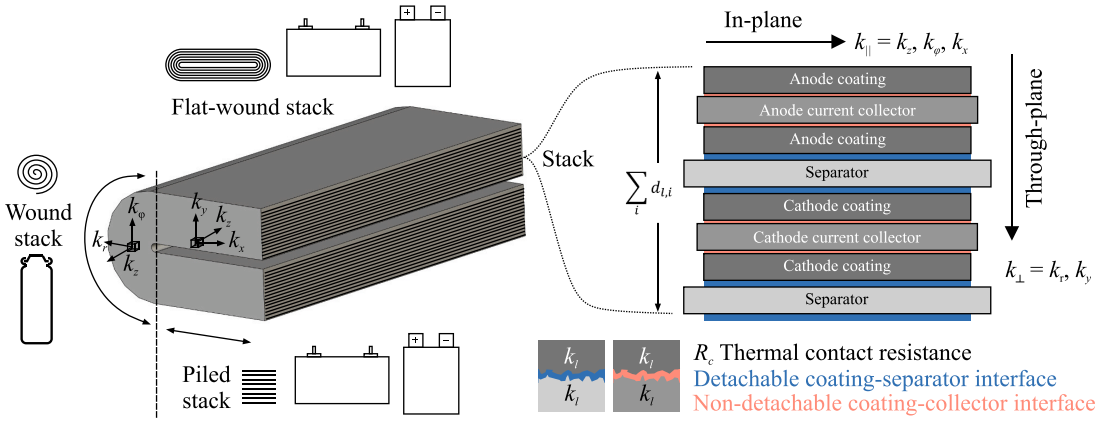

Fig. 5. Definition of in-plane $k_{\parallel}$ and through-plane $k_{\perp}$ thermal conductivity for wound, piled or flat-wound electrode-separator stacks. The through-plane conductivity of the stack is influenced by the thermal conductivity of the stack layers k_l and the thermal contact resistance R_c between them.

Table 7
The total thickness of the electrode-separator stack with the thickness shares of the stack layers, which can be used in Equations (9) and (10).

Ref.	$\frac{Q_{cell}}{Ah}$	Format	Active material	$\frac{\sum_i d_{l,i}}{\mu m}$	$\frac{d_{cat}}{\sum_i d_{l,i}}$	$\frac{d_{ano}}{\sum_i d_{l,i}}$	$\frac{d_{aCC}}{\sum_i d_{l,i}}$	$\frac{d_{cCC}}{\sum_i d_{l,i}}$	$\frac{d_{sep}}{\sum_i d_{l,i}}$
[50]	6.8	Prismatic	LCO-G	490	39%	45%	3%	5%	8%
[119]	2.3	Pouch	LCO-G	364	37%	42%	3%	4%	14%
[127]	41.0	Pouch	NMC/LMO-G	350	43%	37%	3%	6%	11%
[101]	14.0	Pouch	LFP-G	223	44%	30%	6%	9%	11%
[78]	8.0	Prismatic	LFP-G	35	26%	11%	17%	17%	29%
[34]	34.0	Prismatic	NMC-G	315	41%	38%	3%	5%	14%
[59]	25.0	Prismatic	NMC-G	357	40%	38%	3%	4%	14%

thermal conductivity for the entire full-cell with which thermal single-domain models can be parameterized (see Table 1). In the case of pouch cells, the thermal conductivity of the stack [115] can be used with an acceptable uncertainty for full-cells, which is not always the case with prismatic cells [124]. As a result, single-domain models must carefully choose the parameters in this section. In addition, this section does not

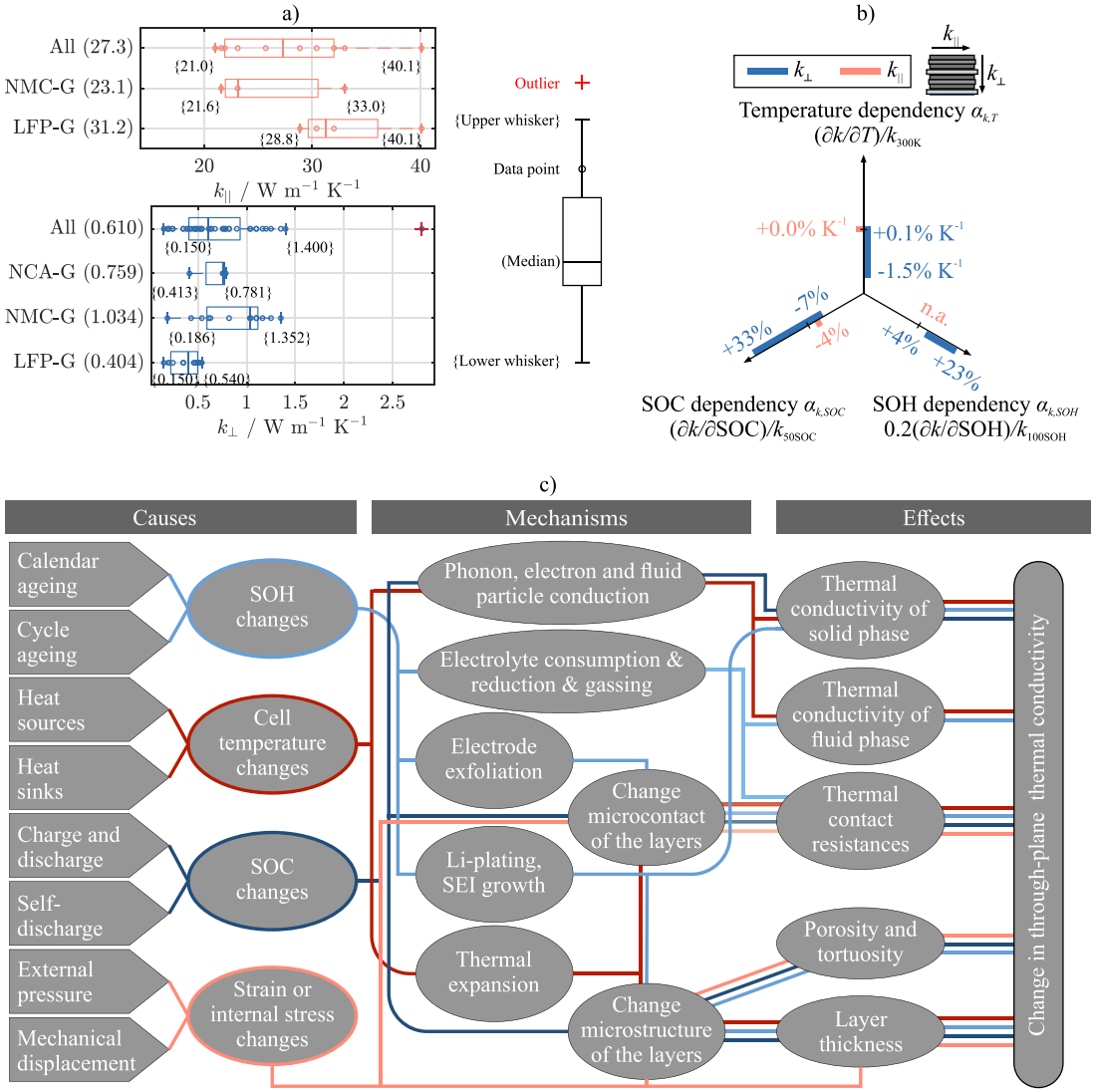

Fig. 6. Range of values and dependencies of the in-plane $k_{\parallel}$ and through-plane $k_{\perp}$ conductivity of the electrode-separator stack and full-cells. a) Boxplot of the mid-range conductivities listed in Table 8 and Table 9. Round brackets indicate recommended values (medians) for thermal modeling. b) Dependencies on cell temperature, SOC, and SOH. c) Schematic of causes, mechanisms and effects for changes in thermal conductivity $k_{\perp}$ in through-plane direction.

deal with unspecific conductivities that are used in lumped thermal models [42]. Dry stack layers are also not discussed as complex models are required to determine the wet thermal conductivity from dry measurements [50,72].

The thermal conductivity measurement methods can be divided into steady-state and transient methods. To determine the thermal conductivity, a temperature gradient must be measured that was previously induced by a heat flow. Common steady-state methods in the field of battery cells are the guarded hot plate [34,96] and the comparative method [52,125] with an uncertainty of 2% and 10–20% [43], respectively. Transient methods such as the laser flash achieve uncertainties between 3–5% [43].

Different arrangements of the electrode-separator stack are used for different formats of lithium-ion cells. On the left of Fig. 5, a flat-wound arrangement is illustrated, which is usually used for prismatic formats [34,50]. This arrangement represents a combination of the wound and piled stack. Piled stacks are commonly applied for pouch cells [39] and wound stacks for cylindrical cells. To save computational costs, a homogeneous volume often replaces the layered structure of the stack. Due to this layer structure, an anisotropic thermal conductivity must be used for the homogeneous volume, also known as the unit cell [50]. This anisotropy is described by a thermal conductivity in the direction of the stack layers $k_{\parallel}$ and through them $k_{\perp}$. In addition, the coordinate system must be adapted to the stack-arrangement. For example a cylindrical coordinate system (r, z, φ) is recommended for wound stacks and a Cartesian (x, y, z) for piled ones [34].

Experiments on the anisotropic thermal conductivity of the stack are reviewed in Subsection 3.1 starting with the in-plane conductivity $k_{\parallel}$. The in-plane value can be calculated with Equation (9), which is a weighted average of the conductivities of the stack layers k_l by their layer thickness $d_{l,i}$. In contrast, the stack layer with the lowest thermal conductivity and the highest layer thickness dominates the through-plane conductivity $k_{\perp}$ in Equation (10). Furthermore, $k_{\perp}$ is affected by thermal contact resistances R_c between the stack layers [126]. R_c can be divided into a detachable coating-separator and a non-detachable coating-collector interface, which are shown in blue and red in Fig. 5. It should be noted that R_c is a specific thermal resistance with the unit $cm^2\ K\ W^{-1}$.

$$k_{\parallel} = \frac{\sum_i d_{l,i} \cdot k_{l,i}}{\sum_i d_{l,i}} \tag{9}$$

$$k_{\perp} = \frac{\sum_i d_{l,i}}{\sum R_c + \sum_i \frac{d_{l,i}}{k_{l,i}}} \tag{10}$$

Equations (9) and (10) [126] depend on the layer thicknesses of the electrode-separator stack. For this reason, Table 7 contains exemplary layer thicknesses of lithium-ion cells, which are discussed in the following subsections. For $k_{\parallel}$, the thickness of the anode and cathode current collectors is particularly important (d_{aCC}, d_{cCC}), while for $k_{\perp}$ the layer thicknesses of the separator, anode and cathode coatings (d_{sep}, d_{ano}, d_{cat}) matters the most [34]. In addition, the total stack thickness $\sum_i d_{l,i}$ determines the influence of the thermal contact resistance on $k_{\perp}$.

After discussing the in-plane $k_{\parallel}$ and through-plane $k_{\perp}$ conductivity, Subsections 3.2 and 3.3 examine experimental results on stack layers k_l. Porous components and solid components are treated separately due to the excellent availability of measurement data for solid components such as copper. For this reason, review articles for the solid components already exist, which is why these are only summarized in this paper. Afterwards, the reviewed results for k_l are discussed in relation to $k_{\parallel}$ and $k_{\perp}$ with the help of Equation (9) and (10). For $k_{\perp}$ this includes results for the thermal contact resistance from the last Subsection 3.4.

3.1. Conductivity of electrode-separator stacks and full-cells

Table 8 lists the thermal conductivities measured in in-plane direction $k_{\parallel}$ of the electrode-separator stack or full-cell. Stack conductivities that compensate for the influence of the cell housing in the measurement evaluation are marked with b) in Table 8. These conductivities can be applied directly to the stack in component-resolved thermal models or in some cases to single domain models (see Table 1). The stack and full-cell thermal conductivity in the in-plane direction is often viewed as the same for the pouch format with acceptable uncertainty. In the case of prismatic and cylindrical formats, the congruence of the stack and full-cell conductivity depends strongly on the stack and housing geometry. This must be taken into account when using No. 3, 4 and 10 for stacks in component-resolved thermal models.

In addition, Q_{cell} and m_{cell} in Table 8 provide information about whether the electrodes are designed for high-energy or high-power applications. The SOH is not included in the header of Table 8 because only Bazinski et al. [128] reported this battery state. It should be noted that in Table 8 only double-coated stacks are taken into account. Therefore, the results of Maleki et al. [29], who only used one separator layer, are not included for reasons of comparability.

LFP and NMC are the most prevalent cathode coatings for in-plane conductivity measurements as can be seen in Fig. 2 c). No experiments are available for the cathode coating NCA and the anode coatings LTO. According to the boxplot in Fig. 6 a), $k_{\parallel}$ is between 21 and 40.1 $W\ m^{-1}\ K^{-1}$, which contains all references in Table 8. This represents an uncertainty of ±31% from the mid-range of 30.6 $W\ m^{-1}\ K^{-1}$. With a known cathode and anode chemistry, the uncertainty from the mid-range is reduced to ±21% and ±18% for NMC-G and LFP-G (see Fig. 2 c)), respectively. No investigation in Table 8 compares its measurement results with material measurements k_l according to Equation (9). Therefore, Equation (9) has not yet been verified, but is often used in the literature [6,34,54].

The in-plane conductivity shows a weak negative dependency on SOC [128], a negligible influence of the temperature T [59], an unknown relation with SOH, and a negative correlation with the specific

Table 8
Measured thermal conductivity in in-plane direction of the separator-electrode stack or full-cell $k_{\parallel}$. All stacks are soaked with electrolyte (wet) and the measurements were carried out on the stack or full-cell level. No information provided is marked with (–).

No.	Ref.	$\frac{Q_{cell}}{Ah}$	$\frac{m_{cell}}{g}$	Format	Active material	$\frac{SOC}{\%}$	$\frac{T}{K}$	$\frac{k_{\parallel}}{W\ m^{-1}K^{-1}}$
1	[128]	14.5	385.0	Pouch	LFP-G	50 ± 50	305	28.8 ± 0.6
2	[128]	10.0	350.0	Pouch	LFP-G	50 ± 50	305	40.1 ± 1.1
3	[109]	–	–	Cylindr.	LFP-G	100	–	32.0
4	[109]	–	–	Cylindr.	LFP-G	100	–	30.4
5	[90]	25.0	1154.0	Pouch	NMC/LMO-G	–	300	21.0[b)]
6	[127]	41.0	–	Pouch	NMC/LMO-G	30	303	25.7 ± 0.9
7	[115]	40.0	1180.0	Pouch[a)]	NMC	–	298	33.0
8	[59]	25.0	–	Prismatic	NMC-G	–	323 ± 30	23.1[b)]
9	[96]	37.0	–	Prismatic	NMC-G	0	313	21.6[b)]
10	[112]	2.6	–	Cylindr.	LCO	–	298	21.9

a) High-energy type. b) The cell housing was compensated for when evaluating the measurement data.

Table 9
Measured thermal conductivity $k_\perp$ in through-plane direction of the separator-electrode stack and full-cells. All stacks are soaked with electrolyte (wet) and the measurements were carried out on the stack or full-cell level. No information provided is marked with (−).

No.	Ref.	Q_{cell} / Ah	m_{cell} / g	Format	Active material	SOC / %	T / K	$k_\perp$ / W m^{-1}K^{-1}	$\alpha_{k,T}$[a] / K^{-1}	$\alpha_{k,SOC}$[b] / %
1	[131]	2.3	70.0	Cylindr.	LFP-G	–	296	0.510	–	–
2	[109]	–		Cylindr.	LFP-G	100	286	0.150	–	–
3	[109]	–		Cylindr.	LFP-G	100	286	0.200	–	–
4	[45]	4.4	194.0	Cylindr.	LFP-G[g]	50	303	0.350[i]	–	–
5	[110]	2.5	70.0	Cylindr.	LFP-G	50 ± 50	314 ± 19	0.472 ± 0.03	−0.2	−4
6	[132]	2.3	–	Cylindr.	LFP	–	–	0.200	–	–
7	[108]	2.5	70	Cylindr.	LFP-G[g]	50 ± 50	–	0.458 ± 0.01	–	−5
8	[100]	14.0	385.0	Pouch[d]	LFP-G	50 ± 50	298 ± 30	0.350 ± 0.01	0.0	−5
9	[78]	9.0	235.0	Pouch[e]	LFP-G	50	293 ± 40	0.522 ± 0.02	0.1	–
10	[101]	14.0	–	Pouch	LFP-G	50 ± 50	–	0.242 ± 0.04	–	-4[c]
11	[78]	8.0	328.0	Prismatic[e]	LFP-G	50 ± 50	293 ± 40	0.540 ± 0.02	0.1	−3
12	[124]	60	2000	Prismatic	LFP-G	–	–	0.485	–	–
13	[50]	6.8	150.0	Prismatic	LCO-G	70	318 ± 15	0.821[i]±0.16	−1.1	–
14	[105]	2.1	45.0	Cylindr.	LCO-G	50	298	0.239	–	–
15	[112]	2.6	–	Cylindr.	LCO	–	298	0.385 ± 0.17	–	–
16	[100]	75.0	–	Pouch[d]	NMC-G	50 ± 50	298	0.430 ± 0.01	–	−7
17	[78]	9.0	222.0	Pouch[e]	NMC-G	50	293 ± 40	0.629 ± 0.02	0.1	–
18	[115]	40.0	1180.0	Pouch[f]	NMC[h]	–	298	0.610	–	–
19	[34]	34.0	–	Prismatic	NMC-G	15	293 ± 22	1.100[i]±0.40	−1.5	–
20	[38]	43.0	840.0	Prismatic	NMC[h]	50	298	0.820	–	–
21	[59]	25.0	–	Prismatic	NMC-G	–	323 ± 30	1.100	0.0	–
22	[96]	37.0	–	Prismatic	NMC-G	0	308	1.034[i]	–	–
23	[105]	3.5	49.0	Cylindr.	NMC-G	50	298	0.186	–	–
24	[79]	2.4	44.7	Cylindr.	NMC-G	–	293 ± 40	1.041 ± 0.04	0.1	–
25	[79]	4.6	65.9	Cylindr.	NMC-G	–	293 ± 40	1.164 ± 0.03	0.1	–
26	[98]	3.4	49.0	Cylindr.	NMC-SiG	40 ± 30	300 ± 15	1.250[i]±0.14	−0.5	10
27	[98]	4.8	69.0	Cylindr.	NMC-SiG	43 ± 28	300 ± 15	1.352[i]±0.21	−0.7	12
28	[108]	4.4	82	Cylindr.	NMC-G[h]	50 ± 50	–	0.540 ± 0.02	–	−7
29	[87]	–	–	Pouch	LMO-LTO[g]	50 ± 40	298	0.641 ± 0.05	–	-6[c]
30	[90]	25.0	1154.0	Pouch	NMC/LMO-G	–	300	0.480[i]	–	–
31	[127]	41.0	–	Pouch	NMC/LMO-G	30	290	0.780 ± 0.06	–	–
32	[129]	41.0	–	Pouch	NMC/LMO-G	50 ± 50	–	0.675 ± 0.13	–	7[c]
33	[110]	2.7	48.0	Cylindr.	NCA-G	50 ± 50	314 ± 19	0.786 ± 0.13	−0.2	24
34	[105]	3.6	48.0	Cylindr.	NCA-G	50	298	0.413	–	–
35	[108]	2.7	48.5	Cylindr.	NCA-G[h]	50 ± 50	–	0.763 ± 0.10	–	25
36	[108]	3.1	48.5	Cylindr.	NCA-SiG[h]	50 ± 50	–	0.754 ± 0.12	–	33
37	[102]	–	–	Cylindr.	–	–	–	0.390	–	–
38	[47]	1.8	42.7	Cylindr.	–	100	296	0.900[i]	–	–
39	[47]	1.5	39.5	Cylindr.	–	100	296	1.400[i]	–	–
40	[47]	1.3	41.6	Cylindr.	–	100	296	2.800[i]	–	–
41	[47]	1.4	40.9	Cylindr.	–	100	296	1.200[i]	–	–

a) The temperature dependency $\alpha_{k,T}$ is determined by dividing the slope of the linear regression $\partial k_\perp/\partial T$ by the thermal conductivity at 300 K $k_\perp$(300K). b) The SOC dependency $\alpha_{k,SOC}$ is determined by dividing the slope of the linear regression $\partial k_\perp/\partial$SOC by the thermal conductivity at a SOC of 50%. c) Nonlinear relation between SOC and $k_\perp$ reported. d) Applied compression load 1500 N. e) Vacuum environment. f) Atmospheric pressure. g) High-power type. h) High-energy type. i) The cell housing was compensated for when evaluating the measurement data.

Table 10
Measured thermal conductivity of solid non-porous components in lithium-ion cells. No information provided is marked with (−).

Material	T / K	k_s / W m^{-1}K^{-1}	$\alpha_{k,T}$[f] / K^{-1}
Copper[a]	300 ± 50 [139]	399.0 ± 5.0 [139]	−0.0
Aluminum[b]	300 ± 50 [139]	237.5 ± 2.5 [139]	+0.0
Aluminum alloy 3003[c]	–	155 [89]	–
PP[d]	273 ± 50 [67]	0.215 ± 0.01 [67]	0.0[g]
PET[d]	301 ± 25 [140]	0.188 ± 0.00 [140]	0.0
PE[d]	313 ± 40 [141]	0.241 ± 0.02 [141]	−0.2[g]
Stainless steel AISI 304[e]	300 ± 50 [138]	14.850 ± 0.86 [138]	+0.1
Pouch foil [37]	–	55.1 (‖), 0.269 (⊥)	–

a) Anode current collector, Negative cell terminal. b) Cathode current collector, Anode current collector (LTO) [87], Positive cell terminal. c) Prismatic cell housing [34,77,78], Cylindrical housing [45]. d) Pouch foil layer, separator. e) Cylindrical housing [79,88], Prismatic cell housing [50], Cylindrical mandrel/center pin [80]. f) The temperature dependency $\alpha_{k,T}$ is determined by dividing the slope of the linear regression $\partial k/\partial T$ by the thermal conductivity at 300 K. g) Nonlinear relation between T and k.

capacity Q_{cell}/m_{cell}. Bazinski et al. [128] and Bohn et al. [59] are the only references in Table 8 who examined the dependence on SOC or temperature. Therefore, further experiments are necessary to validate these results. Nevertheless, the experimental results agree with the fact that the in-plane conductivity is strongly influenced by the current collectors [34], which do not change their thickness with the SOC and have minor temperature dependency (Table 10). In addition, the investigation of Bazinski et al. [128] shows a negative correlation between $k_\parallel$ and the specific energy or capacity Q_{cell}/m_{cell}. Looking at No. 1 and 2 (Table 8), the specific capacity drops from 37.7 to 28.6 Ah kg^{-1}, while the $k_\parallel$ increases from 28.8 to 40.1 W m^{-1} K^{-1}. This is most likely caused by thicker current collectors compared to the total thickness $\sum_i d_{l,i}$ of the stack in Equation (9).

Table 9 contains experimental results for the through-plane conductivity $k_\perp$ defined in Fig. 5. The header of Table 9 is congruent with Table 8 except of the temperature and SOC dependency $\alpha_{k,T}$ and $\alpha_{k,SOC}$, because more than one dependency is reported for $k_\perp$. Both dependencies are determined alike the heat capacity by fitting the reported data with a linear regression. Dividing the slope of the linear regressions ($\partial k_\perp/\partial T$; $\partial k_\perp/\partial$SOC) by the absolute value at 300 K and 50% SOC gives $\alpha_{k,T}$ and $\alpha_{k,SOC}$.

The SOH is not shown in Table 9 because this state was only reported by Bazinski et al. [100], Kovachev et al. [129], Steinhardt et al. [98] and Vertiz et al. [101]. Therefore, future experiments are encouraged to state the SOH of the test cell. Furthermore, measurements are only included in Table 9 if the result is given as a material constant, i.e. it is expressed on specific rather than absolute values. Forgez et al. [42], for example, measured the lumped through-plane (or radial) thermal resistance of a 26650 cylindrical cell. Since they did not convert their absolute resistance between 3.2 and 3.4 K W^{-1} into $k_\perp$ with the unit W m^{-1} K^{-1}, the comparison with other geometries is complicated.

Compared to the in-plane conductivity $k_\parallel$, the through-plane conductivity $k_\perp$ is examined more frequently in the literature. Table 9 lists measurements on 41 different lithium-ion cells, which are analyzed in Fig. 2 c) according to cathode chemistry and cell format. Concerning the cathode, LFP is the most abundant chemistry, followed by NMC. Table 9 lists five measurements for which the cathode chemistry is unknown (n/a). In general, as shown in Fig. 2 c), all common cathodes are available. It should be noted that most cell measurements do not specify electrode structures (i.e. porosity) and the thickness of the stack layers, which can be a source of uncertainties for the thermal conductivity [130].

NMC-G stacks have a higher thermal conductivity $k_\perp$ than LFP-G. This finding is highlighted by the boxplot in Fig. 6 a) that determines a median thermal conductivity $k_\perp$ for NCA-G, NMC-G and LFP-G of 0.759, 1.034 and 0.404 W m^{-1} K^{-1}, respectively. The median of all mid-ranges in Table 9 is 0.610 W m^{-1} K^{-1} with an outlier of 2.8 W m^{-1} K^{-1} (Table 9, No. 40). The mid-range of the whiskers from all measurements is 0.775 W m^{-1} K^{-1} with a large uncertainty of ±81%. This uncertainty is reduced for NMC-G (±76%) and LFP-G (±57%) which is approximately twice the uncertainty of the specific heat capacity c_{cell} from Subsection 2.4.

There are only two references (Table 9, No. 10, 32) that report a strong negative correlation of $k_\perp$ with SOH. Vertiz et al. [101] observed a decrease in $k_\perp$ of −29% between a new and an aged pouch cell (SOH <80%). The reason for this significant decrease was not discussed by Vertiz et al. [101]. Kovachev et al. [129] cycled three pouch cells at 60 °C with different electrical currents (1C–3C) and pretension between 0 and 0.56 MPa. After 700 cycles, an SOH of 80%, 85% and 86% was reached, which correlated positively with the pretention. The decrease in SOH caused an average decrease in $k_\perp$ between 23% and 4% (Fig. 6 b)). Kovachev et al. [129] explained the SOH dependence of $k_\perp$ with an additional thermal resistance on the anode side caused by the SEI growth. In addition, electrolyte consumption and gas development due to the electrolyte reduction could lead to a decrease in $k_\perp$. The results of Vertiz et al. [101] and Kovachev et al. [129] show a significant decrease in $k_\perp$ with SOH, which is reflected in a poorer thermal performance of the cell, since the heat development also increases with SOH. However, more research is needed to confirm the correlation between $k_\perp$ and SOH for cylindrical and prismatic cells. In addition, further studies with various aging causes such as calendar aging are required.

There are contradictory results regarding the influence of temperature on $k_\perp$. As illustrated in Fig. 6 b), the temperature dependency $\alpha_{k,T}$ for $k_\perp$ lies between −1.5 and + 0.1 K^{-1}. Werner et al. [50] and Steinhardt et al. [34,98] explored a dominant decline of $k_\perp$ with rising temperature. Murashko [110] et al. confirmed this trend but the intensity of the decline was lesser. No dependency on temperature was explored by Bazinski et al. [100] and a positive trend by Sheng et al. [78,79]. Different results in temperature dependency can be explained by different magnitude of thermal contact resistances R_c, different layer thicknesses or electrode structures. However, the effect of these explanations is not yet fully understood. In addition, no experiments for $k_\perp$ are available for safety simulations with temperatures above 340 K.

As illustrated in Fig. 6 b), the SOC dependency $\alpha_{k,SOC}$ implies a change in $k_\perp$ between −7% and +33% when the SOC is increased from 0% to 100%. It should be noted that $\alpha_{k,SOC}$ assumes a linear relationship between SOC and $k_\perp$ and three references measured a parabolic relationship (Table 9, No.10, 29, 32). For example, Vertiz et al. [101] observed a reduction in thermal conductivity of −17.22% and −16.23% at a full-cell SOC of 0% and 100%, respectively, compared to the thermal conductivity at 50% SOC. In contrast, the remaining five references in Table 9 are well described by a linear relationship.

The dependence of $k_\perp$ on the SOC is often explained by a changing thermal conductivity of the active particle with the degree of lithiation [78,87,110]. This explanation is supported by the work of Ju et al. [133] and Cho et al. [134], who reported a strong correlation between the thermal conductivity of graphite and LCO with the degree of lithiation. For example, Cho et al. [134] measured a decrease in thermal conductivity from 5.4 to 3.7 W m^{-1} K^{-1} during the delithiation from $Li_{1.0}CoO_2$ to $Li_{0.6}CoO_2$. A strong dependence of $\alpha_{k,SOC}$ on the cathode material also explains the opposite dependence of −4% and +33% for an LFP and NCA cell, which were measured using the same test method (Table 11, No. 5, 33). However, such a strong dependence on the cathode material was not explored by Bazinski et al. [100]. Further measurements are therefore required to clarify whether a linear or non-linear relationship between $k_\perp$ and SOC exists and which cell parameters influence this relationship.

Instead of measuring, the through-plane conductivity can be calculated with Equation (10) if the layer thickness d_l and the layer conductivity k_l are known. The validity of this calculation depends on the thermal contact resistance R_c, which is not a material-specific property. Some of the references in Table 9 determined $k_\perp$ with Equation (10) neglecting R_c. Vertiz et al. [101] and Sheng et al. [78] overestimated $k_\perp$ in their calculation by 255% and 59%, respectively. Both authors explained this overestimation with thermal contact resistances between the stack layers, but uncertainties in the selected layer conductivities k_l could also be an explanation. Uncertainties arising from k_l can be neglected for the calculation of Werner et al. [50], because they used an LCO cell whose k_l was previously measured by Loges et al. [130]. They achieve an excellent agreement between their experiments and calculations, which confirms the assumption that R_c can be neglected. However, more research is needed to understand the relevance of R_c to $k_\perp$.

Variabilities in $k_\perp$ of lithium-ion cells are practically always ignored in thermal models. However, as discussed in this paper, several studies in the literature have shown that changes in SOC, SOH and temperatures can lead to variations in $k_\perp$. One of the remaining challenges is that the causes of these effects on $k_\perp$ are multifaceted in nature, and so far, the causal relationships have been barely investigated. The complexity of the cause-effect chain is illustrated in Fig. 6 c) for $k_\perp$ using a network graph. For the interest of the reader, we provide a visual summary of the main causes and effects, and the mechanisms by which they can be mediated. Note that this network graph is not intended to illustrate every cause, mechanism or effect.

In Fig. 6 c), we have divided the cause-effect chain for $k_\perp$ into causes, mechanisms and effects. The primary causes are fundamental processes related with battery operation, i.e. heat transfer, ageing, mechanical, and charge/discharge processes. These are directly linked to the secondary causes, which are changes in key battery states, such as temperature, SOH, SOC, strain or internal stress. Then these changes in battery states are linked to seven underlying mechanisms leading to five primary effects considered in Equation (10) and porous media theory such as Krischer [50]. For example, 1) a change in thermal conductivity in the liquid phase could result from electrolyte consumption [129] if the electrolyte is replaced by gases with low thermal conductivity. 2) The thermal conductivity of the solid phase depends on the phonon and electron conduction, which are influenced by the crystal lattice parameters [133]. 3) Changes in porosity or tortuosity can influence the weighting between the solid and fluid phase and thus the overall through-plane conductivity. 4) According to Equation (10), thermal contact resistances due to nanoscopic contact points must be taken into account for heat conduction. 5) The change in thickness of the stacked layers due to mechanical stresses within the cell or changes in the

microstructure could further influence $k_{\perp}$.

The line colors in Fig. 6 c) illustrate the cause-effect chain of the individual battery states such as SOH, temperature, SOC or internal mechanical stress. An increase in the stress can, for example, change the microcontacts between the stacked layers [135], which is known to affect the thermal contact resistance. The temperature can influence the thermal conduction by phonons [136] and thus the thermal conductivity of every solid phase within the cell. In addition, the thermal expansion influences the microcontact and the microstructure of the cell layers, which both have effects on $k_{\perp}$. SOC can change $k_{\perp}$ through several mechanisms, which are also triggered by temperature or mechanical stress within the cell. Further mechanisms must be taken into account for the battery state SOH. For example, Li-plating or SEI growth changes the composition of the solid phase and the porosity [15], which can affect the overall $k_{\perp}$. In addition, mechanisms such as electrode exfoliation [137] should have a strong influence on the thermal contact resistance. Overall, Fig. 6 c) shows that the discussion of the relationship between battery states and $k_{\perp}$ is not trivial and further experimental and modeling efforts are required in order to understand the cause-effect chain.

3.2. Conductivity of solid non-porous components

As discussed in Subsection 2.2, lithium-ion cells contain solid non-porous components such as the current collectors, whose dimensions and design may influence the thermal conductivities of the stack, as thoroughly discussed for a cylindrical cell by Li et al. [36]. In addition, thermal models require the thermal conductivity of all subcomponents of the cell housing (see Fig. 1), which are solid too. Table 10 lists the thermal conductivity and temperature dependence $\alpha_{k,T}$ of important solid materials that are often used for the stack or the cell housing.

Most of the thermal conductivities in Table 10 are recommended thermal conductivities based on a variety of measurements in the literature. For example, the thermal conductivity of stainless steel from Bogaard et al. [138] is based on 15 different thermal conductivity measurements. Therefore, the thermal conductivity in Table 10 already has a strong data integrity, which is why a comparison of different investigations is dispensed with.

Copper and aluminum show a slight temperature dependence $\alpha_{k,T}$, but a significant dependence on the composition. According to Equation (9), the in-plane thermal conductivity is strongly influenced by the current collectors made of copper and aluminum. Therefore, the small magnitude of $\alpha_{k,T}$ copper and aluminum explains the temperature dependence of $k_{\parallel}$ in Fig. 6 b), which is also close to zero. In addition to the temperature, the composition is also a dominant factor for thermal conductivity. This can be seen when comparing pure aluminum with the alloy 3003. Due to the 1.1% manganese composition of this alloy, the thermal conductivity drops by −35% from 237.5 to 155 W m^{-1} K^{-1}. The strong dependency on the composition is also observed with stainless steel [138]. Therefore, the composition of each component of the cell must be carefully identified for accurate thermal cell models.

The thermal conductivity of pouch foils has a pronounced anisotropic thermal conductivity, which results from the aluminum and polymer layers discussed in Subsection 2.2. Yi et al. [37] measured the thermal conductivity of a pouch foil used in a commercial cell from LG Chem Ltd.. Their measurement results are listed in Table 10, which have a similar thermal conductivity for the in-plane (||) and through-plan (⊥) directions as discussed for the electrode-separator stack in Subsection 3.1. The result of Yi et al. [37] corresponds to theoretical calculations such as those carried out by Rheinfeld et al. [21], which resulted in a thermal conductivity in in-plane (||) and through-plan (⊥) direction of 67.08 and 0.25 W m^{-1} K^{-1}, respectively. The influence of the pouch foil on the through-plane conductivity of the stack $k_{\perp}$ should be small due to the low ratio between foil thickness and total cell thickness of 4%–5% [21,37] and the similarity of the through-plane conductivity of the stack and pouch film.

Table 11
Measured thermal conductivity of porous stack layers k_l applied in electrode-separator stacks of lithium-ion cells. All stack layers are soaked with electrolyte (wet) and do not contain any collector foils or substrate. No information provided is marked with (−).

No.	Ref.	Stack layer	$\frac{T}{\mathrm{K}}$	$\frac{p}{\mathrm{bar}}$	$\frac{k_l}{\mathrm{W\ m^{-1}K^{-1}}}$
1	[52]	NMC	296	6.9 ± 4.6	0.895 ± 0.02
2	[135]	NMC	–	–	0.830
3	[58]	NMC ($\varepsilon = 0.191$)	298	–	0.660
4	[125]	NMC (Pristine)	296	6.9 ± 4.6	0.550 ± 0.01
5	[125]	NMC (Aged)	296	6.9 ± 4.6	0.540 ± 0.02
6	[52]	Separator (PET, Al_2O_3)	296	6.9 ± 4.6	0.375 ± 0.02
7	[52]	Separator (PET, Al_2O_3)	296	6.9 ± 4.6	0.380 ± 0.02
8	[52]	Separator (PET, Al_2O_3)	296	6.9 ± 4.6	0.335 ± 0.02
9	[52]	Separator (PET, Al_2O_3)	296	6.9 ± 4.6	0.290 ± 0.01
10	[52]	Separator (PP, Al_2O_3)	296	6.9 ± 4.6	0.120 ± 0.02
11	[52]	Separator (glass microfiber)	296	6.9 ± 4.6	0.190 ± 0.01
12	[52]	Separator (No. 13 without $LiPF_6$)	296	6.9 ± 4.6	0.220 ± 0.01
13	[52]	Separator	296	6.9 ± 4.6	0.230 ± 0.01
14	[54]	Separator (PP)	–	–	0.334
15	[53]	Separator (PP, PE)	–	–	0.190
16	[53]	Separator (PVDF-HFP[a)], Al_2O_3)	–	–	0.920 ± 0.21
17	[58]	Separator ($\varepsilon = 0.395$)	298	–	0.680
18	[52]	Graphite	296	6.9 ± 4.6	1.270 ± 0.16
19	[52]	Graphite	296	6.9 ± 4.6	1.130 ± 0.24
20	[52]	Graphite	296	6.9 ± 4.6	1.450 ± 0.27
21	[142]	Graphite	295	9.3	0.890
22	[142]	Graphite	295	9.3	0.360
23	[142]	Graphite	295	9.3	1.260
24	[58]	Graphite ($\varepsilon = 0.308$)	298	–	1.450
25	[135]	Graphite	–	–	1.440
26	[125]	Graphite (Pristine)	296	6.9 ± 4.6	0.685 ± 0.02
27	[125]	Graphite (Aged)	296	6.9 ± 4.6	0.615 ± 0.02
28	[52]	LFP	296	6.9 ± 4.6	0.340 ± 0.02
29	[54]	LCO	–	–	1.580
30	[142]	LCO	295	9.3	1.100

a) Hexafluoropropylene.

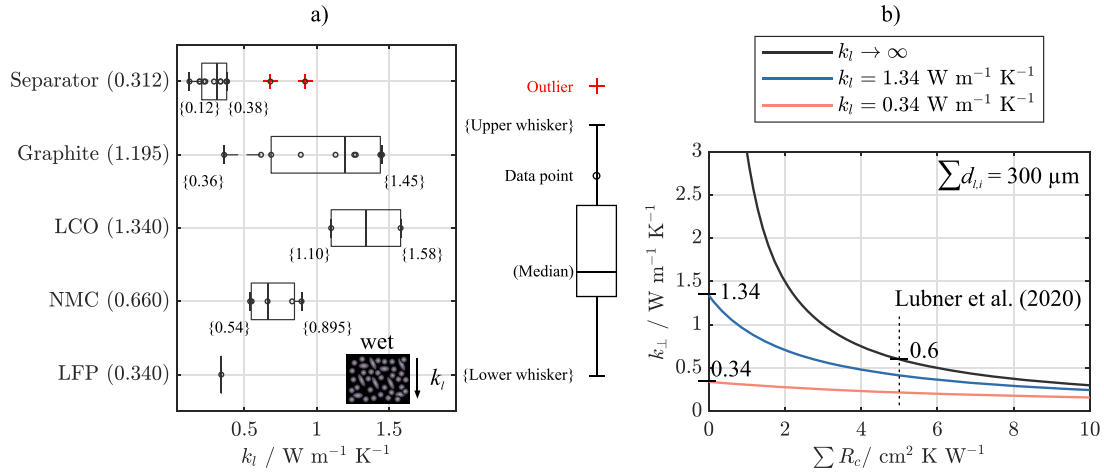

Fig. 7. The thermal conductivity of wet stack layers k_l and the thermal contact resistance R_c, which determine the through-plane conductivity $k_\perp$ of the electrode-separator stack according to Equation (10). a) Boxplot for k_l from Table 11 with recommended (median) conductivities for thermal modeling, indicated by round brackets. b) Dependence of $k_\perp$ on the sum of the thermal contact resistances $\sum R_c$ for a stack thickness of 300 µm and a constant k_l specified in the legend for each stacking layer.

3.3. Conductivity of porous components

This subsection deals with the thermal conductivity of porous stack layers, which can be used in Equations (9) and (10) to calculate $k_\perp$ and $k_\parallel$. Since the pores of an operational lithium-ion cell contain electrolyte, only wet layer conductivities k_l are discussed below. Dry layers are omitted in this subsection, as at least the porosity and tortuosity must be known [50] in order to calculate the wet conductivity, which is often not the case. This is different from heat capacity, where dry measurements are more useful.

Table 11 lists wet conductivities k_l for various separators, anode and cathode coatings used in the electrode-separator stack in Fig. 5. Most of the references in Table 11 give the temperature T, which has a median of 296 K. The SOC and SOH of the full-cell are not included in the header of Table 11 as they are rarely stated in the references, in part because materials such as the separator do not store charge. The compression pressure p is included in Table 11 due to its expected influence on k_l [52].

According to Fig. 2 d), all common stack layers in lithium-ion cells have been measured except of LMO, NCA, silicon-graphite and LTO. Despite the importance of LFP, there is only one experiment for this cathode coating (Table 11, No. 28). Therefore, more k_l measurements are required for LFP to increase integrity and determine uncertainties. It should also be mentioned that the porosity ε is rarely given despite its high effect on k_l. Only Yang et al. [53] and Liebig et al. [58] state the porosity of their stack layers. Therefore, it is recommended to indicate the porosity in future investigations.

Fig. 7 a) displays the medians and whiskers of the mid-ranges of k_l in Table 11. According to this boxplot, separators have a median conductivity of 0.312 W m^{-1} K^{-1} with two identified outliers (Table 11, No. 16, 25). The whiskers and the mid-range of 0.25 W m^{-1} K^{-1} determine the uncertainty of ±52%. Separators in lithium-ion cells are usually made of PET, PE or PP [52], materials with a thermal conductivity below 0.25 W m^{-1} K^{-1} as shown in Table 10. Considering that the thermal conductivity of common electrolytes is below 0.2 W m^{-1} K^{-1} [50,143], the median of 0.312 W m^{-1} K^{-1} is inconsistent. The inconsistency could be explained by the presence of Al_2O_3 (35 W m^{-1} K^{-1} [53]) ceramic particles or coatings, which are used in composite separators to provide pathways for efficient heat transfer [53] and to increase safety [144]. Parikh et al. [145] showed, for example, that the ceramic coatings can increase the thermal conductivity of the separator from 0.2 to 0.6 W m^{-1}K^{-1}, which could explain the outliers in Fig. 7 a). Consequently, the volume of Al_2O_3 particles inside the separator has to be taken into account for the thermal conductivity of the separator, which is rarely the case.

According to the median in Fig. 7 a), wet graphite layers have a thermal conductivity of 1.195 W m^{-1} K^{-1} with an uncertainty of ±60% based on the mid-range of 0.905 W m^{-1} K^{-1}. The large uncertainty is mainly caused by the lower whisker of 0.360 W m^{-1} K^{-1} (Table 11, No. 22). This anode coating was an in-house carbon material that was not graphitized by heat treatments [142]. Therefore, when choosing the right k_l for the anode coating, the heat treatment must also be considered.

According to the box plot in Fig. 7 a), LCO has the highest cathode thermal conductivity followed by NMC and LFP. Yang et al. [146] explained the relationship between LCO and NMC using phonon transport. According to their calculation, the thermal conductivity of NMC decreases with decreasing Co content, which means that LCO has a higher thermal conductivity than NMC111 and NMC111 a higher conductivity than NMC 811. The uncertainties for LCO and NMC in Fig. 7 a) are ±18% and ±25%, respectively. The higher uncertainty of NMC could be caused by different Co contents. Nevertheless, cathode coatings show less uncertainty than graphite coatings.

The temperature dependency $\alpha_{k,T}$ of wet k_l has been poorly investigated in the literature. Only Liebig et al. [58] measured $\alpha_{k,T}$ for a wet graphite, NMC and separator coating and observed an increase in thermal conductivity with increasing temperature. This positive correlation of k_l with T contradicts some of the findings for $k_\perp$ in the literature [34, 50], which is why Liebig et al. [58] questioned the transferability of their results to other battery models. This underscores the need for

Table 12
Estimation of the thermal contact resistance between the stack layers $\sum R_c$ based on thermal conductivity measurements $k_\perp$ in Table 9 (No. 11, 10).

	Sheng et al. [78]	Vertiz et al. [101]	Unit
Calculated $k_\perp$	0.86	1.01	W m^{-1}K^{-1}
Measured $k_\perp$	0.54	0.242	W m^{-1}K^{-1}
Stack thickness $\sum_i d_{l,i}$	35	413	µm
Calculated $\left(\sum_i d_{l,i}\right)/k_\perp$	0.41	4.09	cm^2 K W^{-1}
Measured $\left(\sum_i d_{l,i}\right)/k_\perp$	0.65	17.07	cm^2 K W^{-1}
Estimated $\sum R_c$	0.24	12.98	cm^2 K W^{-1}

further research on the temperature dependence of wet k_l.

The relationship between the degree of lithiation and the thermal conductivity of wet anode and cathode coatings has not yet been measured. Only dry measurements are available in the literature. For example, Gotcu et al. [57] increased the degree of lithiation of dry NMC and LCO coatings from 0 to 1, which in turn increased the thermal conductivity for both coatings by more than 32%. This finding would indicate a negative correlation between the SOC of the full-cell and $k_\perp$ if the graphite conductivity is independent of the SOC. There are neither wet nor dry thermal conductivity measurements for graphite coatings with different degrees of lithiation in the literature. However, molecular dynamics simulations show a strong increase in the graphite thermal conductivity with increasing lithiation [133], which was reasoned by the change in sound velocity with lithiation. This would suggest a positive correlation between the SOC of the full-cell and $k_\perp$. In summary, there are arguments for a positive and arguments for a negative correlation between SOC and $k_\perp$, which is consistent with Fig. 6 b).

According to the study by Richter et al. [52], the thermal conductivity of the wet anode and cathode coatings increases with increasing pressure p, while no significant correlation was measured for the separator. The pressure dependency could be caused either by thermal contact resistances during the measurement or by changing porosity of the active material [147]. The pressure dependence of k_l could explain a correlation between SOC and $k_\perp$ if the pressure in the stack is influenced by the SOC. In addition, Richter et al. [125] examined the effects of different SOH on the thermal conductivity of k_l and found no significant changes with aging. This contradicts Vertiz et al. [101] and Kovachev et al. [129], who measured a sharp drop in $k_\perp$ with aging (Table 9, No. 10, 32). Therefore, more research is needed to clarify this inconsistency.

3.4. Contact resistances

Any heat that flows through a solid-solid [148] or solid-liquid [149] interface must overcome thermal contact resistance in the unit $cm^2\,K\,W^{-1}$. This resistance arises due to the narrowing of the heat flow at the nanoscopic contacts at the interface and the acoustic mismatch between dissimilar materials [135,150]. The thermal contact resistance appears on every length scale of lithium-ion cells. On the nanoscale, intra-grain thermal resistances in active particles such as LCO can reduce the thermal conductivity of the monocrystalline material [151]. In the micrometer scale, there is solid-solid contact resistance between the particles and the binder and solid-liquid contact resistance between the solid phase and the electrolyte. This subsection deals with the macroscale thermal contact resistance within the layer structure of lithium-ion cells (see Fig. 5).

On the macro scale, the thermal contact resistance results from a parallel connection of the resistance caused by the interstitial material and the series connection of the two resistors due to the phonon mismatch and the constriction of the heat flow [135]. Increasing the thermal conductivity of the electrolyte and increasing the particle radius and pressure can therefore reduce the overall contact resistance [135]. In addition, reducing porosity and improving adhesion between the stacked layers can reduce contact thermal resistance [152]. For example, surfactants could be used to control particle size and porosity [153].

There are two types of thermal contact resistance on the macro scale. The first type (R_c) takes into account the interfaces between the stack layers, which are marked in blue and red in Fig. 5. Therefore, this contact resistance occurs several times from the core to the shell of the cell. The second type appears only once, namely between the cell housing and the electrode-separator stack. Gaitonde et al. [154] investigated the second type, which is usually an interface between the separator and the housing. They measured an inverse contact resistance of 670 $W\,m^{-2}\,K^{-1}$ with no significant dependence on pressure or temperature. Gaitonde et al. [154] regarded their results as an upper limit, since the separator was not saturated with electrolyte and the contact resistance generally decreases with liquid interstitial materials [155]. Therefore, further investigations into the thermal contact resistance of the interface between separator and cell housing with electrolyte as interstitial material are warranted.

The thermal contact resistance between the stacked layers was further subdivided into a non-detachable coating-collector interface and a detachable coating-separator interface in Fig. 5. The contact resistance of the coating-collector interface is often neglected [152], probably because of the calendaring during electrode production, but there is no experimental evidence to support this assumption in the literature. Comparable interfaces such as thermally conductive adhesives on aluminum generate a thermal contact resistance between 0.07 and 0.3 $cm^2K\,W^{-1}$ [156]. For the entire stack in Fig. 5, this would mean a contribution of 0.28–1.2 $cm^2K\,W^{-1}$ to the total thermal contact resistance $\sum R_c$ in Equation (10).

In Subsection 3.1, it was mentioned that the measured through-plane conductivity $k_\perp$ of the stack is lower than the calculated value for $k_\perp$ if the contact resistances are neglected ($\sum R_c = 0$). A total thermal contact resistance between the stack layers $\sum R_c$ of 0.24 and 12.98 $cm^2K\,W^{-1}$ could explain the discrepancy between the calculated and measured conductivity $k_\perp$. The range between 0.24 and 12.98 $cm^2K\,W^{-1}$ is described in Table 12 for the experiments conducted by Sheng et al. [78] and Vertiz et al. [101]. To estimate $\sum R_c$, the calculated and measured thermal resistance $\left(\sum_i d_{l,i}\right)/k_\perp$ of the stack is first determined. The difference between these two resistances gives the estimated thermal contact resistance $\sum R_c$ of 0.24 and 12.98 $cm^2\,K\,W^{-1}$. The large variation of the $\sum R_c$ underlines the need for further $k_\perp$ experiments which

Table 13
Measured thermal contact resistances R_c for interfaces within the electrode-separator stack in lithium-ion cells. If R_c can be used in Equation (10) to calculated $k_\perp$, it is cumulated adequately for the total thermal contact resistance $\sum R_c$ for stacks with double coated electrodes. No information provided is marked with (–).

No.	Ref.	Interfaces in R_c	Dry/wet	$\frac{p}{bar}$	$\frac{T}{K}$	$\frac{R_c}{cm^2K\,W^{-1}}$	$\frac{\sum R_c}{cm^2K\,W^{-1}}$
4	[135]	Graphite/Cu	Wet	–	–	0.77 ± 0.04	–
5	[135]	Graphite/Cu	Dry	–	–	2.28 ± 0.22	–
6	[135]	NMC/Cu	Wet	–	–	1.17 ± 0.14	–
7	[135]	NMC/Cu	Dry	–	–	4.84 ± 0.07	–
8	[135]	Separator/NMC Separator/Graphite	Dry	0.34	298	4.76 ± 0.4	9.52
9	[135]	Separator/NMC Separator/Graphite	Wet	0.34	298	2.47 ± 1.4	4.94
10	[152]	Separator/LCO	Dry	–	300	4.20	8.4[a)b)]
11	[152]	Separator/LCO[c)]	Dry	–	300	0.90	1.8[a)b)]
12	[155]	Cu/Graphite Graphite/Separator Separator/LCO LCO/Cu	Wet	8.6 ± 8.6	>263	3.48 ± 0.79	–

a) Thermal contact resistance of coating-collector interface is neglected. b) Thermal contact resistance of anode coating to separator is neglected. c) Separator with amine-based chemical bridging of the interface.

specify the thicknesses and materials of the stacked layers.

The estimates for $\sum R_c$ in Table 12 can be compared with measurement results for $\sum R_c$ in Table 13. All measurement results listed in Table 13 were carried out on stack layers that were either extracted from full-cells or produced in-house. Table 13 also provides information about the interstitial material (dry/wet), the apparent pressure p during the test, the temperature, and the non-detachable interfaces that are included in the measured contact resistance R_c. If R_c can be used to calculate the total contact resistance $\sum R_c$ of the electrode-separator stack, it is also listed in Table 13. For example, No. 9 includes a separator-NMC and a separator-graphite interface. Since both interfaces appear twice in stacks (Fig. 5), R_c is multiplied by two for the total contact resistance $\sum R_c$. By this measure, the results in Table 13 can be used in Equation (10) to calculate $k_\perp$.

Lubner et al. [135] measured a total contact resistance $\sum R_c$ of 4.94 cm^2 W K^{-1}. They investigated R_c with stationary *ex-situ* and transient *in-situ* measurements. For the *ex-situ* measurement, they clamped graphite and NMC electrodes between two copper rods and measured the contact resistance (Table 13, No 4–7) with and without electrolyte. It can be seen that the use of electrolyte as interstitial material (wet) reduces the contact resistance by more than 66% compared to the dry resistance. In addition, wet R_c of the graphite-copper interface is of the same order of magnitude as the cathode-separator interface. This contradicts Vishwakarma et al. [152] who neglected the thermal contact resistance of graphite interfaces. For the *in-situ* measurement, Lubner et al. [135] implemented eight 3-omega thermal conductivity sensors in a single-layer pouch cell. During the formation cycles, they arrived at a contact resistance of 2.47 cm^2 W K^{-1} for an external compaction pressure of 0.34 bar. They assigned this contact resistance to a single anode-separator and cathode-separator interface. Therefore, for double-coated electrode-separator stacks, this would lead to a total contact resistance $\sum R_c$ of 4.94 cm^2 W K^{-1}, which is in the estimated range in Table 12.

Vishwakarma et al. [152] claimed that 88% of the stack's thermal resistance is determined by the cathode-separator interface. They explained the dominance of the cathode-separator interface by a larger mismatch in phonon speed compared to the anode-separator interface. Vishwakarma et al. [152] carried out three stationary conductivity measurements with the same setup as Lubner et al. [135] on dry separator and cathode electrodes. Like Lubner et al. [135], they had to compensate for the resistance of the electrode material. For this compensation, they neglected effects of the electrolyte to the heat transport, which completely contradicts the literature [52,125,142] and overestimates the contact resistance. This likely overestimated and dry contact resistance results in an 8.4 cm^2 W K^{-1} for the entire stack. In addition, Vishwakarma et al. [152] made some surface modifications to the cathode and separator that reduced the $\sum R_c$ to 1.8 cm^2 W K^{-1}.

One of the first R_c measurements was carried out by Ponnappan et al. [155] with a similar test setup as used by Vishwakarma et al. [152] and Lubner et al. [135]. According to the description of the experiment, the resistance of the material $(\sum_i d_{l,i})/k_\perp$ was not subtracted from R_c. Therefore, the R_c stated by Ponnappan et al. [155] includes the contact resistance and the resistance of the material. The R_c of the wet stack (Table 13, No. 1) shows a slight dependence on temperature and pressure. However, due to the detachable Cu-coating interfaces, the results cannot be used directly for $\sum R_c$. The result of Ponnappan et al. [155] of 3.48 cm^2 W K^{-1} can be subtracted by the wet Cu interfaces of Lubner et al. [135] (Table 13, No. 2 and 3), which gives a compensated R_c of 1.54 cm^2 W K^{-1}. This compensated R_c would result in a total contact resistance $\sum R_c$ of 3.08 cm^2 W K^{-1}.

Smaller thermal contact resistances, as reported by Lubner et al. [135], are consistent with the literature. Fig. 7 b) shows the through-plane conductivity $k_\perp$ as a function of the thermal contact resistances $\sum R_c$ with three different values for the stack layers k_l according to Equation (10). The lower value for k_l of 0.34 W m^{-1} K^{-1} is chosen according to the median of wet LFP coating in Figs. 7 a) and 1.34 W m^{-1} K^{-1} according to LCO. The black line ($k_l \to \infty$) represents the maximum $k_\perp$ for a given value of $\sum R_c$. For $\sum R_c$ of Lubner et al. [135] in Table 13, the black line indicates a maximum of 0.6 W m^{-1} K^{-1} for a stack thickness of 300 µm, which is below the maximum of 1.4 W m^{-1} K^{-1} in Table 9 measured for $k_\perp$. Therefore, smaller thermal contact resistances as reported by Lubner et al. [135] are possible. Fig. 7 b) shows that thermal contact resistances $\sum R_c$ and the thermal conductivity of the stack layers k_l equally influence $k_\perp$, which makes their separation difficult.

In summary, the total thermal contact resistance between the stacked stack layers in Equation (10) $\sum R_c$ appears to have a dominant influence on the total through-plane conductivity $k_\perp$. However, compared to other thermophysical properties, $\sum R_c$ is less studied in the literature. In particular, *in-situ* measurements with full-cells of different formats, comparable to the investigations by Lubner et al. [135], could explain different findings for $k_\perp$. In addition, the correlation of $\sum R_c$ with pressure, temperature, and SOH also needs to be better understood.

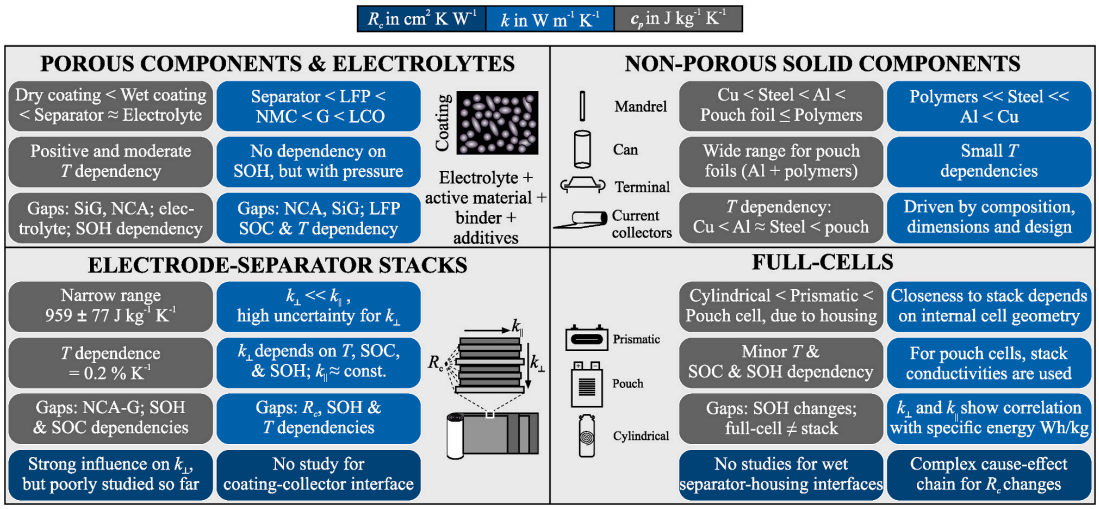

Fig. 8. Summary figure that describes the most important results of this meta-analysis for thermal parameters of lithium-ion cells and their components.

4. Conclusion

This article gives an overview of specific heat capacity and thermal conductivity measurements on cell components and complete lithium-ion cells. To facilitate the parameterization of thermal cell models, this paper calculates recommended medians for both thermal parameters. Furthermore, parameter uncertainties are given which can be used for the error estimation of thermal simulations. The correlation between thermal parameters and common battery states such as temperature, SOC and SOH is also examined. In addition, this review paper reveals missing experiments and gives implication for battery design. A summary of the results is shown in Fig. 8.

4.1. Specific heat capacity

The following conclusion can be drawn for the specific heat capacity of non-porous and porous cell components:

- The electrolyte and dry separator sheets have the highest median heat capacity between 1635 and 1600 J kg^{-1} K^{-1}. Dry anode coatings, cathode coatings and aluminum collectors have a median heat capacity of 718, 764 and 884 J kg^{-1} K^{-1}, respectively. Copper collectors and steel housings introduce the lowest median heat capacity between 387 and 480 J kg^{-1} K^{-1}.
- The specific heat capacity of stack layers is either not correlated with the temperature or is positively correlated (0.0–0.5 K^{-1}). The correlation of SOH or SOC with specific heat capacity has seldom been investigated for stack layers, probably because a characterization would require the disassembly of many cells in different SOHs or SOCs. The few results show either a positive or a negative SOC dependency, while no results are available for the SOH.
- There is a large uncertainty for the heat capacity of the electrolyte of ±80%, which means that further measurements are required to identify outliers and narrow the value range. In addition, no heat capacity experiments were found for dry LTO, silicon-graphite and NCA coatings.

The following conclusion can be drawn for the specific heat capacity of the electrode-separator stack:

- The specific heat capacity of the wet electrode-separator stack shows a slight variation between different stack designs and chemistries of ±77 J kg^{-1} K^{-1} with a median of 959 J kg^{-1} K^{-1}. Variations are caused, for example, by the strong correlation between the coating-collector thickness ratio of the anode and the heat capacity of the stack.
- The temperature dependence of the stack capacity is 0.2 K^{-1}, which corresponds to the temperature dependence of dry cathode coatings for lithium-ion cells.
- Further measurements are required to determine the dependencies of SOC or SOH at the stack level. In addition, no measurements for NCA-G stacks are published in the literature.

The following conclusion can be drawn for the specific heat capacity of full-cells:

- The heat capacity of the full-cell depends heavily on the cell format, which can be explained by the mass fraction of the cell housing. The housing material is responsible for the fact that cylindrical cells (912 J kg^{-1} K^{-1}) have a lower heat capacity than prismatic cells (1041 J kg^{-1} K^{-1}) and prismatic cells have a lower heat capacity than pouch cells (1168 J kg^{-1} K^{-1}).
- The temperature dependence has been well studied with an order of magnitude equal to that of dry cathode coatings. The heat capacity of the full-cell shows a minor SOC dependency between −4% and 7%. In addition, a positive correlation between the specific energy and the specific heat capacity of full-cells can be determined, which is due to a reduced mass fraction of the copper current collectors and cell housing.
- Further experimentation at the stack and full-cell level is required to resolve the discrepancy between the measured heat capacity at the stack and the full-cell level. Moreover, the correlation between the heat capacity of the full-cell and the SOH needs to be deeply studied. Only one study is published, and this study did not reveal any correlation between the heat capacity of full-cells and the SOH.

4.2. Thermal conductivity

The following conclusion can be drawn for the in-plane thermal conductivity of the electrode-separator stack and full-cells:

- The in-plane conductivity ranges within 21 and 40.1 W m^{-1} K^{-1}. Compared to the through-plane conductivity, the in-plane conductivity has a smaller uncertainty and is measured less often in the literature.
- The in-plane conductivity shows a weak negative dependency on SOC, a negligible influence of the temperature, and an unknown relation with SOH. In addition, the measurements indicate a negative correlation between the specific energy of the cell and the in-plane conductivity.
- Experiments for stacks with an NCA cathode or LTO anode are missing for the in-plane conductivity.

The following conclusion can be drawn for the through-plane thermal conductivity of the electrode-separator stack and full-cells:

- The through-plane conductivity of electrode-separator stacks and full-cells is between 0.15 and 1.4 W m^{-1} K^{-1}. The uncertainty of the through-plane conductivity is therefore 81% if the cathode chemistry and the layer thicknesses of the electrode-separators stack are unknown. The high uncertainty likely results from variations in structural parameters such as porosity or thermal contact resistance between the layers.
- In contrast to the in-plane conductivity, the through-plane conductivity shows a dependency on the active material. NMC-G stacks, for example, exceed the median through-plane conductivity of LFP-G by more than 296%. The through-plane conductivity changes between −7% and +33% when the SOC is increased from 0% to 100%. A decrease in SOH significantly reduces the through-plane conductivity, but this statement is only supported by two experimental studies.
- Further tests with specified porosities and layer thicknesses are necessary to quantify the influence of the thermal contact resistance. With regard to temperature dependency, conflicting results have been obtained in the literature, suggesting either a positive or a negative correlation. Therefore, further experiments are needed to correlate the SOH and temperature with the through-plane conductivity.

The following conclusion can be drawn for the thermal conductivity of non-porous and porous cell components:

- The conductivity of all measured stack layers is in the range from 0.12 to 1.58 W m^{-1} K^{-1} with a strong dependence on the material. The uncertainty for the thermal conductivity of the stack layers lies between 18% and 60%. It should be mentioned that porosity is rarely given in the references, which could be a source of uncertainty.
- The relationship between the temperature or the degree of lithiation and the thermal conductivity of the stack layers has been sparsely researched in the literature. Most stack layers have a slight dependence on pressure and weak dependence on SOH. It is therefore unlikely that the SOH dependencies observed at full-cell level are caused by the conductivity of the stack layers.
- Concerning the separator, the volume of inorganic materials such as Al_2O_3 seems to have a strong influence on the thermal conductivity,

which should be taken into account in the cell design. In addition, the effects of the heat treatment of the graphite coating appear to have a large influence on the thermal conductivity, which requires further experimental investigations. Measurements are missing for LMO, NCA, silicon graphite and LTO. Despite the importance of LFP, there is only one experiment for this cathode coating.

Since thermal contact resistances between the stack layers can have a considerable influence on the through-plane conductivity, the test results were summarized in this paper.

- Deviations between the calculated and measured through-plane conductivity indicate a thermal contact resistance between 0.24 and 12.98 $cm^2K\ W^{-1}$. This range of values agrees with the only experiment that directly measured a wet contact resistance of 4.94 $cm^2\ W\ K^{-1}$.
- The paucity of measurements underlines the knowledge gap regarding the thermal contact resistance between the stack layers. In particular, the resistance between the current collector and the active coating has not yet been measured. This can also be found for the thermal contact resistance between the stack and the cell housing, which was not measured for a wet separator interface.

In conclusion, the specific heat capacity and thermal conductivity of lithium-ion cells were measured at every scale, from the stack layers to the entire full-cell. However, there are still gaps in knowledge for both parameters, exacerbated by the increasing variability of cell designs. For specific heat capacity, further research should focus on the inconsistency between the heat capacity of the stack and the heat capacity of the full-cell. With regard to thermal conductivity, there is a need for further research into thermal contact resistance and the dependencies of battery states, particularly SOH. In addition, both thermal parameters must be measured at full-cell level for temperatures above the normal operating window, aiming to improve thermal model parameterization in safety simulations.

Declaration of competing interest

The authors declare that they have no known competing financial interests or personal relationships that could have appeared to influence the work reported in this paper.

Acknowledgements

This work was kindly supported by Innovate UK Battery Advanced for Future Transport Applications (BAFTA) project (104428), the EPSRC Faraday Institution's Multi-Scale Modelling Project [EP/S003053/1, grant number FIRG003], the EPSRC Joint UK-India Clean Energy Centre (JUICE) [EP/P003605/1], the EPSRC Integrated Development of Low-Carbon Energy Systems (IDLES) project [EP/R045518/1], and by the German Federal Ministry for Economic Affairs and Energy (BMWi) [03ET6153C iMoBatt].

Appendix A. Supplementary data

Supplementary data to this article can be found online at https://doi.org/10.1016/j.jpowsour.2021.230829.

Nomenclature

Abbreviations

CC	Current collector
CID	Current interrupt device
CRM	Component-resolved models
DMC	Dimethyl carbonate
EC	Ethylene carbonate
EV	Electric vehicles
HFP	Hexafluoropropylene
ICE	Internal combustion engine
LCO	Lithium-cobalt-oxide
LFP	Lithium-iron-phosphate
LMO	Lithium-manganese-oxide
LRM	Layer-resolved models
LTO	Lithium-titanate-oxide
NCA	Lithium-nickel-cobalt-aluminum-oxide
NiMH	Nickel–metal hydride
NMC	Lithium-nickel-manganese-cobalt-oxide
PA	Polyamide
PE	Polyethylene
PET	Polyethylene terephthalate
PP	Polypropylene
PU	Polyester
PVC	Polyvinyl chloride
PVDF	Polyvinylidene fluoride
SDM	Single-domain models
SEI	Solid-electrolyte interface
SOC	State of charge of full-cell
SOH	State of health of full-cell

Greek symbols and units

$\alpha_{c_p,T}$ in K^{-1}	Temperature dependency of specific heat capacity

$\alpha_{c_p,SOC}$ in %	SOC dependency of specific heat capacity
$\alpha_{c_p,SOH}$ in %	SOH dependency of specific heat capacity
$\alpha_{k,T}$ in K^{-1}	Temperature dependency of thermal conductivity
$\alpha_{k,SOC}$ in %	SOC dependency of thermal conductivity
$\alpha_{k,SOH}$ in %	SOH dependency of thermal conductivity
ε in %	Porosity of cell layer
ε_{ano} in %	Porosity of anode coating
ρ_{solid} in g cm^{-3}	Density of solid phase of porous material
ρ_{fluid} in g cm^{-3}	Density of fluid phase of porous material
ρ_{bulk} in g cm^{-3}	Density of porous material
$\rho_{scm,i}$ in g cm^{-3}	Density of subcomponent inside the solid phase of porous material i

Latin symbols and units

A_{surf} in m^2	Cell surface area
c_{por} in J kg^{-1} K^{-1}	Specific heat capacity of porous material
c_{stack} in J kg^{-1} K^{-1}	Specific heat capacity of the electrode-separator stack
c_{cell} in J kg^{-1} K^{-1}	Specific heat capacity of the full-cell
c_{solid} in J kg^{-1} K^{-1}	Specific heat capacity of solid phase inside porous material
c_{fluid} in J kg^{-1} K^{-1}	Specific heat capacity of fluid phase inside porous material
c_n in J kg^{-1} K^{-1}	Specific heat capacity of solid components outside the electrode-separator stack
c_{ano} in J kg^{-1} K^{-1}	Specific heat capacity of dry anode coating
c_{cat} in J kg^{-1} K^{-1}	Specific heat capacity of dry cathode coating
c_{aCC} in J kg^{-1} K^{-1}	Specific heat capacity of anode current collector
c_{cCC} in J kg^{-1} K^{-1}	Specific heat capacity of cathode current collector
c_{sep} in J kg^{-1} K^{-1}	Specific heat capacity of the dry separator
c_{ele} in J kg^{-1} K^{-1}	Specific heat capacity of the electrolyte
c_m in J kg^{-1} K^{-1}	Molar heat capacity
c_p in J kg^{-1} K^{-1}	Specific heat capacity at constant pressure
c_{scmi} in J kg^{-1} K^{-1}	Specific heat capacity of subcomponent inside the solid phase of porous material i
$d_{l,i}$ in m	Thickness of layer inside the electrode-separator stack
d_{ano} in m	Thickness of anode coating
d_{aCC} in m	Thickness of anode current collector
d_{cat} in m	Thickness of cathode coating
d_{cCC} in m	Thickness of cathode current collector
d_{sep} in m	Thickness of separator
e_{cell} in Wh kg^{-1}	Specific energy of the cell
h_{surf} in W m^{-2} K^{-1}	Heat transfer coefficient at the outer surface of the cell
k_x in W m^{-1} K^{-1}	Thermal conductivity in x-axis direction
k_y in W m^{-1} K^{-1}	Thermal conductivity in y-axis direction
k_z in W m^{-1} K^{-1}	Thermal conductivity in z-axis direction
k_l in W m^{-1} K^{-1}	Thermal conductivity of the electrode-separator stack layer
$k_{\parallel}$ in W m^{-1} K^{-1}	Thermal conductivity in in-plane direction of the electrode-separator stack
$k_{\perp}$ in W m^{-1} K^{-1}	Thermal conductivity in through-plane direction of the electrode-separator stack
k_s in W m^{-1} K^{-1}	Thermal conductivity of solid non-porous components
m_{cell} in kg	Mass of full-cell
m_{ano} in kg	Mass of dry anode coating
m_{cat} in kg	Mass of dry cathode coating
m_{aCC} in kg	Mass of anode current collector
m_{cCC} in kg	Mass of cathode current collector
m_{sep} in kg	Mass of dry separator
m_n in kg	Mass of cell components outside the electrode-separator stack
m_{stack} in kg	Mass of electrode-separator stack
$m_{scm,i}$ in kg	Mass subcomponent inside the solid phase of porous materia
m_c in kg	Mass of cell component
$\dot{q}$ in W m^{-3}	Heat generation inside the cell
Q_{cell} in Ah	Nominal capacity of the full-cell
T_{cell} in K	Cell temperature
T_{amb} in K	Ambient temperature
U_{cell} in V	Nominal voltage of the cell
V_{cell} in m^3	Cell volume

p in bar	Pressure during the measurement
$R_{c,i}$ in cm^2 K W^{-1}	Thermal contact resistance of interface i

References

[1] A. Arya, A.L. Sharma, A glimpse on all-solid-state Li-ion battery (ASSLIB) performance based on novel solid polymer electrolytes: a topical review, J. Mater. Sci. 55 (2020) 6242–6304, https://doi.org/10.1007/s10853-020-04434-8.

[2] T.M. Bandhauer, S. Garimella, T.F. Fuller, A critical review of thermal issues in lithium-ion batteries, J. Electrochem. Soc. 158 (2011) R1, https://doi.org/10.1149/1.3515880.

[3] Y. Zhao, O. Pohl, A.I. Bhatt, G.E. Collis, P.J. Mahon, T. Rüther, A.F. Hollenkamp, A review on battery market trends, second-life reuse, and recycling, Sustain. Chem. 2 (2021) 167–205, https://doi.org/10.3390/suschem2010011.

[4] J.J. Gómez Vilchez, P. Jochem, Powertrain technologies and their impact on greenhouse gas emissions in key car markets, Transport. Res. Transport Environ. 80 (2020) 102214, https://doi.org/10.1016/j.trd.2019.102214.

[5] Y. Liu, Y. Zhu, Y. Cui, Challenges and opportunities towards fast-charging battery materials, Nat. Energy 4 (2019) 540–550, https://doi.org/10.1038/s41560-019-0405-3.

[6] L. Kraft, A. Hoefling, T. Zünd, A. Kunz, M. Steinhardt, J. Tübke, A. Jossen, Implications of the heat generation of LMR-NCM on the thermal behavior of large-format lithium-ion batteries, J. Electrochem. Soc. 168 (2021) 53505, https://doi.org/10.1149/1945-7111/ac0069.

[7] J.V. Barreras, R. de Castro, Y. Wan, T. Dragicevic, A consensus algorithm for multi-objective battery balancing, Energies 14 (2021) 4279, https://doi.org/10.3390/en14144279.

[8] L. Ahmadi, M. Fowler, S.B. Young, R.A. Fraser, B. Gaffney, S.B. Walker, Energy efficiency of Li-ion battery packs re-used in stationary power applications, Sustain. Energy Technol. Asses. 8 (2014) 9–17, https://doi.org/10.1016/j.seta.2014.06.006.

[9] T. Waldmann, M. Wilka, M. Kasper, M. Fleischhammer, M. Wohlfahrt-Mehrens, Temperature dependent ageing mechanisms in Lithium-ion batteries – a Post-Mortem study, J. Power Sources 262 (2014) 129–135, https://doi.org/10.1016/j.jpowsour.2014.03.112.

[10] M. Schimpe, J.V. Barreras, B. Wu, G.J. Offer, Battery degradation-aware current derating: an effective method to prolong lifetime and ease thermal management, J. Electrochem. Soc. 168 (2021) 60506, https://doi.org/10.1149/1945-7111/ac0553.

[11] E. Cabrera-Castillo, F. Niedermeier, A. Jossen, Calculation of the state of safety (SOS) for lithium ion batteries, J. Power Sources 324 (2016) 509–520, https://doi.org/10.1016/j.jpowsour.2016.05.068.

[12] J. Warner, The Handbook of Lithium-Ion Battery Pack Design: Chemistry, Components, Types and Terminology, Elsevier, Amsterdam, 2015.

[13] A. Loges, S. Herberger, P. Seegert, T. Wetzel, A study on specific heat capacities of Li-ion cell components and their influence on thermal management, J. Power Sources 336 (2016) 341–350, https://doi.org/10.1016/j.jpowsour.2016.10.049.

[14] G. Karimi, X. Li, Thermal management of lithium-ion batteries for electric vehicles, Int. J. Energy Res. 37 (2013) 13–24, https://doi.org/10.1002/er.1956.

[15] X.-G. Yang, C.-Y. Wang, Understanding the trilemma of fast charging, energy density and cycle life of lithium-ion batteries, J. Power Sources 402 (2018) 489–498, https://doi.org/10.1016/j.jpowsour.2018.09.069.

[16] M.-T.F. Rodrigues, G. Babu, H. Gullapalli, K. Kalaga, F.N. Sayed, K. Kato, J. Joyner, P.M. Ajayan, A materials perspective on Li-ion batteries at extreme temperatures, Nat. Energy 2 (2017), https://doi.org/10.1038/nenergy.2017.108.

[17] J. Park, W.A. Appiah, S. Byun, D. Jin, M.-H. Ryou, Y.M. Lee, Semi-empirical long-term cycle life model coupled with an electrolyte depletion function for large-format graphite/LiFePO 4 lithium-ion batteries, J. Power Sources 365 (2017) 257–265, https://doi.org/10.1016/j.jpowsour.2017.08.094.

[18] X. Feng, M. Ouyang, X. Liu, L. Lu, Y. Xia, X. He, Thermal runaway mechanism of lithium ion battery for electric vehicles: a review: a review, Energy Storage Mater. 10 (2018) 246–267, https://doi.org/10.1016/j.ensm.2017.05.013.

[19] R. Spotnitz, J. Franklin, Abuse behavior of high-power, lithium-ion cells, J. Power Sources 113 (2003) 81–100, https://doi.org/10.1016/S0378-7753(02)00488-3.

[20] D.D. MacNeil, D. Larcher, J.R. Dahn, Comparison of the reactivity of various carbon electrode materials with electrolyte at elevated temperature, J. Electrochem. Soc. 146 (1999) 3596–3602, https://doi.org/10.1149/1.1392520.

[21] A. Rheinfeld, S. Kosch, S.V. Erhard, P.J. Osswald, B. Rieger, A. Jossen, Electro-thermal modeling of large format lithium-ion pouch cells: a cell temperature dependent linear polarization expression, J. Electrochem. Soc. 163 (2016) A3046–A3062, https://doi.org/10.1149/2.0701614jes.

[22] X. Zhang, R. Klein, A. Subbaraman, S. Chumakov, X. Li, J. Christensen, C. Linder, S.U. Kim, Evaluation of convective heat transfer coefficient and specific heat capacity of a lithium-ion battery using infrared camera and lumped capacitance method, J. Power Sources 412 (2019) 552–558, https://doi.org/10.1016/j.jpowsour.2018.11.064.

[23] W. Mei, Q. Duan, W. Lu, J. Sun, Q. Wang, An investigation on expansion behavior of lithium ion battery based on the thermal-mechanical coupling model, J. Clean. Prod. 274 (2020) 122643, https://doi.org/10.1016/j.jclepro.2020.122643.

[24] X. Feng, L. Lu, M. Ouyang, J. Li, X. He, A 3D thermal runaway propagation model for a large format lithium ion battery module, Energy 115 (2016) 194–208, https://doi.org/10.1016/j.energy.2016.08.094.

[25] X.-G. Yang, G. Zhang, C.-Y. Wang, Computational design and refinement of self-heating lithium ion batteries, J. Power Sources 328 (2016) 203–211, https://doi.org/10.1016/j.jpowsour.2016.08.028.

[26] J. Sturm, A. Frank, A. Rheinfeld, S.V. Erhard, A. Jossen, Impact of electrode and cell design on fast charging capabilities of cylindrical lithium-ion batteries, J. Electrochem. Soc. 167 (2020) 130505, https://doi.org/10.1149/1945-7111/abb40c.

[27] K. Shah, V. Vishwakarma, A. Jain, Measurement of multiscale thermal transport phenomena in Li-ion cells: a review, J. Electrochem. Energy Conserv. Strorage 13 (2016), 030801, https://doi.org/10.1115/1.4034413.

[28] S.-C. Chen, Y.-Y. Wang, C.-C. Wan, Thermal analysis of spirally wound lithium batteries, J. Electrochem. Soc. 153 (2006) A637, https://doi.org/10.1149/1.2168051.

[29] H. Maleki, S.A. Hallaj, J.R. Selman, R.B. Dinwiddie, B. Wang, Thermal properties of lithium-ion battery and components, J. Electrochem. Soc. 146 (1999) 947, https://doi.org/10.1149/1.1391704.

[30] S. Madani, E. Schaltz, S. Knudsen Kær, Review of parameter determination for thermal modeling of lithium ion batteries, Batteries 4 (2018) 20, https://doi.org/10.3390/batteries4020020.

[31] Y. Tang, T. Li, X. Cheng, Review of specific heat capacity determination of lithium-ion battery, Energy Procedia 158 (2019) 4967–4973, https://doi.org/10.1016/j.egypro.2019.01.671.

[32] R. Kantharaj, A.M. Marconnet, Heat generation and thermal transport in lithium-ion batteries: a scale-bridging perspective, Nanoscale Microscale Thermophys. Eng. 23 (2019) 128–156, https://doi.org/10.1080/15567265.2019.1572679.

[33] C.G. Thomas, Research Methodology and Scientific Writing, second ed., Springer; ANE Books, Cham, India, 2021.

[34] M. Steinhardt, E.I. Gillich, M. Stiegler, A. Jossen, Thermal conductivity inside prismatic lithium-ion cells with dependencies on temperature and external compression pressure, J. Energy Storage 32 (2020) 101680, https://doi.org/10.1016/j.est.2020.101680.

[35] M. Guo, R.E. White, Mathematical model for a spirally-wound lithium-ion cell, J. Power Sources 250 (2014) 220–235, https://doi.org/10.1016/j.jpowsour.2013.11.023.

[36] S. Li, N. Kirkaldy, C. Zhang, K. Gopalakrishnan, T. Amietszajew, L.B. Diaz, J. V. Barreras, M. Shams, X. Hua, Y. Patel, G.J. Offer, M. Marinescu, Optimal cell tab design and cooling strategy for cylindrical lithium-ion batteries, J. Power Sources 492 (2021) 229594, https://doi.org/10.1016/j.jpowsour.2021.229594.

[37] J. Yi, U.S. Kim, C.B. Shin, T. Han, S. Park, Three-dimensional thermal modeling of a lithium-ion battery considering the combined effects of the electrical and thermal contact resistances between current collecting tab and lead wire, J. Electrochem. Soc. 160 (2013) A437–A443, https://doi.org/10.1149/2.039303jes.

[38] M. Akbarzadeh, T. Kalogiannis, J. Jaguemont, J. He, L. Jin, M. Berecibar, J. van Mierlo, Thermal modeling of a high-energy prismatic lithium-ion battery cell and module based on a new thermal characterization methodology, J. Energy Storage 32 (2020) 101707, https://doi.org/10.1016/j.est.2020.101707.

[39] A. Rheinfeld, J. Sturm, A. Frank, S. Kosch, S.V. Erhard, A. Jossen, Impact of cell size and format on external short circuit behavior of lithium-ion cells at varying cooling conditions: modeling and simulation, J. Electrochem. Soc. 167 (2020) 13511, https://doi.org/10.1149/2.0112001JES.

[40] H. Lundgren, P. Svens, H. Ekström, C. Tengstedt, J. Lindström, M. Behm, G. Lindbergh, Thermal management of large-format prismatic lithium-ion battery in PHEV application, J. Electrochem. Soc. 163 (2016) A309–A317, https://doi.org/10.1149/2.09411602jes.

[41] Y. Zhao, Y. Patel, T. Zhang, G.J. Offer, Modeling the effects of thermal gradients induced by tab and surface cooling on lithium ion cell performance, J. Electrochem. Soc. 165 (2018) A3169–A3178, https://doi.org/10.1149/2.0901813jes.

[42] C. Forgez, D. Vinh Do, G. Friedrich, M. Morcrette, C. Delacourt, Thermal modeling of a cylindrical LiFePO4/graphite lithium-ion battery, J. Power Sources 195 (2010) 2961–2968, https://doi.org/10.1016/j.jpowsour.2009.10.105.

[43] H. Czichos, T. Saito, L. Smith (Eds.), Springer Handbook of Materials Measurement Methods, Springer, Berlin, 2006.

[44] L. ' Kubičár, V. Bohač, V. Vretanár, Š. Barta, G. Neuer, R. Brandt, Thermophysical properties of heterogeneous structures measured by pulse transient method, Int. J. Thermophys. 26 (2005) 1949–1962, https://doi.org/10.1007/s10765-005-8607-2.

[45] M. Fleckenstein, S. Fischer, O. Bohlen, B. Bäker, Thermal Impedance Spectroscopy - a method for the thermal characterization of high power battery cells, J. Power Sources 223 (2013) 259–267, https://doi.org/10.1016/j.jpowsour.2012.07.144.

[46] P.-L. Lapointe, Application of the thermal impedance spectroscopy method in three dimensions to a large prismatic Li-ion cell, in: 2013 World Electric Vehicle Symposium and Exhibition (EVS27), IEEE, Barcelona, Spain, 2013, pp. 1–6.

[47] E. Barsoukov, J.H. Jang, H. Lee, Thermal impedance spectroscopy for Li-ion batteries using heat-pulse response analysis, J. Power Sources 109 (2002) 313–320, https://doi.org/10.1016/S0378-7753(02)00080-0.

[48] P. Keil, K. Rumpf, A. Jossen, in: Thermal Impedance Spectroscopy for Li-Ion Batteries with an IR Temperature Sensor System, EVS, Barcelona, Spanien, World Electric Vehicle Association, 2013, p. 27.

[49] A. Kwade, W. Haselrieder, R. Leithoff, A. Modlinger, F. Dietrich, K. Droeder, Current status and challenges for automotive battery production technologies, Nat. Energy 3 (2018) 290–300, https://doi.org/10.1038/s41560-018-0130-3.

[50] D. Werner, A. Loges, D.J. Becker, T. Wetzel, Thermal conductivity of Li-ion batteries and their electrode configurations – a novel combination of modelling and experimental approach, J. Power Sources 364 (2017) 72–83, https://doi.org/10.1016/j.jpowsour.2017.07.105.

[51] S.S. Zhang, A review on the separators of liquid electrolyte Li-ion batteries, J. Power Sources 164 (2007) 351–364, https://doi.org/10.1016/j.jpowsour.2006.10.065.

[52] F. Richter, S. Kjelstrup, P.J.S. Vie, O.S. Burheim, Thermal conductivity and internal temperature profiles of Li-ion secondary batteries, J. Power Sources 359 (2017) 592–600, https://doi.org/10.1016/j.jpowsour.2017.05.045.

[53] Y. Yang, X. Huang, Z. Cao, G. Chen, Thermally conductive separator with hierarchical nano/microstructures for improving thermal management of batteries, Nano Energy 22 (2016) 301–309, https://doi.org/10.1016/j.nanoen.2016.01.026.

[54] S.C. Chen, C.C. Wan, Y.Y. Wang, Thermal analysis of lithium-ion batteries, J. Power Sources 140 (2005) 111–124, https://doi.org/10.1016/j.jpowsour.2004.05.064.

[55] M. Lewerenz, G. Fuchs, L. Becker, D.U. Sauer, Irreversible calendar aging and quantification of the reversible capacity loss caused by anode overhang, J. Energy Storage 18 (2018) 149–159, https://doi.org/10.1016/j.est.2018.04.029.

[56] W. Li, K.R. Crompton, C. Hacker, J.K. Ostanek, Comparison of current interrupt device and vent design for 18650 format lithium-ion battery caps, J. Energy Storage 32 (2020) 101890, https://doi.org/10.1016/j.est.2020.101890.

[57] P. Gotcu, W. Pfleging, P. Smyrek, H.J. Seifert, Thermal behaviour of LixMeO2 (Me = Co or Ni + Mn + Co) cathode materials, Phys. Chem. Chem. Phys. 19 (2017) 11920–11930, https://doi.org/10.1039/C7CP00513J.

[58] G. Liebig, U. Kirstein, S. Geißendörfer, F. Schuldt, C. Agert, The impact of environmental factors on the thermal characteristic of a lithium–ion battery, Batteries 6 (2020) 3, https://doi.org/10.3390/batteries6010003.

[59] P. Bohn, G. Liebig, L. Komsiyska, G. Wittstock, Temperature propagation in prismatic lithium-ion-cells after short term thermal stress, J. Power Sources 313 (2016) 30–36, https://doi.org/10.1016/j.jpowsour.2016.02.055.

[60] U. Seong Kim, J. Yi, C.B. Shin, T. Han, S. Park, Modeling the dependence of the discharge behavior of a lithium-ion battery on the environmental temperature, J. Electrochem. Soc. 158 (2011) A611, https://doi.org/10.1149/1.3565179.

[61] V. Vishwakarma, A. Jain, Measurement of in-plane thermal conductivity and heat capacity of separator in Li-ion cells using a transient DC heating method, J. Power Sources 272 (2014) 378–385, https://doi.org/10.1016/j.jpowsour.2014.08.066.

[62] P. Gotcu, H.J. Seifert, Thermophysical properties of $LiCoO_2$-$LiMn_2O_4$ blended electrode materials for Li-ion batteries, Phys. Chem. Chem. Phys. 18 (2016) 10550–10562, https://doi.org/10.1039/c6cp00887a.

[63] J. Nanda, S.K. Martha, W.D. Porter, H. Wang, N.J. Dudney, M.D. Radin, D. J. Siegel, Thermophysical properties of LiFePO4 cathodes with carbonized pitch coatings and organic binders: experiments and first-principles modeling, J. Power Sources 251 (2014) 8–13, https://doi.org/10.1016/j.jpowsour.2013.11.022.

[64] C. Heumann, Introduction to Statistics and Data Analysis: with Exercises, Solutions and Applications in R, Springer, Cham, 2016.

[65] W.J. Peppel, Preparation and properties of the alkylene carbonates, Ind. Eng. Chem. 50 (1958) 767–770, https://doi.org/10.1021/ie50581a030.

[66] F. Comelli, A. Bigi, D. Vitalini, K. Rubini, Densities, viscosities, refractive indices, and heat capacities of poly(ethylene glycol- ran -propylene glycol) + esters of carbonic acid at (293.15 and 313.15) K and at atmospheric pressure, J. Chem. Eng. Data 55 (2010) 205–210, https://doi.org/10.1021/je900307z.

[67] Verein Deutscher Ingenieure, VDI-Gesellschaft Verfahrenstechnik und Chemieingenieurwesen, VDI-Wärmeatlas: Mit 320 Tabellen, eleventh., bearb. und erw. Aufl., Springer Vieweg, Berlin, 2013.

[68] M. Singh, J. Kaiser, H. Hahn, Thick electrodes for high energy lithium ion batteries, J. Electrochem. Soc. 162 (2015) A1196–A1201, https://doi.org/10.1149/2.0401507jes.

[69] U. Gaur, S.-f. Lau, B.B. Wunderlich, B. Wunderlich, Heat capacity and other thermodynamic properties of linear macromolecules. VIII. Polyesters and polyamides, J. Phys. Chem. Ref. Data 12 (1983) 65–89, https://doi.org/10.1063/1.555678.

[70] U. Gaur, B. Wunderlich, Heat capacity and other thermodynamic properties of linear macromolecules. II. Polyethylene, J. Phys. Chem. Ref. Data 10 (1981) 119–152, https://doi.org/10.1063/1.555636.

[71] J.E. Mark, Physical Properties of Polymers Handbook, second., Springer Science+Business Media LLC, New York, NY, 2007.

[72] D. Oehler, J. Bender, P. Seegert, T. Wetzel, Investigation of the Effective Thermal Conductivity of Cell Stacks of Li-Ion Batteries, Energy Technology, 2020, p. 2000722, https://doi.org/10.1002/ente.202000722.

[73] S. Picard, D.T. Burns, P. Roger, Determination of the specific heat capacity of a graphite sample using absolute and differential methods, Metrologia 44 (2007) 294–302, https://doi.org/10.1088/0026-1394/44/5/005.

[74] T. Aree, H.-B. Bürgi, Specific heat of molecular crystals from atomic mean square displacements with the Einstein, Debye, and Nernst-Lindemann models, J. Phys. Chem. B 110 (2006) 26129–26134, https://doi.org/10.1021/jp0636322.

[75] Y.S. Touloukian, E.H. Buyco, Specific heat - metallic elements and alloys, in: Defense Technical Information Center, Thermophysical Properties of Matter, 1970.

[76] D.R. Lide, CRC Handbook of Chemistry and Physics, 2003-2004: A Ready-Reference Book of Chemical and Physical Data, eighthfourthth ed., CRC Press, Boca Raton, Fla, 2003.

[77] T. Bandhauer, S. Garimella, T.F. Fuller, Electrochemical-thermal modeling to evaluate battery thermal management strategies: I. Side cooling, J. Electrochem. Soc. 162 (2015) A125–A136, https://doi.org/10.1149/2.0571501jes.

[78] L. Sheng, L. Su, H. Zhang, Experimental determination on thermal parameters of prismatic lithium ion battery cells, Int. J. Heat Mass Tran. 139 (2019) 231–239, https://doi.org/10.1016/j.ijheatmasstransfer.2019.04.143.

[79] L. Sheng, Z. Zhang, L. Su, H. Zhang, H. Zhang, Y. Fang, K. Li, W. Ye, Quasi steady state method to measure thermophysical parameters of cylindrical lithium ion batteries, J. Power Sources 485 (2021) 229342, https://doi.org/10.1016/j.jpowsour.2020.229342.

[80] P.J. Osswald, S.V. Erhard, A. Noel, P. Keil, F.M. Kindermann, H. Hoster, A. Jossen, Current density distribution in cylindrical Li-Ion cells during impedance measurements, J. Power Sources 314 (2016) 93–101, https://doi.org/10.1016/j.jpowsour.2016.02.070.

[81] A. Petit, P.L. Dulong, Recherches sur quelques points importants de la théorie de la chaleur, Annales de chimie et de physique, 1819, pp. 395–413.

[82] U. Grigull, W. Blanke, Thermophysikalische Stoffgrößen, Springer Berlin Heidelberg, Berlin, Heidelberg, 1989.

[83] Y. Saito, K. Kanari, K. Takano, T. Masuda, A calorimetric study on a cylindrical type lithium secondary battery by using a twin-type heat conduction calorimeter, Thermochim. Acta 296 (1997) 75–85, https://doi.org/10.1016/S0040-6031(97)00083-X.

[84] W. Hesse, Aluminium-Werkstoff-Datenblätter: Deutsch, seventhth ed., Beuth Verlag GmbH, Berlin, 2016.

[85] Y.S. Touloukian, C.Y. Ho, Part II: thermophyslcal properties of seven materials, in: THERMOPHYSICAL PROPERTIES OF SELECTED AEROSPACE MATERIALS, Defense Technical Information Center, 1977.

[86] R.H. Bogaard, P.D. Desai, H.H. Li, C.Y. Ho, Thermophysical properties of stainless steels, Thermochim. Acta 218 (1993) 373–393, https://doi.org/10.1016/0040-6031(93)80437-F.

[87] K.A. Murashko, A.V. Mityakov, J. Pyrhönen, V.Y. Mityakov, S.S. Sapozhnikov, Thermal parameters determination of battery cells by local heat flux measurements, J. Power Sources 271 (2014) 48–54, https://doi.org/10.1016/j.jpowsour.2014.07.117.

[88] M. Shadman Rad, D.L. Danilov, M. Baghalha, M. Kazemeini, P.H.L. Notten, Adaptive thermal modeling of Li-ion batteries, Electrochim. Acta 102 (2013) 183–195, https://doi.org/10.1016/j.electacta.2013.03.167.

[89] C. Vargel, Corrosion of Aluminium, first. ed., Elsevier, Amsterdam, 2004.

[90] J. Zhang, B. Wu, Z. Li, J. Huang, Simultaneous estimation of thermal parameters for large-format laminated lithium-ion batteries, J. Power Sources 259 (2014) 106–116, https://doi.org/10.1016/j.jpowsour.2014.02.079.

[91] A.W. Golubkov, D. Fuchs, J. Wagner, H. Wiltsche, C. Stangl, G. Fauler, G. Voitic, A. Thaler, V. Hacker, Thermal-runaway experiments on consumer Li-ion batteries with metal-oxide and olivin-type cathodes, RSC Adv. 4 (2014) 3633–3642, https://doi.org/10.1039/C3RA45748F.

[92] A.W. Golubkov, S. Scheikl, R. Planteu, G. Voitic, H. Wiltsche, C. Stangl, G. Fauler, A. Thaler, V. Hacker, Thermal runaway of commercial 18650 Li-ion batteries with LFP and NCA cathodes – impact of state of charge and overcharge, RSC Adv. 5 (2015) 57171–57186, https://doi.org/10.1039/c5ra05897j.

[93] C. Essl, A.W. Golubkov, E. Gasser, M. Nachtnebel, A. Zankel, E. Ewert, A. Fuchs, Comprehensive hazard analysis of failing automotive lithium-ion batteries in overtemperature experiments, Batteries 6 (2020) 30, https://doi.org/10.3390/batteries6020030.

[94] J. Marshall, D. Gastol, R. Sommerville, B. Middleton, V. Goodship, E. Kendrick, Disassembly of Li ion cells—characterization and safety considerations of a recycling scheme, Metals 10 (2020) 773, https://doi.org/10.3390/met10060773.

[95] Di Pan, H. Guo, S. Tang, X. Li, Z. Wang, W. Peng, J. Wang, G. Yan, Evaluating the accuracy of electro-thermal coupling model in lithium-ion battery via altering internal resistance acquisition methods, J. Power Sources 463 (2020) 228174, https://doi.org/10.1016/j.jpowsour.2020.228174.

[96] X. Cheng, Y. Tang, Z. Wang, Thermal property measurements of a large prismatic lithium-ion battery for electric vehicles, J. Therm. Sci. (2021), https://doi.org/10.1007/s11630-021-1398-3.

[97] R. Zhao, J. Liu, J. Gu, The effects of electrode thickness on the electrochemical and thermal characteristics of lithium ion battery, Appl. Energy 139 (2015) 220–229, https://doi.org/10.1016/j.apenergy.2014.11.051.

[98] M. Steinhardt, E.I. Gillich, A. Rheinfeld, L. Kraft, M. Spielbauer, O. Bohlen, A. Jossen, Low-effort determination of heat capacity and thermal conductivity for cylindrical 18650 and 21700 lithium-ion cells, J. Energy Storage 42 (2021) 103065, https://doi.org/10.1016/j.est.2021.103065.

[99] J. Geder, R. Arunachala, S. Jairam, A. Jossen, Thermal Behavior of Aged Lithium-Ion Batteries: Calorimetric Observations, IEEE Green Energy and Systems Conference (IGESC), Long Beach, CA, USA, 2015, pp. 24–29.

[100] S.J. Bazinski, X. Wang, Experimental study on the influence of temperature and state-of-charge on the thermophysical properties of an LFP pouch cell, J. Power Sources 293 (2015) 283–291, https://doi.org/10.1016/j.jpowsour.2015.05.084.

[101] G. Vertiz, M. Oyarbide, H. Macicior, O. Miguel, I. Cantero, P. Fernandez de Arroiabe, I. Ulacia, Thermal characterization of large size lithium-ion pouch cell based on 1d electro-thermal model, J. Power Sources 272 (2014) 476–484, https://doi.org/10.1016/j.jpowsour.2014.08.092.

[102] M.B. Ahmed, S. Shaik, A. Jain, Measurement of radial thermal conductivity of a cylinder using a time-varying heat flux method, Int. J. Therm. Sci. 129 (2018) 301–308, https://doi.org/10.1016/j.ijthermalsci.2018.03.008.

[103] A.A. Pesaran, M. Keyser, Thermal characteristics of selected EV and HEV batteries, in: 2001 16th Annual Battery Conference on Applications and Advances, Long Beach, CA, USA, I E E E, Piscataway, Jan, 2001, pp. 219–225.

[104] T.S. Bryden, B. Dimitrov, G. Hilton, C. Ponce de León, P. Bugryniec, S. Brown, D. Cumming, A. Cruden, Methodology to determine the heat capacity of lithium-ion cells, J. Power Sources 395 (2018) 369–378, https://doi.org/10.1016/j.jpowsour.2018.05.084.

[105] M. Al-Zareer, A. Michalak, C. Da Silva, C.H. Amon, Predicting specific heat capacity and directional thermal conductivities of cylindrical lithium-ion

batteries: a combined experimental and simulation framework, Appl. Therm. Eng. 182 (2021) 116075, https://doi.org/10.1016/j.applthermaleng.2020.116075.
[106] X. Liu, Z. Wu, S.I. Stoliarov, M. Denlinger, A. Masias, K. Snyder, Heat release during thermally-induced failure of a lithium ion battery: impact of cathode composition, Fire Saf. J. 85 (2016) 10–22, https://doi.org/10.1016/j.firesaf.2016.08.001.
[107] C. Lin, H. Wen, L. Liu, S. Liu, T. Ma, B. Fan, F. Wang, Heat generation quantification of high-specific-energy 21700 battery cell using average and variable specific heat capacities, Appl. Therm. Eng. 184 (2021) 116215, https://doi.org/10.1016/j.applthermaleng.2020.116215.
[108] K. Murashko, D. Li, D.L. Danilov, P.H.L. Notten, J. Pyrhönen, J. Jokiniemi, Applicability of heat generation data in determining the degradation mechanisms of cylindrical Li-ion batteries, J. Electrochem. Soc. 168 (2021) 10511, https://doi.org/10.1149/1945-7111/abd832.
[109] S.J. Drake, D.A. Wetz, J.K. Ostanek, S.P. Miller, J.M. Heinzel, A. Jain, Measurement of anisotropic thermophysical properties of cylindrical Li-ion cells, J. Power Sources 252 (2014) 298–304, https://doi.org/10.1016/j.jpowsour.2013.11.107.
[110] K.A. Murashko, J. Pyrhönen, J. Jokiniemi, Determination of the through-plane thermal conductivity and specific heat capacity of a Li-ion cylindrical cell, Int. J. Heat Mass Tran. 162 (2020) 120330, https://doi.org/10.1016/j.ijheatmasstransfer.2020.120330.
[111] L.H. Saw, H.M. Poon, H.S. Thiam, Z. Cai, W.T. Chong, N.A. Pambudi, Y.J. King, Novel thermal management system using mist cooling for lithium-ion battery packs, Appl. Energy 223 (2018) 146–158, https://doi.org/10.1016/j.apenergy.2018.04.042.
[112] N.S. Spinner, R. Mazurick, A. Brandon, S.L. Rose-Pehrsson, S.G. Tuttle, Analytical, numerical and experimental determination of thermophysical properties of commercial 18650 LiCoO 2 lithium-ion battery, J. Electrochem. Soc. 162 (2015) A2789–A2795, https://doi.org/10.1149/2.0871514jes.
[113] J.-S. Hong, H. Maleki, S. Al Hallaj, L. Redey, J.R. Selman, Electrochemical-calorimetric studies of lithium-ion cells, J. Electrochem. Soc. 145 (1998) 1489–1501, https://doi.org/10.1149/1.1838509.
[114] H. Ruan, J. Jiang, B. Sun, W. Gao, L. Wang, W. Zhang, Online estimation of thermal parameters based on a reduced wide-temperature-range electro-thermal coupled model for lithium-ion batteries, J. Power Sources 396 (2018) 715–724, https://doi.org/10.1016/j.jpowsour.2018.03.075.
[115] J.V. Barreras, C. Fleischer, A.E. Christensen, M. Swierczynski, E. Schaltz, S. J. Andreasen, D.U. Sauer, An advanced HIL simulation battery model for battery management system testing, IEEE Trans. Ind. Appl. 52 (2016) 5086–5099, https://doi.org/10.1109/TIA.2016.2585539.
[116] A. Eddahech, O. Briat, J.-M. Vinassa, Thermal characterization of a high-power lithium-ion battery: potentiometric and calorimetric measurement of entropy changes, Energy 61 (2013) 432–439, https://doi.org/10.1016/j.energy.2013.09.028.
[117] E. Schuster, C. Ziebert, A. Melcher, M. Rohde, H.J. Seifert, Thermal behavior and electrochemical heat generation in a commercial 40 Ah lithium ion pouch cell, J. Power Sources 286 (2015) 580–589, https://doi.org/10.1016/j.jpowsour.2015.03.170.
[118] S. Balkur, N. Roy Chowdhury, J. Groot, T. Thiringer, A cost and time effective novel methodology to determine specific heat capacity of lithium-ion cells, J. Power Sources 500 (2021) 229981, https://doi.org/10.1016/j.jpowsour.2021.229981.
[119] B. Rieger, S.V. Erhard, K. Rumpf, A. Jossen, A new method to model the thickness change of a commercial pouch cell during discharge, J. Electrochem. Soc. 163 (2016) A1566–A1575, https://doi.org/10.1149/2.0441608jes.
[120] C.-H. Doh, Y.-C. Ha, S.-w. Eom, Entropy measurement of a large format lithium ion battery and its application to calculate heat generation, Electrochim. Acta 309 (2019) 382–391, https://doi.org/10.1016/j.electacta.2019.04.026.
[121] J. Jaguemont, M. Sokkeh, S. Hosen, L. Jin, G. Qiao, T. Kalogiannis, J. van Mierlo, 1D-Thermal analysis and electro-thermal modeling of prismatic-shape LTO and NMC batteries, in: 2019 IEEE Vehicle Power and Propulsion Conference (VPPC), IEEE, Hanoi, Vietnam, 14.10.2019 - 17.10.2019, pp. 1–5.
[122] F.J. Günter, C. Burgstaller, F. Konwitschny, G. Reinhart, Influence of the electrolyte quantity on lithium-ion cells, J. Electrochem. Soc. 166 (2019) A1709–A1714, https://doi.org/10.1149/2.0121910jes.
[123] S.J. An, J. Li, D. Mohanty, C. Daniel, B.J. Polzin, J.R. Croy, S.E. Trask, D.L. Wood, Correlation of electrolyte volume and electrochemical performance in lithium-ion pouch cells with graphite anodes and NMC532 cathodes, J. Electrochem. Soc. 164 (2017) A1195–A1202, https://doi.org/10.1149/2.1131706jes.
[124] R. Rizk, H. Louahlia, H. Gualous, P. Schaetzel, Experimental analysis and transient thermal modelling of a high capacity prismatic lithium-ion battery, Int. Commun. Heat Mass Tran. 94 (2018) 115–125, https://doi.org/10.1016/j.icheatmasstransfer.2018.03.018.
[125] F. Richter, P.J.S. Vie, S. Kjelstrup, O.S. Burheim, Measurements of ageing and thermal conductivity in a secondary NMC-hard carbon Li-ion battery and the impact on internal temperature profiles, Electrochim. Acta 250 (2017) 228–237, https://doi.org/10.1016/j.electacta.2017.07.173.
[126] Y. Ye, L.H. Saw, Y. Shi, K. Somasundaram, A.A.O. Tay, Effect of thermal contact resistances on fast charging of large format lithium ion batteries, Electrochim. Acta 134 (2014) 327–337, https://doi.org/10.1016/j.electacta.2014.04.134.
[127] L. Aiello, G. Kovachev, B. Brunnsteiner, M. Schwab, G. Gstrein, W. Sinz, C. Ellersdorfer, In situ measurement of orthotropic thermal conductivity on commercial pouch lithium-ion batteries with thermoelectric device, Batteries 6 (2020) 10, https://doi.org/10.3390/batteries6010010.
[128] S.J. Bazinski, X. Wang, B.P. Sangeorzan, L. Guessous, Measuring and assessing the effective in-plane thermal conductivity of lithium iron phosphate pouch cells, Energy 114 (2016) 1085–1092, https://doi.org/10.1016/j.energy.2016.08.087.
[129] G. Kovachev, A. Astner, G. Gstrein, L. Aiello, J. Hemmer, W. Sinz, C. Ellersdorfer, Thermal conductivity in aged Li-ion cells under various compression conditions and state-of-charge, Batteries 7 (2021) 42, https://doi.org/10.3390/batteries7030042.
[130] A. Loges, S. Herberger, D. Werner, T. Wetzel, Thermal characterization of Li-ion cell electrodes by photothermal deflection spectroscopy, J. Power Sources 325 (2016) 104–115, https://doi.org/10.1016/j.jpowsour.2016.05.082.
[131] K.A. Murashko, A.V. Mityakov, V.Y. Mityakov, S.Z. Sapozhnikov, J. Pyrhonen, Heat flux based method for determination of thermal parameters of the cylindrical Li-ion battery: uncertainty analysis, in: 2017 19th European Conference on Power Electronics and Applications (EPE'17 ECCE Europe), IEEE, Warsaw, Poland, 2017. P.1-P.10.
[132] Y. Ye, Y. Shi, A.A.O. Tay, Electro-thermal cycle life model for lithium iron phosphate battery, J. Power Sources 217 (2012) 509–518, https://doi.org/10.1016/j.jpowsour.2012.06.055.
[133] W. Ju, C. Zhu, Z. Wei, Intercalated ion tuning of the cross-plane thermal transport properties of graphite, AIP Adv. 10 (2020) 95225, https://doi.org/10.1063/5.0023229.
[134] J. Cho, M.D. Losego, H.G. Zhang, H. Kim, J. Zuo, I. Petrov, D.G. Cahill, P. V. Braun, Electrochemically tunable thermal conductivity of lithium cobalt oxide, Nat. Commun. 5 (2014) 4035, https://doi.org/10.1038/ncomms5035.
[135] S.D. Lubner, S. Kaur, Y. Fu, V. Battaglia, R.S. Prasher, Identification and characterization of the dominant thermal resistance in lithium-ion batteries using operando 3-omega sensors, J. Appl. Phys. 127 (2020) 105104, https://doi.org/10.1063/1.5134459.
[136] H. Ibach, H. Lüth, Solid-State Physics: an Introduction to Principles of Materials Science, second ed., Springer, Berlin, Heidelberg, 1996.
[137] C.R. Birkl, M.R. Roberts, E. McTurk, P.G. Bruce, D.A. Howey, Degradation diagnostics for lithium ion cells, J. Power Sources 341 (2017) 373–386, https://doi.org/10.1016/j.jpowsour.2016.12.011.
[138] R.H. Bogaard, Thermal conductivity of selected stainless steels, in: T. Ashworth, D. R. Smith (Eds.), Thermal Conductivity 18, Springer Verlag, Boston, MA, 2012, pp. 175–185.
[139] R.W. Powell, C.Y. Ho, P.E. Liley, Thermal Conductivity of Selected Materials, 1966.
[140] F.C. Chen, Y.M. Poon, C.L. Choy, Thermal diffusivity of polymers by the flash method, Polymer 18 (1977) 129–136, https://doi.org/10.1016/0032-3861(77)90027-1.
[141] D.E. Kline, Thermal conductivity studies of polymers, J. Polym. Sci. 50 (1961) 441–450, https://doi.org/10.1002/pol.1961.1205015413.
[142] O.S. Burheim, M.A. Onsrud, J.G. Pharoah, F. Vullum-Bruer, P.J.S. Vie, Thermal conductivity, heat sources and temperature profiles of Li-ion batteries, ECS Trans. 58 (2014) 145–171, https://doi.org/10.1149/05848.0145ecst.
[143] D. Oehler, P. Seegert, T. Wetzel, Modeling the Thermal Conductivity of Porous Electrodes of Li-Ion Batteries as a Function of Microstructure Parameters, Energy Technol, 2020, p. 2000574, https://doi.org/10.1002/ente.202000574.
[144] D.H. Doughty, Vehicle Battery Safety Roadmap Guidance, 2012.
[145] D. Parikh, C.J. Jafta, B.P. Thapaliya, J. Sharma, H.M. Meyer, C. Silkowski, J. Li, Al2O3/TiO2 coated separators: roll-to-roll processing and implications for improved battery safety and performance, J. Power Sources 507 (2021) 230259, https://doi.org/10.1016/j.jpowsour.2021.230259.
[146] H. Yang, C.N. Savory, B.J. Morgan, D.O. Scanlon, J.M. Skelton, A. Walsh, Chemical trends in the lattice thermal conductivity of Li(Ni, Mn, Co)O 2 (NMC) battery cathodes, Chem. Mater. 32 (2020) 7542–7550, https://doi.org/10.1021/acs.chemmater.0c02908.
[147] A. Vadakkepatt, B. Trembacki, S.R. Mathur, J.Y. Murthy, Bruggeman's exponents for effective thermal conductivity of lithium-ion battery electrodes, J. Electrochem. Soc. 163 (2016) A119–A130, https://doi.org/10.1149/2.0151602jes.
[148] C.V. Madhusudana, Thermal Contact Conductance, Springer, New York, NY, 1996.
[149] S.C. Somé, D. Delaunay, V. Gaudefroy, Comparison and validation of thermal contact resistance models at solid–liquid interface taking into account the wettability parameters, Appl. Therm. Eng. 61 (2013) 531–540, https://doi.org/10.1016/j.applthermaleng.2013.08.032.
[150] F. Hao, D. Fang, Z. Xu, Thermal transport in crystalline Si/Ge nano-composites: atomistic simulations and microscopic models, Appl. Phys. Lett. 100 (2012) 91903, https://doi.org/10.1063/1.3688943.
[151] J. He, L. Zhang, L. Liu, Thermal transport in monocrystalline and polycrystalline lithium cobalt oxide, Phys. Chem. Chem. Phys. 21 (2019) 12192–12200, https://doi.org/10.1039/c9cp01585j.
[152] V. Vishwakarma, C. Waghela, Z. Wei, R. Prasher, S.C. Nagpure, J. Li, F. Liu, C. Daniel, A. Jain, Heat transfer enhancement in a lithium-ion cell through improved material-level thermal transport, J. Power Sources 300 (2015) 123–131, https://doi.org/10.1016/j.jpowsour.2015.09.028.
[153] C. Li, W. Yang, W. He, X. Zhang, J. Zhu, Multifunctional surfactants for synthesizing high-performance energy storage materials, Energy Storage Mater. 43 (2021) 1–19, https://doi.org/10.1016/j.ensm.2021.08.033.
[154] A. Gaitonde, A. Nimmagadda, A. Marconnet, Measurement of interfacial thermal conductance in Lithium ion batteries, J. Power Sources 343 (2017) 431–436, https://doi.org/10.1016/j.jpowsour.2017.01.019.
[155] R. Ponnappan, T.S. Ravigururajan, Contact thermal resistance of Li-ion cell electrode stack, J. Power Sources 129 (2004) 7–13, https://doi.org/10.1016/j.jpowsour.2003.11.006.
[156] P. Teertstra, Thermal conductivity and contact resistance measurements for adhesives, in: Proceedings of the ASME InterPACK Conference - 2007, Vancouver, British Columbia, Canada, ASME, New York, NY, 2007, pp. 381–388.

5 Conclusion and outlook

The performance of lithium-ion cells is largely determined by their temperature. For example, if the cell temperature is outside the optimal range, cell aging can increase significantly and the state of safety of a lithium-ion cell deteriorates at temperatures above 80 °C, as self-sustaining exothermic reactions can occur. Due to aging or safety concerns, the battery management system can reduce battery power if the temperature rises too much, affecting consumer acceptance in situations such as fast charging. In addition, design trends toward a more sustainable battery cell could increase cell volume to facilitate recycling and favor high-power over high-energy electrodes to reduce overall battery energy. Both design trends have the potential to worsen temperature rise and gradients due to higher C-rates and a longer characteristic length from the cell core to the cell environment. Therefore, the modeling and optimization of the temperature behavior of lithium-ion cells is an important research discipline both now and in the future.

The thermal conductivity through the layers of the electrode-separator stack influences both the spatial temperature distribution and the temperature increase of the cell over time. In most cases, the heat within the cell flows perpendicularly through the stack-layers to the external heat sink. This applies, for example, to surface-cooled cylindrical cells, base plate-cooled prismatic cells or stacked pouch cells with cooling fins in between. In general, the spatial temperature difference is small when the through-plane conductivity is high. Smaller spatial temperature differences mean less uncertainty about the maximum cell temperature and lower aging rates are likely because the cell is operated more homogeneously. The increase in the mean cell temperature is strongly influenced by the thermal conductivity in the presence of strong cooling or heating. Since the mean temperature influences the mechanical, electrochemical and aging properties, the temperature is taken into account in various simulation studies. Therefore, the through-plane conductivity is very important for thermal modeling of lithium-ion cells, especially in connection with battery thermal management systems. As a result, this thesis aims to measure the through-plane conductivity and examine its dependencies on battery state variables such as temperature and state of charge.

In this thesis, the guarded hot plate method for measuring thermal conductivity was adapted for prismatic lithium-ion cells for the first time. The advantage of the guarded hot plate method is the low measurement uncertainty and the widespread use in the field of thermal conductivity measurement. When a prismatic cell is measured using this method, the result will be affected by the thermal conductivity of the cell housing and the stack inside the cell. The challenge of evaluating the through-plane conductivity from the measurement data is to compensate for the influences emanating from the cell housing. The effects of the cell housing were compensated by first measuring the electrical resistance of the housing and using theories such as Wiedemann-Franz to derive the thermal conductivity of the housing. This compensation constitutes the main innovation to the field by this thesis but it also increases the measurement uncertainty significantly from 2% to 6%.

The variant-convective cooling method for cylindrical cells was developed in this thesis to measure the through-plane conductivity of the jelly roll in cylindrical cells. Similar to thermal impedance

spectroscopy, the variant-convective cooling method can measure the conductivity of any cell format and only requires standard laboratory equipment. Besides being one of the first studies to introduce this method for cylindrical cells, an evaluation technique has been developed that does not require complex finite element method models to calculate the through-plane conductivity. In addition, a detailed analysis of the measurement uncertainties for the variant-convective cooling method is presented for the first time. According to this analysis, the uncertainty is 6%, as in the GHPs method.

The through-plane conductivity increases by 7% to 9% when the SOC of an NMC-G cell was increased from approximately 10% to 70% in this thesis. Theoretical calculations showed that this increase with SOC could be explained by a change in the thermal conductivity in the active material, as these calculations predicted an increase of around 12%. Nevertheless, the literature review revealed a variety of possible reasons for the SOC dependency such as: changes in phonon, electron and liquid particle conduction, changes in the microcontacts between the stack-layers and changes in the microstructure of the layers. The literature search revealed a range between -7% and +33% for the SOC dependency for the entire SOC range. Therefore, according to the current state of knowledge, there is no generally valid statement about the correlation between SOC and through-plane conductivity.

In two experiments on two different cell formats with two different measurement methods it could be shown in this thesis that the through-plane conductivity decreases significantly by -1.5 to -0.5% K^{-1} with increasing cell temperature. The theoretical calculation of the temperature dependency resulted in a range between -1.7 and -0.2% K^{-1} for NMC-G stacks, which agrees with the measurement results. The literature review revealed a range between -1.5 and +0.1% K^{-1} for the temperature dependence. The variation in temperature dependency can be explained by many influencing factors. Temperature can influence, for example, the thermal conductivity of the solid and liquid phase in porous stack-layers, thermal contact resistance and the layer thickness through thermal expansion. Although this thesis concludes that the temperature dependence is negative, this may not hold true for other cell designs, for example, due to a dominance of the thermal contact resistances.

In the case of the prismatic cell in this thesis, the through-plane conductivity was enhanced by increasing the external pressure on the cell housing, which is evidence that thermal contact resistances play an important role in heat conduction. Normally prismatic cells have to be installed under compression in order to counteract the swelling of the jelly roll. This compression was increased in the range from 37.1 to 74.2 kPa, which increased the thermal conductivity through the stack-layers by 11.9%. This increase is most likely caused by thermal contact resistance, which suggests that thermal conductivity is determined not only by the thermal resistance of the stack-layers, but also by the interfaces between the layers.

With regard to the measurement methods for the thermal conductivity in lithium-ion cells, future work should concentrate on the quantification of measurement uncertainties. In particular, the comparison of different measurement methods on the same test cell would be beneficial to assess current findings about the through-plane conductivity. In addition, there is a need for the development of in-operando methods for commercial lithium-ion cells. A combination of the new variant-convective cooling method and thermal impedance spectroscopy could be a new method for determining the thermal conductivity.

From the literature review, which includes the experimental investigation of this thesis, the following further research directions for the better understanding of the through-plane conductivity in lithium-ion cells were identified: 1) More experimental studies are needed to investigate state of health dependence. 2) Future experiments should specify the porosity and layer thicknesses of the stack in order to

quantify the influence of thermal contact resistances. 3) Further experiments are needed to improve the understanding of the temperature dependence. 4) For safety simulations, thermal conductivity measurements with temperatures above 60 °C are required. 5) The thermal contact resistance between the stack and the cell housing as well as between the stack-layers are still insufficiently quantified in commercial cells. 6) It should be investigated whether the thermal contact resistance between the active coating and the current collector can be neglected.

List of Publications

I Brand, Martin J.; Hofmann, Markus H.; **Steinhardt, Marco**; Schuster, Simon F.; Jossen, Andreas (2016): Current distribution within parallel-connected battery cells. In: J. Power Sources 334, pp. 202–212.

II Hofmann, Markus H.; Czyrka, Kevin; Brand, Martin J.; **Steinhardt, Marco**; Noel, Andreas; Spingler, Franz B.; Jossen, Andreas (2018): Dynamics of current distribution within battery cells connected in parallel. In: Journal of Energy Storage 20, pp. 120–133.

III **Steinhardt, Marco**; Gillich, Elisabeth Irene; Stiegler, Maximilian; Jossen, Andreas (2020): Thermal conductivity inside prismatic lithium-ion cells with dependencies on temperature and external compression pressure. In: Journal of Energy Storage 32, pp. 101680.

IV Jocher, P.; **Steinhardt, M.**; Ludwig, S.; Schindler, M.; Martin, J.; Jossen, A. (2021): A novel measurement technique for parallel-connected lithium-ion cells with controllable interconnection resistance. In: J. Power Sources 503, pp. 230030.

V **Steinhardt, Marco**; Gillich, Elisabeth Irene; Rheinfeld, Alexander; Kraft, Ludwig; Spielbauer, Markus; Bohlen, Oliver; Jossen, Andreas (2021): Low-effort determination of heat capacity and thermal conductivity for cylindrical 18650 and 21700 lithium-ion cells. In: Journal of Energy Storage 42, pp. 103065.

VI Kraft, Ludwig; Hoefling, Alexander; Zünd, Tanja; Kunz, Alexander; **Steinhardt, Marco**; Tübke, Jens; Jossen, Andreas (2021): Implications of the Heat Generation of LMR-NCM on the Thermal Behavior of Large-Format Lithium-Ion Batteries. In: J. Electrochem. Soc. 168 (5), pp. 53505.

VII **Steinhardt, Marco**; Barreras, Jorge V.; Ruan, Haijun; Wu, Billy; Offer, Gregory J.; Jossen, Andreas (2022): Meta-analysis of experimental results for heat capacity and thermal conductivity in lithium-ion batteries: A critical review. In: J. Power Sources 522, pp. 230829.

Acknowledgment

First of all, I would like to thank Prof. Dr.-Ing. Andreas Jossen for giving me the opportunity to carry out the research in this thesis, and for his guidance and supervision during my time as a PhD student at the Technical University of Munich. Finding my research topic might have taken much longer without the help, advice and patience of Prof. Jossen.

As a PhD candidate there are many phases in which the assistance of excellent colleagues is invaluable. I would therefore like to thank my team members Dr. Markus Hofmann, Dr. Philipp Berg, Elisabeth Gillich, Philipp Jocher, Franziska Peteler, Markus Spielbauer and Jonathan Martin for the numerous discussions, the administrative support and the after-work beers. Special thanks go to Korbinian Schmidt, Dr. Alexander Rheinfeld, Dr. Ludwig Kraft, Philipp Jocher and all the students for their work in building the Therminator wind tunnel, which has enormously assisted my scientific achievements. Maintaining the institute's IT-infrastructure was a challenge that I was happy to master in collaboration with Dr. Maik Naumann, Erfan Moyassari, Thomas Roth and Marco Fischer. I would also like to thank all other colleagues at the institute for the interesting exchanges either professionally or personally, especially Andreas Noel, who helped me to sharpen my understanding of scientific thinking.

I would also like to thank Dr. Jorge Varela Barreras and Dr. Haijun Ruan from Imperial College London for the excellent collaboration. I drew great inspiration from our weekly meetings. In addition, I would like to thank all 17 students who received their degrees under my supervision for the discussions and efforts that greatly improved the quality of my research. Thanks also to my mentor Dr. Simon Schuster for the happy after-work meetings and to Dr. Martin Brand for sparking my passion for batteries.

My time at the institute was enhanced by the excellent work of the research management, the secretariat and the technical team. Thank you to Korbinian Schmidt and Jens Dietrich for their help in building battery test benches that have always exceeded my expectations. I would also like to thank Carolin Nierwetberg and Dr. Gudrun Rahn-Koltermann for their administrative support with students, industrial projects and my own HR inquiries.

Finally, I would like to thank my family for their unconditional support over the past decades and during my doctoral studies. Another special thank you goes to my friends, who have always made it possible for me to have an appropriate work-life balance. The greatest thanks go to my wife Nadine, who always supports my decisions, and my newborn son Leon.

References

[1] W. Steffen et al. "Trajectories of the Earth System in the Anthropocene". In: *Proceedings of the National Academy of Sciences* 115.33 (2018), pp. 8252–8259. ISSN: 0027-8424. DOI: 10.1073/pnas.1810141115.

[2] United Nations. *PARIS AGREEMENT*. 2015. URL: https://treaties.un.org/Pages/ViewDetails.aspx?src=IND&mtdsg_no=XXVII-7-d&chapter=27&clang=_en (visited on 09/23/2021).

[3] IPCC. *Climate Change 2021: The Physical Science Basis*. 2021. URL: https://www.ipcc.ch/report/ar6/wg1/downloads/report/IPCC_AR6_WGI_Full_Report.pdf (visited on 09/29/2021).

[4] W. F. Lamb et al. "A review of trends and drivers of greenhouse gas emissions by sector from 1990 to 2018". In: *Environmental Research Letters* 16.7 (2021), p. 073005. DOI: 10.1088/1748-9326/abee4e.

[5] United Nations. *Report of the Conference of the Parties on its nineteenth session, held in Warsaw from 11 to 23 November 2013: Part two: Action taken by the Conference of the Parties at its nineteenth session*. 2014.

[6] M. Roelfsema et al. "Taking stock of national climate policies to evaluate implementation of the Paris Agreement". In: *Nature communications* 11.1 (2020), p. 2096. ISSN: 2041-1723. DOI: 10.1038/s41467-020-15414-6.

[7] F. Knobloch, S. Hanssen, A. Lam, H. Pollitt, P. Salas, U. Chewpreecha, M. A. J. Huijbregts, and J.-F. Mercure. "Net emission reductions from electric cars and heat pumps in 59 world regions over time". In: *Nature Sustainability* 3.6 (2020), pp. 437–447. DOI: 10.1038/s41893-020-0488-7.

[8] G. Bieker. *A GLOBAL COMPARISON OF THE LIFE-CYCLE GREENHOUSE GAS EMISSIONS OF COMBUSTION ENGINE AND ELECTRIC PASSENGER CARS*. Ed. by International Council on Clean Transportation. 2021. URL: https://theicct.org/wp-content/uploads/2021/12/Global-LCA-passenger-cars-jul2021_0.pdf (visited on 02/08/2022).

[9] B. Cox, C. L. Mutel, C. Bauer, A. Mendoza Beltran, and D. P. van Vuuren. "Uncertain Environmental Footprint of Current and Future Battery Electric Vehicles". In: *Environmental Science & Technology* 52.8 (2018), pp. 4989–4995. ISSN: 0013-936X. DOI: 10.1021/acs.est.8b00261.

[10] A. König, L. Nicoletti, D. Schröder, S. Wolff, A. Waclaw, and M. Lienkamp. "An Overview of Parameter and Cost for Battery Electric Vehicles". In: *World Electric Vehicle Journal* 12.1 (2021), p. 21. DOI: 10.3390/wevj12010021.

[11] T. Gersdorf, P. Hertzke, P. Schaufuss, and S. Schenk. *McKinsey Electric Vehicle Index: Europe cushions a global plunge in EV sales*. Ed. by McKinsey & Company. 2020. URL: http://www.libralato.co.uk/docs/McKinsey%20EV%20Index%202020.pdf.

[12] M. Marinaro et al. “Bringing forward the development of battery cells for automotive applications: Perspective of R&D activities in China, Japan, the EU and the USA”. In: *Journal of Power Sources* 459 (2020), p. 228073. ISSN: 03787753. DOI: 10.1016/j.jpowsour.2020.228073.

[13] G. Gardner. *Mercedes-Benz To Spend $47 Billion To Speed Conversion To Electric-Only Lineup*. Ed. by Forbes. Forbes, 2021. URL: https://www.forbes.com/sites/greggardner/2021/07/22/mercedes-benz-to-spend-47-billion-to-speed-conversion-to-electric-only-production/?sh=3813f2595327 (visited on 10/11/2021).

[14] S. Dühnen, J. Betz, M. Kolek, R. Schmuch, M. Winter, and T. Placke. “Toward Green Battery Cells: Perspective on Materials and Technologies”. In: *Small Methods* 4.7 (2020), p. 2000039. ISSN: 2366-9608. DOI: 10.1002/smtd.202000039.

[15] Y. Liu, Y. Zhu, and Y. Cui. “Challenges and opportunities towards fast-charging battery materials”. In: *Nature Energy* 4.7 (2019), pp. 540–550. DOI: 10.1038/s41560-019-0405-3.

[16] M. Keyser et al. “Enabling fast charging – Battery thermal considerations”. In: *Journal of Power Sources* 367 (2017), pp. 228–236. ISSN: 03787753. DOI: 10.1016/j.jpowsour.2017.07.009.

[17] D. L. Thompson et al. “The importance of design in lithium ion battery recycling – a critical review”. In: *Green Chemistry* 22.22 (2020), pp. 7585–7603. ISSN: 1463-9262. DOI: 10.1039/D0GC02745F.

[18] L. Kraft, A. Hoefling, T. Zünd, A. Kunz, M. Steinhardt, J. Tübke, and A. Jossen. “Implications of the Heat Generation of LMR-NCM on the Thermal Behavior of Large-Format Lithium-Ion Batteries”. In: *Journal of the Electrochemical Society* 168.5 (2021), p. 053505. ISSN: 0013-4651. DOI: 10.1149/1945-7111/ac0069.

[19] J. V. Barreras, R. de Castro, Y. Wan, and T. Dragicevic. “A Consensus Algorithm for Multi-Objective Battery Balancing”. In: *Energies* 14.14 (2021), p. 4279. ISSN: 1996-1073. DOI: 10.3390/en14144279.

[20] I. A. Hunt, Y. Zhao, Y. Patel, and J. Offer. “Surface Cooling Causes Accelerated Degradation Compared to Tab Cooling for Lithium-Ion Pouch Cells”. In: *Journal of The Electrochemical Society* 163.9 (2016), A1846–A1852. ISSN: 00134651. DOI: 10.1149/2.0361609jes.

[21] D. Werner, S. Paarmann, A. Wiebelt, and T. Wetzel. “Inhomogeneous Temperature Distribution Affecting the Cyclic Aging of Li-Ion Cells. Part II: Analysis and Correlation”. In: *Batteries* 6.1 (2020), p. 12. ISSN: 2313-0105. DOI: 10.3390/batteries6010012.

[22] T. Waldmann, M. Wilka, M. Kasper, M. Fleischhammer, and M. Wohlfahrt-Mehrens. “Temperature dependent ageing mechanisms in Lithium-ion batteries – A Post-Mortem study”. In: *Journal of Power Sources* 262 (2014), pp. 129–135. ISSN: 03787753. DOI: 10.1016/j.jpowsour.2014.03.112.

[23] X. Feng, M. Ouyang, X. Liu, L. Lu, Y. Xia, and X. He. “Thermal runaway mechanism of lithium ion battery for electric vehicles: A review: A review”. In: *Energy Storage Materials* 10 (2018), pp. 246–267. ISSN: 24058297. DOI: 10.1016/j.ensm.2017.05.013.

[24] R. Spotnitz and J. Franklin. “Abuse behavior of high-power, lithium-ion cells”. In: *Journal of Power Sources* 113.1 (2003), pp. 81–100. ISSN: 03787753. DOI: 10.1016/S0378-7753(02)00488-3.

[25] D. D. MacNeil, D. Larcher, and J. R. Dahn. “Comparison of the Reactivity of Various Carbon Electrode Materials with Electrolyte at Elevated Temperature”. In: *Journal of The Electrochemical Society* 146.10 (1999), pp. 3596–3602. ISSN: 00134651. DOI: 10.1149/1.1392520.

[26] F. Larsson, P. Andersson, P. Blomqvist, and B.-E. Mellander. “Toxic fluoride gas emissions from lithium-ion battery fires”. In: *Scientific reports* 7.1 (2017), p. 10018. ISSN: 2045-2322. DOI: 10.1038/s41598-017-09784-z.

[27] X.-G. Yang, T. Liu, and C.-Y. Wang. “Thermally modulated lithium iron phosphate batteries for mass-market electric vehicles”. In: *Nature Energy* 6.2 (2021), pp. 176–185. DOI: 10.1038/s41560-020-00757-7.

[28] M. Fichtner. “Recent Research and Progress in Batteries for Electric Vehicles”. In: *Batteries & Supercaps* 5.2 (2022). ISSN: 2566-6223. DOI: 10.1002/batt.202100224.

[29] M. Steinhardt, J. V. Barreras, H. Ruan, B. Wu, G. J. Offer, and A. Jossen. “Meta-analysis of experimental results for heat capacity and thermal conductivity in lithium-ion batteries: A critical review”. In: *Journal of Power Sources* 522 (2022), p. 230829. ISSN: 03787753. DOI: 10.1016/j.jpowsour.2021.230829.

[30] J. Liebl, ed. *Der Antrieb von morgen 2021: Gemeinsam mit Grid Integration + Electrified Mobility*. 1. Aufl. 2021. Berlin, Heidelberg: Springer Berlin Heidelberg, 2021. ISBN: 9783662634035. URL: http://nbn-resolving.org/urn:nbn:de:bsz:31-epflicht-1879077.

[31] L. Lander, E. Kallitsis, A. Hales, J. S. Edge, A. Korre, and G. Offer. “Cost and carbon footprint reduction of electric vehicle lithium-ion batteries through efficient thermal management”. In: *Applied Energy* 289.289 (2021), p. 116737. ISSN: 03062619. DOI: 10.1016/j.apenergy.2021.116737.

[32] A. Tomaszewska et al. “Lithium-Ion Battery Fast Charging: A Review”. In: *eTransportation* (2019), p. 100011. ISSN: 25901168. DOI: 10.1016/j.etran.2019.100011.

[33] W. Ju, C. Zhu, and Z. Wei. “Intercalated ion tuning of the cross-plane thermal transport properties of graphite”. In: *AIP Advances* 10.9 (2020), p. 095225. DOI: 10.1063/5.0023229.

[34] X. Qian, X. Gu, M. S. Dresselhaus, and R. Yang. “Anisotropic Tuning of Graphite Thermal Conductivity by Lithium Intercalation”. In: *The journal of physical chemistry letters* 7.22 (2016), pp. 4744–4750. DOI: 10.1021/acs.jpclett.6b02295.

[35] H. Yang, C. N. Savory, B. J. Morgan, D. O. Scanlon, J. M. Skelton, and A. Walsh. “Chemical Trends in the Lattice Thermal Conductivity of Li(Ni, Mn, Co)O 2 (NMC) Battery Cathodes”. In: *Chemistry of Materials* 32.17 (2020), pp. 7542–7550. ISSN: 0897-4756. DOI: 10.1021/acs.chemmater.0c02908.

[36] Y. Xie, X. Wang, X. Hu, W. Li, Y. Zhang, and X. Lin. “An Enhanced Electro-Thermal Model for EV Battery Packs Considering Current Distribution in Parallel Branches”. In: *IEEE Transactions on Power Electronics* 37.1 (2022), pp. 1027–1043. ISSN: 0885-8993. DOI: 10.1109/TPEL.2021.3102292.

[37] U. Iraola, I. Aizpuru, L. Gorrotxategi, J. M. C. Segade, A. E. Larrazabal, and I. Gil. “Influence of Voltage Balancing on the Temperature Distribution of a Li-Ion Battery Module”. In: *IEEE Transactions on Energy Conversion* 30.2 (2015), pp. 507–514. ISSN: 0885-8969. DOI: 10.1109/TEC.2014.2366375.

[38] G. Liebig, U. Kirstein, S. Geißendörfer, F. Schuldt, and C. Agert. “The Impact of Environmental Factors on the Thermal Characteristic of a Lithium–ion Battery”. In: *Batteries* 6.1 (2020), p. 3. ISSN: 2313-0105. DOI: 10.3390/batteries6010003.

[39] W. Mei, Q. Duan, W. Lu, J. Sun, and Q. Wang. “An investigation on expansion behavior of lithium ion battery based on the thermal-mechanical coupling model”. In: *Journal of Cleaner Production* 274 (2020), p. 122643. ISSN: 09596526. DOI: 10.1016/j.jclepro.2020.122643.

[40] M. Steinhardt, E. I. Gillich, M. Stiegler, and A. Jossen. “Advanced Thermal Conductivity Characterization with Implications for Thermal Control Strategies during Fast Charging”. In: *ECS Meeting Abstracts* MA2020-02.3 (2020), p. 630. DOI: 10.1149/MA2020-023630mtgabs.

[41] C. Julien. *Lithium Batteries: Science and Technology*. Springer eBook Collection. Cham: Springer, 2016. ISBN: 9783319191089. DOI: 10.1007/978-3-319-19108-9.

[42] M. Steinhardt, E. I. Gillich, A. Rheinfeld, L. Kraft, M. Spielbauer, O. Bohlen, and A. Jossen. “Low-effort determination of heat capacity and thermal conductivity for cylindrical 18650 and 21700 lithium-ion cells”. In: *Journal of Energy Storage* 42 (2021), p. 103065. ISSN: 2352152X. DOI: 10.1016/j.est.2021.103065.

[43] R. Hentschke. *Thermodynamics: For physicists, chemists and materials scientists*. Undergraduate lecture notes in physics. Heidelberg et al.: Springer, 2014. ISBN: 9783642367113. DOI: 10.1007/978-3-642-36711-3.

[44] L. Rao and J. Newman. “Heat–Generation Rate and General Energy Balance for Insertion Battery Systems”. In: *Journal of The Electrochemical Society* 144.8 (1997), pp. 2697–2704. ISSN: 00134651. DOI: 10.1149/1.1837884.

[45] D. Bernardi. “A General Energy Balance for Battery Systems”. In: *Journal of The Electrochemical Society* 132.1 (1985), p. 5. ISSN: 00134651. DOI: 10.1149/1.2113792.

[46] W. B. Gu and C. Y. Wang. “Thermal-Electrochemical Modeling of Battery Systems”. In: *Journal of The Electrochemical Society* 147.8 (2000), p. 2910. ISSN: 00134651. DOI: 10.1149/1.1393625.

[47] T. Bandhauer, S. Garimella, and T. F. Fuller. “Electrochemical-Thermal Modeling to Evaluate Battery Thermal Management Strategies: II. Edge and Internal Cooling”. In: *Journal of the Electrochemical Society* 162.1 (2014), A137–A148. ISSN: 0013-4651. DOI: 10.1149/2.0581501jes.

[48] A. F. Gunnarshaug, S. Kjelstrup, and D. Bedeaux. “The heat of transfer and the Peltier coefficient of electrolytes”. In: *Chemical Physics Letters: X* 5 (2020), p. 100040. ISSN: 2590-1419. DOI: 10.1016/j.cpletx.2019.100040. URL: https://www.sciencedirect.com/science/article/pii/S2590141919300492.

[49] A. F. Gunnarshaug, P. J. S. Vie, and S. Kjelstrup. “Review—Reversible Heat Effects in Cells Relevant for Lithium-Ion Batteries”. In: *Journal of the Electrochemical Society* 168.5 (2021), p. 050522. ISSN: 0013-4651. DOI: 10.1149/1945-7111/abfd73.

[50] L. Spitthoff, A. F. Gunnarshaug, D. Bedeaux, O. Burheim, and S. Kjelstrup. “Peltier effects in lithium-ion battery modeling”. In: *The Journal of chemical physics* 154.11 (2021), p. 114705. DOI: 10.1063/5.0038168. URL: https://aip.scitation.org/doi/pdf/10.1063/5.0038168.

[51] C. Heubner, M. Schneider, C. Lämmel, and A. Michaelis. “Local Heat Generation in a Single Stack Lithium Ion Battery Cell”. In: *Electrochimica Acta* 186 (2015), pp. 404–412. ISSN: 00134686. DOI: 10.1016/j.electacta.2015.10.182.

[52] S. Zhu, J. Han, Y.-N. Wang, T.-S. Pan, Y.-M. Wei, W.-L. Song, H.-S. Chen, and D. Fang. "In–situ heat generation measurement of the anode and cathode in a single–layer lithium ion battery cell". In: *International Journal of Energy Research* 44.11 (2020), pp. 9141–9148. ISSN: 0363907X. DOI: 10.1002/er.5507.

[53] S. Ludwig, I. Zilberman, M. F. Horsche, T. Wohlers, and A. Jossen. "Pulse resistance based online temperature estimation for lithium-ion cells". In: *Journal of Power Sources* 490 (2021), p. 229523. ISSN: 03787753. DOI: 10.1016/j.jpowsour.2021.229523.

[54] M. J. Brand, P. Berg, E. I. Kolp, T. Bach, P. Schmidt, and A. Jossen. "Detachable electrical connection of battery cells by press contacts". In: *Journal of Energy Storage* 8 (2016), pp. 69–77. ISSN: 2352152X. DOI: 10.1016/j.est.2016.09.011.

[55] E. Hosseinzadeh, J. Marco, and P. Jennings. "Combined electrical and electrochemical-thermal model of parallel connected large format pouch cells". In: *Journal of Energy Storage* 22 (2019), pp. 194–207. ISSN: 2352152X. DOI: 10.1016/j.est.2019.02.004.

[56] T. Zimmermann, M. Hofmann, M. Steinhardt, G. Rahn-Koltermann, and A. Jossen. *"Intelligente Steuerungs- und Verschaltungskonzepte für modulare Elektrofahrzeug-Batteriesysteme zur Steigerung der Effizienz und Sicherheit sowie zur Senkung der Systemkosten" : Abschlussbericht des Verbundvorhabens DriveBattery2015 Phase 2 : Laufzeit des Vorhabens: 01.09.2015-28.02.2017 (erweitert bis 31.05.2017), Berichtszeitraum: 01.09.2015-31.05.2017*. 2017. DOI: 10.2314/GBV:1012348172.

[57] H. Sun and R. Dixon. "Development of a Liquid Cooled Battery Module". In: *Journal of The Electrochemical Society* 163.10 (2016), E313–E321. ISSN: 00134651. DOI: 10.1149/2.1081610jes.

[58] M. Gepp, H. Reisenweber, V. Lorentz, and M. Marz. "Temperature gradient reduction in high-power battery systems using prismatic cells combined with Phase-Change Sheets and Graphite foils". In: *IECON 2016 - 42nd Annual Conference of the IEEE Industrial Electronics Society*. 2016, pp. 5519–5524. DOI: 10.1109/IECON.2016.7793497.

[59] H. Yang, J.-Y. Yang, C. N. Savory, J. M. Skelton, B. J. Morgan, D. O. Scanlon, and A. Walsh. "Highly Anisotropic Thermal Transport in LiCoO2". In: *The journal of physical chemistry letters* 10.18 (2019), pp. 5552–5556. DOI: 10.1021/acs.jpclett.9b02073.

[60] X. Hu, Y. Zheng, D. A. Howey, H. Perez, A. Foley, and M. Pecht. "Battery warm-up methodologies at subzero temperatures for automotive applications: Recent advances and perspectives". In: *Progress in Energy and Combustion Science* 77 (2020), p. 100806. ISSN: 03601285. DOI: 10.1016/j.pecs.2019.100806.

[61] S. Ahmadou. "Battery Electrical Vehicles-Analysis of Thermal Modelling and Thermal Management". Dissertation. Universite de Caen, 2016. URL: https://hal.archives-ouvertes.fr/tel-01298416/document.

[62] Q. Wang, B. Jiang, B. Li, and Y. Yan. "A critical review of thermal management models and solutions of lithium-ion batteries for the development of pure electric vehicles". In: *Renewable and Sustainable Energy Reviews* 64 (2016), pp. 106–128. ISSN: 13640321. DOI: 10.1016/j.rser.2016.05.033.

[63] J. Xu, C. Lan, Y. Qiao, and Y. Ma. "Prevent thermal runaway of lithium-ion batteries with minichannel cooling". In: *Applied Thermal Engineering* 110 (2017), pp. 883–890. ISSN: 13594311. DOI: 10.1016/j.applthermaleng.2016.08.151.

[64] C. Huber. “Phase Change Material in Battery Thermal Management Applications”. Dissertation. Technische Universität München, 2017.

[65] Y. Zhao, L. B. Diaz, Y. Patel, T. Zhang, and G. J. Offer. “How to Cool Lithium Ion Batteries: Optimising Cell Design using a Thermally Coupled Model”. In: *Journal of The Electrochemical Society* 166.13 (2019), A2849–A2859. ISSN: 00134651. DOI: 10.1149/2.0501913jes.

[66] J. Sturm, A. Frank, A. Rheinfeld, S. V. Erhard, and A. Jossen. “Impact of Electrode and Cell Design on Fast Charging Capabilities of Cylindrical Lithium-Ion Batteries”. In: *Journal of The Electrochemical Society* 167.13 (2020), p. 130505. ISSN: 00134651. DOI: 10.1149/1945-7111/abb40c.

[67] S. Li et al. “Optimal cell tab design and cooling strategy for cylindrical lithium-ion batteries”. In: *Journal of Power Sources* 492 (2021), p. 229594. ISSN: 03787753. DOI: 10.1016/j.jpowsour.2021.229594.

[68] S. Paul, C. Diegelmann, H. Kabza, and W. Tillmetz. “Analysis of ageing inhomogeneities in lithium-ion battery systems”. In: *Journal of Power Sources* 239 (2013), pp. 642–650. ISSN: 03787753. DOI: 10.1016/j.jpowsour.2013.01.068.

[69] W. Ai, L. Kraft, J. Sturm, A. Jossen, and B. Wu. “Electrochemical Thermal-Mechanical Modelling of Stress Inhomogeneity in Lithium-Ion Pouch Cells”. In: *Journal of the Electrochemical Society* 167.1 (2020), p. 013512. ISSN: 0013-4651. DOI: 10.1149/2.0122001JES.

[70] M. Schimpe, J. V. Barreras, B. Wu, and G. J. Offer. “Battery Degradation-Aware Current Derating: An Effective Method to Prolong Lifetime and Ease Thermal Management”. In: *Journal of The Electrochemical Society* 168.6 (2021), p. 060506. ISSN: 00134651. DOI: 10.1149/1945-7111/ac0553.

[71] C. Campestrini. “Practical feasibility of Kalman filters forthe state estimation of lithium-ion batteries”. Dissertation. Technische Universität München, 2017.

[72] J. Sturm, H. Ennifar, S. V. Erhard, A. Rheinfeld, S. Kosch, and A. Jossen. “State estimation of lithium-ion cells using a physicochemical model based extended Kalman filter”. In: *Applied Energy* 223 (2018), pp. 103–123. ISSN: 03062619. DOI: 10.1016/j.apenergy.2018.04.011.

[73] F. Feng, S. Teng, K. Liu, J. Xie, Y. Xie, B. Liu, and K. Li. “Co-estimation of lithium-ion battery state of charge and state of temperature based on a hybrid electrochemical-thermal-neural-network model”. In: *Journal of Power Sources* 455 (2020), p. 227935. ISSN: 03787753. DOI: 10.1016/j.jpowsour.2020.227935.

[74] G.-H. Kim, A. Pesaran, and R. Spotnitz. “A three-dimensional thermal abuse model for lithium-ion cells”. In: *Journal of Power Sources* 170.2 (2007), pp. 476–489. ISSN: 03787753. DOI: 10.1016/j.jpowsour.2007.04.018.

[75] X. Feng, X. He, M. Ouyang, L. Lu, P. Wu, C. Kulp, and S. Prasser. “Thermal runaway propagation model for designing a safer battery pack with 25Ah LiNixCoyMnzO2 large format lithium ion battery”. In: *Applied Energy* 154 (2015), pp. 74–91. ISSN: 03062619. DOI: 10.1016/j.apenergy.2015.04.118.

[76] J. K. Ostanek, W. Li, P. P. Mukherjee, K. R. Crompton, and C. Hacker. “Simulating onset and evolution of thermal runaway in Li-ion cells using a coupled thermal and venting model”. In: *Applied Energy* 268 (2020), p. 114972. ISSN: 03062619. DOI: 10.1016/j.apenergy.2020.114972.

[77] H. Hopp. *Thermomanagement von Hochleistungsfahrzeug-Traktionsbatterien anhand gekoppelter Simulationsmodelle*. Wissenschaftliche Reihe Fahrzeugtechnik Universität Stuttgart. 2016. ISBN: 9783658142469. URL: http://dx.doi.org/10.1007/978-3-658-14247-6.

[78] M. Doyle. "Modeling of Galvanostatic Charge and Discharge of the Lithium/Polymer/Insertion Cell". In: *Journal of The Electrochemical Society* 140.6 (1993), p. 1526. ISSN: 00134651. DOI: 10.1149/1.2221597.

[79] M. H. Hofmann, K. Czyrka, M. J. Brand, M. Steinhardt, A. Noel, F. B. Spingler, and A. Jossen. "Dynamics of current distribution within battery cells connected in parallel". In: *Journal of Energy Storage* 20 (2018), pp. 120–133. ISSN: 2352152X. DOI: 10.1016/j.est.2018.08.013.

[80] X. Hua, C. Zhang, and G. Offer. "Finding a better fit for lithium ion batteries: A simple, novel, load dependent, modified equivalent circuit model and parameterization method". In: *Journal of Power Sources* 484 (2021), p. 229117. ISSN: 03787753. DOI: 10.1016/j.jpowsour.2020.229117.

[81] S. Nejad, D. T. Gladwin, and D. A. Stone. "A systematic review of lumped-parameter equivalent circuit models for real-time estimation of lithium-ion battery states". In: *Journal of Power Sources* 316 (2016), pp. 183–196. ISSN: 03787753. DOI: 10.1016/j.jpowsour.2016.03.042.

[82] S. Yang. "A Review of Lithium-Ion Battery Thermal Management System Strategies and the Evaluate Criteria". In: *International Journal of Electrochemical Science* (2019), pp. 6077–6107. DOI: 10.20964/2019.07.06.

[83] Y. Troxler, B. Wu, M. Marinescu, V. Yufit, Y. Patel, A. J. Marquis, N. P. Brandon, and G. J. Offer. "The effect of thermal gradients on the performance of lithium-ion batteries". In: *Journal of Power Sources* 247 (2014), pp. 1018–1025. ISSN: 03787753. DOI: 10.1016/j.jpowsour.2013.06.084.

[84] M. Naumann, F. B. Spingler, and A. Jossen. "Analysis and modeling of cycle aging of a commercial LiFePO4/graphite cell". In: *Journal of Power Sources* 451 (2020), p. 227666. ISSN: 03787753. DOI: 10.1016/j.jpowsour.2019.227666.

[85] M. Schimpe, M. E. von Kuepach, M. Naumann, H. C. Hesse, K. Smith, and A. Jossen. "Comprehensive Modeling of Temperature-Dependent Degradation Mechanisms in Lithium Iron Phosphate Batteries". In: *Journal of The Electrochemical Society* 165.2 (2018), A181–A193. ISSN: 00134651. DOI: 10.1149/2.1181714jes.

[86] X.-G. Yang and C.-Y. Wang. "Understanding the trilemma of fast charging, energy density and cycle life of lithium-ion batteries". In: *Journal of Power Sources* 402 (2018), pp. 489–498. ISSN: 03787753. DOI: 10.1016/j.jpowsour.2018.09.069.

[87] Y. Yin and S.-Y. Choe. "Actively temperature controlled health-aware fast charging method for lithium-ion battery using nonlinear model predictive control". In: *Applied Energy* 271 (2020), p. 115232. ISSN: 03062619. DOI: 10.1016/j.apenergy.2020.115232.

[88] Y. Zeng, D. Chalise, S. D. Lubner, S. Kaur, and R. S. Prasher. "A review of thermal physics and management inside lithium-ion batteries for high energy density and fast charging". In: *Energy Storage Materials* 41 (2021), pp. 264–288. ISSN: 24058297. DOI: 10.1016/j.ensm.2021.06.008.

[89] M. Fleckenstein, O. Bohlen, and B. Bäker. "Aging Effect of Temperature Gradients in Li-ion Cells Experimental and Simulative Investigations and the Consequences on Thermal Battery Management". In: *World Electric Vehicle Journal* 5.2 (2012), pp. 322–333. DOI: 10.3390/wevj5020322.

[90] G. M. Cavalheiro, T. Iriyama, G. J. Nelson, S. Huang, and G. Zhang. "Effects of Nonuniform Temperature Distribution on Degradation of Lithium-Ion Batteries". In: *Journal of Electrochemical Energy Conversion and Storage* 17.2 (2020), p. 378. ISSN: 2381-6872. DOI: 10.1115/1.4045205.

[91] H. J. Gonzalez Malabet, G. M. Cavalheiro, T. Iriyama, A. Gabhart, G. J. Nelson, and G. Zhang. "Electrochemical and Post-Mortem Degradation Analysis of Parallel-Connected Lithium-Ion Cells with Non-Uniform Temperature Distribution". In: *Journal of The Electrochemical Society* 168.10 (2021), p. 100507. ISSN: 00134651. DOI: 10.1149/1945-7111/ac2a7c.

[92] R. Carter and C. T. Love. "Modulation of Lithium Plating in Li-Ion Batteries with External Thermal Gradient". In: *ACS applied materials & interfaces* 10.31 (2018), pp. 26328–26334. DOI: 10.1021/acsami.8b09131.

[93] B. Rieger. "Methodik zur Simulation des mechanischen Verhaltens von Lithium-Ionen-Zellen". Dissertation. Technische Universität München, 2016.

[94] X. Duan, W. Jiang, Y. Zou, W. Lei, and Z. Ma. "A coupled electrochemical–thermal–mechanical model for spiral-wound Li-ion batteries". In: *Journal of Materials Science* 53.15 (2018), pp. 10987–11001. ISSN: 0022-2461. DOI: 10.1007/s10853-018-2365-6.

[95] O. Valentin, P.-X. Thivel, T. Kareemulla, F. Cadiou, and Y. Bultel. "Modeling of thermo-mechanical stresses in Li-ion battery". In: *Journal of Energy Storage* 13 (2017), pp. 184–192. ISSN: 2352152X. DOI: 10.1016/j.est.2017.07.018.

[96] K.-Y. Oh and B. I. Epureanu. "Characterization and modeling of the thermal mechanics of lithium-ion battery cells". In: *Applied Energy* 178 (2016), pp. 633–646. ISSN: 03062619. DOI: 10.1016/j.apenergy.2016.06.069.

[97] W. Wu, X. Xiao, and D. Shi. "Heat Transfer and Thermal Stress in a Lithium-Ion Battery". In: *Volume 5: Energy Systems Analysis, Thermodynamics and Sustainability; NanoEngineering for Energy; Engineering to Address Climate Change, Parts A and B*. ASMEDC, 11122010, pp. 343–351. ISBN: 978-0-7918-4429-8. DOI: 10.1115/IMECE2010-37870.

[98] S. Kalnaus, Y. Wang, J. Li, A. Kumar, and J. A. Turner. "Temperature and strain rate dependent behavior of polymer separator for Li-ion batteries". In: *Extreme Mechanics Letters* 20 (2018), pp. 73–80. ISSN: 23524316. DOI: 10.1016/j.eml.2018.01.006.

[99] K.-Y. Oh and B. I. Epureanu. "A phenomenological force model of Li-ion battery packs for enhanced performance and health management". In: *Journal of Power Sources* 365 (2017), pp. 220–229. ISSN: 03787753. DOI: 10.1016/j.jpowsour.2017.08.058.

[100] M. Alipour, C. Ziebert, F. V. Conte, and R. Kizilel. "A Review on Temperature-Dependent Electrochemical Properties, Aging, and Performance of Lithium-Ion Cells". In: *Batteries* 6.3 (2020), p. 35. ISSN: 2313-0105. DOI: 10.3390/batteries6030035.

[101] M. Jafari, K. Khan, and L. Gauchia. "Deterministic models of Li-ion battery aging: It is a matter of scale". In: *Journal of Energy Storage* 20 (2018), pp. 67–77. ISSN: 2352152X. DOI: 10.1016/j.est.2018.09.002.

[102] R. Fu, M. Xiao, and S.-Y. Choe. "Modeling, validation and analysis of mechanical stress generation and dimension changes of a pouch type high power Li-ion battery". In: *Journal of Power Sources* 224 (2013), pp. 211–224. ISSN: 03787753. DOI: 10.1016/j.jpowsour.2012.09.096.

[103] V. Müller, R.-G. Scurtu, M. Memm, M. A. Danzer, and M. Wohlfahrt-Mehrens. "Study of the influence of mechanical pressure on the performance and aging of Lithium-ion battery cells". In: *Journal of Power Sources* 440 (2019), p. 227148. ISSN: 03787753. DOI: 10.1016/j.jpowsour.2019.227148.

[104] D. Sauerteig, N. Hanselmann, A. Arzberger, H. Reinshagen, S. Ivanov, and A. Bund. "Electrochemical-mechanical coupled modeling and parameterization of swelling and ionic transport in lithium-ion batteries". In: *Journal of Power Sources* 378 (2018), pp. 235–247. ISSN: 03787753. DOI: 10.1016/j.jpowsour.2017.12.044.

[105] K. Takahashi and V. Srinivasan. "Examination of Graphite Particle Cracking as a Failure Mode in Lithium-Ion Batteries: A Model-Experimental Study". In: *Journal of The Electrochemical Society* 162.4 (2015), A635–A645. ISSN: 00134651. DOI: 10.1149/2.0281504jes.

[106] X. Zhang, R. Klein, A. Subbaraman, S. Chumakov, X. Li, J. Christensen, C. Linder, and S. U. Kim. "Evaluation of convective heat transfer coefficient and specific heat capacity of a lithium-ion battery using infrared camera and lumped capacitance method". In: *Journal of Power Sources* 412 (2019), pp. 552–558. ISSN: 03787753. DOI: 10.1016/j.jpowsour.2018.11.064.

[107] J. Sturm, F. B. Spingler, B. Rieger, A. Rheinfeld, and A. Jossen. "Non-Destructive Detection of Local Aging in Lithium-Ion Pouch Cells by Multi-Directional Laser Scanning". In: *Journal of The Electrochemical Society* 164.7 (2017), A1342–A1351. ISSN: 00134651. DOI: 10.1149/2.0161707jes.

[108] T. Weaver, A. Allam, and S. Onori. "A Novel Lithium-ion Battery Pack Modeling Framework - Series-Connected Case Study". In: *2020 American Control Conference (ACC)*. IEEE, 1.07.2020 - 03.07.2020, pp. 365–372. ISBN: 978-1-5386-8266-1. DOI: 10.23919/ACC45564.2020.9147546.

[109] F. Richter, S. Kjelstrup, P. J. Vie, and O. S. Burheim. "Thermal conductivity and internal temperature profiles of Li-ion secondary batteries". In: *Journal of Power Sources* 359 (2017), pp. 592–600. ISSN: 03787753. DOI: 10.1016/j.jpowsour.2017.05.045.

[110] D. Werner, A. Loges, D. J. Becker, and T. Wetzel. "Thermal conductivity of Li-ion batteries and their electrode configurations – A novel combination of modelling and experimental approach". In: *Journal of Power Sources* 364 (2017), pp. 72–83. ISSN: 03787753. DOI: 10.1016/j.jpowsour.2017.07.105.

[111] G. Kovachev, A. Astner, G. Gstrein, L. Aiello, J. Hemmer, W. Sinz, and C. Ellersdorfer. "Thermal Conductivity in Aged Li-Ion Cells under Various Compression Conditions and State-of-Charge". In: *Batteries* 7.3 (2021), p. 42. ISSN: 2313-0105. DOI: 10.3390/batteries7030042.

[112] S. J. Bazinski and X. Wang. "Experimental study on the influence of temperature and state-of-charge on the thermophysical properties of an LFP pouch cell". In: *Journal of Power Sources* 293 (2015), pp. 283–291. ISSN: 03787753. DOI: 10.1016/j.jpowsour.2015.05.084.

[113] G. Vertiz, M. Oyarbide, H. Macicior, O. Miguel, I. Cantero, P. Fernandez de Arroiabe, and I. Ulacia. "Thermal characterization of large size lithium-ion pouch cell based on 1d electro-thermal model". In: *Journal of Power Sources* 272 (2014), pp. 476–484. ISSN: 03787753. DOI: 10.1016/j.jpowsour.2014.08.092.

[114] K. A. Murashko, J. Pyrhönen, and J. Jokiniemi. "Determination of the through-plane thermal conductivity and specific heat capacity of a Li-ion cylindrical cell". In: *International Journal of Heat and Mass Transfer* 162 (2020), p. 120330. ISSN: 00179310. DOI: 10.1016/j.ijheatmasstransfer.2020.120330.

[115] M. Fleckenstein, S. Fischer, O. Bohlen, and B. Bäker. "Thermal Impedance Spectroscopy - A method for the thermal characterization of high power battery cells". In: *Journal of Power Sources* 223 (2013), pp. 259–267. ISSN: 03787753. DOI: 10.1016/j.jpowsour.2012.07.144.

[116] A. Rheinfeld, S. Kosch, S. V. Erhard, P. J. Osswald, B. Rieger, and A. Jossen. "Electro-Thermal Modeling of Large Format Lithium-Ion Pouch Cells: A Cell Temperature Dependent Linear Polarization Expression". In: *Journal of The Electrochemical Society* 163.14 (2016), A3046–A3062. ISSN: 00134651. DOI: 10.1149/2.0701614jes.

[117] Y. Zhang, C. Zhao, and Z. Guo. "Simulation of crack behavior of secondary particles in Li-ion battery electrodes during lithiation/de-lithiation cycles". In: *International Journal of Mechanical Sciences* 155 (2019), pp. 178–186. ISSN: 00207403. DOI: 10.1016/j.ijmecsci.2019.02.042.

[118] Z. Wei, F. Yang, K. Bi, J. Yang, and Y. Chen. "Tunable Anisotropic Thermal Conductivity and Elastic Properties in Intercalated Graphite via Lithium Ions". In: *The Journal of Physical Chemistry C* 122.3 (2018), pp. 1447–1455. ISSN: 1932-7447. DOI: 10.1021/acs.jpcc.7b09717.

[119] S. Loos, D. Gruner, M. Abdel-Hafiez, J. Seidel, R. Hüttl, A. U. Wolter, K. Bohmhammel, and F. Mertens. "Heat capacity (C) and entropy of olivine-type LiFePO4 in the temperature range (2 to 773) K". In: *The Journal of Chemical Thermodynamics* 85 (2015), pp. 77–85. ISSN: 00219614. DOI: 10.1016/j.jct.2015.01.007.

[120] D. Oehler, J. Bender, P. Seegert, and T. Wetzel. "Investigation of the Effective Thermal Conductivity of Cell Stacks of Li–Ion Batteries". In: *Energy Technology* (2020), p. 2000722. ISSN: 2194-4296. DOI: 10.1002/ente.202000722. URL: https://onlinelibrary.wiley.com/doi/full/10.1002/ente.202000722.

[121] D. Oehler, P. Seegert, and T. Wetzel. "Modeling the Thermal Conductivity of Porous Electrodes of Li–Ion Batteries as a Function of Microstructure Parameters". In: *Energy Technology* (2020), p. 2000574. ISSN: 21944288. DOI: 10.1002/ente.202000574.

[122] A. Vadakkepatt, B. Trembacki, S. R. Mathur, and J. Y. Murthy. "Bruggeman's Exponents for Effective Thermal Conductivity of Lithium-Ion Battery Electrodes". In: *Journal of The Electrochemical Society* 163.2 (2016), A119–A130. ISSN: 00134651. DOI: 10.1149/2.0151602jes.

[123] J. Wilhelm. "Cycling capacity recovery effect: A coulombic efficiency and post-mortem study". In: *Journal of Power Sources* 365 (2017), pp. 327–338. DOI: 10.1016/j.jpowsour.2017.08.090.

[124] P. M. Gomadam, R. E. White, and J. W. Weidner. "Modeling Heat Conduction in Spiral Geometries". In: *Journal of the Electrochemical Society* 150.10 (2003), A1339. ISSN: 0013-4651. DOI: 10.1149/1.1605743.

[125] O. Queisser, L. Cloos, F. Boehm, D. Oehler, and T. Wetzel. "Impact of the Level of Homogenization in 3D Thermal Simulation on the Internal Temperature Distribution of Li–Ion Battery Cells". In: *Energy Technology* (2021), p. 2000915. ISSN: 2194-4296. DOI: 10.1002/ente.202000915.

[126] B. Shi, H. Zhang, Y. Qi, and L. Yang. "Calculation Model of Effective Thermal Conductivity of a Spiral-wound Lithium Ion Battery". In: *Journal of Thermal Science* 27.6 (2018), pp. 572–579. ISSN: 1003-2169. DOI: 10.1007/s11630-018-1060-x.

[127] M. Guo and R. E. White. "Mathematical model for a spirally-wound lithium-ion cell". In: *Journal of Power Sources* 250 (2014), pp. 220–235. ISSN: 03787753. DOI: 10.1016/j.jpowsour.2013.11.023.

[128] Y. Yang, H.-Y. An, M.-L. Zhang, W.-L. Song, Le Yang, and H.-S. Chen. “Temperature field evolution of cylindrical battery: In-situ visualizing experiments and high fidelity internal morphology simulations”. In: *Journal of Power Sources* 499 (2021), p. 229910. ISSN: 03787753. DOI: 10.1016/j.jpowsour.2021.229910.

[129] J. Yi, U. S. Kim, C. B. Shin, T. Han, and S. Park. “Three-Dimensional Thermal Modeling of a Lithium-Ion Battery Considering the Combined Effects of the Electrical and Thermal Contact Resistances between Current Collecting Tab and Lead Wire”. In: *Journal of The Electrochemical Society* 160.3 (2013), A437–A443. ISSN: 00134651. DOI: 10.1149/2.039303jes.

[130] M. Akbarzadeh, T. Kalogiannis, J. Jaguemont, J. He, L. Jin, M. Berecibar, and J. van Mierlo. “Thermal modeling of a high-energy prismatic lithium-ion battery cell and module based on a new thermal characterization methodology”. In: *Journal of Energy Storage* 32 (2020), p. 101707. ISSN: 2352152X. DOI: 10.1016/j.est.2020.101707.

[131] D. Mishra and A. Jain. “Multi-Mode Heat Transfer Simulations of the Onset and Propagation of Thermal Runaway in a Pack of Cylindrical Li-Ion Cells”. In: *Journal of the Electrochemical Society* 168.2 (2021), p. 020504. ISSN: 0013-4651. DOI: 10.1149/1945-7111/abdc7b.

[132] J. V. Barreras, C. Fleischer, A. E. Christensen, M. Swierczynski, E. Schaltz, S. J. Andreasen, and D. U. Sauer. “An Advanced HIL Simulation Battery Model for Battery Management System Testing”. In: *IEEE Transactions on Industry Applications* 52.6 (2016), pp. 5086–5099. ISSN: 00939994. DOI: 10.1109/TIA.2016.2585539.

[133] T. Dong, Y. Wang, W. Cao, W. Zhang, and F. Jiang. “Analysis of lithium-ion battery thermal models inaccuracy caused by physical properties uncertainty”. In: *Applied Thermal Engineering* 198 (2021), p. 117513. ISSN: 13594311. DOI: 10.1016/j.applthermaleng.2021.117513.

[134] Z. Li, J. Zhang, B. Wu, J. Huang, Z. Nie, Y. Sun, F. An, and N. Wu. “Examining temporal and spatial variations of internal temperature in large-format laminated battery with embedded thermocouples”. In: *Journal of Power Sources* 241 (2013), pp. 536–553. ISSN: 03787753. DOI: 10.1016/j.jpowsour.2013.04.117.

[135] T. Amietszajew, E. McTurk, J. Fleming, and R. Bhagat. “Understanding the limits of rapid charging using instrumented commercial 18650 high-energy Li-ion cells”. In: *Electrochimica Acta* 263 (2018), pp. 346–352. ISSN: 00134686. DOI: 10.1016/j.electacta.2018.01.076.

[136] T. Waldmann and M. Wohlfahrt-Mehrens. “In-Operando Measurement of Temperature Gradients in Cylindrical Lithium-Ion Cells during High-Current Discharge”. In: *ECS Electrochemistry Letters* 4.1 (2015), A1–A3. ISSN: 2162-8726. DOI: 10.1149/2.0031501eel.

[137] G. Zhang, L. Cao, S. Ge, C.-Y. Wang, C. E. Shaffer, and C. D. Rahn. “In Situ Measurement of Radial Temperature Distributions in Cylindrical Li-Ion Cells”. In: *Journal of the Electrochemical Society* 161.10 (2014), A1499–A1507. ISSN: 0013-4651. DOI: 10.1149/2.0051410jes.

[138] M. Al-Zareer, C. Da Silva, and C. H. Amon. “Predicting anisotropic thermophysical properties and spatially distributed heat generation rates in pouch lithium-ion batteries”. In: *Journal of Power Sources* 510 (2021), p. 230362. ISSN: 03787753. DOI: 10.1016/j.jpowsour.2021.230362.

[139] S. Balkur, N. Roy Chowdhury, J. Groot, and T. Thiringer. “A cost and time effective novel methodology to determine specific heat capacity of lithium-ion cells”. In: *Journal of Power Sources* 500 (2021), p. 229981. ISSN: 03787753. DOI: 10.1016/j.jpowsour.2021.229981.

[140] R. Rizk, H. Louahlia, H. Gualous, and P. Schaetzel. “Experimental analysis and transient thermal modelling of a high capacity prismatic lithium-ion battery”. In: *International Communications in Heat and Mass Transfer* 94 (2018), pp. 115–125. ISSN: 07351933. DOI: 10.1016/j.icheatmasstransfer.2018.03.018.

[141] C. Forgez, D. Vinh Do, G. Friedrich, M. Morcrette, and C. Delacourt. “Thermal modeling of a cylindrical LiFePO4/graphite lithium-ion battery”. In: *Journal of Power Sources* 195.9 (2010), pp. 2961–2968. ISSN: 03787753. DOI: 10.1016/j.jpowsour.2009.10.105.

[142] H. D. Baehr and K. Stephan. *Heat and Mass Transfer*. 3rd ed. 2011. Berlin, Heidelberg: Springer Berlin Heidelberg, 2011. ISBN: 978-3-642-20021-2.

[143] A. Hales, M. W. Marzook, L. Bravo Diaz, Y. Patel, and G. Offer. “The Surface Cell Cooling Coefficient: A Standard to Define Heat Rejection from Lithium Ion Battery Pouch Cells”. In: *Journal of the Electrochemical Society* 167.2 (2020), p. 020524. ISSN: 0013-4651. DOI: 10.1149/1945-7111/ab6985.

[144] A. Hales, L. B. Diaz, M. W. Marzook, Y. Zhao, Y. Patel, and G. Offer. “The Cell Cooling Coefficient: A Standard to Define Heat Rejection from Lithium-Ion Batteries”. In: *Journal of the Electrochemical Society* 166.12 (2019), A2383–A2395. ISSN: 0013-4651. DOI: 10.1149/2.0191912jes.

[145] M. Steinhardt, E. I. Gillich, M. Stiegler, and A. Jossen. “Thermal conductivity inside prismatic lithium-ion cells with dependencies on temperature and external compression pressure”. In: *Journal of Energy Storage* 32 (2020), p. 101680. ISSN: 2352152X. DOI: 10.1016/j.est.2020.101680.

[146] S.-C. Chen, Y.-Y. Wang, and C.-C. Wan. “Thermal Analysis of Spirally Wound Lithium Batteries”. In: *Journal of The Electrochemical Society* 153.4 (2006), A637. ISSN: 00134651. DOI: 10.1149/1.2168051.

[147] T. M. Bandhauer, S. Garimella, and T. F. Fuller. “Temperature-dependent electrochemical heat generation in a commercial lithium-ion battery”. In: *Journal of Power Sources* 247 (2014), pp. 618–628. ISSN: 03787753. DOI: 10.1016/j.jpowsour.2013.08.015.

[148] Z. Sun, C. Wang, Q. Zhou, and H. Xu. “Sensitivity Study of Battery Thermal Response to Cell Thermophysical Parameters”. In: *SAE Technical Paper Series*. SAE Technical Paper Series. SAE International400 Commonwealth Drive, Warrendale, PA, United States, 2021. DOI: 10.4271/2021-01-0751.

[149] M. Lagnoni, C. Nicolella, and A. Bertei. “Survey and sensitivity analysis of critical parameters in lithium-ion battery thermo-electrochemical modeling”. In: *Electrochimica Acta* 394 (2021), p. 139098. ISSN: 00134686. DOI: 10.1016/j.electacta.2021.139098.

[150] *VDI-Wärmeatlas: Mit 320 Tabellen*. 11., bearb. und erw. Aufl. VDI-Buch. Berlin: Springer Vieweg, 2013. ISBN: 978-3-642-19981-3. DOI: 10.1007/978-3-642-19981-3.

[151] D. R. Lide. *CRC handbook of chemistry and physics, 2003-2004: A ready-reference book of chemical and physical data*. 84th ed. Boca Raton, Fla.: CRC Press, 2003. ISBN: 978-0849304842.

[152] K.-H. Schröder and J. Weiser. *Elektrische Kontakte, Werkstoffe und Anwendungen: Grundlagen, Technologien, Prüfverfahren*. 3. Aufl. 2016. Berlin, Heidelberg: Springer Berlin Heidelberg, 2016. ISBN: 978-3-642-45427-1. URL: http://nbn-resolving.org/urn:nbn:de:bsz:31-epflicht-1503208.

[153] G. Scheller and S. Krummeck. *Measurement uncertainty of a temperature measurement chain: With sample calculations*. Fulda: JUMO, 2018. ISBN: 978-3-935742-13-9.

[154] M. Grabe. *Measurement uncertainties in science and technology*. Second edition. Cham et al.: Springer, 2014. ISBN: 9783319048888. DOI: 10.1007/978-3-319-04888-8. URL: http://search.ebscohost.com/login.aspx?direct=true&scope=site&db=nlebk&db=nlabk&AN=779729.

[155] L. Sheng, L. Su, and H. Zhang. "Experimental determination on thermal parameters of prismatic lithium ion battery cells". In: *International Journal of Heat and Mass Transfer* 139 (2019), pp. 231–239. ISSN: 00179310. DOI: 10.1016/j.ijheatmasstransfer.2019.04.143.

[156] S. J. Bazinski, X. Wang, B. P. Sangeorzan, and L. Guessous. "Measuring and assessing the effective in-plane thermal conductivity of lithium iron phosphate pouch cells". In: *Energy* 114 (2016), pp. 1085–1092. ISSN: 03605442. DOI: 10.1016/j.energy.2016.08.087.

[157] L. Aiello, G. Kovachev, B. Brunnsteiner, M. Schwab, G. Gstrein, W. Sinz, and C. Ellersdorfer. "In Situ Measurement of Orthotropic Thermal Conductivity on Commercial Pouch Lithium-Ion Batteries with Thermoelectric Device". In: *Batteries* 6.1 (2020), p. 10. ISSN: 2313-0105. DOI: 10.3390/batteries6010010.

[158] S. J. Drake, D. A. Wetz, J. K. Ostanek, S. P. Miller, J. M. Heinzel, and A. Jain. "Measurement of anisotropic thermophysical properties of cylindrical Li-ion cells". In: *Journal of Power Sources* 252 (2014), pp. 298–304. ISSN: 03787753. DOI: 10.1016/j.jpowsour.2013.11.107.

[159] J. G. Hust and P. J. Giarratano. *Thermal Conductivity and Electrical Resistivity Standard Reference Materials: Austenitic Stainless Steel, SRM's 735 and 798, from 4 to 1200 (March 1975)*. Vol. 260-46. NBS Special Publication. 1975.

[160] V. V. Mirkovich, ed. *Thermal Conductivity 15*. Boston, MA: Springer US, 1978. ISBN: 978-1-4615-9083-5. DOI: 10.1007/978-1-4615-9083-5. URL: http://dx.doi.org/10.1007/978-1-4615-9083-5.

[161] C. Vargel. *Corrosion of Aluminium*. 1st ed. Oxford: Elsevier Science & Technology, 2004. ISBN: 0-08-044495-4.

[162] R. W. Powell, C. Y. Ho, and P. E. Liley. *Thermal Conductivity of Selected Materials*. Vol. 8. NSRDS-NBS. 1966.

[163] H. Czichos, T. Saito, and L. Smith, eds. *Springer handbook of materials measurement methods*. Springer handbooks. Berlin: Springer, 2006. ISBN: 978-3-540-30300-8. URL: http://dx.doi.org/10.1007/978-3-540-30300-8.

[164] A. Palacios, L. Cong, M. E. Navarro, Y. Ding, and C. Barreneche. "Thermal conductivity measurement techniques for characterizing thermal energy storage materials – A review". In: *Renewable and Sustainable Energy Reviews* 108 (2019), pp. 32–52. ISSN: 13640321. DOI: 10.1016/j.rser.2019.03.020.

[165] I. Williams and R. E. Shawyer. *Certification report for a pyrex glass reference material for thermal conductivity between -75°C and 195°C CRM 039*. 1991.

[166] R. P. Tye and D. Hume. "Reference materials for thermal transport properties measurements". In: *Journal of Thermal Analysis and Calorimetry* 131.1 (2018), pp. 289–299. ISSN: 1388-6150. DOI: 10.1007/s10973-017-6532-9.

[167] S. Koch. "Thermal Propagation in Lithium-Ionen-Batterien Methoden, Maßnahmen und Auswirkungen". Dissertation. Stuttgart, 2019.

[168] S. D. Lubner, S. Kaur, Y. Fu, V. Battaglia, and R. S. Prasher. "Identification and characterization of the dominant thermal resistance in lithium-ion batteries using operando 3-omega sensors". In: *Journal of Applied Physics* 127.10 (2020), p. 105104. ISSN: 00218979. DOI: 10.1063/1.5134459.

[169] W. N. D. Santos and R. Gregorio. "Hot-wire parallel technique: A new method for simultaneous determination of thermal properties of polymers". In: *Journal of Applied Polymer Science* 85.8 (2002), pp. 1779–1786. ISSN: 0021-8995. DOI: 10.1002/app.10681.

[170] M. J. Assael, M. Dix, K. Gialou, L. Vozar, and W. A. Wakeham. "Application of the Transient Hot-Wire Technique to the Measurement of the Thermal Conductivity of Solids". In: *International Journal of Thermophysics* 23.3 (2002), pp. 615–633. DOI: 10.1023/A:1015494802462.

[171] J. Zhang, B. Wu, Z. Li, and J. Huang. "Simultaneous estimation of thermal parameters for large-format laminated lithium-ion batteries". In: *Journal of Power Sources* 259 (2014), pp. 106–116. ISSN: 03787753. DOI: 10.1016/j.jpowsour.2014.02.079.

[172] O. Almanza, M. A. Rodríguez-Pérez, and J. A. de Saja. "Applicability of the transient plane source method to measure the thermal conductivity of low-density polyethylene foams". In: *Journal of Polymer Science Part B: Polymer Physics* 42.7 (2004), pp. 1226–1234. ISSN: 08876266. DOI: 10.1002/polb.20005.

[173] X. Pan, X. Cui, S. Liu, Z. Jiang, Y. Wu, and Z. Chen. "Research Progress of Thermal Contact Resistance". In: *Journal of Low Temperature Physics* 201.3-4 (2020), pp. 213–253. ISSN: 0022-2291. DOI: 10.1007/s10909-020-02497-0.

[174] M. B. Ahmed, S. Shaik, and A. Jain. "Measurement of radial thermal conductivity of a cylinder using a time-varying heat flux method". In: *International Journal of Thermal Sciences* 129 (2018), pp. 301–308. ISSN: 12900729. DOI: 10.1016/j.ijthermalsci.2018.03.008.

[175] O. S. Burheim, M. A. Onsrud, J. G. Pharoah, F. Vullum-Bruer, and P. J. S. Vie. "Thermal Conductivity, Heat Sources and Temperature Profiles of Li-Ion Batteries". In: *ECS Transactions* 58.48 (2014), pp. 145–171. ISSN: 1938-6737. DOI: 10.1149/05848.0145ecst.

[176] A. Arzberger, M. Hellenbrand, and D. Sauer. "The change of thermal conductivity of Lithium-Ion pouch cells with operating point and what this means for battery thermal management". In: *AABC 2014 - Advanced Automotive Battery Confernce, AABTAM Symposium - Advanced Automotive Battery Technology, Application and Market, AABTAM 2014*. 2014.

[177] E. Barsoukov, J. H. Jang, and H. Lee. "Thermal impedance spectroscopy for Li-ion batteries using heat-pulse response analysis". In: *Journal of Power Sources* 109.2 (2002), pp. 313–320. ISSN: 03787753. DOI: 10.1016/S0378-7753(02)00080-0.

[178] J. P. Schmidt, D. Manka, D. Klotz, and E. Ivers-Tiffée. "Investigation of the thermal properties of a Li-ion pouch-cell by electrothermal impedance spectroscopy". In: *Journal of Power Sources* 196.19 (2011), pp. 8140–8146. ISSN: 03787753. DOI: 10.1016/j.jpowsour.2011.05.047.

[179] P. Keil, K. Rumpf, and A. Jossen. "Thermal characterization of Li-ion batteries: Accelerating Thermal Impedance Spectroscopy". In: *Lecture notes on impedance spectroscopy*. Ed. by O. Kanoun. Boca Raton, Fla.: CRC Press, 2015, pp. 39–52. ISBN: 978-1-138-02754-1. DOI: 10.1201/b18134-9.

[180] T. S. Bryden, B. Dimitrov, G. Hilton, C. Ponce de León, P. Bugryniec, S. Brown, D. Cumming, and A. Cruden. "Methodology to determine the heat capacity of lithium-ion cells". In: *Journal of Power Sources* 395 (2018), pp. 369–378. ISSN: 03787753. DOI: 10.1016/j.jpowsour.2018.05.084.

[181] M. Al-Zareer, A. Michalak, C. Da Silva, and C. H. Amon. "Predicting specific heat capacity and directional thermal conductivities of cylindrical lithium-ion batteries: A combined experimental and simulation framework". In: *Applied Thermal Engineering* 182 (2021), p. 116075. ISSN: 13594311. DOI: 10.1016/j.applthermaleng.2020.116075.

[182] N. S. Spinner, R. Mazurick, A. Brandon, S. L. Rose-Pehrsson, and S. G. Tuttle. "Analytical, Numerical and Experimental Determination of Thermophysical Properties of Commercial 18650 LiCoO 2 Lithium-Ion Battery". In: *Journal of The Electrochemical Society* 162.14 (2015), A2789–A2795. ISSN: 00134651. DOI: 10.1149/2.0871514jes.

[183] R. C. Kerschbaumer et al. "Comparison of steady-state and transient thermal conductivity testing methods using different industrial rubber compounds". In: *Polymer Testing* 80 (2019), p. 106121. ISSN: 01429418. DOI: 10.1016/j.polymertesting.2019.106121.

[184] P.-L. Lapointe. "Application of the thermal impedance spectroscopy method in three dimensions to a large prismatic Li-ion cell". In: *2013 World Electric Vehicle Symposium and Exhibition (EVS27)*. IEEE, 2013, pp. 1–6. ISBN: 978-1-4799-3832-2. DOI: 10.1109/EVS.2013.6915051.

[185] A. L. Woodcraft. "Predicting the thermal conductivity of aluminium alloys in the cryogenic to room temperature range". In: *Cryogenics* 45.6 (2005), pp. 421–431. ISSN: 00112275. DOI: 10.1016/j.cryogenics.2005.02.003.

[186] C. G. Thomas. *Research methodology and scientific writing*. Second edition. Cham and India: Springer and ANE Books, 2021. ISBN: 9783030648657.